AD-A267 943

NTATION PAGE

Form Approved
OMB No 0704-0188

[illegible] Paperwork Reduction Project (0704-0188), Washington, DC 20503

1. AGENCY USE ONLY *(Leave blank)*

2. REPORT DATE
May 1993

3. REPORT TYPE AND DATES COVERED
THESIS/DISSERTATION

4. TITLE AND SUBTITLE
Interfacial Shear Behavior and Its Influence on Fiber Damage in Sapphire-Reinforced Gamma Titamium Aluminide Composites.

5. FUNDING NUMBERS

6. AUTHOR(S)
Capt Jay M. Galbraith

7. PERFORMING ORGANIZATION NAME(S) AND ADDRESS(ES)
AFIT Student Attending: Pennsylvania State University

8. PERFORMING ORGANIZATION REPORT NUMBER
AFIT/CI/CIA-93-001D

9. SPONSORING/MONITORING AGENCY NAME(S) AND ADDRESS(ES)
DEPARTMENT OF THE AIR FORCE
AFIT/CI
2950 P STREET
WRIGHT-PATTERSON AFB OH 45433-7765

DTIC
ELECTE
AUG 17 1993
S C D

10. SPONSORING/MONITORING AGENCY REPORT NUMBER

11. SUPPLEMENTARY NOTES

12a. DISTRIBUTION/AVAILABILITY STATEMENT
Approved for Public Release IAW 190-1
Distribution Unlimited
MICHAEL M. BRICKER, SMSgt, USAF
Chief Administration

12b. DISTRIBUTION CODE

13. ABSTRACT *(Maximum 200 words)*

93-19028

14. SUBJECT TERMS

15. NUMBER OF PAGES
184

16. PRICE CODE

17. SECURITY CLASSIFICATION OF REPORT

18. SECURITY CLASSIFICATION OF THIS PAGE

19. SECURITY CLASSIFICATION OF ABSTRACT

20. LIMITATION OF ABSTRACT

NSN 7540-01-280-5500

Standard Form 298 (Rev. 2-89)

The Pennsylvania State University

The Graduate School

Department of Materials Science and Engineering

INTERFACIAL SHEAR BEHAVIOR AND ITS INFLUENCE ON FIBER DAMAGE IN SAPPHIRE-REINFORCED GAMMA TITANIUM ALUMINIDE COMPOSITES

A Thesis in

Metals Science and Engineering

by

Jay M. Galbraith

Submitted in Partial Fulfillment
of the Requirements
for the Degree of

Doctor of Philosophy

May 1993

Accession For
NTIS CRA&I ☑
DTIC TAB ☐
Unannounced ☐
Justification
By
Distribution /
Availability Codes
Dist | Avail and / or Special
A-1

DTIC QUALITY INSPECTED 3

We approve the thesis of Jay M. Galbraith.

Date of Signature

Donald A. Koss — 12/21/92

Donald A. Koss
Professor of Metallurgy
In Charge of Graduate Programs in
Metals Science and Engineering
Thesis Co-Adviser
Chair of Committee

John R Hellmann — 12/21/92

John R. Hellmann
Assistant Professor of Ceramic Science
and Engineering
Thesis Co-Adviser

Lee J Cuddy — 12/21/92

Lee J. Cuddy
Associate Professor of Metallurgy

12/21/92

Paul R. Howell
Professor of Metallurgy

12/21/92

M. Nabil Kallas
Assistant Professor of Engineering Graphics
Special Member

ABSTRACT

The interfacial shear behavior and its influence on fiber damage in sapphire-reinforced TiAl composites was investigated using a combination of microscopic characterization, indentation crack growth results, fiber pushout testing, fiber displacement measurements, and computational analyses. Two inter-related phenomena were studied: (1) residual stresses and resulting damage within fibers intersecting a free surface and (2) fiber/matrix interfacial strength behavior. In the first aspect of this study, experimental observations, finite element analysis, as well as analytical computations were all used to analyze the evolution of fiber damage that was observed in fibers intersecting a free surface in sapphire-reinforced Ti-48Al-1V composites. Experimental observations indicate that, under certain conditions, surface cracks introduced during specimen preparation will propagate along the fiber axis due to thermally-induced residual stresses. Finite element computations predict that significant thermally-induced residual tensile stresses exist in sapphire fibers embedded within TiAl-based matrices when they intersect and are oriented normal to a free surface. Indentation crack growth behavior within the sapphire fibers provided experimental validation of the predicted stress state. Finally, the application of an exact elastic analysis indicates that tensile stresses also exist within fibers oriented parallel to and near a free surface. The results suggest that ductile fiber coatings or a decreased interfacial shear strength can decrease the thermally-induced tensile stresses and reduce or eliminate fiber damage.

The interfacial shear behavior was examined using thin-slice fiber pushout testing. The results indicate that the average interfacial shear strength of the Ta-coated sapphire/Ti-48Al-1V system (336 ± 11 MPa) is nearly twice the magnitude of that measured in sapphire/Ti-48Al-2Cr-2Nb (170 ± 22 MPa). A significant observation is that both systems show that interfacial failure initiates on the specimen's backface, opposite the indenter. The results, when combined with those wherein specimen bending was eliminated, suggest that the criterion for interfacial shear is based on a critical value of the shear stress at the interface. Fiber pushout and reverse push-back test results show that matrix plasticity plays a dominant role in the "frictional" sliding resistance of debonded fibers and interface wear. In all cases, experimental observations could only be understood through careful attention to the associated mechanics of fiber pushout testing.

TABLE OF CONTENTS

LIST OF FIGURES........ vii

LIST OF TABLES........ xii

ACKNOWLEDGEMENTS........ xiii

Chapter 1. INTRODUCTION........ 1

Chapter 2. LITERATURE SURVEY........ 4

- 2.1. Background........ 4
- 2.2. Damage to Sapphire Fibers in Metal and Intermetallic Matrix Composites........ 6
- 2.3. Residual Stress and Resulting Microdamage........ 8
- 2.4. Use of Fiber Coatings........ 11
- 2.5. Interfacial Shear Strength........ 12
  - 2.5.1. Chemical Interaction........ 17
  - 2.5.2. Mechanical Interlocking........ 19
  - 2.5.3. Effect of Fiber Coatings........ 21
  - 2.5.4. Tantalum Fiber Coatings for Sapphire/TiAl IMCs........ 22
- 2.6. Interfacial Shear Strength Determination........ 23
  - 2.6.1. Test Methods........ 24
  - 2.6.2. Mechanics of the Thin-Slice Fiber Pushout Test........ 26
- 2.7. Fiber Sliding Stress........ 30
- 2.8. Statement of Purpose........ 32

Chapter 3. EXPERIMENTAL PROCEDURES........ 35

- 3.1. Specimen Fabrication........ 35
- 3.2. Microscopic Characterization........ 41
- 3.3. Assessment of Fiber Damage........ 42
- 3.4. Experimental Validation of FEM Predicted Stress States Using Indentation Crack Growth Analysis........ 44
- 3.5. Indentation Fiber Pushout Testing........ 49
  - 3.5.1. Indentation Pushout Test Apparatus........ 49
  - 3.5.2. Specimen Support Configuration........ 51
  - 3.5.3. Test Methods........ 55
- 3.6. Fiber Displacement Measurements Using Scanning Laser Microscopy........ 58

Chapter 4. RESULTS AND DISCUSSION ... 61

- 4.1. Interface Microscopic Characterization. ... 61
- 4.2. Residual Stresses and Resulting Damage within Fibers Intersecting a Free Surface ... 79
  - 4.2.1. Characteristics of Fiber Damage. ... 79
  - 4.2.2. Computational Analysis of Thermally-Induced Residual Stress States. ... 84
    - 4.2.2.1. Finite Element Analysis and Experimental Validation of its Predicted Stress State. ... 86
    - 4.2.2.2. Exact Elastic Analysis of a Fiber Parallel to a Free Surface. ... 93
- 4.3. Fiber/Matrix Interfacial Strength Behavior. ... 106
  - 4.3.1. Finite Element Computations of the Interfacial Stress Distributions ... 107
  - 4.3.2. Interfacial Failure Sequence. ... 115
    - 4.3.2.1. Interfacial Failure Sequence in the Tantalum-Coated Sapphire/Ti-48Al-1V System. ... 116
    - 4.3.2.2. Interfacial Failure Sequence in the Sapphire/Ti-48Al-2Cr-2Nb System ... 129
    - 4.3.2.3. Comparison of Interfacial Failure Behaviors. ... 133
  - 4.3.3. Analysis of Top and Backface Fiber Displacement Measurements ... 141
  - 4.3.4. Influence of Specimen Bending on Interface Shear Behavior during Thin-Slice Pushout Testing ... 157
  - 4.3.5. Contribution of Matrix Plasticity to the "Frictional" Sliding Resistance of Debonded Fibers. ... 165

Chapter 5. SUMMARY ... 172

REFERENCES ... 177

LIST OF FIGURES

Figure 1. Thermally-induced residual stress state in the interfacial region................ 10

Figure 2. Influence of fiber/matrix interfacial shear strength on intermetallic matrix composite failure behavior (adapted from Evans [47]).................. 14

Figure 3. Three methods commonly used to examine the interfacial shear behavior of fiber-reinforced composites (adapted from Ferber et al. [79]).. 25

Figure 4. Effect of specimen thickness on (a) the shear stress and (b) radial stress distributions at the fiber/matrix interface of a sapphire-reinforced niobium composite (taken from Kallas et al. [84]).................... 28

Figure 5. Helium gas-atomized Ti-48Al-1V powder (a) in the as-received (-35 mesh, i.e., < 500 μm) condition and (b) after grinding to -325 mesh (< 45 μm) in a Bleuler Laboratory Swing Mill.................................. 37

Figure 6. A typical uncoated, flame-polished fiber prior to hot pressing. 39

Figure 7. Tantalum-coated fiber prior to incorporating into the Ti-48Al-1V matrix. 40

Figure 8. Fracture pattern formed following indentation of a sapphire fiber............. 46

Figure 9. Configuration of the indentation pushout test apparatus (photographs courtesy of Moose [64]).................................. 50

Figure 10. Stainless steel support plate with 254 μm diameter holes and brass spring-clips that secure specimens (photograph courtesy of Moose [64]).. 53

Figure 11. Procedure for producing a hole on the specimen's backface exactly the same size and shape as the fiber's cross-section (taken from Koss et al. [105]).. 54

Figure 12. Backface of a typical specimen (a) before and (b) after the nickel "back-plating" procedure. 56

Figure 13. Evidence of low specimen/nickel plate adherence at the edge of the hole over the fiber. 57

Figure 14. Micrograph of a typical scanning laser microscope surface profile measurement. 60

Figure 15. Typical photomicrographs showing the distribution of the α_2 and γ phases in the Ti-48Al-1V matrix following vacuum hot pressing.............. 63

Figure 16. Backscattered electron micrograph of a polished and unetched Ti-48Al-1V specimen. 65

Figure 17. High magnification SEM image of the uncoated sapphire/Ti-48Al-1V interface following vacuum hot pressing. 67

Figure 18. Sapphire fiber surface (a) before and (b) after being vacuum hot pressed in the Ti-48Al-1V matrix. 68

Figure 19. High magnification SEM micrographs showing the sapphire fiber surface (a) after and (b) before being vacuum hot pressed in the Ti-48Al-1V matrix. 69

Figure 20. Evidence that the tantalum layer in the Ta-coated sapphire Ti-48Al-1V system acts as a diffusion barrier and forms a 0.5 to 1.0 μm wide interphase zone adjacent to the fiber 70

Figure 21. Surface of a Ta-coated sapphire fiber following hot pressing in the Ti-48Al-1V matrix and subsequent chemical removal of the matrix and tantalum coating. 71

Figure 22. Semi-quantitative tantalum concentration profile across the sapphire/Ta/Ti-48Al-1V interface obtained from electron probe microanalysis. 73

Figure 23. Typical SEM micrograph of the sapphire-reinforced Ti-48Al-2Cr-2Nb microstructure following composite fabrication. 74

Figure 24. Evidence that a severe reaction occurs between uncoated sapphire and the Ti-48Al-2Cr-2Nb matrix during composite fabrication 76

Figure 25. Sapphire fiber surface following hot pressing in the Ti-48Al-2Cr-2Nb matrix and subsequent chemical removal. 77

Figure 26. Evidence that cracks are only at the ends of fibers intersecting a free surface. 80

Figure 27. SEM micrographs showing the extent of fiber fracture and crack orientation with respect to the fiber axis in uncoated sapphire-reinforced Ti-48Al-1V (taken from [93]). 83

Figure 28. Saw-toothed fracture surface showing (a) the crystallographic nature of the fracture path and (b) the presence of voids that may act as stress concentrations. 85

Figure 29. Free and sub-surface thermoelastic residual stress profiles in the fiber for a sapphire-reinforced TiAl composite with a 0.1 fiber volume fraction (predicted by FEM [84] and taken from [93]). 88

Figure 30. SEM micrographs showing the characteristic "mud cake" fracture pattern on the cross-sectioned fiber surface in sapphire-reinforced Ti-48Al-1V (taken from [93]) 89

Figure 31. Predicted stress intensity as a function of crack size in sapphire-reinforced TiAl for a 4.9 N indentation load. 91

Figure 32. The plots of the predicted stress intensities K_r and K as a function of crack size in sapphire-reinforced TiAl (4.9 N indentation load) showing the importance of the threshold stress intensity factors for sapphire in reactive environments. 94

Figure 33. Fiber of radius R (whose cross-section is shown) embedded within the matrix and located near a free surface (adapted from Lee et al. [119]). 96

Figure 34. Thermally-induced residual stress profiles within a sapphire-reinforced TiAl composite as a function of the relative distance between a fiber and a free surface (predicted by exact elastic model). 97

Figure 35. Micrographs showing the extent of fiber fracture and crack orientation with respect to the axis of a sapphire fiber that is partially embedded within the Ti-48Al-1V matrix and oriented nearly parallel to a free surface. 101

Figure 36. Thermoelastic residual stress profiles within a sapphire fiber when it just intersects a free surface. 104

Figure 37. Thermally-induced interfacial shear stress ($\tau_{r\theta}$) as a function of angular distance, θ, around the sapphire/TiAl interface when a fiber just intersects a free surface. 105

Figure 38. Schematic of the fiber pushout test configuration used for axisymmetric finite element modeling 108

Figure 39. Thermally-induced residual stress distribution within the matrix adjacent to the fiber for a sapphire-reinforced TiAl composite with a 0.1 fiber volume fraction (predicted by FEM [84]). 109

Figure 40. Mechanically-induced stress distributions within the matrix adjacent to the fiber for several indenter loads on a sapphire-reinforced TiAl pushout specimen (predicted by FEM). 111

Figure 41. Combined thermal and mechanical interfacial stress distributions within the TiAl matrix for a thermal cool-down of 780 °C and indenter loads of (a) 20 N and (b) 30 N on a sapphire-reinforced TiAl pushout specimen. 114

Figure 42. Typical load-displacement behavior of the Ta-coated sapphire/Ti-48Al-1V system during fiber pushout testing. 117

Figure 43. Micrographs of scanning laser microscope surface profile measurements made at the (a) backface and (b) topface, but at the same position on the fiber perimeter, of a Ta-coated sapphire/Ti-48Al-1V specimen during region 2 load-displacement behavior. 119

Figure 44. Evidence that the interfacial crack on the backface of a Ta-coated sapphire/Ti-48Al-1V specimen deviates into the matrix instead of propagating around the fiber's perimeter. 121

Figure 45. Characterization of interfacial failure during region 3 load-displacement behavior of a Ta-coated sapphire/Ti-48Al-1V specimen. 123

Figure 46. Evidence that the topface interfacial crack deviates into the fiber and leaves a bonded fiber fragment adhering to the matrix during interface shear in the remaining bonded ligament. 128

Figure 47. Typical load-displacement behavior of the sapphire/Ti-48Al-2Cr-2Nb system during fiber pushout testing. 130

Figure 48. SEM micrograph of the topface of a sapphire/Ti-48Al-2Cr-2Nb specimen following fiber pushout shows that large-scale fiber displacement requires localized matrix plasticity to accommodate asperities on the fiber surface. 132

Figure 49. SEM micrograph of a sapphire/Ti-48Al-2Cr-2Nb specimen that was cut along a fiber axis. 135

Figure 50. Evidence of less plastic grooving and the occurrence of numerous interfacial cracks in the matrix following fiber pushout testing of a Ta-coated sapphire/Ti-48Al-1V specimen. 137

Figure 51. Comparison of the amount of matrix plasticity that occurs during fiber pushout and push-back testing of: (a) sapphire/Ti-48Al-2Cr-2Nb and (b) Ta-coated sapphire/Ti-48Al-1V. 138

Figure 52. The backface of fiber pushout specimens showing the fiber surface following testing. 140

Figure 53. Schematic illustration of a thin-slice fiber pushout specimen following a test that was stopped prior to load-drop/large-scale fiber displacement. 142

Figure 54. Net axial fiber/matrix displacement measurements (i.e., the differences between δ_B and δ_T given in Tables 5 and 6) as a function of average interfacial shear stress applied during interrupted pushout tests performed using a support hole configuration. 151

Figure 55. Net axial fiber/matrix displacement measurements (i.e., the differences between δ_B and δ_T given in Tables 5 and 6) as a function of average interfacial shear stress applied during interrupted pushout tests performed using a nickel back-plated configuration. 152

Figure 56. The fiber/matrix interface on the backface of Ta-coated sapphire/Ti-48Al-1V specimens following large-scale fiber displacement. 159

Figure 57. Evidence that the interfacial failure sequence in the Ta-coated sapphire/Ti-48Al-1V system is unaffected by test configuration. 161

Figure 58. The influence of support hole-to-fiber diameter ratio on the mechanically-induced stress distributions within the matrix adjacent to the fiber for the sapphire/NiAl system (taken from Koss et al. [105]). 163

Figure 59. Typical fiber sliding behavior during pushout and reverse push-back tests of a sapphire/Ti-48Al-2Cr-2Nb specimen. 167

LIST OF TABLES

Table 1. Typical room temperature properties of gamma titanium aluminide alloys and single-crystal sapphire 5

Table 2. Chemical analysis (atomic %) of matrix materials used in this study at various stages of processing 36

Table 3. Vickers and Knoop microhardness numbers (i.e., VHN and KHN respectively) measured in the matrix materials used for this study 78

Table 4. Summary of the thin-slice fiber pushout test results for the Ta-coated sapphire/Ti-48Al-1V and sapphire/Ti-48Al-2Cr-2Nb systems 133

Table 5. Fiber displacement measurements (made with respect to the matrix) as a function of average applied interfacial shear stress (τ_{AVG}) during pushout testing of the Ta-coated sapphire/Ti-48Al-1V system 143

Table 6. Fiber displacement measurements (made with respect to the matrix) as a function of average applied interfacial shear stress (τ_{AVG}) during pushout testing of the sapphire/Ti-48Al-2Cr-2Nb system 145

Table 7. Normalized backface debond crack length (l_B/t) estimates as a function of average applied interfacial shear stress (τ_{AVG}) during region 2 load-displacement behavior of the Ta-coated sapphire/Ti-48Al-1V system 155

Table 8. Normalized backface debond crack length (l_B/t) estimates as a function of average applied interfacial shear stress (τ_{AVG}) during region 2 load-displacement behavior of the sapphire/Ti-48Al-2Cr-2Nb system 156

Table 9. Effect of test configuration: comparison of results with (i.e., use of a support hole-to-fiber diameter ratio of ≈1.6) and without (i.e., use of a Ni back-plate) specimen bending 158

ACKNOWLEDGEMENTS

I wish to express my sincere thanks to Drs. Donald A. Koss and John R. Hellmann, my thesis advisors, for their patience, guidance, and encouragement during this research project. Special thanks are also extended to Drs. M. Nabil Kallas, Lee J. Cuddy, and Paul R. Howell for their helpfulness and for serving on my doctoral committee. I would like to acknowledge and thank my colleagues who provided valuable assistance in many ways: Nabil Kallas (for his FEM work), Clark Moose, Rick Petrich, and Ed Rhyne. Also, the assistance of many of the students, faculty, and staff of the Center for Advanced Materials and the Metals Science and Engineering Program at Penn State is gratefully acknowledged.

I would like to gratefully acknowledge the research funding of the National Aeronautics and Space Administration through grant No. NAGW-1381. Special thanks is given to the many individuals at the NASA Lewis Research Center for their technical advice and assistance.

I am very grateful to the US Air Force which selected me for this position and provided funding for my studies. Special appreciation is given to my program manager, Lt. Col. James P. Waller, and the personnel at the Wright Research and Development Center's Materials Laboratory.

I am deeply indebted to my wife, Diane, and our six children for their steadfast love, gentle patience, and perseverance in prayer during my long hours of study. I am sincerely thankful for the unselfish support and encouragement of my father and mother during my entire education.

Most of all, I give all the credit to my heavenly Father who led me by His Holy Spirit, instructed me by His Word, and gave me His Son, Jesus Christ, as an example to

follow throughout this project, and He will continue to do so the rest of my life because of Jesus. It is my prayer that this research project will bring glory to Him.

"Trust in the Lord with all your heart, and do not lean on your own understanding. In all your ways acknowledge Him, and He will make your paths straight."

Proverbs 3: 5-6 (New American Standard Bible)

Chapter 1

INTRODUCTION

Over the last several years, the combined efforts of researchers from government, industry, and academia have focused on the development of high temperature engine and structural materials for the next generation of military and civil aircraft [1-4]. Materials for these applications must possess high strength, stiffness, creep resistance, and oxidation resistance at elevated temperatures without the weight penalties of most currently available high temperature materials (e.g., nickel-based superalloys). They must also maintain adequate fracture toughness and strength at room temperature. As a result, a great deal of interest has been generated in intermetallic matrix composites (IMCs). Sapphire fiber-reinforced gamma titanium aluminide (TiAl) IMCs offer great technological potential for high temperature applications due to their high specific strength and stiffness. However, one of the major drawbacks associated with these materials is their lack of damage tolerance [4-5].

The interfacial bond between the fibers and the matrix is an important factor influencing the mechanical properties, performance, and failure modes of a composite [6]. It is generally accepted that the shear strength of this bond dictates the composite's longitudinal strength, creep behavior, and fracture toughness under conditions where the crack plane is normal to the fiber direction. In addition, this investigation demonstrates that the magnitude of thermally-induced residual stresses and resulting damage within fibers intersecting a free surface are also a sensitive function of the interfacial shear strength. A weak interfacial shear strength in limited-ductility matrix composites (i.e., IMCs) results in improved fracture toughness and little or no damage within fibers intersecting a free surface. On the other hand, to obtain significant composite strength at room temperature and creep strength at elevated temperatures, a strong fiber/matrix bond is required. These two extremes suggest that an optimum interfacial shear strength exists that improves damage tolerance at low temperatures while maintaining adequate strength.

As a result of a strong interfacial shear strength in sapphire-reinforced TiAl composites [7-10], fiber damage and low fracture toughness are a commonly reported problem [8, 11-15]. Therefore, the interfacial shear strength must be reduced to improve the damage tolerance in these materials. To obtain an optimum shear strength, the chemical interaction and mechanical interlocking between the fibers and the matrix must be controlled (e.g., through the use of fiber coatings). To determine the success of these controls, it is important that experimental techniques are developed for measuring interfacial shear strength and that their results are correctly analyzed. Therefore, the purpose of this research program is to establish a fundamental understanding of: (1) fiber/matrix interfacial shear behavior within sapphire-reinforced TiAl composites and (2) the influence of the interfacial strength on the development of residual stresses and resulting damage within fibers intersecting a free surface. This was accomplished by using a combination of microscopic characterization, indentation crack growth results, thin-slice fiber pushout testing, fiber displacement measurements, and computational stress state analysis.

This thesis research is presented in four chapters. Chapter 2 reviews previous studies that have addressed the problem of sapphire fiber damage, the thermoelastic residual stresses in IMCs, the importance of the fiber/matrix interfacial shear strength, the factors that influence the interfacial shear strength in IMCs, and the mechanics of the thin-slice fiber pushout test. Chapter 2 concludes with a section describing the purpose of this study. The experimental procedures used in this investigation, including specimen fabrication, microscopic characterization, assessment of fiber damage, validation of the FEM predicted stress states, fiber pushout testing, and fiber displacement measurements, are presented in Chapter 3. In Chapter 4, the specific results of this investigation are presented and discussed. These results are grouped into three major sections: (1) interface microscopic characterization, (2) damage within fibers intersecting a free surface, and (3) fiber/matrix interfacial shear behavior. The results and conclusions are summarized in Chapter 5.

Chapter 2

LITERATURE SURVEY

2.1. Background

Titanium aluminide alloys and composites have been identified as candidate high temperature structural materials for a new generation of military and civil aircraft [1-4]. Current research programs are aggressively pursuing the development and applications of Ti_3Al-based (designated α_2) as well as conducting initial assessments of TiAl-based (designated γ) intermetallic matrix composites (IMCs) for components requiring higher temperature capability [5]. Unfortunately, unreinforced TiAl suffers from poor ductility, impact resistance, and fracture toughness at low-to-intermediate temperatures. It may be possible to minimize these last two shortcomings by using TiAl-based alloys as the matrix constituent in a fiber-reinforced composite. Efforts to produce both Ti_3Al IMCs (reinforced with silicon carbide fibers) and TiAl IMCs (reinforced with either silicon carbide or sapphire fibers) have revealed problems related to the poor matrix ductility, a large coefficient of thermal expansion (CTE) mismatch between constituents, and fiber/matrix interactions [16-20]. To alleviate these problems, several studies have been initiated on using fiber coatings to tailor the fiber/matrix interfacial region [5, 7, 20-24].

The TiAl intermetallic phase has the $L1_0$ ordered face-centered tetragonal structure and a composition that can range from 48.5 to 66 atomic % aluminum (Al), depending upon the temperature [25]. Gamma-TiAl alloys consist of titanium, 46-52 atomic % Al, and 1-10 atomic % M, where M is at least one element from the group V, Cr, Mn, W, Mo, Nb, and Ta. Gamma alloys can be divided into single phase (γ) and two-phase ($\gamma+\alpha_2$) alloys [26]. The highest plasticities are observed in duplex (i.e., two-phase) alloys containing 48 atomic % Al that have microstructures based on both primary γ and transformed γ/α_2 lamellar grains [27]. The compositions recommended from early alloy development programs (i.e., Ti-48Al and Ti-48Al-1V) exhibited room-temperature ductility of 2 %, fracture toughness of 12 MPa(m)$^{1/2}$, and good creep and oxidation resistance. More recently, several important alloys such as Ti-48Al-2Nb-2M (where M is Cr, Mn, or V) have been identified that offer improved room temperature ductility and fracture toughness [25]. Some typical room temperature properties of TiAl-based alloys are given in Table 1.

The leading fiber reinforcement for high temperature IMCs probably is single-crystal sapphire (i.e., α-Al_2O_3). Sapphire possesses a rhombohedral (pseudo-hexagonal) structure (i.e., $R\bar{3}C$ space group). Single-crystal fibers are fabricated by an edge-defined, film-fed growth process such that the crystal c-axis is nearly parallel to the fiber axis [29].

Table 1. Typical room temperature properties of gamma titanium aluminide alloys and single-crystal sapphire.

Property	TiAl-based alloys	Sapphire
Coefficient of thermal expansion (0-1000 °C)	13.0×10^{-6} °C^{-1} [9]	9.0×10^{-6} °C^{-1}(c-axis) [30] 8.3×10^{-6} °C^{-1} (transverse)
Density (gm/cm^3)	3.7 - 3.9 [26]	4.0 [31]
Elastic modulus (GPa)	160 -176 [26]	350 -450 [31, 32]
Poisson's ratio	0.3 [28]	0.28 -0.33 [32]
Yield strength (MPa)	400 -630 [26]	-
Tensile strength (MPa)	450 -700 [26]	2100 -3400 [31]
Fracture toughness (MPa-m$^{1/2}$)	7.7 -30 [25, 26]	1.1 -2.5 [33, 34]

Fibers in various diameters are commercially available from Saphikon, Inc. These continuous, ceramic oxide fibers have useful high temperature properties such as high melting point, high stiffness, high strength, creep resistance, and environmental resistance. Some typical room temperature properties of sapphire are given in Table 1. However, due to their relatively low fracture toughness, sapphire fibers are sensitive to surface damage resulting in strength degradation. Tressler and Crane [35] noted that composite fabrication can significantly reduce the strength of sapphire fibers (e.g., strength reductions by as much as 45%) through: (1) self-abrasion during handling and/or (2) surface roughening due to chemical interaction with the matrix during consolidation.

2.2. Damage to Sapphire Fibers in Metal and Intermetallic Matrix Composites

In the mid-1960's and early 70's, considerable interest developed in the use of single-crystal sapphire fibers for reinforcements in medium and high temperature metal matrix composites (MMCs). In studies of these systems, a disturbing amount of damage was observed in the form of extensive twinning and cleavage fracture in fibers extracted from the as-fabricated composites, in addition to significant loss of fiber strength [35-37]. In fact, Calow and Moore [36], in their study of the sapphire/Ni system, found such a disheartening amount of degradation of mechanical properties and gross fiber fracture that they concluded that the successful reinforcement of metals by ceramic fibers for high temperature use was impossible. Tressler and Crane [35] performed experiments to determine the cause of extensive fracture of Tyco sapphire fibers in a Ti-6Al-4V matrix during composite fabrication by diffusion bonding (i.e., vacuum hot pressing). They found regularly spaced characteristic fracture planes that made a 34° angle to the fiber axis in fibers mechanically as well as chemically extracted from the matrix. These fracture surfaces were identified as $\{10\bar{1}1\}$ rhombohedral planes[a]. In a further experiment with boron nitride-coated Ti-6Al-4V metal foils pressed with sapphire fibers, no fiber/matrix bonding occurred. However, the same fiber fracture pattern prevailed. Therefore, they concluded that the compressive consolidation load applied during hot pressing was responsible for fiber fracture [35].

A similar pattern of fiber damage was found in high volume fraction sapphire/nichrome (i.e., 80Ni-20Cr) composites by Mehan and Harris [37]. Following composite fabrication via hot pressing they examined the as-consolidated fibers by partially removing the matrix by chemical leaching. They found extensive fiber fracture in the form of cleavage and longitudinal splitting. The fracture appearance of the longitudinally split fibers appeared "conchoidal" in nature, and, although the angular features of the fracture surface coincided with orientations that resembled the prismatic planes, they were not considered crystallographic in nature. Rather, they speculated that fiber splitting occurred during hot pressing in regions of the fibers containing defects introduced during fiber production [37].

It is noteworthy to mention at this point that, during the edge-defined, film-fed growth of c-axis sapphire fibers, shrinkage voids 1 μm in diameter form within the fibers due to liquid entrapment behind the advancing solid interface. These voids assume nearly conical arrays that lie along the rhombohedral planes in sapphire [38]. Furthermore, Mehan and Harris [37] concluded that fiber fracture occurred during the hot pressing operation due to a multiaxial stress state, which included axial tensile stresses and local contact stresses. However, following a series of experiments conducted to optimize hot pressing parameters, fiber fracture still occurred. Although they noted that thermally-induced residual stresses due to the CTE mismatch between constituents could contribute to the damage, they concluded that these stresses could not be entirely responsible for fiber fracture [37].

---

[a] Indices used here refer to the morphological hexagonal unit cell of Al_2O_3.

In recent studies of sapphire-reinforced IMCs, several researchers have also noted damage in fibers following consolidation in composites. In the sapphire/NiAl system, Eldridge [39] observed that sapphire fibers in thin-slice fiber pushout specimens were cracked following specimen preparation when the composite fabrication method produced a strong fiber/matrix bond. However, specimens fabricated to produce little or no bonding contained only uncracked fibers. Misra [40] has also found consistent fiber cracking in single fiber experiments in which a sapphire fiber was hot pressed between two NiAl plates. In recent studies of the sapphire/TiAl system, a number of researchers noted that fibers were routinely split along their axis [11-15]. In an attempt to account for this type of fiber cracking, several explanations were proposed: (1) fiber cracking is caused by the combined states of stress induced in the fiber during hot pressing [11, 12, 14]; (2) the thermally-induced residual stresses in the fiber result in fiber fracture [15]; and (3) fiber cracking is initiated during cross-sectioning of the composite (e.g., with a high-speed saw) [12]. However, no substantial evidence or analysis was given to prove or disprove these explanations.

2.3. Residual Stress and Resulting Microdamage

Due to their differences in CTE, the sapphire fibers ($\alpha_{c\text{-axis}} = 9.0\text{x}10^{-6}\ ^{\circ}\text{C}^{-1}$, $\alpha_{\text{transverse}} = 8.3\text{x}10^{-6}\ ^{\circ}\text{C}^{-1}$ [30]) and TiAl matrix ($\alpha = 13.0\text{x}10^{-6}\ ^{\circ}\text{C}^{-1}$ [9]) will contract different amounts during cooling from the fabrication temperature. Uninhibited contraction, however, is not possible because the components are bonded at the interface. Hence, a state of triaxial residual stress will remain within the components at room temperature as depicted qualitatively in Figure 1. Note that due to the cylindrical symmetry of the fiber/matrix system, the displacements, strains, and stresses can be conveniently expressed in cylindrical polar coordinates.

In addition to the possible contribution of thermally-induced residual stress to fiber damage as already mentioned, they may also lead to detrimental effects in the fiber/matrix interfacial region within a composite. For example, several studies of SiC-reinforced titanium aluminides have shown that the low ductilities and fracture toughness of the composites are a consequence of brittle fiber/matrix reaction products and subsequent crack formation resulting from residual stress relaxation[b] [21, 41, 42]. Wawner and Gundel [43] found cracks in the matrix in the interfacial region of an as-fabricated sapphire/Ti-14Al-21Nb composite. They attributed this to the presence of extensive fiber/matrix reaction and a large β-depleted zone. However, no similar evidence of interface cracks have been observed in sapphire/TiAl systems.

Due to the size of the sapphire and SiC fibers (≈125 to 175 μm in diameter) used in IMCs and the scale of the localized residual stresses within the constituents, direct experimental verification of the predicted residual stress distributions by conventional methods is extremely difficult at best. A number of researchers [44-46] have attempted to measure residual stress distributions in the matrix by x-ray diffraction techniques. Cox et al. [44] determined the compressive residual stresses in SiC fibers embedded in a Ti_3Al matrix from measurements of the change in their length when the matrix was entirely removed by etching.

---

[b] Thermally-induced stresses can be relieved by plastic deformation or fracture of the matrix and/or reaction products in the interfacial region [22-24, 28] at temperatures below which creep effects are considered to cease and significant stress levels build, i.e., below the "stress-free temperature" [24].

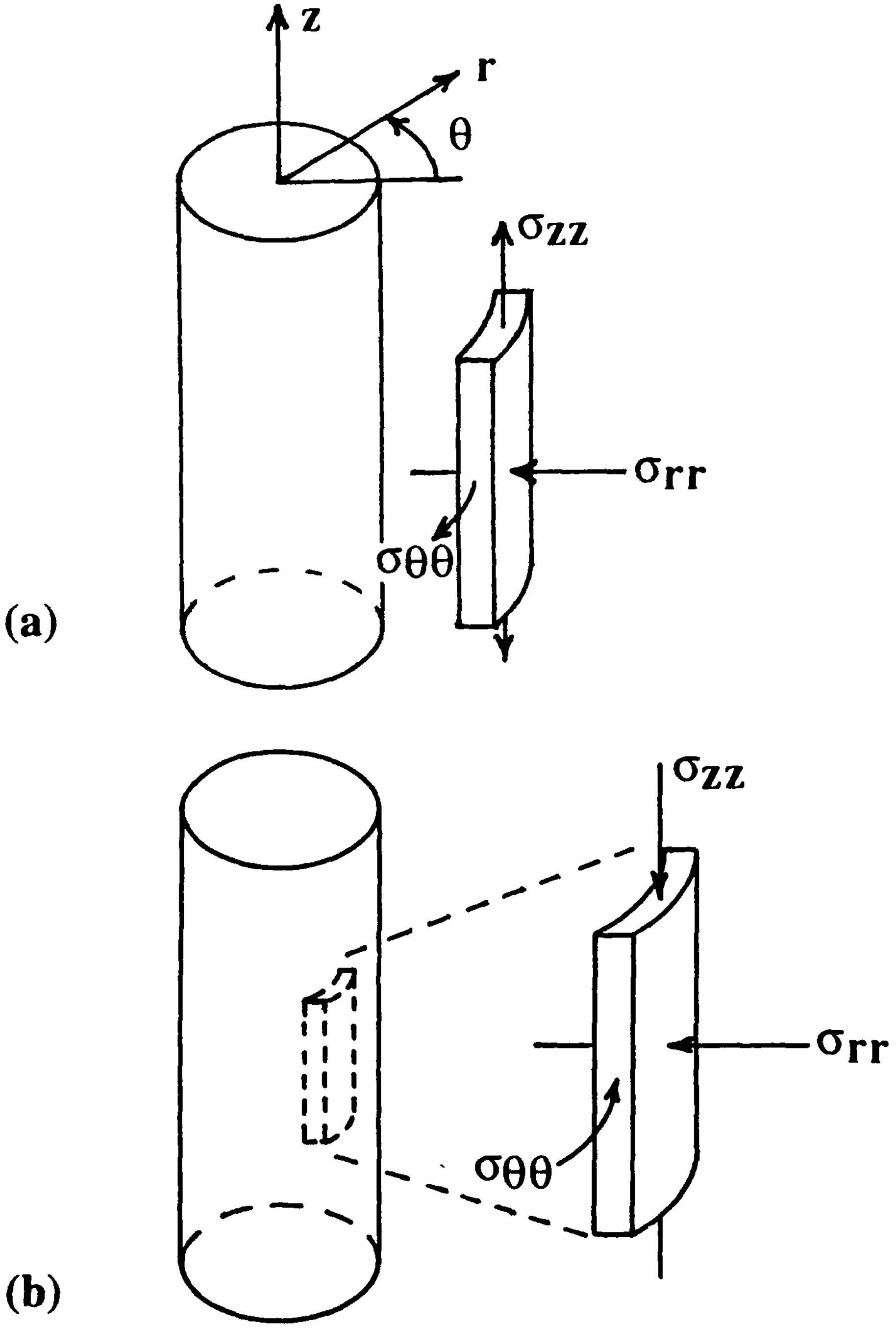
z
r
θ
σ_{zz}
σ_{rr}
$\sigma_{\theta\theta}$
(a)
σ_{zz}
σ_{rr}
$\sigma_{\theta\theta}$
(b)

Figure 1. Thermally-induced residual stress state in the interfacial region. (a) Within the matrix, (b) within the fiber.

2.4. Use of Fiber Coatings

In an attempt to reduce the high residual stresses in the interfacial region and accompanying microdamage in the fibers and matrix of IMCs, there is an increasing interest in the use of fiber coatings. Coatings may also serve as diffusion barriers to interdiffusion of matrix and fiber elements and thus prevent: (1) the formation of undesirable intermediate, brittle phases and (2) fiber strength degradation due to roughening of the fiber surface during composite processing and subsequent elevated temperature exposure. If the coating is soft and ductile, it may also provide: (1) a shearable layer between the fibers and the matrix during fiber pullout and/or (2) a crack-blunting layer by arresting cracks that initiate when fibers fail, thus preventing the crack from rapid propagation through the matrix [47]. Of special interest to this program is the role of coatings in modifying interfacial strength behavior. This will be discussed in more detail in sections 2.5.3 and 2.5.4.

The concept of "compliant" and "compensating" fiber coatings has been proposed by several researchers as a means of reducing or eliminating the initiation of cracks in the fiber/matrix interfacial region [20-24, 40, 48, 49]. A "compliant" layer is a coating that will increase or maintain ductility at the fiber/matrix interface, but not necessarily reduce the thermally-induced residual stresses. This is accomplished by the coating: (1) having a greater ductility than that of the matrix (e.g., a Nb fiber coating), (2) diffusing into the matrix to stabilize a more ductile matrix phase at the fiber/matrix interface (e.g., a Nb fiber coating could stabilize the β-Ti phase in a Ti_3Al matrix), and/or (3) acting as a diffusion barrier that reduces or eliminates the formation of brittle reaction products [24, 43]. In separate experimental studies, it has been verified that compliant fiber coatings of Nb [49] and W [43] in the SiC/Ti_3Al system and W [21] and duplex Ag-Ta [20] in the SiC/TiAl system eliminate radial matrix cracks that commonly occurred near the interface.

A "compensating" fiber coating, on the other hand, not only will act as a compliant layer but also will reduce the residual stresses in the interfacial region [24]. In their investigation of the SiC/Ti_3Al+Nb system, Arnold et al. [23] identified the important properties of a compensating fiber coating via a parametric study using a three-dimensional, thermoelastic-plastic finite element model (FEM). Computational predictions from their study indicated that CTE and thickness are the most important coating parameters. Other important mechanical properties are yield stress, strain-hardening response, and elastic modulus. A representative compensating interface layer for the SiC/Ti_3Al+Nb composite system was a duplex Cu-Nb fiber coating [24, 49].

2.5. Interfacial Shear Strength

The interfacial bond is an important factor influencing the mechanical properties, performance, and failure modes in composites [6]. The properties of a composite can be divided into those controlled principally by the tensile strength of the interfacial bond (σ_i) and those governed by the interfacial shear strength (τ_i) [50]. It is generally accepted that the interfacial shear strength dictates the composite's longitudinal strength, creep behavior, and fracture toughness under conditions where the crack plane is normal to the fiber direction and fiber pullout occurs [6, 47, 51-57].

In order to design an optimum fiber/matrix interfacial bond in TiAl-based IMCs (e.g., through proper processing or the use of fiber coatings), it is necessary to understand the manner in which they fail. Since the strain-to-failure of the fiber is less than that of the matrix in IMCs (e.g., sapphire-reinforced TiAl), multiple cracking of the fibers can be expected to precede complete failure of the composite [51]. Fiber cracks will subsequently develop into matrix cracks.

The failure behavior of IMCs (i.e., see Figure 2 [47]) can be classified as either: (1) catastrophic (i.e., linear stress-strain behavior, high strength, but little toughness) or (2) non-catastrophic (i.e., non-linear stress strain behavior, lower strength, but higher toughness). The behavior that occurs in a given fiber/matrix system is determined by the manner in which the applied load is transferred from the matrix to the fibers (which contribute the greater portion of the composite strength [6]) via the interfacial shear strength. In the case of IMCs, where fiber fracture precedes composite failure, the applied load is transferred to a broken fiber through the fiber's end and the cylindrical surface of the fiber near the broken end. The stress in the fiber increases from zero at its end to $(\sigma_{fracture})_f$, the fiber fracture stress, at a distance $l_c/2$ from its end. The critical fiber length (l_c) is the minimum length in which the fiber fracture stress can be achieved and is inversely dependent on the fiber/matrix interfacial shear strength (τ_i) [52]:

$$l_c = \frac{(\sigma_{fracture})_f R_f}{\tau_i}, \tag{1}$$

where R_f is the fiber's radius. The applied stress on the composite will continue to increase as the fibers break into shorter and shorter lengths until they reach the critical length (assuming that matrix cracks do not initiate at the stress concentrations produced by fiber fractures). Thus, a high interfacial shear strength promotes a short critical length and, as a result, yields a high macroscopic, longitudinal composite strength [53] (see Figure 2b [47]).

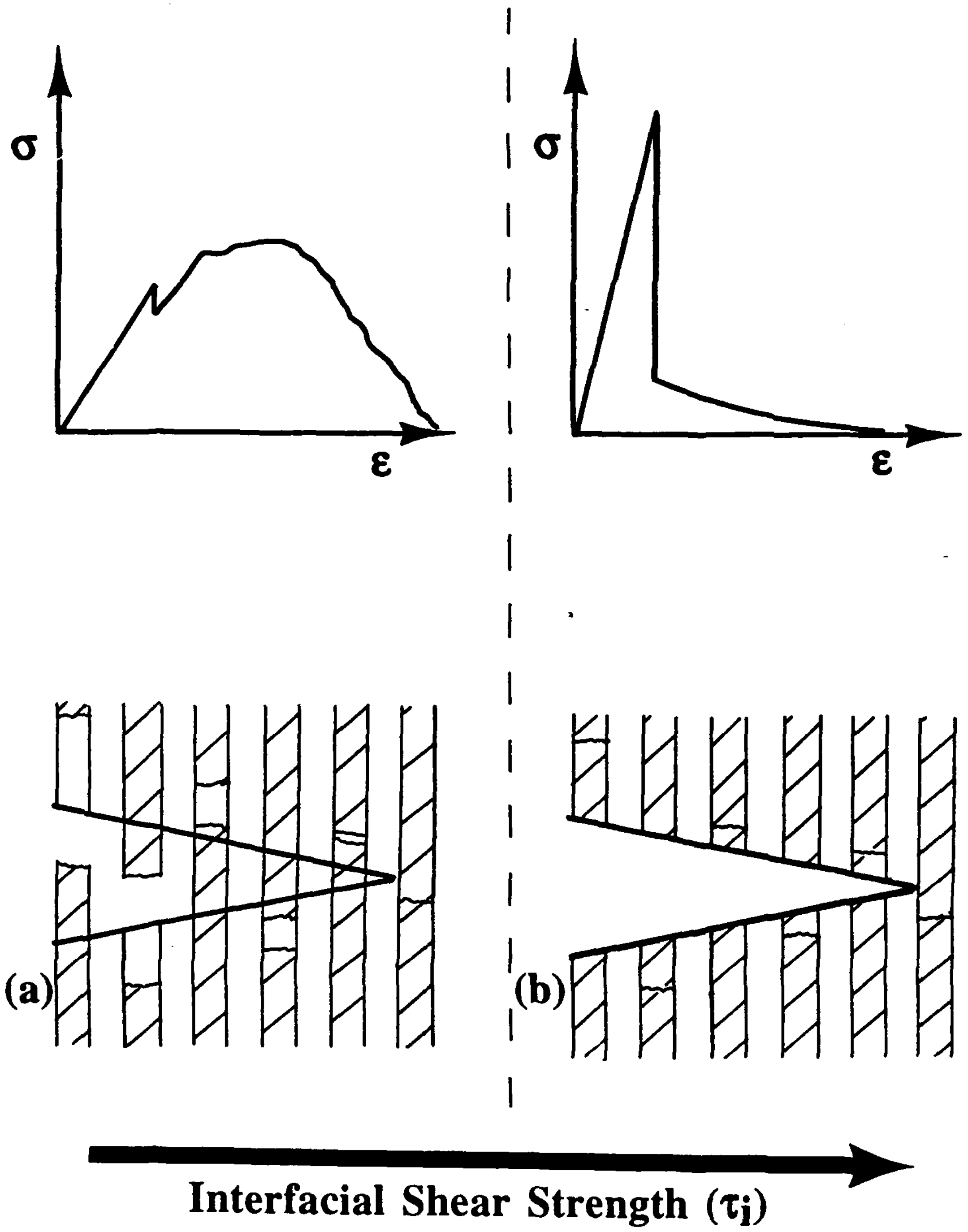
σ
ε
σ
ε
(a)
(b)
Interfacial Shear Strength (τ_i)

Figure 2. Influence of fiber/matrix interfacial shear strength on intermetallic matrix composite failure behavior (adapted from Evans [47]). (a) Non-catastrophic and (b) catastrophic failure.

Fracture toughness of a composite, on the other hand, benefits from a lower interfacial shear strength. This is demonstrated by expressing the fracture toughness of a composite in terms of a critical strain energy release rate for the onset of mode I crack growth, G_{IC}. It can be formulated as the sum of the macroscopic fracture toughness of an anisotropic, but homogeneous, body with the composite properties ($(G_I)_{macro}$) and the energy absorbing mechanisms of matrix plastic deformation (W_P) and fiber pullout (W_{PO}) [54]:

$$G_{IC} = (G_I)_{macro} + W_P + W_{PO}. \tag{2}$$

At room temperature, the matrix plastic deformation term (W_P) can be ignored for TiAl. Therefore, fiber pullout is the primary mechanism that increases a TiAl-based IMC's fracture toughness. As illustrated in Figure 2a [47], fiber ends, created by fracture at their weakest cross-sections, do not necessarily lie in the plane of the composite fracture. As fracture proceeds, fibers whose ends are within a distance $\leq 1/2\ l_c$ of the composite crack plane will pull out of the matrix rather than fracturing [55]. In this case, the work to pullout per unit area (W_{PO}) can be expressed by [55, 56]:

$$W_{PO} = \frac{V_f(\sigma_{fracture})_f l_c}{12}, \tag{3}$$

where Vf is the fiber volume fraction. Substituting equation (1) into (3) yields [54]:

$$W_{PO} = \frac{V_f R_f (\sigma_{fracture})_f^2}{12\tau_i}. \tag{4}$$

If R_f, V_f, and $(\sigma_{fracture})_f$ are taken to be constant, these equations show that a weaker interfacial shear strength allows for a larger length of fiber to be pulled out of the matrix and, as a result, increases the pullout energy (and, therefore, G_{Ic}).

Finally, the failure criterion for an IMC is given by:

$$G_{eff} \geq G_{IC}, \tag{5}$$

where G_{eff} is the strain energy release rate "felt" at the crack tip. It is given by [57]:

$$G_{eff} = G_{applied} - G_{deflect} - G_{bridge}. \tag{6}$$

Thus, the applied strain energy release rate ($G_{applied}$) is modified by the crack tip shielding mechanisms of crack tip deflection along the fiber/matrix interface ($G_{deflect}$) and crack tip bridging (G_{bridge})[c]. These mechanisms reduce G_{eff} by "shielding" the crack tip from the applied stress field. Therefore, in addition to fiber pullout, composite fracture can be inhibited by crack tip deflection and bridging [51].

The two extremes of IMC failure behavior illustrated in Figure 2 [47] suggest the existence of an optimum interfacial shear strength that improves fracture toughness at low temperatures while maintaining significant strength. Designing a fiber/matrix interface with an optimum shear strength in an IMC such as sapphire-reinforced TiAl requires control of: (1) the chemical interaction and (2) the mechanical interlocking between the fibers and the matrix.

---

[c] Crack tip bridging occurs when cracks in the matrix are bridged by intact fibers that, as a result, inhibit crack opening [57] (see Figure 2a [47]).

2.5.1. Chemical Interaction

The degree of chemical interaction that occurs between the fibers and the matrix during composite fabrication and subsequent use (i.e., at elevated temperatures) can significantly affect the strength of the interfacial bond (i.e., both τ_i and σ_i) as well as the properties of the fiber and matrix in the interfacial region. Therefore, when evaluating a potential composite system, it is important to address the chemical compatibility of the fiber/matrix combination [58]. Chemical bonding between the fibers and the matrix can occur in widely varying degrees such as (1) dissolution bonding, (2) reaction bonding, or (3) no reaction at all. However, composite systems that are in thermodynamic equilibrium (i.e., no driving force for chemical reaction) are the most desirable [58]. In order to predict the chemical compatibility of various composite constituents, both thermodynamic (i.e., phase equilibrium) and kinetic (i.e., reaction and diffusion rates) data for the fiber and matrix components must be considered over the anticipated range of fabrication and use temperatures [58]. Unfortunately, such data are usually difficult to find for IMCs.

The compatibility of the Al_2O_3/TiAl system has been investigated in several studies [59-62]. Misra [42, 59] studied the chemical compatibility of sapphire fibers with several binary Ti-Al alloys. He showed that Ti-Al alloys with concentrations less than 50 atomic % Al are not compatible with Al_2O_3, resulting in dissolution of Al and atomic oxygen into the alloy. For example, in the Al_2O_3/Ti-43Al system, diffusion of Al into the matrix resulted in the formation of a TiAl layer at the Al_2O_3/alloy interface, and the dissolved oxygen remained in solution in the TiAl phase. On the other hand, no reaction occurred between Ti-54Al and Al_2O_3, and electron probe microanalysis (EPMA) indicated no Al or oxygen enrichment in the alloy near the Al_2O_3/Ti-54Al interface [59]. From a thermodynamic standpoint, Dekock et al. [60] calculated the Ti-Al-O phase diagram at 1100

°C using available thermodynamic data and the program SOLGASMIX [63]. According to this diagram, TiAl is in equilibrium with Al_2O_3 and TiO. Experimentally, by optical microscopy and EPMA, they found no evidence of reaction at the interface of Al_2O_3/Ti-52.1Al-2.0Ta after 192 hours at 1100 °C. Das and Krishnamurthy [62] provide perhaps the best microstructural characterization of the sapphire/TiAl interface. In their investigation, they used both scanning and transmission electron microscopy (SEM and TEM) to characterize the interface between sapphire and three TiAl-based alloys: Ti-44.7Al-0.3Ta, Ti-47.2Al-1.3V (both two-phase $\alpha_2+\gamma$ alloys) and Ti-50.5Al-0.1Ta-3.9Nb (single phase γ alloy) where compositions are given in atomic percent. Samples were fabricated at 1200 °C for 6 hours and subsequently heat treated at 1000 °C or 1150 °C for different periods of time. SEM examination indicated no reaction zone formation at the fiber/matrix interface of these composites. However, the sapphire-reinforced two-phase $\alpha_2+\gamma$ composites revealed fiber/matrix instability in the form of cracks in the matrix, serrations of the fiber surface, and voids at the interface. In contrast, the sapphire/single phase γ alloy was relatively free of these defects. TEM examination revealed the presence of a 0.16 to 0.35 μm-wide reaction zone that was amorphous in nature in all composites. Energy dispersive spectrometry (EDS) showed that the reaction zone was Al enriched and Ti depleted; no information was available on the concentration profile of atomic oxygen, however [62].

From the results of these studies, it can be concluded that some form of dissolution chemical bonding (i.e., dissolution of Al and atomic oxygen from sapphire into the matrix) occurs in sapphire-reinforced TiAl alloys based on a two-phase microstructure. However, it is evident that the formation of a brittle fiber/matrix reaction zone does not occur in this system as in SiC-reinforced TiAl alloys, for example. Chemical interaction in the sapphire/TiAl system may result in high interfacial shear and tensile strengths, especially with high temperature exposure. In this case, composite failure could transition from non-catastrophic to catastrophic behavior (see Figure 2 [47]). However, an increase in σ_i will result in enhanced composite transverse strength. Furthermore, dissolution of the fiber into the matrix will result in fiber strength degradation via surface roughening as previously noted in section 2.1 [35].

2.5.2. Mechanical Interlocking

The contribution of fiber/matrix mechanical interlocking to interfacial shear strength is determined by: (1) the magnitude of the radial clamping stress across the interface, (2) the surface roughness of the fiber, and (3) the matrix yield stress in the interfacial region. Coulomb friction develops whenever the fiber and matrix are in contact. Friction stresses act parallel to the contacting surfaces, and they resist motion or attempted motion. Coulomb friction stresses are expressed according to:

$$\tau_{\text{friction}} = \mu\sigma_{rr}, \tag{7}$$

where σ_{rr} is the radial clamping stress that acts perpendicular to the interface and μ is the coefficient of static or kinetic friction (depending on whether the fiber is sliding or not). It is important to note that σ_{rr} is temperature dependent, decreasing to zero as the temperature increases to the composite's stress-free temperature.

The non-uniform surface topography of the single-crystal sapphire fibers produced by Saphikon, Inc. has been documented by Moose [64]. He observed asperities randomly located on the surface of these fibers as well as variations in their diameter. This diametrial variation occurs in a periodic pattern produced during fiber production. Mackin et al. [7]

measured the wavelength and amplitude of this variation as 10 μm and 0.3 μm respectively. This as-received fiber surface roughness, however, may be significantly different (i.e., less severe) than that following composite processing when fiber dissolution or reaction with the matrix occurs.

The importance of fiber surface roughness to interfacial shear was first addressed by Jero et al. [65, 66]. Assuming the fiber and matrix to deform in a purely elastic manner (e.g., ceramic fiber in a glass matrix), they argued that the translation of initially mating rough surfaces results in a radial displacement of the fiber and matrix surfaces equal to the amplitude of fiber roughness. This elastic displacement simply manifests itself as a compressive stress that adds to existing radial clamping [67]. In the case of metallic and intermetallic matrix composites, however, plastic as well as elastic deformation of the matrix must be considered in the interfacial region. Despite their tendency to be brittle in tension, many intermetallics may plastically deform on a localized level where stress states consist of large compressive and high equivalent shear stresses [68]. Examination of the interface following fiber pushout testing of the sapphire/NiAl system by Moose [64] showed that fiber displacement required matrix plasticity in the form of grooves to accommodate asperities on the fiber surface.

At first glance, "frictional" fiber sliding resistance due to fiber/matrix mechanical interlocking appears to make an important contribution to the toughening mechanisms of fiber pullout and crack tip bridging in brittle matrix composites. As a crack extends into the composite, crack opening is inhibited by "frictional" fiber sliding resistance along the debonded fiber/matrix interface of bridging fibers (see Figure 2a [47]). In addition, broken fibers whose ends are within a distance $\leq 1/2\ l_c$ of the crack plane will pullout against a "frictional" sliding stress that resists fiber displacement [69]. However, a rough fiber surface, as in the sapphire/TiAl system following composite processing, may also lead to a higher interfacial shear strength (τ_i) due to the requirement for the mode II interface debond crack to follow a tortuous failure path. In addition, the significant thermally-induced radial clamping stresses in sapphire-reinforced TiAl composites may inhibit the propagation of the debond crack [70]. Reference to equation (1) shows that this increase in τ_i due to fiber/matrix mechanical interlocking will result in a smaller critical length, l_c. This, in turn, leads to a tendency toward catastrophic composite failure behavior, i.e., higher longitudinal strength but lower fracture toughness (see section 2.5). Finally, the contribution of fiber/matrix mechanical interlocking to composite performance will vary with temperature due to the temperature dependence of the clamping stress and matrix yield strength.

2.5.3. Effect of Fiber Coatings

Unfortunately, the interfacial shear strength of directly bonded interfaces between sapphire fibers and TiAl-based matrices is relatively "strong," and interface debonding does not occur easily during fracture [7-10]. In a study conducted by Amato [8] on the same sapphire/Ti-48Al-2Cr-2Nb composite investigated in this thesis research, the fracture toughness of the composite material was found to be less than that of the unreinforced matrix; it should be noted that the toughness data were measured using the Charpy notch three-point bend test. Evaluation of the fracture surfaces indicated an absence of fiber pullout in the sapphire/Ti-48Al-2Cr-2Nb specimen, suggesting a high interfacial shear strength [8]. These results suggest that the fiber/matrix interfacial shear strength in sapphire-reinforced TiAl-based IMCs must be tailored to obtain an optimum balance between strength and toughness. Specifically, the interfacial shear strength must be reduced if toughness enhancement is to be achieved in sapphire-reinforced TiAl composites.

As noted in section 2.4, one approach is through the use of fiber coatings. There appears to be two general ways that a fiber coating can be used to tailor the interfacial shear strength. First, as a diffusion barrier, a coating can tailor the degree of chemical bonding at either the fiber/coating or the coating/matrix interface thus, controlling the interfacial debond toughness (i.e., work to fracture) to initiate fiber pullout. He and Hutchinson [71] have proposed that if an interface is to fail ahead of an incident crack it should have an interfacial debond toughness (Γ_i) less than 1/4 of the fiber fracture energy (Γ_f). Evans et al. [72] reported $\Gamma_i \approx 16.2$ J/m^2 for a TiAl coating on the basal plane of sapphire. However, to meet He and Hutchinson's criteria, Γ_i must be on the order of 3 J/m^2 for the sapphire/TiAl interface [7]. In addition, a diffusion barrier coating can retain sapphire fiber strength by limiting the degree of degradation-induced fiber surface roughness incurred during composite processing and subsequent elevated temperature exposure. Secondly, a fiber coating can serve as a "shearable" layer between fiber and matrix by increasing or maintaining ductility at the fiber/matrix interface in the same way as a "compliant" layer described in section 2.4. Other desirable properties of a shearable coating are a low yield strength and hardening modulus. This type of coating may be especially effective if it is thick enough to accommodate fiber surface roughness. Mackin et al. [7] have also shown that a porous ceramic coating can act as a shearable/debond layer.

2.5.4. Tantalum Fiber Coatings for Sapphire/TiAl IMCs

Tantalum has a body-centered cubic structure, is very ductile (e.g., ≈35% tensile elongation), has a very low rate of work hardening, but possesses a high yield strength (e.g., ≈220 MPa) [73]. Thermodynamically, the sapphire/Ta interface appears to be stable since Al_2O_3 has a lower free energy of formation than Ta_2O_3 and $2Ta_2O_5 \cdot 3Al_2O_3$ [74].

Diffusion couples of 1 μm-thick Ta coatings sputter-deposited onto single-crystal sapphire were studied by Joshi et al. [75]. They characterized the interface using Auger depth profiling and TEM, and found that Ta did not react with sapphire in vacuum anneals of up to 4 hours at 1200 °C. Little or no atomic oxygen was found in the Ta coating [75]. Moreover, Ta is a β-Ti phase stabilizer in Ti alloys. An 1100 °C isothermal section of the Ta-Ti-Al phase diagram constructed by Das and Perepezko [76] reveals that only 30 atomic % Ta is required to stabilize the β-phase in TiAl alloys.

Several studies have investigated the use of Ta fiber coatings in SiC- and sapphire-reinforced TiAl IMCs [5, 11, 20]. Following composite fabrication, these investigators found that a Ta-Ti-Al interdiffusion zone surrounds the Ta coating with no evidence of brittle reaction product formation. Graves and Bampton [20] concluded that this interdiffusion zone was a ductile β-Ti phase. Therefore, a Ta fiber coating in sapphire/TiAl-based IMCs can be speculated to have a similar effect on the interfacial region as a "compliant" Nb layer investigated in Ti_3Al-based IMC studies (see section 2.4).

2.6. Interfacial Shear Strength Determination

As previously discussed, the shear strength of the fiber/matrix interface is an important factor influencing the mechanical properties, performance, and failure modes in composites [6]. The two extremes in IMC performance illustrated in Figure 2 [47] (i.e., catastrophic versus non-catastrophic failure behavior) suggest that the interfacial shear strength must be tailored to obtain composite systems that exhibit low temperature fracture toughness while maintaining significant strength. Designing a fiber/matrix interface in sapphire-reinforced TiAl IMCs with an optimum shear strength requires control of the chemical interaction and mechanical interlocking between the fibers and the matrix (e.g., through the use of fiber coatings). To determine the success of these controls, it is important to be able to measure accurately the interfacial shear strength and the accompanying interfacial failure process.

In an attempt to quantify the shear strength of a fiber/matrix interface in brittle matrix composites, both mechanics and experimental approaches have separated the interfacial shear process into two distinct events: (1) interface debonding characterized by an average interfacial shear strength (i.e., τ_{AVG}) and (2) subsequent large-scale fiber displacement described by a "frictional" sliding stress (i.e., τ_{slide}) [72, 77, 78]. In the following section, the methods used to experimentally assess these properties will be described.

2.6.1. Test Methods

The three methods commonly used to examine the interfacial shear behavior of fiber-reinforced composites are illustrated in Figure 3 [79]. Each method relies on careful measurements of load and displacement during the test. The push-in test [80, 81] is relatively simple to perform and allows interfacial property determination from a single test [79]. This type of test, however, is limited to composites where the interface is typically "weak." The fiber pullout test, on the other hand, is more representative of the actual toughening mechanism that occurs during composite fracture. However, both specimen preparation and test methodology are very difficult [79]. Therefore, many studies directed at determining the interfacial failure response in IMCs (as in this thesis research) use the fiber pushout test for experimental convenience.

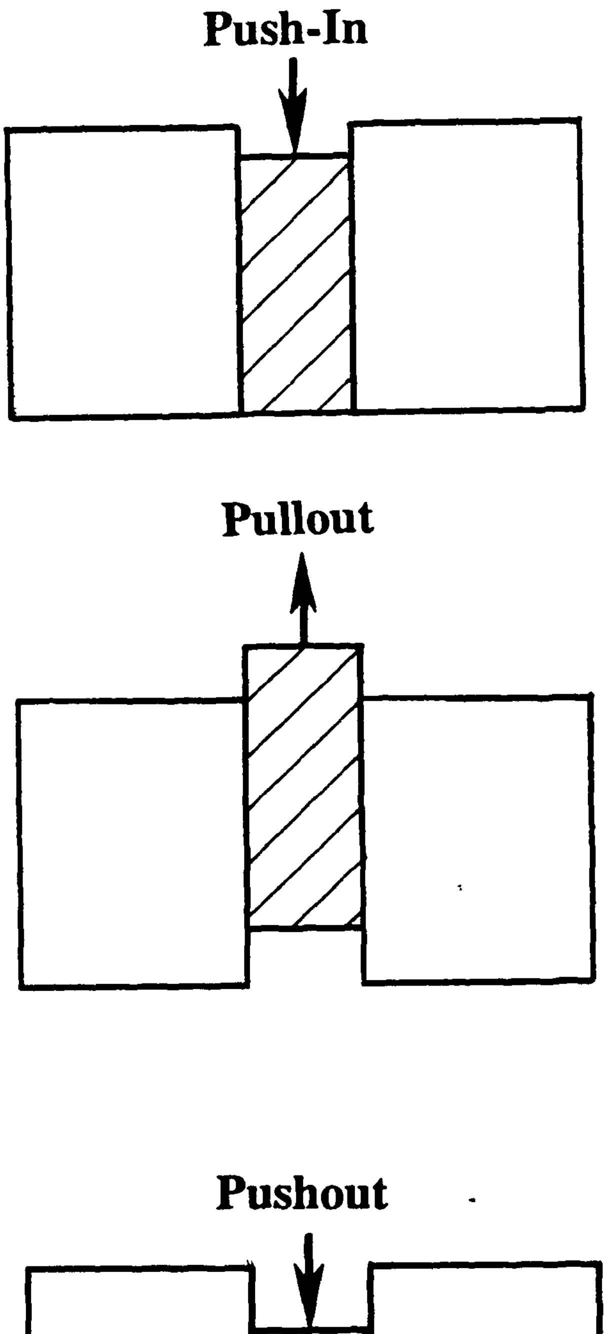
Push-In
Pullout
Pushout

Figure 3. Three methods commonly used to examine the interfacial shear behavior of fiber-reinforced composites (adapted from Ferber et al. [79]).

2.6.2. Mechanics of the Thin-Slice Fiber Pushout Test

The mechanics of the fiber pushout test for ceramic matrix composites (CMCs) has been addressed in detail where the high stiffness matrix and typically weak fiber/matrix interface permits testing of "thick" specimens (i.e., thickness > 1 mm) [67, 77, 78, 82]. Under these conditions, specimen bending does not occur during application of the indenter load. For these "thick-slice" specimens it is assumed that the interfacial failure sequence occurs in the following manner. First, a mode II (i.e., shear) debond crack initiates along the fiber/matrix interface at the point of maximum shear stress just below the specimen's topface (where the "topface" is the side of the specimen where the indenter is loaded onto the fiber). Subsequently, the debond crack propagates in a stable manner towards the bottom of the specimen as the load increases. Stability of the interface crack comes from the frictional resistance of the debonded interface. As stable debonding progresses, the relative displacement of the fiber below the matrix can be as much as 1 μm [83]. At peak load, the crack becomes unstable and spontaneously propagates through the remaining bonded ligament, resulting in a load drop [83].

However, the use of "thin-slice" specimens for pushout testing (i.e., typically 0.2 to 0.4 mm thick) is required in IMCs since high interfacial shear strengths limit specimen thickness if large-scale fiber displacements are achieved prior to indenter failure. In order to accommodate the displaced fiber during testing, these specimens are commonly supported over holes or slots which are typically ≥2 times the fiber diameter [68]. As a result, this test configuration results in specimen bending that can complicate the interpretation of results and create interfacial failure sequences that are test-dependent and not representative of fiber pullout behavior [68]. The most notable consequence of specimen bending is the development of tensile stresses that may initiate mode I cracks at the fiber/matrix interface on the specimen's backface opposite the indenter.

Figure 4 (taken from Kallas et al. [84]) demonstrates the importance of the tensile radial component at the specimen's backface (i.e., d/t = 0 in Figure 4). In this figure, the stress distributions within the matrix adjacent to the fiber were computed from an axisymmetric finite element model (FEM) developed by Kallas [84] that assumed perfect bonding at the fiber/matrix interface and no thermally-induced residual stresses (e.g., the sapphire/niobium system where the CTE mismatch is nearly zero). In order to demonstrate the effect of specimen thickness, the thickness was varied from 0.5 to 1.0 mm. In this figure, the interfacial stress components were normalized with respect to indenter pressure (p) and plotted as a function of position (d) along the fiber normalized with respect to specimen thickness (t) [84]. As shown in Figure 4a, the shear stress along the interface is not uniform but peaks at a location approximately one fiber radius below the topface.

However, the failure sequence of topface shear initiation generally assumed for "thick-slice" specimens may not be correct for "thin-slice" specimens [68]. Figure 4b shows that a significant tensile radial stress component exists at the specimen's backface. The consequences of this analysis for TiAl IMCs, where a strong fiber/matrix bond exists, is that thinner specimens and higher indenter pressures must be used, resulting in large tensile stresses due to bending. These mechanically-induced tensile stresses at the backface may be large enough to exceed the chemical bond strength and thermally-induced residual clamping stress, thus initiating a mode I circumferential interface crack at the backface. Subsequently, the circumferential debond crack may propagate in a mixed-mode I and II manner up along the interface [68] . Crack propagation up from the backface in turn increases the shear stress within the bonded ligament that exists between the debond crack tip and specimen's topface. This is a result of the crack-tip stress field as well as the

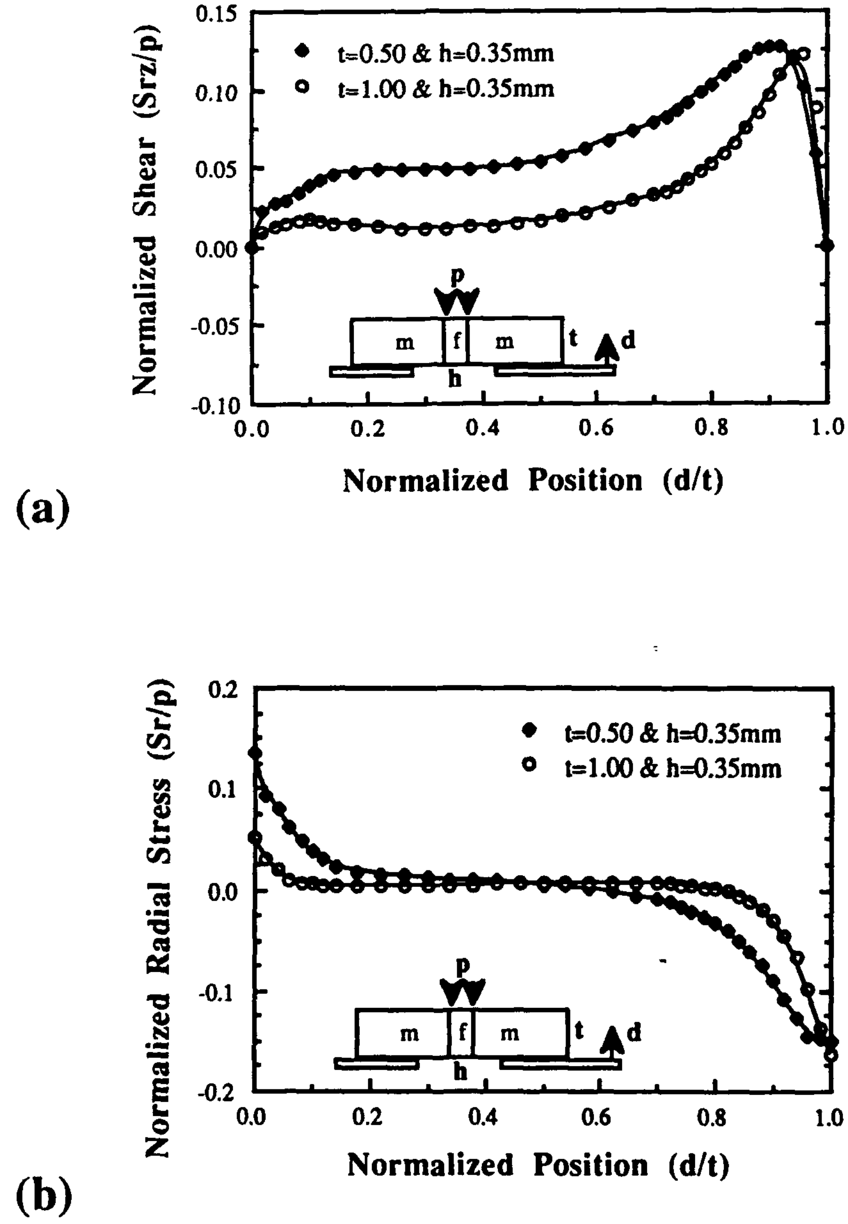

Figure 4. Effect of specimen thickness on (a) the shear stress and (b) radial stress distributions at the fiber/matrix interface of a sapphire-reinforced niobium composite (taken from Kallas et al. [84]).

decreased ligament length. As a result, a mode II debond crack can initiate at the topface near the indenter or, alternately, the fiber may slide abruptly as a rigid "plug" due to plastic flow within the matrix [68].

A complete analysis of the fiber pushout test for "thin-slice" IMC specimens (notably sapphire/TiAl) must take into account both thermally- and mechanically-induced stress distributions within the matrix along the fiber/matrix interface. The combination of these stresses dictate the overall interfacial stress state. One of the most significant aspects of the thermally- and mechanically-induced stress components is the sign of the shear stress component near the fiber ends. At the specimen's topface, the signs of the thermal and mechanical shear stresses are opposite while at the backface they are in the same direction. Thus, conditions may exist where the overall shear stress may peak near the backface of the specimen, being larger than near the topface. Thus, it is possible that a mode II debond crack may initiate at the backface [68].

The interfacial failure sequence that occurs during fiber pushout testing of IMCs is a sensitive function of the overall stress distribution along the fiber/matrix interface. The difficulty encountered in thin-slice fiber pushout testing is that the overall stress distribution is dependent on the interfacial shear strength, the magnitude of thermally-induced stresses, the indenter pressure (which controls the mechanical stresses), and the specimen thickness [68]. A straight-forward analysis is not available, and use of an "average" interfacial shear strength (i.e., maximum load recorded during testing divided by the interfacial area) persists.

2.7. Fiber Sliding Stress

Following complete fiber debond (usually accompanied by a load-drop and large-scale displacement of the fiber from the matrix), the fiber slides along the debonded interface under the action of a "frictional" stress, τ_{slide}, that resists further fiber displacement. Liang and Hutchinson [78] analyzed fiber sliding using a generalized sliding law where they combined the cases of constant friction and Coulomb friction (see equation (7) in section 2.5.2) from results in an earlier paper by Hutchinson and Jensen [77]:

$$\tau_{slide} = \tau_0 - \mu\sigma_{rr}, \tag{8}$$

where τ_0 is a constant friction term, μ is the friction coefficient, and σ_{rr} is the radial clamping stress acting across the sliding fiber/matrix interface. Mackin et al. [85] suggested that the constant friction term, τ_0, is the sliding stress that would be experienced by the fiber if $\sigma_{rr} = 0$, i.e., τ_0 is governed by the surface roughness of the fiber. This is the same surface roughness interaction that was first addressed by Jero and Kerans [65, 66] (see the description in section 2.5.2).

The "fiber reseating" phenomenon[d] is the most commonly reported evidence that fiber surface roughness makes a significant contribution to the sliding stress, i.e., it can not be explained by the frictional sliding of smooth surfaces [65, 66, 85-88]. Upon pushing a fiber back to its origin, an abrupt load drop occurs in the load-displacement behavior of CMCs. In IMCs, however, matrix plasticity should be expected to play a role in how fiber reseating is manifested during reverse push-back tests. In fact, from the data presented in the papers by Warren et al. (SiC/β-Ti alloy) [86], Kantzos et al. (SiC/Ti-24Al-11Nb) [87], and Eldridge (SiC/Ti-24Al-11Nb) [88], fiber reseating is manifested by a distinct load increase. However, these authors did not comment on this different behavior found between CMCs and IMCs (and MMCs).

---

[d] "Fiber reseating" is a phenomenon that occurs when a fiber, that has been initially displaced during a pushout test, is pushed back beyond its original position (i.e., the "origin") [65].

Another significant observation during fiber sliding is the evidence of interface wear and/or degradation during continued monotonic or cyclic loading [85-87]. It has been found that with increasing amounts of fiber sliding displacement (i.e., monotonically or cyclically): (1) fiber sliding stress continuously decreases [85-87] and (2) fiber reseating load drop decreases and eventually disappears [85, 86, 89]. By considering the generalized sliding law (see equation (8)), a decrease in τ_{slide} may be explained in terms of a decrease in τ_0 (constant friction term) or σ_{rr} (radial clamping stress) or both. Mackin et al. [85, 86] suggested that the wear of fiber asperities occurred in a SiC/glass system as the interface slid during pushout, causing τ_0 to decrease. However, the much larger decrease in τ_{slide} with fiber displacement found in a SiC/β-Ti system could not be accounted for by asperity wear alone. In this case, the authors [85, 86] suggested that matrix plasticity may account for a reduction in misfit strain with pushout, but they gave no explanation of how this may occur. Similar observations have been made by Kantzos et al. [87] in SiC/Ti-24Al-11Nb and SiC/Ti-15V-3Cr-3Al-3Sn specimens subject to cyclic fatigue and multiple reverse pushout tests. The reduction of τ_{slide} in these specimens was accounted for by fracture and wear of the outer carbon coatings on the SCS-6 (SiC) fiber. In a separate calculation by Kantzos [90], he found that only 0.4 μm of radial displacement is required at the interface of these two systems in order to relieve all of the thermally-induced clamping stress (σ_{rr}). All of the above mentioned mechanisms for interfacial wear/degradation have been suggested where the asperities are comprised of carbon coatings that wear readily [87]. In other composite systems, e.g., sapphire/TiAl, fiber roughness/asperities may not wear readily [87], and matrix plasticity may become increasingly important. For example, during elevated temperature reverse push-back tests of sapphire/NiAl, Eldridge [88] noted that τ_{slide} was higher at 700 °C than at 23 °C even though the clamping stress on the fiber should be negligible at the higher temperature. However, he explained this in terms of large increases in the friction coefficient due to greater matrix ductility [88].

2.8. Statement of Purpose

Sapphire-reinforced TiAl composites offer great technological potential for high temperature aerospace applications. Due to their high strength and stiffness, they have the potential to replace conventional titanium alloys, as well as nickel-based superalloys, at 40 to 60% lower weight [5]. However, as previously described, one of the major problems associated with these materials is their lack of damage tolerance. This includes, but is not limited to, fiber damage and low composite fracture toughness. It is well recognized that the fiber/matrix interfacial shear strength can control the strength and crack growth behavior of fiber-reinforced composites [68]. Therefore, the purpose of this research program is to establish a fundamental understanding of (1) the residual stresses and resulting damage within fibers intersecting a free surface, (2) the fiber/matrix interfacial shear behavior and its characterization, and (3) the role of matrix plastic deformation during fiber sliding within sapphire-reinforced TiAl composites.

Although the problem of sapphire fiber cracking or splitting has plagued the MMC industry for nearly 30 years, no one has been able to satisfactorily analyze this phenomenon, identify those factors that contribute to its occurrence, and consistently correct the problem through fiber/matrix interface and/or processing modification. This research program examines this phenomenon in terms of (1) thermally-induced residual tensile stresses, (2) the use of brittle fibers with low toughness values, and (3) damage that can result in pre-existing flaws in a fiber intersecting a free surface. Both computationally-predicted stress states and experimental validation are used to analyze the fiber splitting problem.

Previous studies have shown that the interfacial shear strength of directly bonded interfaces between sapphire fibers and TiAl-based matrices is relatively strong [7-10]. As a result, fiber damage and low fracture toughness are a commonly reported problem in sapphire-reinforced TiAl composites [8, 11-15]. Therefore, the interfacial shear strength must be reduced to improve the damage tolerance of these materials. To obtain an optimum shear strength, the chemical interaction and mechanical interlocking between the fibers and the matrix must be controlled (e.g., through the use of fiber coatings). To determine the success of these controls, it is important to be able to measure accurately the interfacial shear strength and the accompanying interfacial failure process.

Fiber pushout testing is currently performed routinely at various labs across the country for the purpose of determining interfacial shear strength in fiber-reinforced IMCs. However, specimen support configuration, interfacial stress distributions, and their effect on the observed results are largely ignored. This research program uses a unique experimental approach to characterize the interfacial failure sequence in a manner that permits an accurate physical description of the interfacial "debond" process.

The "frictional" sliding resistance (i.e., τ_{slide}) of debonded fibers during monotonic and cyclic loading makes an important contribution to the toughening mechanisms of fiber pullout and crack tip bridging in CMCs and IMCs [69, 87]. Previous studies have addressed the importance of residual stress [69] and fiber surface roughness [65, 66, 85-88] to τ_{slide}. The present study examines large-scale fiber displacement following complete fiber debond from the standpoint of addressing the contribution of matrix plastic deformation to τ_{slide} and its role in interface wear/degradation with continued monotonic or cyclic loading in IMCs. This research program gives substantial evidence that matrix plasticity plays a dominant role in the "frictional" sliding resistance of debonded fibers and interface wear in sapphire/TiAl composites.

Chapter 3

EXPERIMENTAL PROCEDURES

In this chapter, the experimental procedures used in this study are described in detail. The procedures are broken down into six stages: (1) specimen fabrication, (2) microscopic characterization, (3) assessment of fiber damage, (4) experimental validation of FEM predicted stress states, (5) indentation pushout testing, and (6) fiber displacement measurements.

3.1. Specimen Fabrication

This study is based on low volume fraction fiber-reinforced matrices consisting of sapphire fibers embedded in two different matrices based on the intermetallic TiAl: Ti-48Al-1V (hereafter referred to as Ti-48-1) and Ti-48Al-2Cr-2Nb (i.e., Ti-48-2-2) where compositions are given in atomic percent. Unidirectionally reinforced fiber composites were prepared via vacuum hot pressing pre-alloyed matrix powder and 160 μm (average) diameter fibers. The Ti-48-2-2 matrix material was consolidated by G. E. Aircraft Engines (GEAE), Evendale, OH, and contained approximately 9 volume percent of uncoated sapphire fibers. A much lower volume fraction of sapphire reinforcement (0.1 volume percent) was produced for the Ti-48-1 material where both uncoated and tantalum-coated fibers were incorporated in the matrix. This material (i.e., Ti-48-1) was consolidated at Penn State as part of this study.

Both matrices were provided by Crucible Research, Pittsburgh, PA, in the form of helium gas-atomized powder. The concentration of interstitial elements in as-received -35 mesh powder (i.e., < 500 μm in diameter) is given in Table 2. (Chemical analysis of the

Table 2. Chemical analysis (atomic %) of matrix materials used in this study at various stages of processing. (Chemical analysis for Ti-48Al-2Cr-2Nb is taken from Amato [8].)

Nominal Composition	Condition	Ti	Al	V	Fe*	O*	N*	C*	H*
Ti-48Al-1V	As-received	Bal.	48.7	0.8	380	590	120	540	48
Ti-48Al-1V	Following powder size reduction	Bal.	46.6	0.8	1310	11500	1000	1100	NR
Ti-48Al-2Cr-2Nb	As-received	NR	NR	NR	NR	800	50	310	NR
Ti-48Al-2Cr-2Nb	Following composite fabrication	NR	NR	NR	NR	1100	90	630	NR

NR = not reported
* ppm (weight basis)

Ti-48-1 powder was performed by Chemsys, Inc., while that for the Ti-48-2-2 material was reported by Amato [8].) The concentration of unwanted interstitial elements in titanium-based alloys is very important since strength, toughness, and ductility are a sensitive function of their relative concentrations. As-received powder shapes were generally spherical as shown in Figure 5a.

Although only low volume fraction samples were fabricated and tested in this study, the original intent of this part of the investigation was to fabricate high volume-fraction (e.g., 20%) sapphire/Ti-48-1 samples. Therefore, due to the large particle size of the as-received powder and the high hardness of this alloy at fabrication temperatures, initial efforts early in this study were focused on reducing the powder particle size below the magnitude of the interfiber spacing required to produce high volume-fraction composites. Powder sizes greater than the interfiber spacing will displace the fibers when pressure is applied for consolidation [20]. Therefore, a wide range of mechanical grinding methods were attempted in order to reduce powder particle sizes from -35 mesh (i.e., < 500 μm) to -325 mesh (i.e., < 45 μm). The method yielding the greatest success was

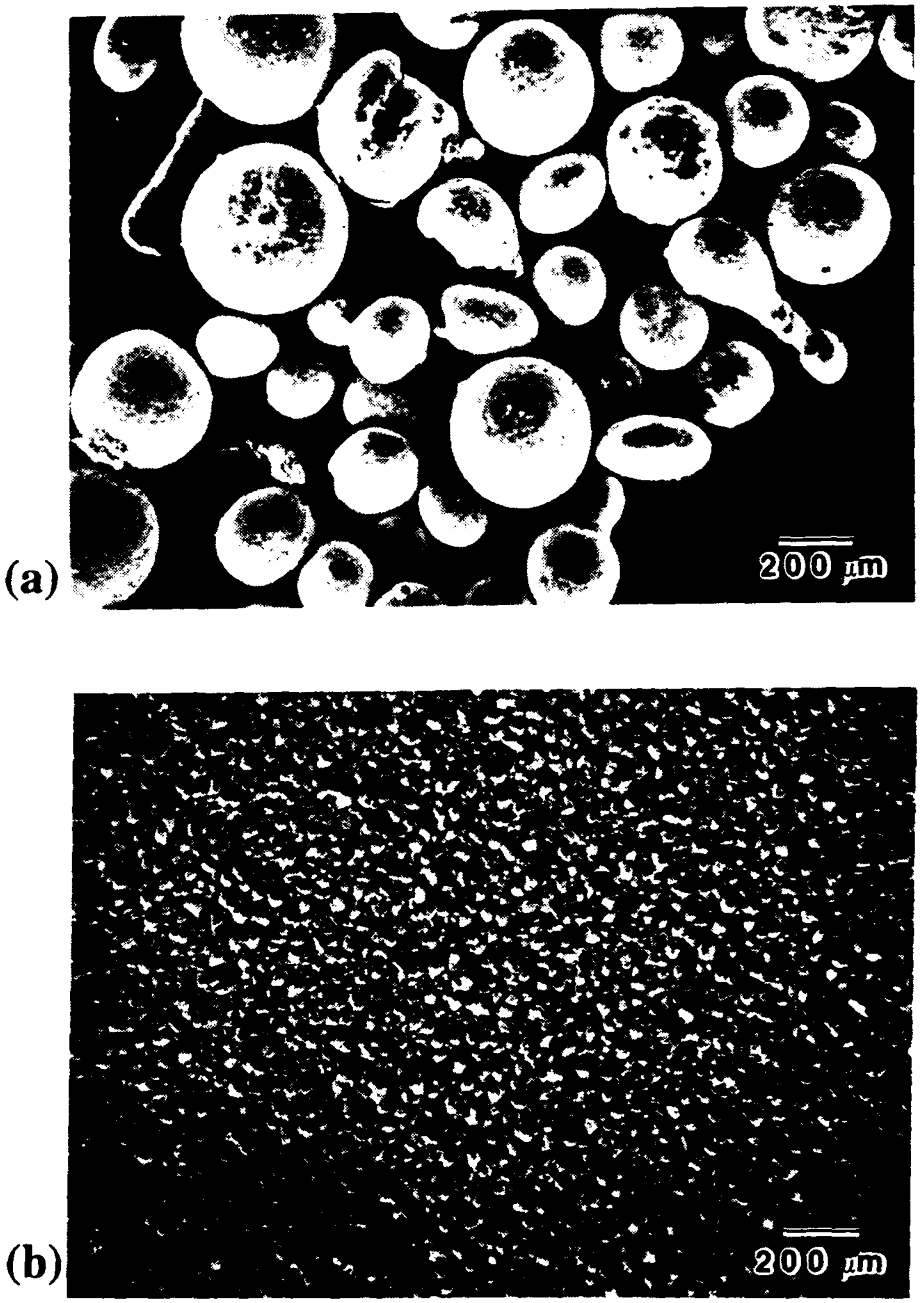

Figure 5. Helium gas-atomized Ti-48Al-1V powder (a) in the as-received (-35 mesh, i.e., < 500 µm) condition and (b) after grinding to -325 mesh (< 45 µm) in a Bleuler Laboratory Swing Mill.

shatter-box grinding with a Bleuler Laboratory Swing Mill manufactured by Hans Naef AG. This mill uses a stainless steel grinding ring and stone arrangement to pulverize the powder. Figure 5b shows the size and morphology of the powder particles following this grinding step. Since the mill was operated in air, a significant increase in interstitial contamination occurred as shown in Table 2. Most notable is the 20-fold increase in oxygen content. This is a direct result of: (1) TiAl's high affinity for oxygen and (2) the large increase in surface area exposed to air as a result of the much smaller powder particle size. This second point is clearly shown by comparing Figures 5a and 5b (both micrographs are at the same magnification). It is also important to note the increase in iron contamination from the grinding container.

The single-crystal sapphire fibers were fabricated by Saphikon, Inc. and have a range in diameter from 150 to 175 μm. The protective, organic, Dow *Methocel*^{TM} *coating* present on as-received fibers (to protect them from self-abrasion during handling) was removed prior to hot pressing by: (1) flame-polishing in an oxygen-rich gas flame for fibers incorporated into the Ti-48-1 matrix and (2) soaking in cold water followed by rinsing in acetone for fibers incorporated into the Ti-48-2-2 matrix. A typical uncoated, flame-polished fiber prior to hot pressing is shown in Figure 6. A faint contrast from the diametrial variation that occurs in a periodic pattern produced during fiber production (arrowed) can be seen in this micrograph. The wavelength of the variation is 12.5 μm which is in good agreement with measurements made by Mackin et al. [7]. The tantalum (Ta) coating on fibers supplied by Pratt and Whitney, East Hartford, CT, was deposited via sputtering at Midwest Research Technologies, Milwaukee, WI. As shown in Figure 7, the coating was ≈0.2 μm thick and appeared to be continuous. The Ta-coated fibers were subsequently incorporated into the Ti-48-1 matrix.

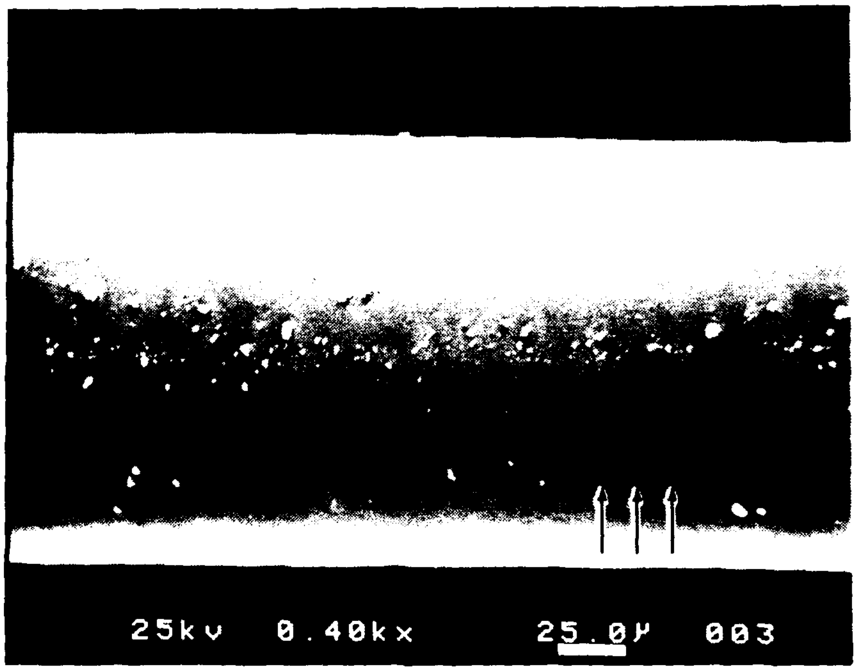
25kv 0.40kx 25.0µ 003

Figure 6. A typical uncoated, flame-polished fiber prior to hot pressing. Note the faint contrast from the diametrial variation that occurs in a periodic pattern (arrowed).

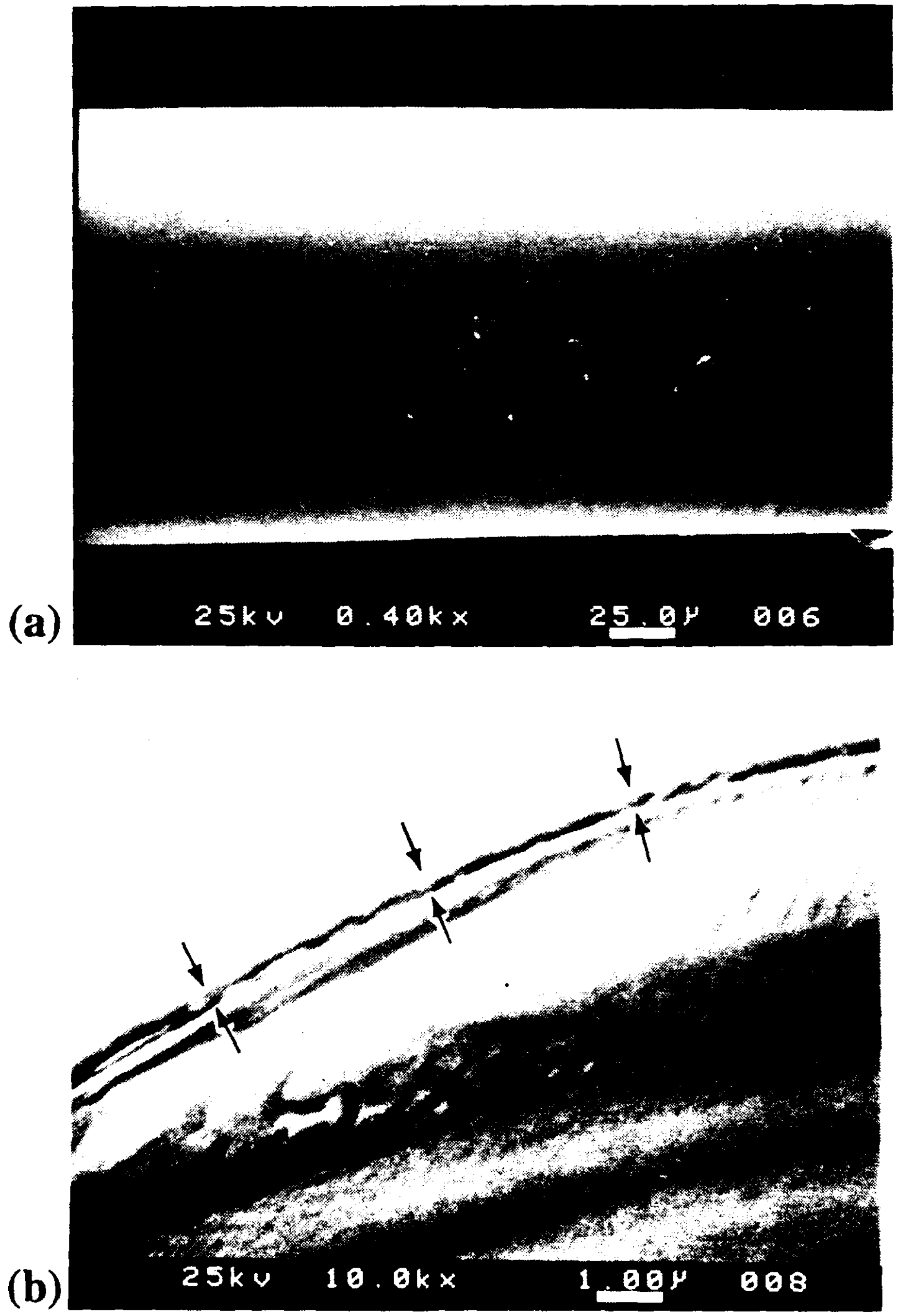
(a)
25kv 0.40kx 25.0µ 006
(b)
25kv 10.0kx 1.00µ 008

Figure 7. Tantalum-coated fiber prior to incorporating into the Ti-48Al-1V matrix. (a) Coating appeared to be continuous and (b) ≈0.2 µm thick (arrowed on fiber's cross-section).

A low volume fraction (≈0.1 volume percent) Ti-48-1 composite was fabricated via vacuum hot pressing both uncoated and Ta-coated fibers in the same specimen. The -325 mesh, Ti-48-1 matrix powder previously produced by grinding as-received powder was used to fabricate this specimen. The Ti-48-2-2 composite produced by GEAE was fabricated via a two-stage vacuum hot press followed by hot isostatic press procedure. Only uncoated fibers were incorporated into the -35 mesh Ti-48-2-2 matrix powder. The matrix powder contained an organic binder that was subsequently removed during fabrication [8].

3.2. Microscopic Characterization

Optical and scanning electron microscopy (SEM) were used in this study to characterize: (1) the microstructure of the interfacial region, (2) the condition of the fiber surface before and after composite fabrication, (3) the extent and nature of cracks within fibers embedded in the matrix, and (4) the fiber/matrix interface and fiber displacement following pushout testing. To identify the phases within the matrix, their distribution, and to determine the grain size, a two-stage etching procedure developed for TiAl-based alloys at the Rockwell International Science Center [91] was used. First, a 50 ml lactic acid-20 ml nitric acid-1.5 ml hydrofluoric acid etchant (hereafter referred to as a lactic acid etchant) was used to differentiate the α_2 (i.e., Ti_3Al) phase from the rest of the microstructure. Next, a Kroll's etchant consisting of 8.0 ml nitric acid and 1.0 ml hydrofluoric acid in 91.5 ml distilled water was used to reveal the matrix grain structure and distribution of the α_2 and γ phases within the alloys. Each etchant was applied to the specimen's surface by swabbing with cotton for ≈10 seconds at room temperature.

To further characterize the fiber/matrix interfacial region, microhardness, electron microprobe, and x-ray microanalysis were used. The hardness values near the fiber/matrix interface were measured with a Leco M-400 Microhardness Tester using both Knoop and Vickers diamond indenters at loads ranging from 10 to 100 grams and a dwell time of 10 seconds. A microcomputer-operated Cameca-Camebax SX 50 Electron Microprobe was used to obtain a qualitative description of the distribution of elements within the interfacial region (through elemental x-ray maps) and semi-quantitative concentration profiles of different elements across the interface. To identify the interface along which failure occurred during fiber pushout testing, a Kevex Energy-Dispersive X-Ray Microanalysis System attached to a SEM was used to identify semi-quantitatively the material on the fiber surface and matrix wall following large-scale fiber displacement.

3.3. Assessment of Fiber Damage

The extent and nature of cracks within sapphire fibers were characterized when they were embedded in the matrix as well as after they had been removed. Frequently, cracks within embedded fibers could not be seen using reflected light metallography. Therefore, to reveal the presence of cracks, a fiber optic light source was used to transmit light through the optically transparent sapphire fibers oriented normal to the surfaces of a thin-slice specimen. By viewing a fiber end opposite the light source with a metallograph at 1000x and taking into account the refractive index of sapphire, the depth of fiber surface cracks could be measured to an accuracy of ±2 μm via metallograph stage movement. In an attempt to minimize the development of surface cracks in the fibers during cutting, several cross-sectioning methods were attempted:

(1) high speed (i.e., ≈3500 rpm) abrasive wheel cutting using a wafering blade impregnated with 60 μm diamond abrasive,

(2) low speed (i.e., ≈250 rpm) abrasive wheel cutting using wafering blades impregnated with 60 μm and 6 μm diamond abrasives,

(3) wire saw cutting with a 254 μm diameter stainless steel wire coated with slurries of 12 μm SiC (glycerin-based) and 6 μm diamond (oil-based) abrasives,

(4) laser beam cutting with a 1.5 kW CO_2 gas laser (performed by Applied Research Laboratory, University Park, PA), and

(5) abrasive water jet cutting with a high pressure (60,000 psi) stream of water and alumina abrasive (performed by Quest Integrated, Inc., Kent, WA).

The extent of fiber fracture and crack orientation with respect to the fiber axis was characterized by chemically removing the matrix with a concentrated Kroll's etchant (i.e., 15 ml nitric acid and 10 ml hydrofluoric acid in 75 ml distilled water). Care was taken to avoid residual stress-induced fiber buckling that was observed by Marshall and Graves [92] when the matrix was not uniformly removed from around the fiber via complete immersion of the sample in acid. Therefore, in this study, only small portions of matrix were incrementally removed along the fiber axis by suspending the specimen in a beaker of etchant.

3.4. Experimental Validation of FEM Predicted Stress States Using Indentation Crack Growth Analysis

Finite element computations predicted that significant thermally-induced residual tensile stresses exist near the ends of sapphire fibers that are embedded within TiAl-based matrices and are oriented normal to a free surface (see section 4.2.2.1) [93]. It has been shown in several studies of brittle materials that indentation cracks can be used to estimate the magnitude of pre-existing residual stresses [94-97]. This method offers the advantage of being experimentally straight forward, and its analysis enables residual stresses to be probed on a small scale. Therefore, this study used indentation crack growth behavior within the sapphire fibers to experimentally verify the predicted stress states.

The specimens for determining residual stresses were prepared in the form of thin (i.e., 0.3 to 0.6 mm) sections cut perpendicular to the fiber axis with a low speed saw using a diamond wafering blade. Care was taken to align the fibers normal to the specimen surface, i.e., the (0001) basal plane parallel to the specimen surface. The specimens were ground flat on a glass plate with 3 μm diamond and subsequently polished with 1 μm diamond paste on nylon cloth. As will be discussed in section 4.2.2.1, it is important to note that all specimens were exposed to water during their preparation. In addition, all specimens tested were in the as-fabricated condition.

Indentation of the fibers was performed using a Vickers diamond pyramid indenter and a Leco M-400 Microhardness Tester for loads ranging from 0.98 to 4.9 N such that well developed radial crack patterns were obtained (i.e., $c \geq 2a$, where c is the crack radius and a is the indentation diagonal [94]). In addition, the overall crack length, 2c, was maintained less than 75% of the fiber's diameter. These indentations were made in air with a load dwell time of 10 seconds.

In addition to sapphire fibers embedded in Ti-48-1 and Ti-48-2-2, an indentation crack growth analysis of fibers hot pressed in pure niobium (0.1 volume percent fibers) was also performed. Since the coefficient of thermal expansion (CTE) mismatch between niobium (Nb) and sapphire is small, the predicted thermally-induced residual stresses upon cooling from the fabrication temperature are also very small (i.e., $\sigma_{rr} \approx \sigma_{\theta\theta} \approx -13$ MPa) [98]. Therefore, the indentation of fibers embedded in Nb served as a convenient calibration for the indentation crack size in a stress-free sapphire fiber.

The cracks formed during the contact between a sharp indenter and a brittle material have been classified into two systems: (1) half-penny shaped, radial/median cracks (hereafter referred to as radial cracks, shown in Figure 8) that form on symmetry planes containing the load axis and principal indenter diagonals and (2) lateral cracks that form on shallow sub-surface planes approximately normal to the load axis [99, 100]. Of these two crack systems, the radial cracks are of interest here since they closely model the type of damage experimentally observed in as-cut sapphire fibers. The lengths of the radial cracks induced within the fibers (i.e., see Figure 8) were measured using the microhardness tester's measuring eyepiece with an accuracy of ±0.2 µm. Mean crack sizes were determined from 2 to 9 indentations for each fiber/matrix system.

After making the above measurements, it was necessary to: (1) apply the appropriate fracture mechanics relations in order to obtain a predicted crack size for a given indentation load and the residual stress state calculated by FEM and (2) compare this predicted crack size with that measured experimentally. The fracture mechanics analysis is as follows: First, for a residual stress-free substrate, the driving force for the growth of radial cracks that emanate from the indentation corners is assumed to result from the residual contact stress field [101]. For an indentation load, P, the radius, c, of the radial

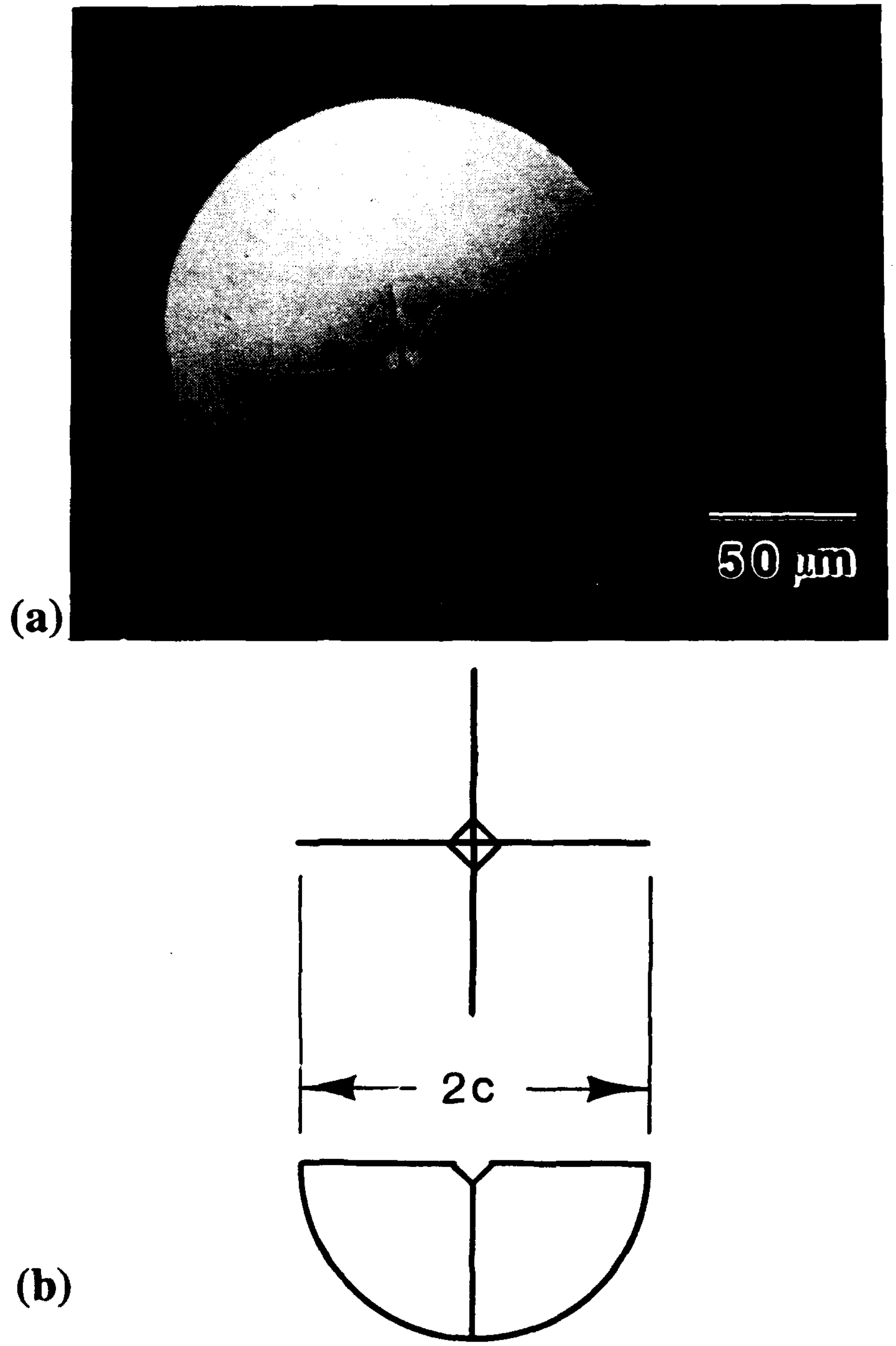

Figure 8. Fracture pattern formed following indentation of a sapphire fiber. (a) Transmitted light optical micrograph of a 4.9 N Vickers indentation in an uncoated fiber embedded in Ti-48Al-2Cr-2Nb. (b) Schematic showing surface traces and ideal shape of the half-penny, radial cracks (adapted from Marshall and Lawn [95]).

half-penny shaped cracks may be determined from the residual stress intensity factor K_i due solely to the indenter load [101, 102]:

$$K_i = \frac{\chi P}{c^{3/2}}, \tag{9}$$

where χ is a dimensionless parameter dependent on the indenter cone half angle and the stiffness-to-hardness ratio of the substrate. For the present study, χ has a value of 0.0687 based on indentation crack size measurements in the assumed stress-free sapphire fibers embedded in Nb[e]. It should be noted that the form of K_i is such that it decreases with increasing crack length. This will result in crack propagation and subsequent arrest at a length dictated by the fracture toughness of the fiber.

If a radial crack is also acted upon by thermally-induced residual stresses, the net mode I stress intensity factor, K, can be obtained by use of the superposition principle:

$$K = K_i + K_r, \tag{10}$$

where K_r is the stress intensity factor for an identical half-penny shaped crack subject to a thermally-induced residual stress field. For equilibrium conditions, the crack extends until K equals the fracture toughness of the material, K_{Ic} [94].

By generalizing an earlier approach by Lawn and Fuller [94], K_r may be obtained for any depth profile of stress, even if the thermally-induced stresses vary with position in the material. Taking the fracture mechanics solutions for a concentrated force acting on an elemental area within the crack perimeter [103] and integrating this solution over the entire crack area, the stress intensity due to the residual stresses only is obtained [94]:

---

[e] For equilibrium conditions, the crack induced by a given indentation load in a residual stress-free substrate extends until K_i equals the material's fracture toughness. Therefore, by substituting the mean crack size (c) measured in the assumed stress-free sapphire fibers embedded in Nb for a given indentation load (P) into equation (9), as well as the fracture toughness of sapphire (measured by Wiederhorn [34] as 2.5 MPa-m$^{1/2}$), a value for the dimensionless parameter (χ) was obtained.

$$K_r = \frac{\psi}{\sqrt{c}} \int_0^c \left(\sqrt{\frac{c}{z}} - 1\right) \sigma(z)\,dz, \tag{11}$$

where $\sigma(z)$ defines the residual stress field profile as a function of depth, z, into the fiber from the free surface, and ψ is a crack geometry term approximately equal to unity. In the present study, the residual stress profiles within the fiber, as calculated by FEM, were assumed to fit 4th-order polynomials according to:

$$\sigma(z) = \sigma_R(1 + az + bz^2 + dz^3 + ez^4), \tag{12}$$

where σ_R is the maximum tensile stress in the free surface of the fiber and a, b, d, and e are constants. Note that $\sigma(z)$ refers to either the radial, σ_{rr}, or hoop stress, $\sigma_{\theta\theta}$, component, whichever is greater. Subsituting equation (12) into (11) and combining the result with equations (9) and (10) yields an expression that permits the calculation of the net mode I stress intensity:

$$K = \frac{\chi P}{c^{3/2}} + [\psi \sigma_R \sqrt{c}(1 + \frac{a}{6}c + \frac{b}{15}c^2 + \frac{d}{28}c^3 + \frac{e}{45}c^4)]. \tag{13}$$

Note that the presence of thermally-induced residual tensile surface stresses assist the residual contact stresses in propagating a crack.

By setting K = K_{Ic} in equation (13), an equilibrium radial crack size (c) can be predicted for a given indentation load (P) and the residual stress state calculated by FEM. Comparison of the predicted crack size with those experimentally measured within the embedded sapphire fibers then serves to test the validity of the FEM predicted stress state.

3.5. Indentation Fiber Pushout Testing

Pushout and push-back tests were performed on thin-slice specimens ranging in thickness from 0.31 to 0.37 mm. Care was taken to align the fibers normal to the specimen surface. The specimen surface was ground flat and polished to a 1 μm diamond paste finish on nylon cloth (i.e., in the same manner as described in section 3.4). The indentation fiber pushout test apparatus used in this study was designed and developed by Moose et al. [64, 98] in a parallel effort by NASA Lewis Research Center [104].

3.5.1. Indentation Pushout Test Apparatus

The configuration of the indentation pushout test apparatus is shown in Figure 9 [64]. The tests were performed on an Instron universal test frame equipped with a 1 KN load cell. A flat-bottomed, 127 μm diameter tungsten carbide indenter (manufactured by National Jet, Inc.) was used to apply the load to the fiber selected for testing. This resulted in an indenter-to-fiber diameter ratio of ≈75 to 85 %. Alignment of the indenter with the fiber end-face was achieved through position control of the specimen with a joystick controlled, high load capacity, x-y micropositioning table. Alignment was visually monitored by using two optical telescopic microscopes (manufactured by Gartner Scientific, Inc.) offset at ≈90° equipped with high resolution, black and white video

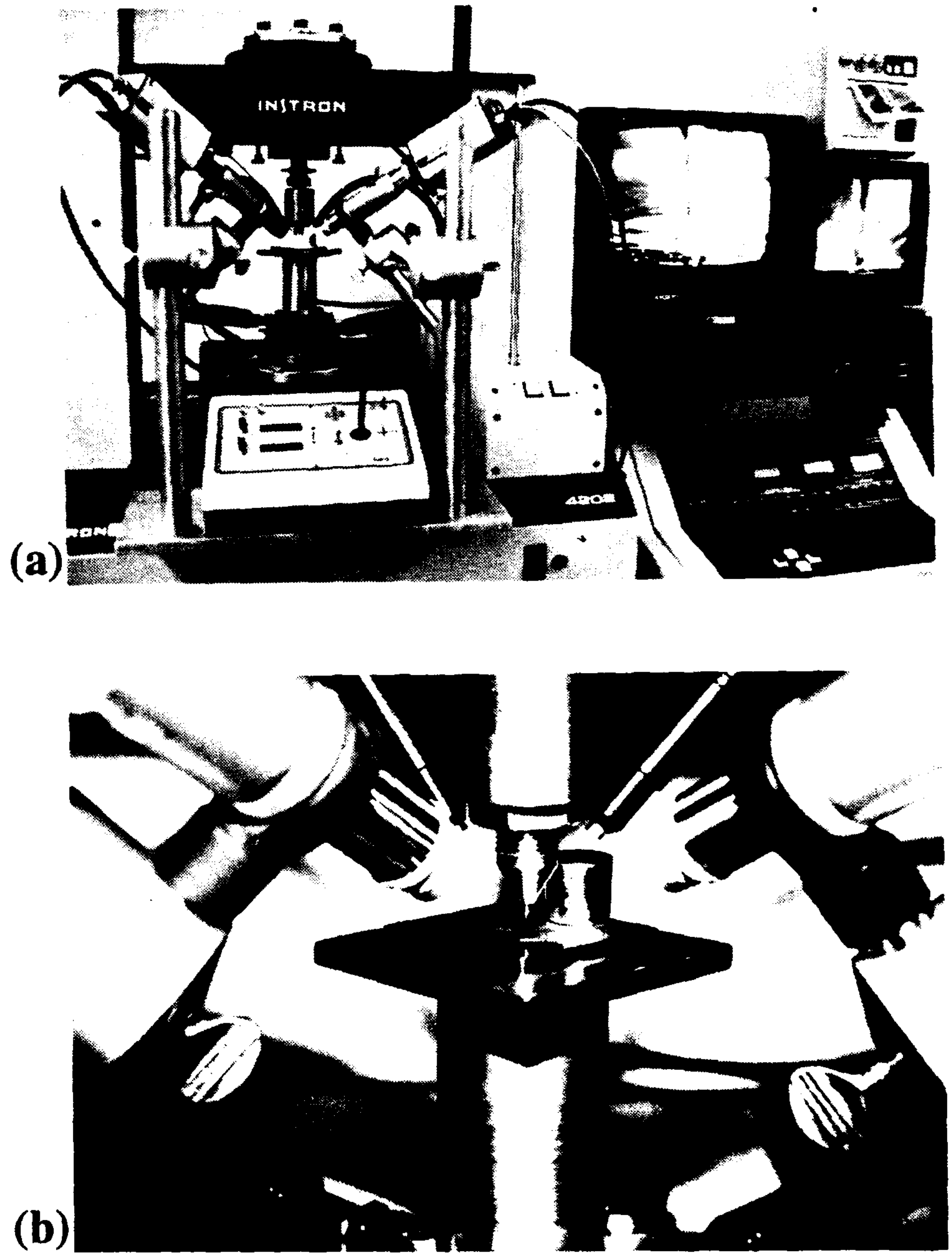

Figure 9. Configuration of the indentation pushout test apparatus (photographs courtesy of Moose [64]). Views showing (a) test frame, and cameras and monitors that aid alignment of the indenter with the fiber, and (b) indenter/specimen/x-y positioning table arrangement.

cameras. This setup also allowed continuous monitoring of fiber displacement and indenter alignment throughout the test [64].

Load measurements were recorded every 0.1 seconds using a high resolution, computer controlled, data acquisition board by Strawberry Tree, Inc. Tests were done using a constant cross-head displacement rate of 30 or 50 μm/minute. In addition, acoustic emissions were recorded during the test by mounting a small (5 mm diameter and 5 mm high), 100 to 1200 KHz broad band transducer to the stainless steel support plate on which the specimen rested. Coupling of the transducer to the support plate was accomplished with vacuum grease. Acoustic emission signals were collected as a function of time by a Locan AT microcomputer [64].

3.5.2. Specimen Support Configuration

In order to accommodate the displaced fiber during testing, specimens must be supported over a hole or slot. In this study, specimens were supported over very small holes in order to: (1) minimize bending of the specimen and (2) simplify FEM analysis of the biaxial stress state peculiar to the test configuration. Two types of support configurations were used. First, fibers were concentrically aligned over a 254 μm diameter support hole that was electro-discharge machined (EDM) through a 1/8 inch thick 316 stainless steel plate. This resulted in a support hole to fiber diameter ratio of ≈1.6. Most fiber pushout tests performed by other researchers are performed with this ratio typically ≥2 [68]. Precise concentric alignment of the fiber over the hole was accomplished with the aid of an inverted stage metallograph and a fiber optic light source. Rough alignment was achieved by aligning the microscope's stage, support plate, and specimen such that light from the metallograph passed through the bottom of the support plate and up through the optically transparent fiber. Next, the metallograph's light source was switched off and light from the fiber optic light source was transmitted through the top of the fiber. The metallograph was focused on the fiber's bottom side by focusing up through the support hole. While viewing the fiber in the metallograph's eyepiece, precise alignment was achieved by gently tapping the specimen until the fiber was concentric with the hole. Finally, a brass spring-clip type fixture (shown in Figure 10) was used to gently secure the specimen to the support plate [64].

The second type of support configuration was one in which the support hole was exactly the same size and shape as the fiber's cross-section (i.e., the fibers are not perfectly round) in an effort to eliminate specimen bending. This was achieved by depositing a 2 to 8 μm thick layer of nickel on the specimen's backface via electroplating. A hole exactly the same size and shape as the fiber's cross-section was preserved in the plated nickel layer by masking the fiber's end prior to electroplating with a negative photoresist that is sensitive to light. This is possible in sapphire-reinforced composites due to the ability of the fibers to transmit light [105]. The detailed procedure, described elsewhere [105], is summarized in Figure 11 (taken from Koss et al. [105]) and involves the following steps: (1) A coating (≈25 μm thick) of KTI 752 negative photoresist (produced by KTI Chemicals, Inc.) was applied to the specimen's backface. (2) The photoresist coating was cured at 80 °C for 2 hours. (3) Ultraviolet (UV) light (wavelength of 365 nm) was shown on the specimen's topface, transmitted through the fiber, and, therefore, exposed only the photoresist on the fiber's end. During exposure, the molecular weight of the exposed photoresist is increased [106] thus rendering it insoluble. (4) The specimen was immersed in a negative photoresist developer (KTI 802) that dissolved the unexposed photoresist and left the fiber coated with exposed photoresist (see Figure 11b). (5) The specimen was baked at 165 °C for 45 minutes to solidify the remaining photoresist to a final thickness ranging from 8 to 14 μm.

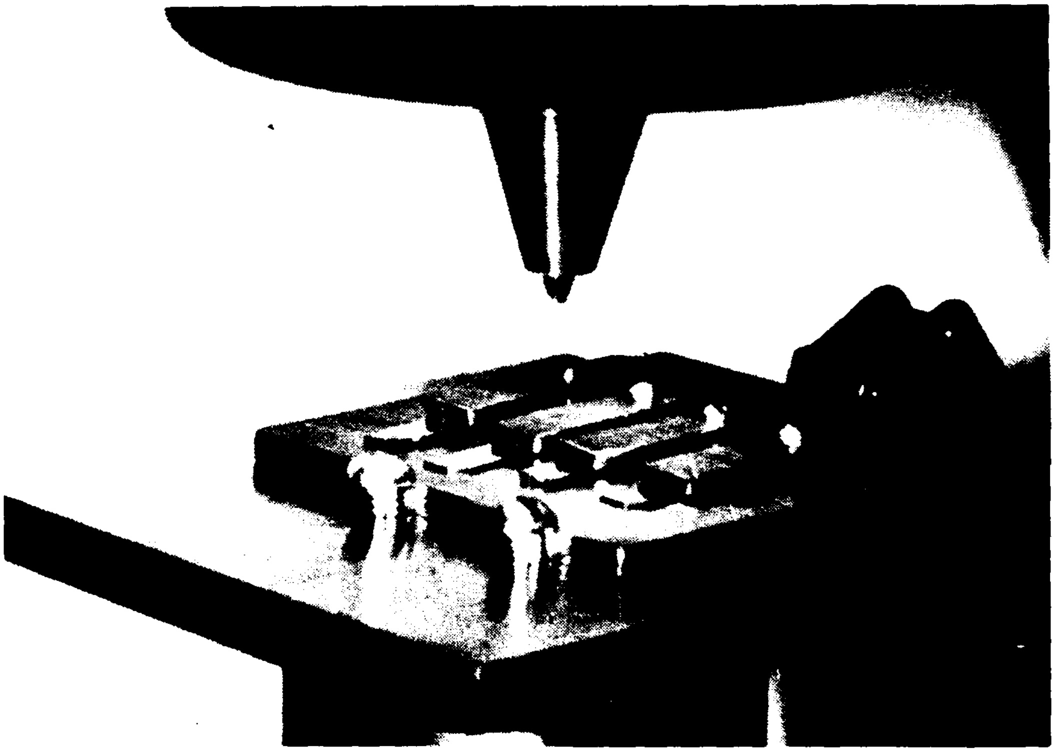

Figure 10. Stainless steel support plate with 254 μm diameter holes and brass spring-clips that secure specimens (photograph courtesy of Moose [64]). Note that the support plate is secured to the x-y table via two large screws (in front) and small clamps (in back).

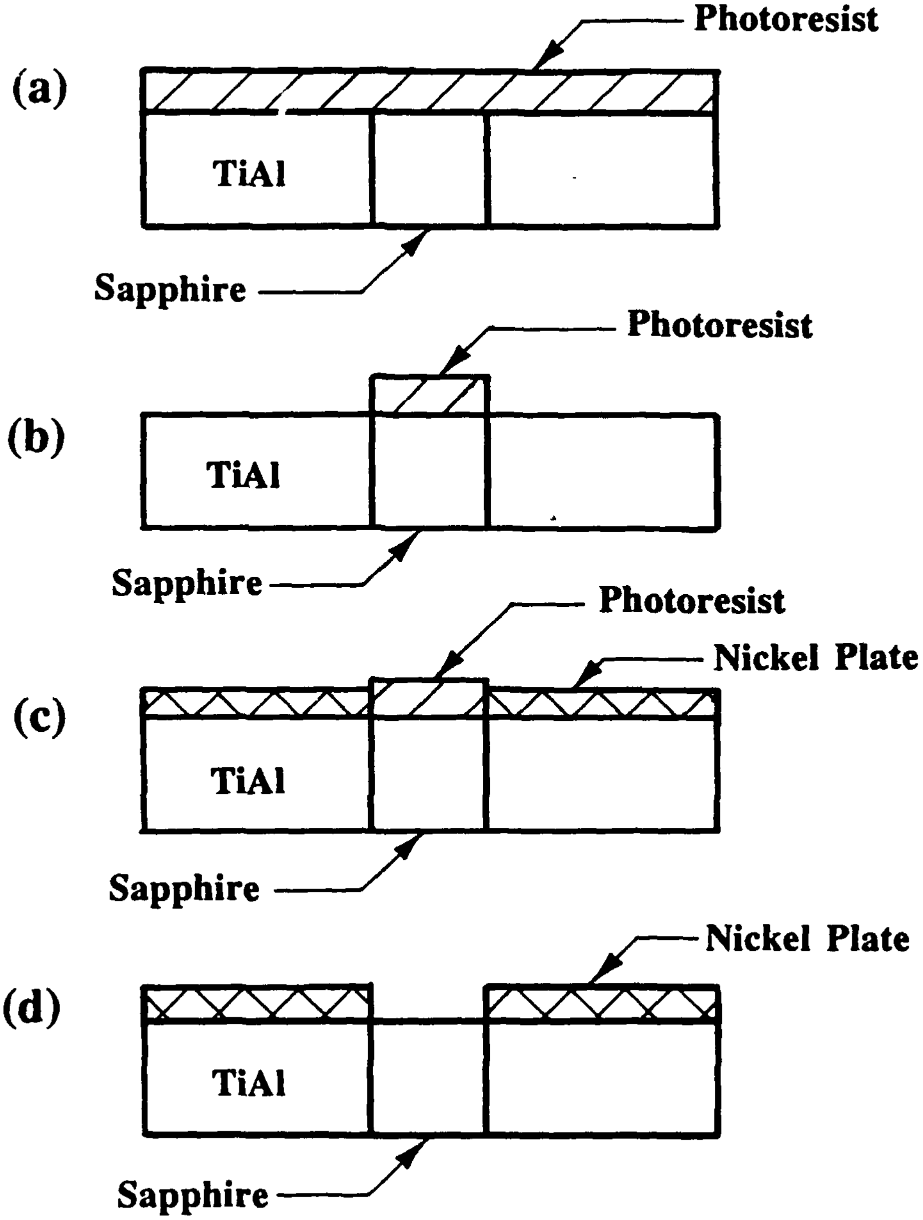
Photoresist
(a)
TiAl
Sapphire
Photoresist
(b)
TiAl
Sapphire
Photoresist
Nickel Plate
(c)
TiAl
Sapphire
Nickel Plate
(d)
TiAl
Sapphire

Figure 11. Procedure for producing a hole on the specimen's backface exactly the same size and shape as the fiber's cross-section (taken from Koss et al. [105]). (a) Apply negative photoresist to surface, cure, and expose to UV light. (b) Dissolve unexposed photoresist in developer and bake. (c) Plate nickel onto surface. (d) Remove remaining photoresist.

(6) After attaching lead wires to the specimen's topface and masking everything but the backface with a lacquer, nickel was plated onto the specimen's backface using a plating bath consisting of 180 gm nickel sulfate, 30 gm ammonium chloride, and 0.15 gm sodium lauryl sulfate in 1 liter of distilled water. The bath was maintained at a temperature of 50 °C and pH of 5.9. Using a pure nickel anode and maintaining a current density of ≈50 mA/cm^2 for 5 to 15 minutes resulted in a plate thickness of 2 to 8 μm on the specimen's backface (see Figure 11c). (7) The remaining photoresist covering the fiber was removed using a negative photoresist stripper (ACSI SN-10) maintained at 90 to 100 °C.

Figure 12 shows the backface of a typical specimen before and after the nickel "back-plating" procedure. Initial attempts at using this procedure revealed problems with adherence of the nickel plate to the specimen (i.e., the plate peeled-up). Evidence of this problem is shown in Figure 13 which shows a high magnification view of the nickel plate's edge at the hole over the fiber in Figure 12b. Although the plate's edge is not in contact with the specimen, it was assumed that it would flatten against the specimen during the early stages of the pushout test. To enhance mechanical adherence, the specimen's backface was not polished, i.e., it was ground flat with 3 μm diamond paste. This resulted in a somewhat rougher specimen surface, seen in Figure 12a, but improved plating adherence. Comparing measurements of the fiber's diameter on the backface and corresponding hole in the nickel plate verified that the plate did not overlap the fiber.

3.5.3. Test Methods

Before testing, the fibers were closely examined for the presence of cracks by using reflected and transmitted light metallography. By focusing through the fiber, the fiber

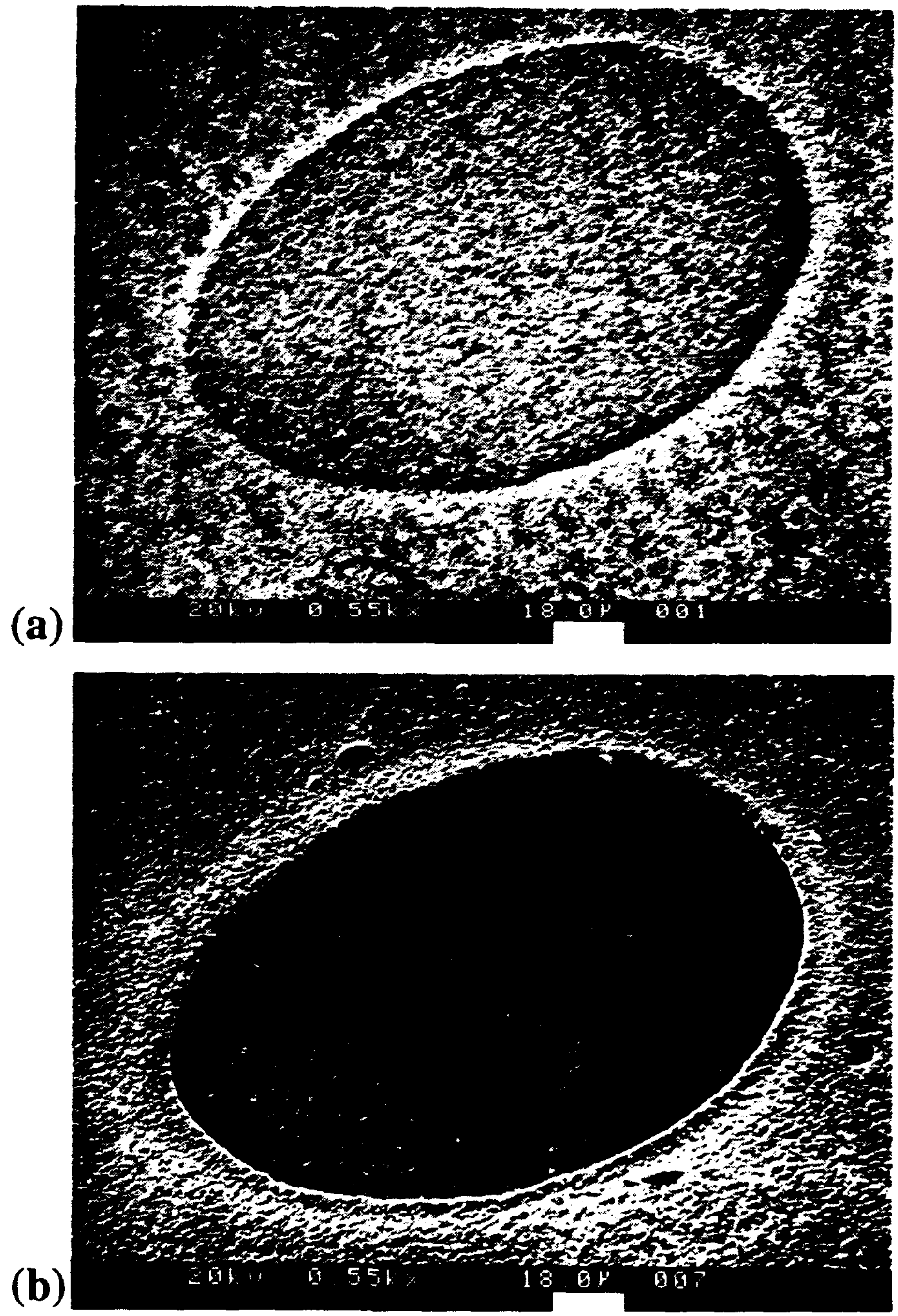
(a)
20kV 0.55kx 18.0P 001
(b)
20kV 0.55kx 18.0P 007

Figure 12. Backface of a typical specimen (a) before and (b) after the nickel "back-plating" procedure. Specimen surface was ground flat with 3 μm diamond paste to enhance mechanical adherence of the plate.

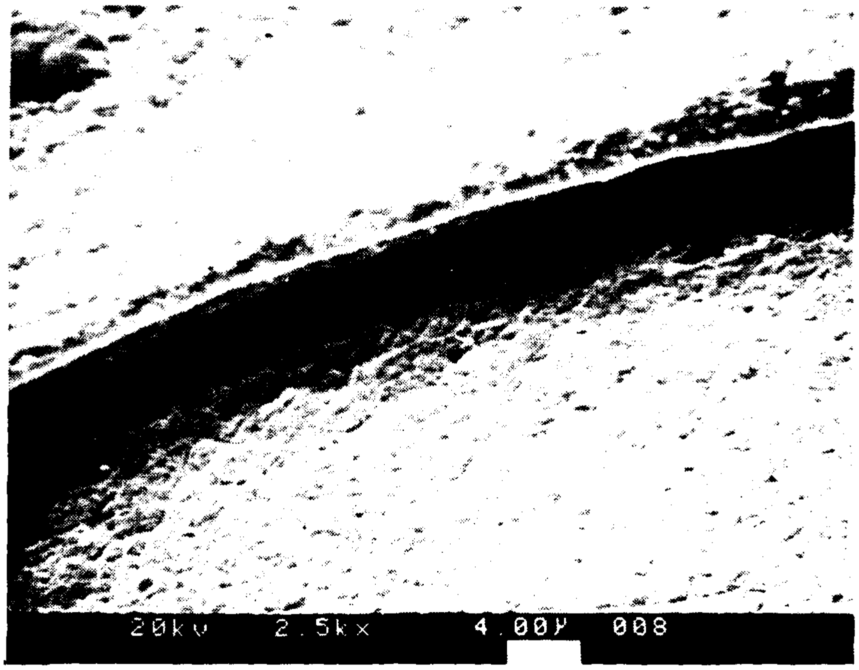
20kV 2.5kx 4.00μ 008

Figure 13. Evidence of low specimen/nickel plate adherence at the edge of the hole over the fiber.

could be examined for cracks along its entire length. Fibers containing cracks were not tested.

Three general types of tests were performed using the indentation test apparatus. First, tests in which the fiber was loaded, debonded, and displaced out of the matrix by as much as 120 μm were performed to assess the general interfacial failure (e.g., maximum load, load-drop following fiber/matrix debond, etc.) and fiber sliding behavior. In other tests, the fiber was incrementally loaded up to the load required for complete debond (established in the first type of test). After each incremental load, the specimen was carefully characterized via SEM examination and scanning laser microscope (SLM) surface profile measurements of top and backface fiber displacement in order to establish the interfacial failure sequence prior to the large-scale fiber displacement which occurs at maximum load. Finally, tests were performed in which an initially debonded and displaced fiber was pushed back beyond its original position (i.e., the "origin") to characterize fiber sliding and interfacial wear/degradation behavior.

3.6. Fiber Displacement Measurements Using Scanning Laser Microscopy

Following pushout testing, very accurate measurements of fiber displacement with respect to the matrix on the specimen's top and backface were obtained by using the 1LM11 Confocal Scanning Laser Microscope (SLM), which is manufactured by Lasertec Corporation. In this SLM system, the helium-neon laser scans the specimen point by point as the specimen stage moves vertically through a pre-determined range under computer control. Reflected light is detected by a confocal point detector in confocal optics, where only the position in focus gives maximum intensity. Non-contact surface profilometry is accomplished via the SLM's computer by memorizing the stage position at maximum intensity with respect to each scanned pixel [107]. In the surface profiling mode, the 1LM11 SLM's minimum measurement unit is 0.01 μm with a measuring repeatability of ±0.03 μm [107]. The accuracy of the particular SLM used in this study was verified experimentally by Moose [108] who reported a ±0.02 μm measuring repeatability while measuring steps (0.88 to 0.91 μm high) etched into silicon wafers.

Figure 14 is a micrograph of a typical SLM surface profile measurement made using the microscope's 50x lens (resulting in a micrograph at ≈2400x). Shown is the topface of a sapphire/Ti-48-2-2 specimen following a pushout test that was interrupted before fiber debonding occurred. The solid horizontal line is the trace along which the measurement was made. The "Manual" measurement is the actual distance between the vertical dashed lines, and "Depth" is the distance between the horizontal dashed lines, i.e., the distance the fiber is displaced below the matrix. Surface profile measurements were made on both top and bottom faces at 3, 6, 9, and 12 o'clock positions around the perimeter of each fiber tested. To insure that specimens that were subsequently re-loaded and re-measured were consistently measured at the same positions around the fiber's perimeter, position locations were scribed onto the specimen's topface. In addition to measuring fiber displacements, matrix plastic deformation that occurred within the interfacial region on the specimen's top and backface during pushout testing was also measured using SLM surface profilometry.

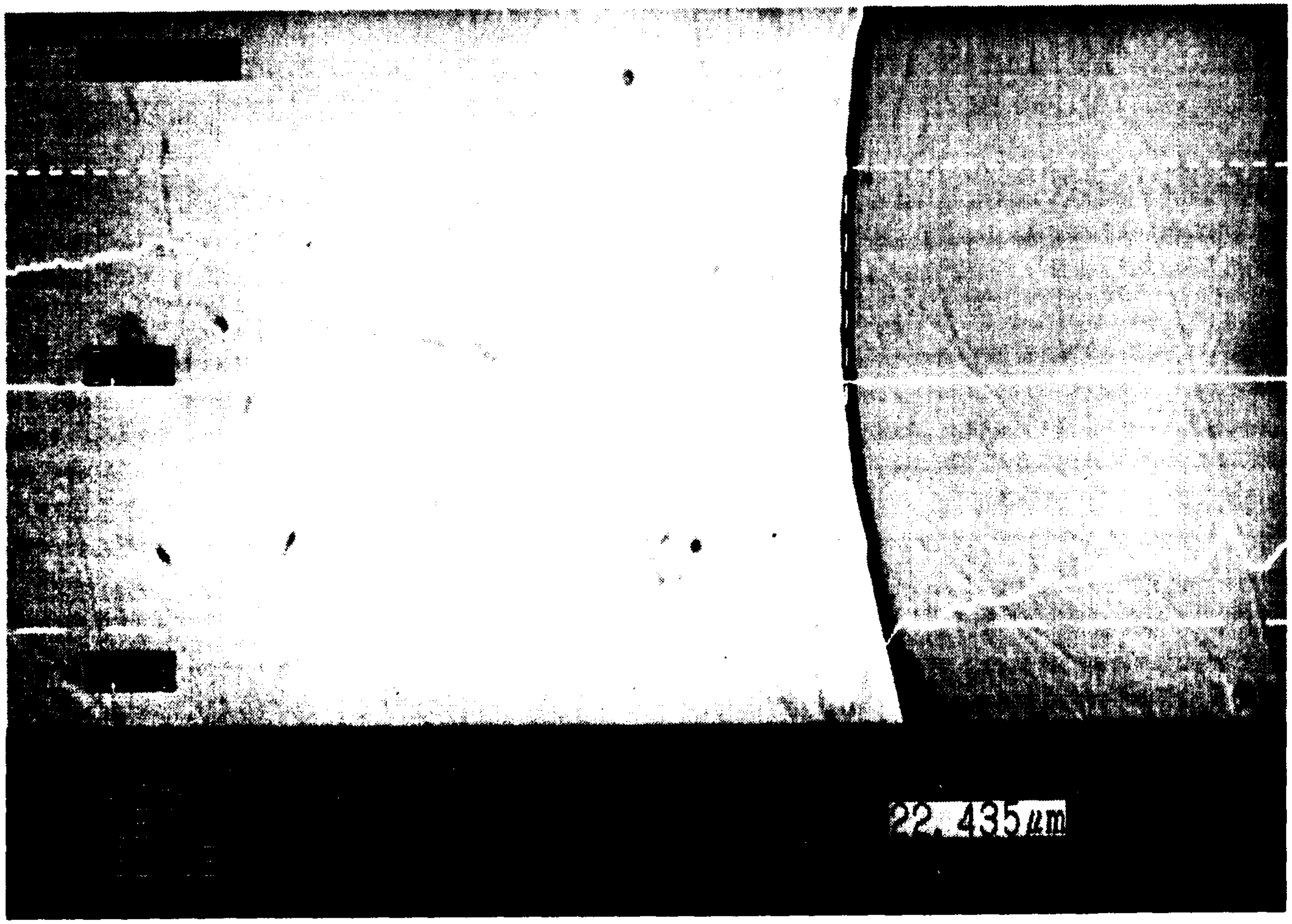

Figure 14. Micrograph of a typical scanning laser microscope surface profile measurement. The solid horizontal line is the trace along which the measurement was made. "Manual" and "Depth" are the distances between the vertical and horizontal dashed lines respectively.

Chapter 4

RESULTS AND DISCUSSION

Sapphire-reinforced TiAl composites offer great technological potential for future aerospace applications. However, one of the major problems associated with these materials is their lack of damage tolerance. This includes, but is not limited to, poor matrix toughness which is accompanied by low composite fracture toughness. This research program recognizes that this problem can be improved by reducing the interfacial shear strength in these composite systems. In addition, to ensure the success of attempts at controlling the shear strength in sapphire-reinforced TiAl, interfacial shear behavior (i.e., both debonding and sliding) must be carefully characterized and analyzed through testing techniques. Finally, for a sapphire-reinforced composite to exhibit optimum performance, fiber damage must be minimized.

In this chapter, the specific results of this study are presented and discussed. These results are grouped into three major sections: (1) interface microscopic characterization, (2) damage within fibers intersecting a free surface, and (3) fiber/matrix interfacial shear behavior.

4.1. Interface Microscopic Characterization

Before investigating the interfacial shear behavior of the three sapphire-reinforced TiAl composite systems in this study, a baseline was established by characterizing the microstructure of the interfacial region. This included: (1) phase distribution and grain size determination within the matrix (2) fiber surface characterization following composite fabrication, and (3) matrix microhardness measurement.

The Ti-48-1 and Ti-48-2-2 matrices selected for this study are two-phase alloys containing γ-TiAl and α_2-Ti_3Al intermetallic phases. Following vacuum hot pressing matrix powder and sapphire fibers, the Ti-48-1 matrix exhibited a duplex microstructure, as shown in Figure 15a, consisting of α_2- and γ-phases. In Figure 15b, the α_2-phase is more clearly delineated following the first stage of a two-stage etching procedure [91] (lactic etchant followed by Kroll's etchant) designed to reveal only the α_2-phase after the first stage, and the grain structure and distribution of both α_2- and γ-phases after the second stage (as shown in Figure 15c). Close examination of Figure 15b shows that α_2 precipitates outline the prior matrix powder particle boundaries (i.e., one particle boundary is arrowed). Figure 15c reveals that a fine, equiaxed γ grain structure exists in this material with a grain size of approximately 2.5 μm. Figure 16 is a backscattered electron SEM micrograph[f] from a polished and unetched Ti-48-1 specimen that clearly shows the distribution of α_2 (the light phase) and γ (the gray phase), as well as the presence of ≤ 1 μm diameter particles (the black phase) that decorate the prior powder particle boundaries. Electron probe microanalysis (EPMA) showed that these particles are aluminum- and oxygen-rich, but titanium-depleted, indicating that they may be Al_2O_3. The distribution of Al_2O_3 particles and α_2 grains on the prior particle boundaries is a direct result of the 20-fold increase in oxygen contamination that occurred during comminution of the matrix powder from an as-received size of -500 μm to -45 μm (i.e., see Table 2 in section 3.1). Since oxygen stabilizes the α_2-phase [12] and is concentrated on the powder particle surfaces, α_2 will be stabilized on the prior particle boundaries following consolidation, and any excess oxygen will combine with Al to form Al_2O_3.

---

[f] The backscattered electron signal from a smooth, polished surface gives atomic number contrast with the phase of higher atomic number providing the higher (i.e., brighter) signal level [109].

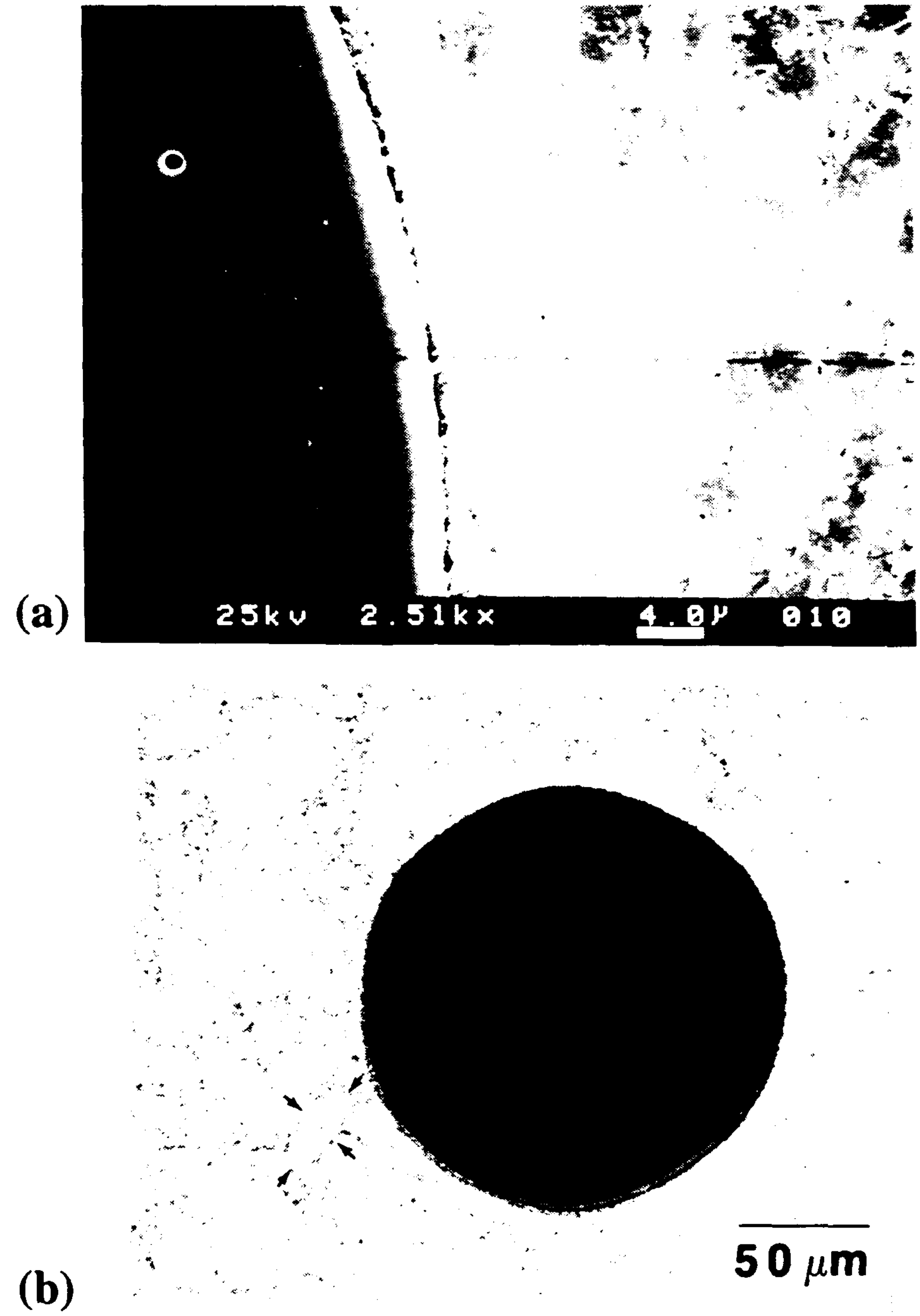

Figure 15. Typical photomicrographs showing the distribution of the α_2 and γ phases in the Ti-48Al-1V matrix following vacuum hot pressing. (a) SEM image, (b) optical image following etching with lactic etchant, and (c) optical image following two-stage lactic/Kroll's etching procedure. Note that (b) and (c) are recorded from the same area. (cont. on next page)

(c)

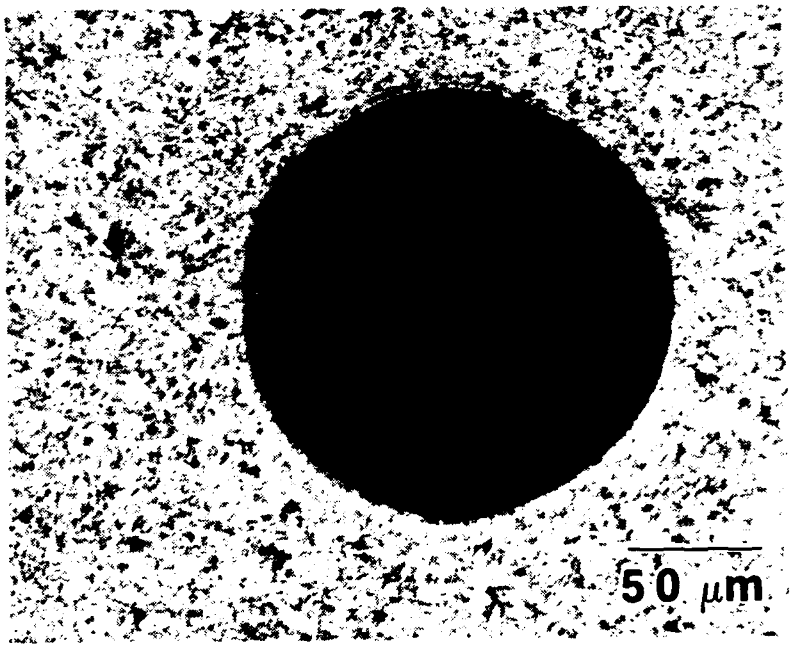

Figure 15. (cont.)

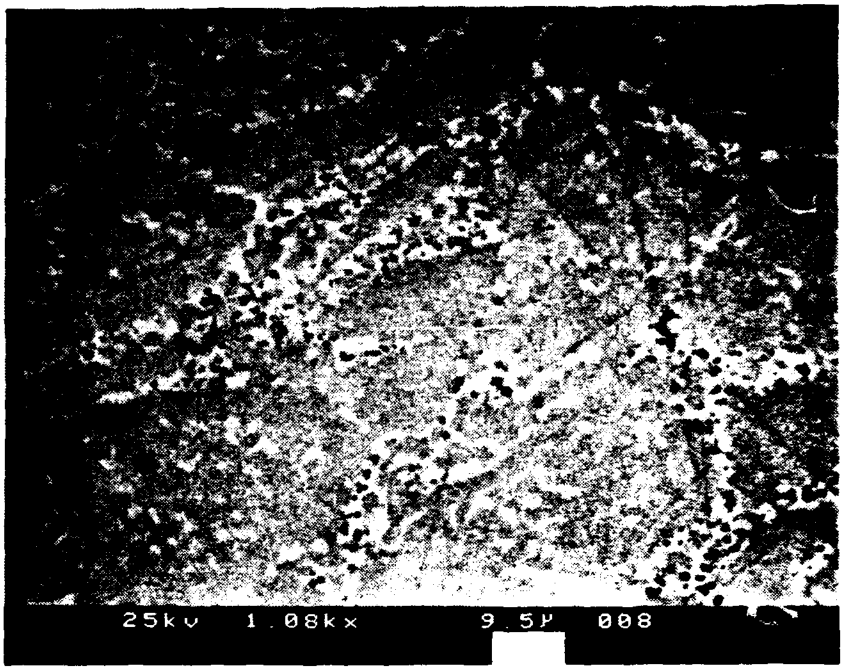

Figure 16. Backscattered electron micrograph of a polished and unetched Ti-48Al-1V specimen. The distribution of α_2 (light phase), γ (gray phase), and small (i.e., ≤ 1 μm) particles (black phase) are clearly shown.

Microstructural characterization of the uncoated sapphire/Ti-48-1 interfacial region shows that the fiber cross-section is somewhat serrated in appearance following composite fabrication (Figure 16 and 17). Figure 17 also reveals that voids may be present at the interface (arrowed) as well as a thin (i.e., $< 1\ \mu m$) interphase zone adjacent to the fiber (also see Figure 16) that is speculated to be either: (1) γ-phase as reported by Misra [59] in Ti-Al alloys containing less than 50 atomic % Al or (2) an amorphous reaction zone as observed by Das and Krishnamurthy [62] (also see section 2.5.1). It should be noted that the possible voids shown in this micrograph may be a result of preferential attack of the etchant at the fiber/matrix interface. However, the presence of voids at the interface and a serrated fiber surface is also in agreement with observations made by Das and Krishnamurthy [62] of sapphire-reinforced two-phase $\alpha_2 + \gamma$ composites. Evidence of Al and atomic oxygen dissolution from sapphire into two-phase TiAl-based matrices given by Misra [59], and Das and Krishnamurthy [62] could account for the thin region of γ stabilized adjacent to the fiber [59].

Further evidence of the severity of the fiber/matrix interaction in the uncoated sapphire/Ti-48-1 system is shown in Figure 18 following chemical removal of the matrix with a concentrated Kroll's reagent. Comparison between the as-received (Figure 18a) and as-consolidated (Figure 18b) fiber surfaces shows that a reaction occurs that degrades (i.e., roughens) the fiber surface. Figure 19a shows the extent of fiber degradation at higher magnification. To verify that this is not an artifact of chemical attack on the fiber surface by the Kroll's reagent, an as-received fiber was "etched" under identical conditions. As shown in Figure 19b, examination of this fiber at the same magnification revealed a very smooth, clean surface.

In contrast, Figures 20 and 21 show that the tantalum layer in the Ta-coated sapphire/Ti-48-1 system has two important effects: (1) it acts as a diffusion barrier

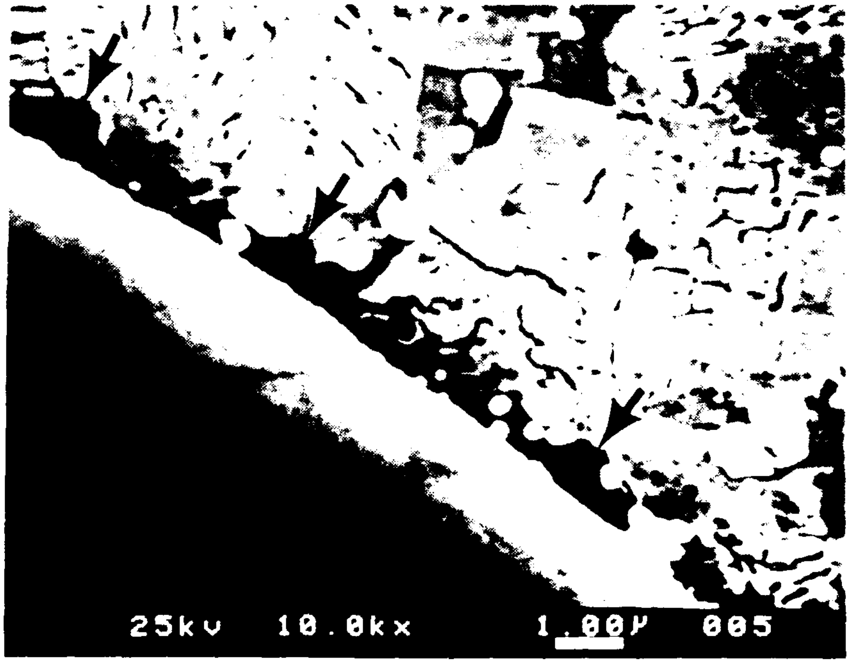
25kv 10.0kx 1.00µ 005

Figure 17. High magnification SEM image of the uncoated sapphire/Ti-48Al-1V interface following vacuum hot pressing.

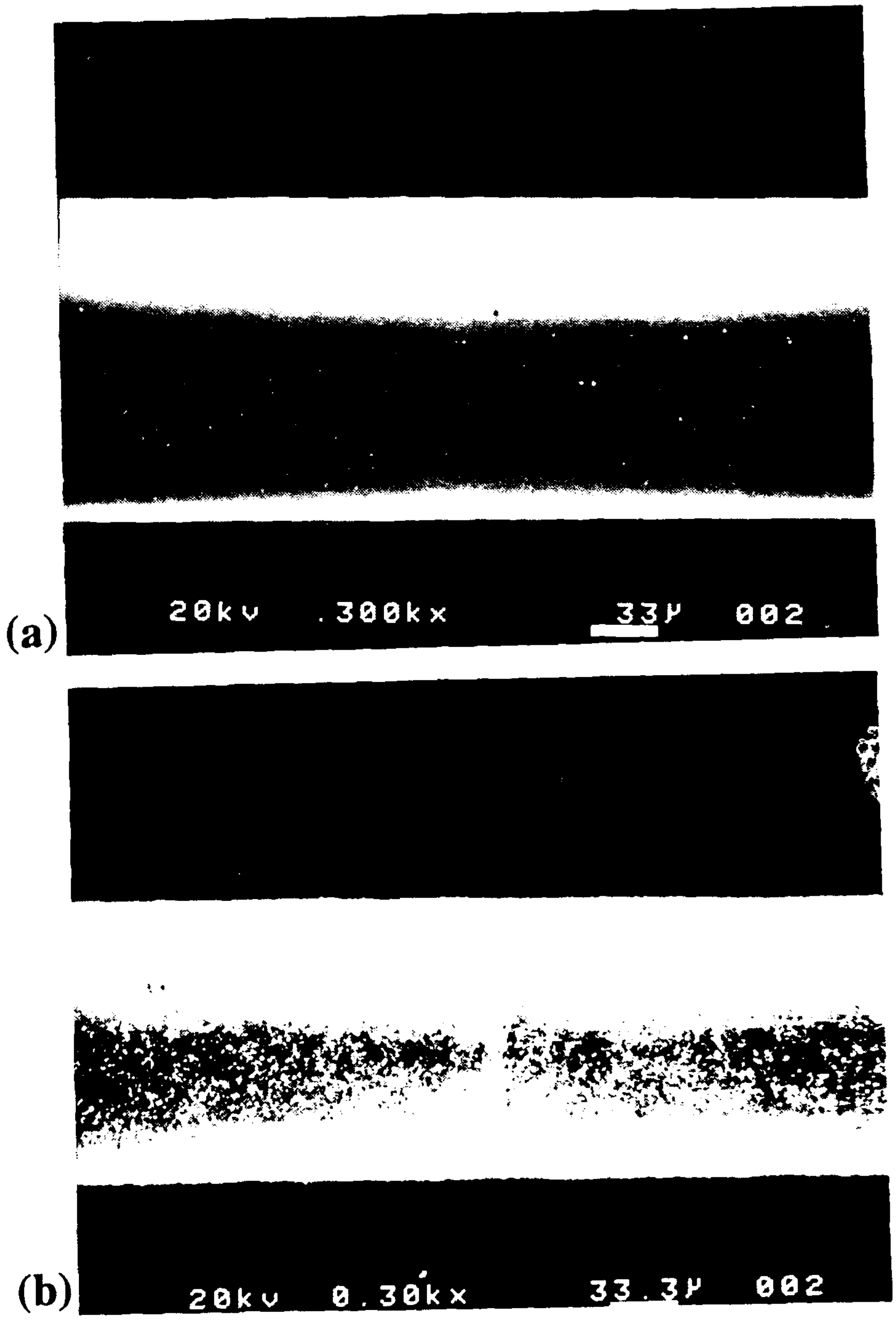
20kv .300kx 33μ 002
(a)
(b)
20kv 0.30kx 33.3μ 002

Figure 18. Sapphire fiber surface (a) before and (b) after being vacuum hot pressed in the Ti-48Al-1V matrix. It was experimentally verified that the smaller diameter of the as-consolidated fiber was not due to fiber dissolution during hot pressing.

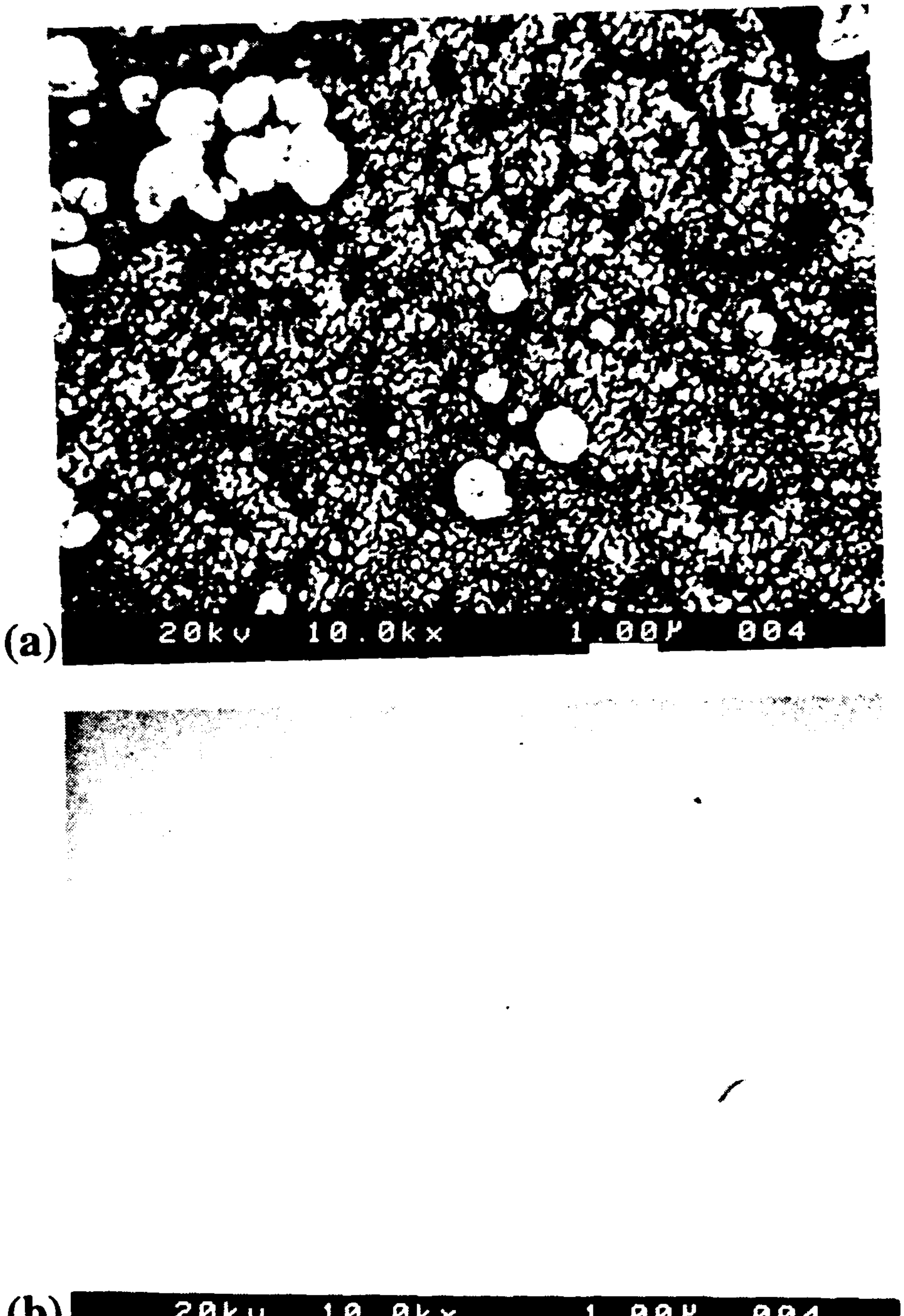
(a)
20kv 10.0kx 1.00µ 004
(b)
20kv 10.0kx 1.00µ 004

Figure 19. High magnification SEM micrographs showing the sapphire fiber surface (a) after and (b) before being vacuum hot pressed in the Ti-48Al-1V matrix. Both fibers shown were etched under identical conditions.

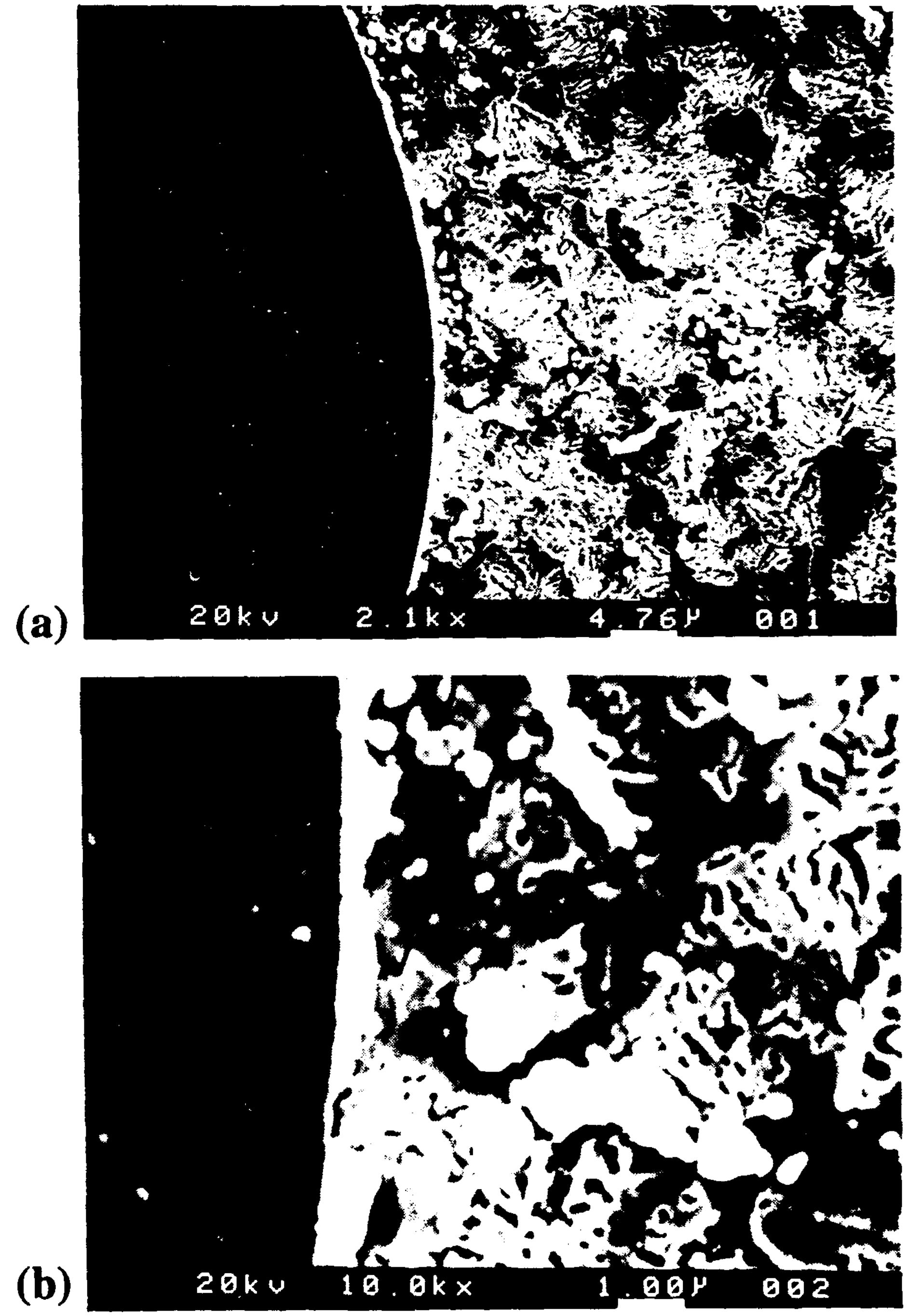
(a)
20kv 2.1kx 4.76µ 001
(b)
20kv 10.0kx 1.00µ 002

Figure 20. Evidence that the tantalum layer in the Ta-coated sapphire Ti-48Al-1V system acts as a diffusion barrier and forms a 0.5 to 1.0 µm wide interphase zone adjacent to the fiber. (a) SEM micrograph and (b) high magnification view of area shown in (a).

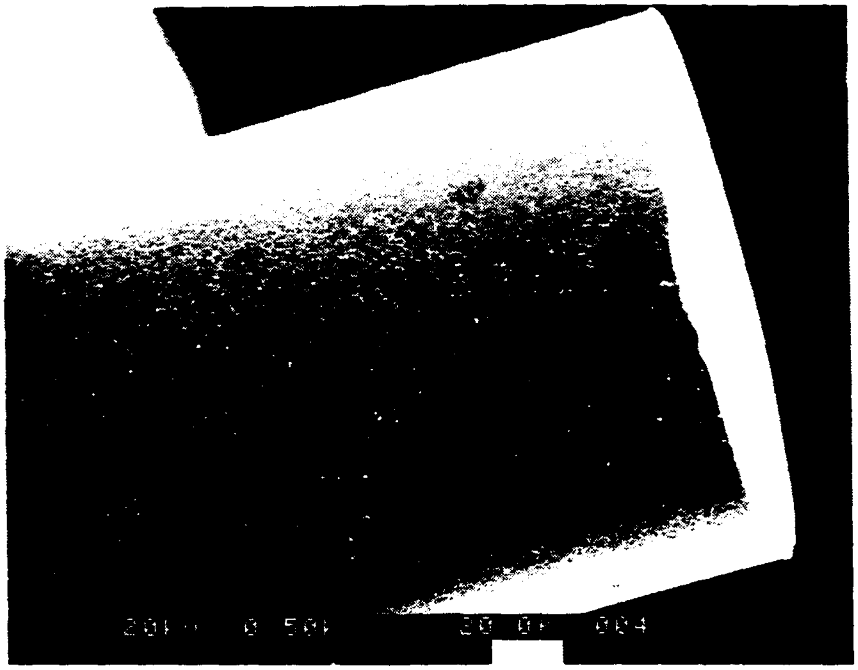
20kV
0.50K
30.0µm
004

Figure 21. Surface of a Ta-coated sapphire fiber following hot pressing in the Ti-48Al-1V matrix and subsequent chemical removal of the matrix and tantalum coating.

between the matrix and fiber resulting in a much smoother fiber interface (compare Figures 20a and b with Figures 15a and 17), the absence of voids at the interface (compare Figure 20b with Figure 17), and a less degraded fiber surface (compare Figure 21 with Figure 18b); and (2) it forms a 0.5 to 1.0 μm-wide interphase zone adjacent to the fiber (Figure 20b) that is believed to be the more ductile β-Ti phase. Indirect evidence that the interphase zone is Ta-stabilized β-phase is given by the semi-quantitative concentration profile across the sapphire/Ta/Ti-48-1 interface shown in Figure 22 obtained from EPMA. This concentration profile shows that the initially 0.2 μm-thick Ta coating diffused ≈7.4 μm into the matrix with the highest Ta concentration appearing to be within ≈3.0 μm of the sapphire/Ta-coating interface. Furthermore, EPMA-derived elemental x-ray maps showed that an ≈2.25 μm-wide zone adjacent to the sapphire/Ta coating interface appears to be aluminum-depleted, but not oxygen-enriched. Since Ta is a β-phase stabilizer and a relatively high concentration of it diffused ≈3.0 μm into the matrix, it is reasonable to assume that the interphase zone is β-phase. This was also observed by Graves and Bampton [20] who found that a Ta coating on SiC fibers stabilized the β-phase in a Ti-46Al-3(Nb, V) matrix.

Examination of the Ti-48-2-2 microstructure following composite fabrication (Figure 23) reveals that one difference between the Ti-48-1 and Ti-48-2-2 microstructures is the approximately 10 fold larger grain size in the Ti-48-2-2 alloy (i.e., compare Figure 23 with Figure 15c). In addition, due to the much lower oxygen contamination of the Ti-48-2-2 matrix powder during processing (i.e., see Table 2 in section 3.1), the α_2-phase was not preferentially stabilized at the prior powder particle boundaries as was found in the Ti-48-1 matrix. This was verified by examining the Ti-48-2-2 matrix following etching with the lactic etchant.

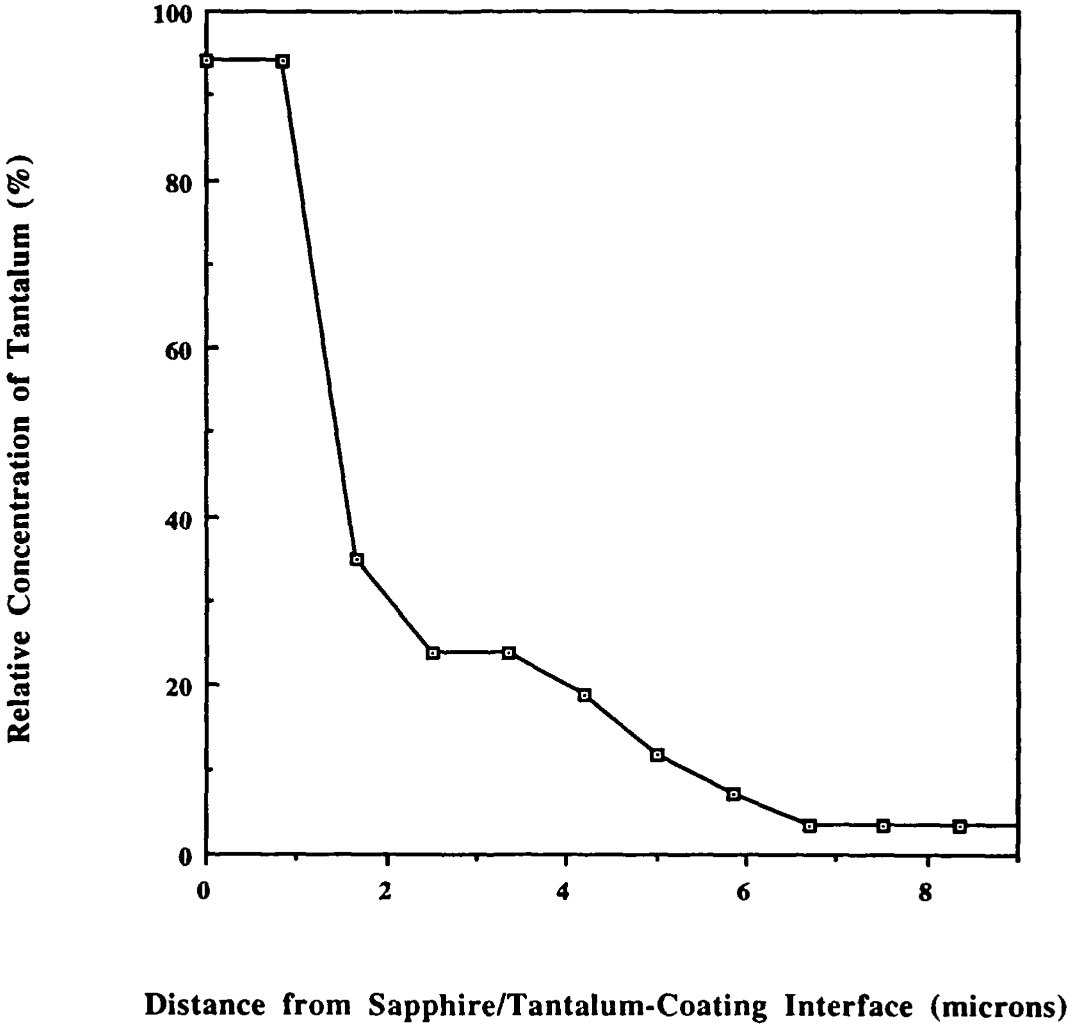

Figure 22. Semi-quantitative tantalum concentration profile across the sapphire/Ta/Ti-48Al-1V interface obtained from electron probe microanalysis.

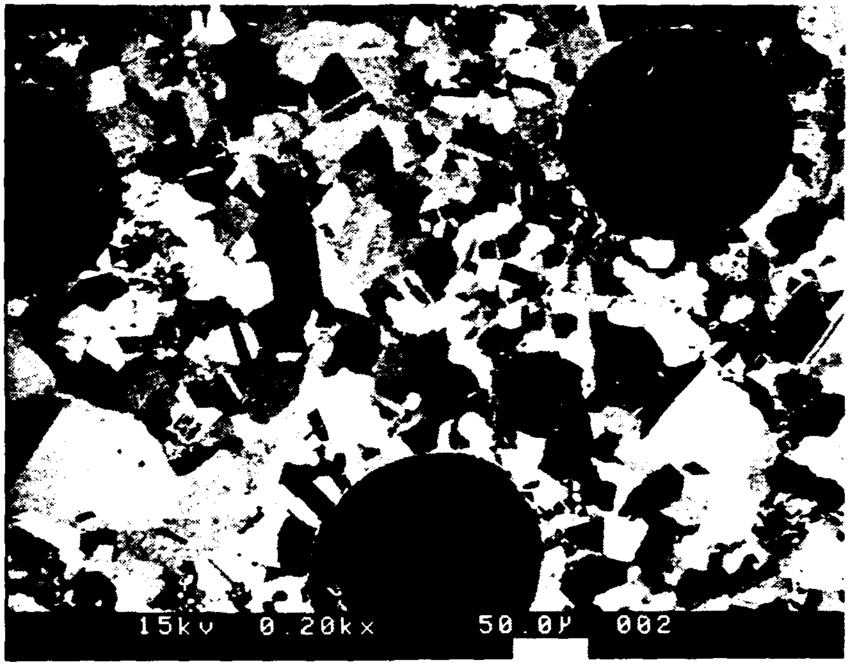
15kv 0.20kx 50.0µ 002

Figure 23. Typical SEM micrograph of the sapphire-reinforced Ti-48Al-2Cr-2Nb microstructure following composite fabrication.

Figures 24a and b shows that a severe reaction occurs between uncoated sapphire and the Ti-48-2-2 matrix during composite fabrication. In addition to a serrated fiber surface, a reaction product forms at the interface. It appears to be discontinuous and may preferentially nucleate (or re-precipitate, if it is derived from dissolved Al_2O_3) along the matrix grain boundaries (arrowed in Figure 24b). A discrete reaction product in the sapphire/two-phase ($\alpha_2 + \gamma$) TiAl system has not been reported by other investigators [59, 62, 110], even after long elevated temperature exposure times [59, 62].

One possible explanation for the development of this reaction product may be reaction of the matrix or fiber with residual contamination left behind at or near the fiber/matrix interface due to incomplete removal of: (1) the organic binder from the matrix during composite fabrication and/or (2) the protective organic coating from the as-received fibers during soaking in cold water prior to incorporation into the matrix. For example, evidence that the fiber/matrix bond characteristics are modified by the use of an organic binder in the matrix during composite fabrication has been reported by Bowman et al. [111, 112] in the sapphire-reinforced NiAl system. Draper et al. [113] reported that the surface of sapphire fibers hot pressed in an organic binder-containing NiAl matrix were coated with carbon particles following extraction from the matrix. It is feasible that in a TiAl-based matrix, these carbon particles could lead to the formation of carbides (i.e., TiC or Ti_2AlC) at the fiber/matrix interface. In addition, Trumbauer et al. [114] have shown that soaking as-received sapphire fibers in cold water to remove the protective, organic, Dow Methocel™ coating is not totally effective.

Further evidence that a severe fiber/matrix reaction occurs in the sapphire/Ti-48-2-2 system during composite fabrication is shown in Figure 25. The fiber surface, shown following chemical removal of the matrix by the concentrated Kroll's reagent, is very

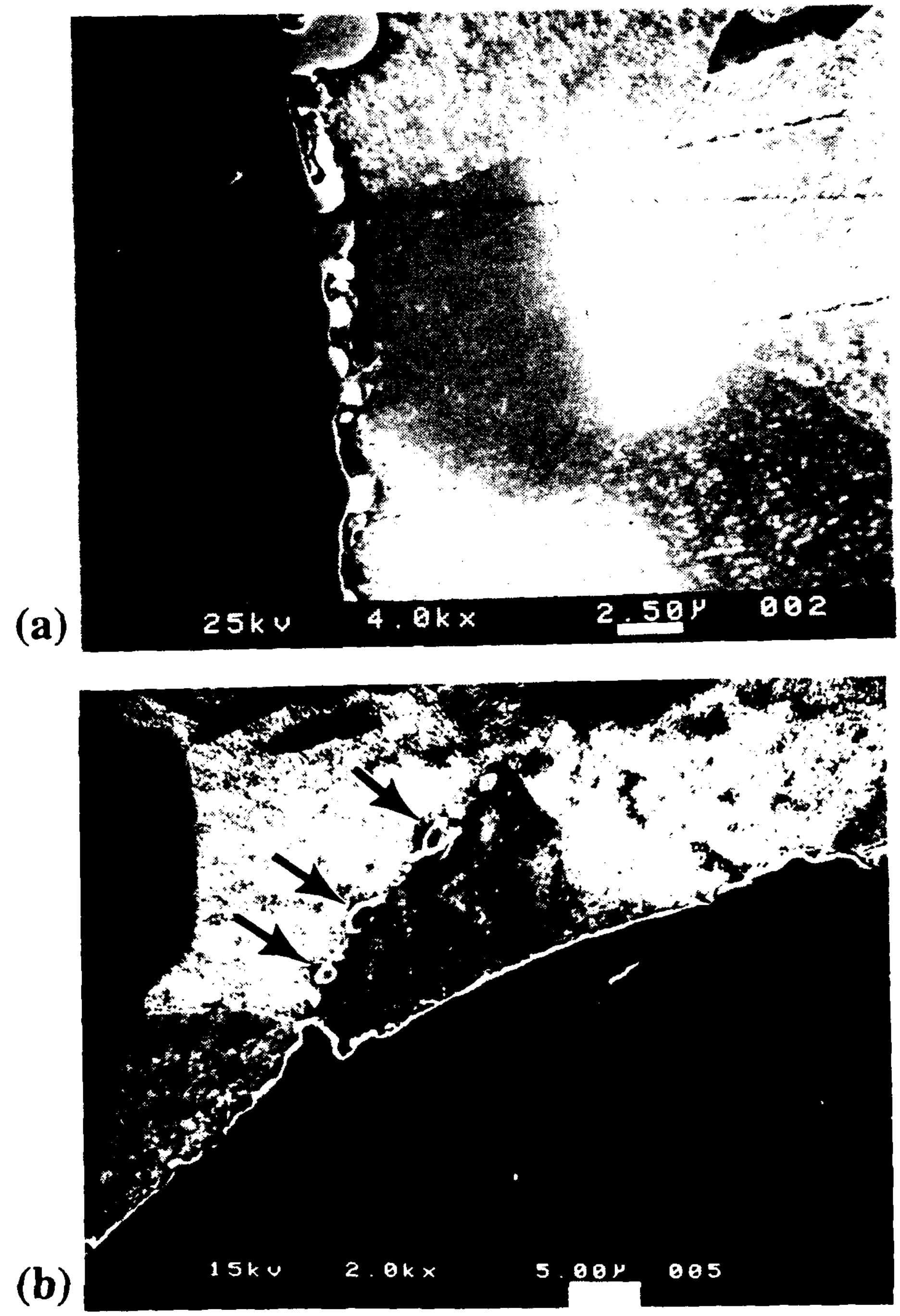
(a)
25kv 4.0kx 2.50µ 002
(b)
15kv 2.0kx 5.00µ 005

Figure 24. Evidence that a severe reaction occurs between uncoated sapphire and the Ti-48Al-2Cr-2Nb matrix during composite fabrication. (a) Reaction product appears to be discontinuous and (b) may nucleate along matrix grain boundaries.

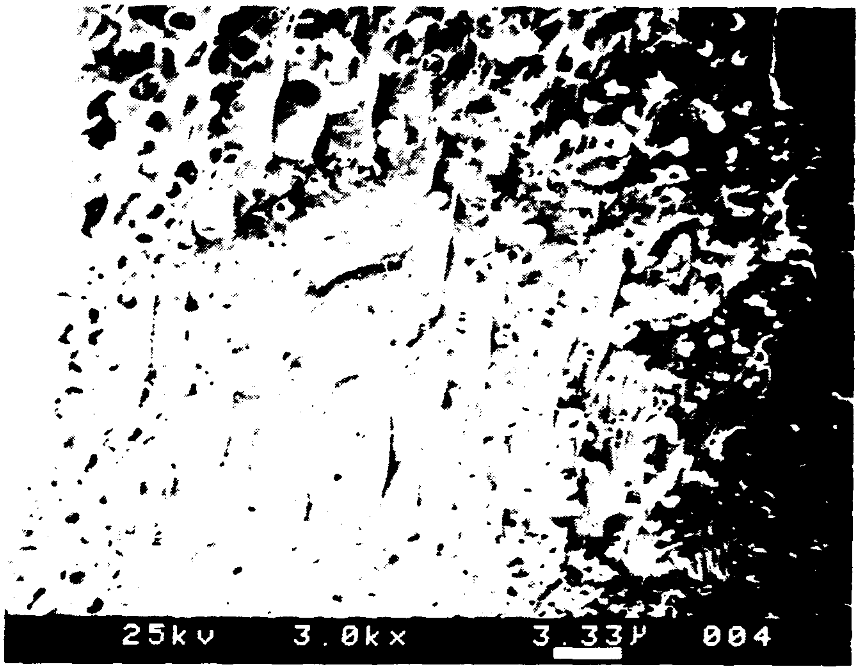
25kv
3.0kx
3.33µ
004

Figure 25. Sapphire fiber surface following hot pressing in the Ti-48Al-2Cr-2Nb matrix and subsequent chemical removal.

rough. The discrete reaction product that was viewed in cross-section in Figure 24 appears to remain attached to the fiber surface and unaffected by the etchant.

Finally, microhardness measurements using Vickers and Knoop indenters in the vicinity of the fiber/matrix interfacial region of all three composite systems revealed no detectable change in hardness (and, therefore, yield strength) as the interface was approached. However, as shown in Table 3, the Ti-48-1 matrix was found to be 17 to 27% harder than the Ti-48-2-2 matrix. This is most likely due to the much greater concentrations of oxygen, nitrogen, and carbon interstitial elements in the Ti-48-1 matrix (see Table 2 in section 3.1). As shown in Table 3, the hardness of the Ti-48-2-2 matrix compares well with the value reported by Krishnamurthy [115] for a Ti-48Al-1Ta matrix in a sapphire-reinforced composite. In addition, it is significant to mention that the level of oxygen and carbon contamination in the Ti-48Al-1Ta matrix powder [115] was comparable to that in the Ti-48-2-2 matrix (see Table 2 in section 3.1). Krishnamurthy [115] also found no detectable change in hardness as the sapphire/Ti-48Al-1Ta interface was approached.

Table 3. Vickers and Knoop microhardness numbers (i.e., VHN and KHN respectively) measured in the matrix materials used for this study. Comparison is made with values measured by Krishnamurthy [115] in a Ti-48Al-1Ta matrix.

Matrix	VHN (25 gm load)	KHN (25 gm load)
Ti-48Al-1V	300	400
Ti-48Al-2Cr-2Nb	250	290
Ti-48Al-1Ta		270 - 300 [115]

4.2. Residual Stresses and Resulting Damage within Fibers Intersecting a Free Surface

The purpose of this portion of the research program is to illustrate that the combination of brittle fibers, significant tensile residual stress, and machining damage can result in longitudinal cracks (i.e., fiber splitting) when a fiber intersects a free surface. Assuming a well-bonded interface, FEM as well as exact elastic model predictions of the thermally-induced residual stress distributions in a sapphire fiber embedded within a TiAl matrix are presented for the case of a fiber intersecting a free surface. The computations predict a gradient of tensile stresses within the fiber such that given the relatively low fracture toughness of single crystal sapphire (i.e., see Table 1 in section 2.1), fiber splitting will occur as matrix material is removed. In addition, this section presents an experimental validation of the predicted stress state using indentation crack behavior within the sapphire fibers.

4.2.1. Characteristics of Fiber Damage

This portion of the research program was initiated by the observation that thin-slice specimens (i.e., 0.3 to 0.6 mm) of uncoated sapphire-reinforced Ti-48-1 contained fibers with cracks at their ends created by sectioning. Evidence that cracks were only at the ends of fibers intersecting a free surface (i.e., surface cracks) is given in Figure 26. Figure 26a is a reflected light micrograph showing an uncoated sapphire fiber embedded in the Ti-48-1 matrix with its axis aligned normal to the specimen's surface. The specimen had been sectioned using a diamond wafering blade, ground flat, and polished to a 1 μm diamond paste finish. Other that a chip near the fiber's center, no other damage is visible. However, by transmitting light through the optically transparent fiber, the extent of damage

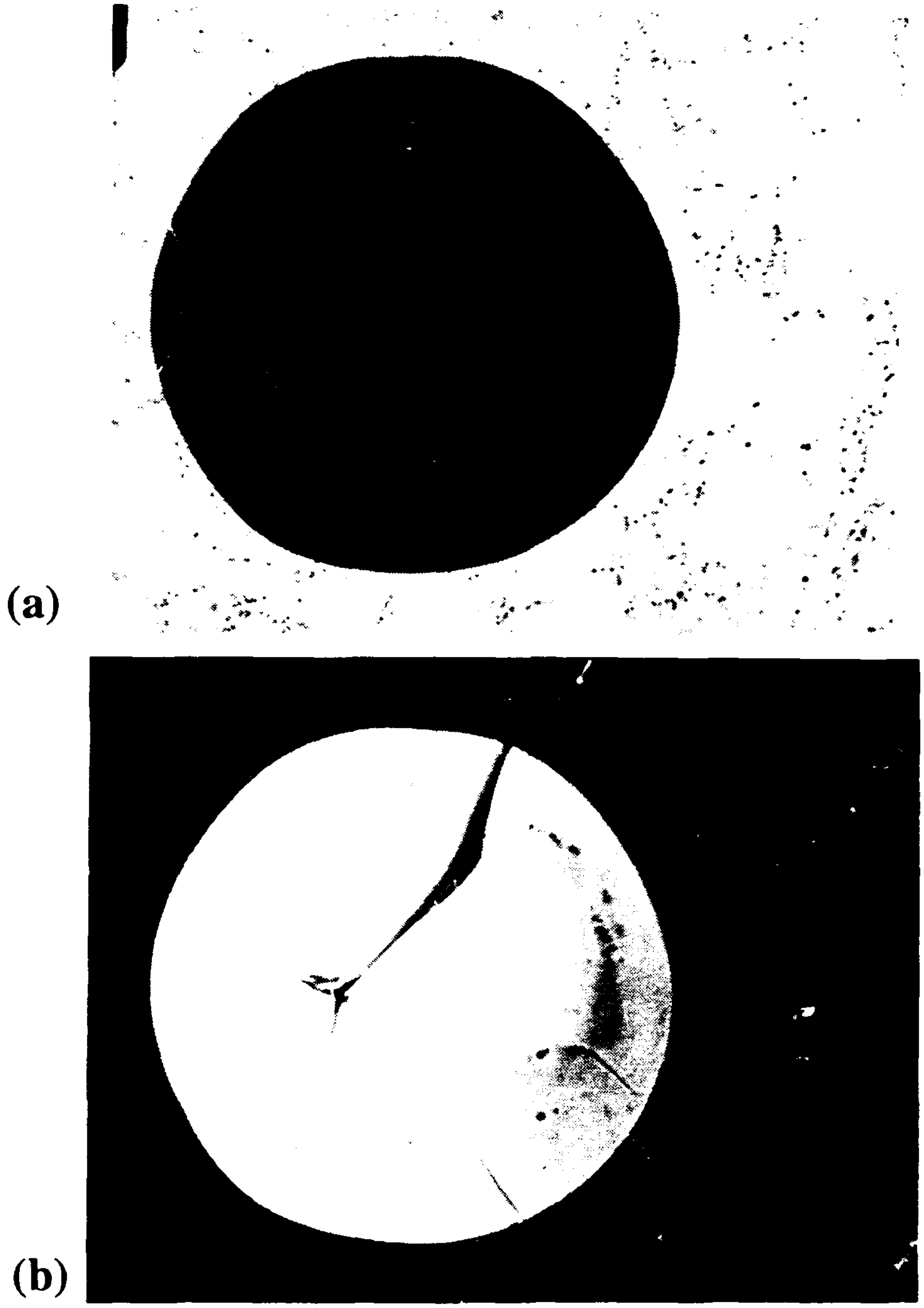

Figure 26. Evidence that cracks are only at the ends of fibers intersecting a free surface. (a) Reflected light micrograph and (b) corresponding micrograph formed using only light transmitted through the fiber. Focus at the same specimen's (c) middle and (d) opposite side. (cont. on next page)

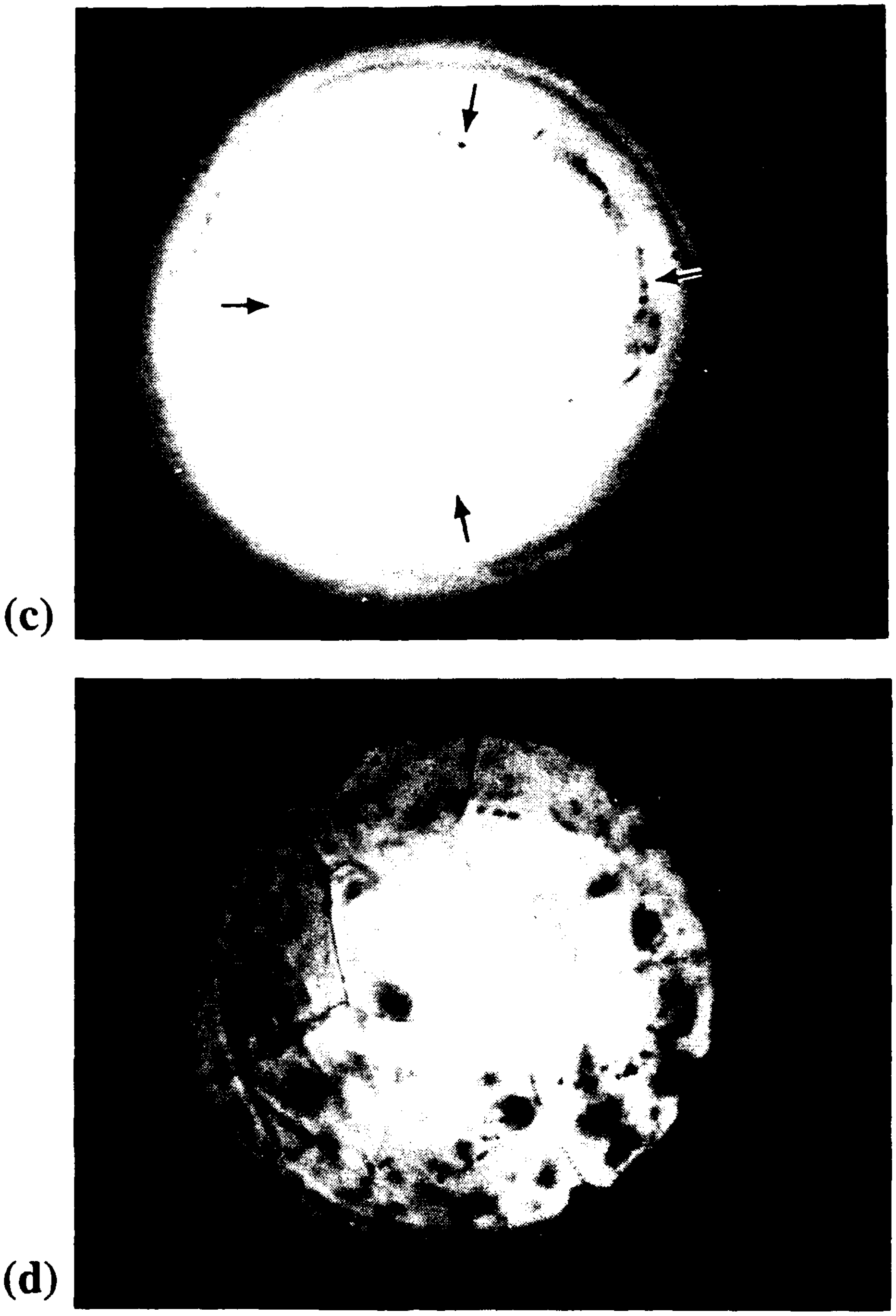

Figure 26. (cont.)

in the form of cracks is made clearly visible at the fiber's end (Figure 26b). This observation highlights the requirement to closely examine fibers for the presence of cracks using transmitted light metallography before subsequent pushout testing because cracks within embedded fibers usually can not be seen using reflected light metallography alone. By focusing through the fiber, the fiber was examined for cracks along its entire length. Figure 26c is taken at the middle of the specimen, and as shown, cracks are not present at this depth. The only visible internal features within the fiber are the ring of shrinkage voids (arrowed) produced during sapphire fiber growth [38]. At the opposite side of the specimen (shown in Figure 26d), surface cracks are again clearly visible. In this manner, the average depth of surface cracks[g] was found to be ≈25 μm. Regardless of several different cross-sectioning methods attempted to minimize the development of surface cracks (i.e., see section 3.3) and subsequent efforts to remove them by polishing, the observed damage could not be removed in the uncoated sapphire/Ti-48-1 system. In fact, even after removing tens of microns of material by grinding and polishing the specimen's surface, the depth of surface cracks remained essentially unchanged.

The extent of fiber fracture and crack orientation with respect to the fiber axis is shown in Figure 27 in which the matrix was chemically removed by etching with a concentrated Kroll's reagent. Crack depth measurements showed that incrementally removing the matrix along the fiber axis caused surface cracks to propagate, resulting in a "split" fiber as shown in Figure 27a. The zigzag crack path shown in Figure 27a appears to follow the rhombohedral planes, the preferred fracture planes in sapphire at room temperature[h]. Further evidence of the crystallographic nature of the fracture path is shown

---

[g] "Depth" is defined as the distance measured along the fiber's axis from the free surface to the crack tip.

[h] The rhombohedral planes in sapphire have the lowest fracture surface energy at room temperature [34].

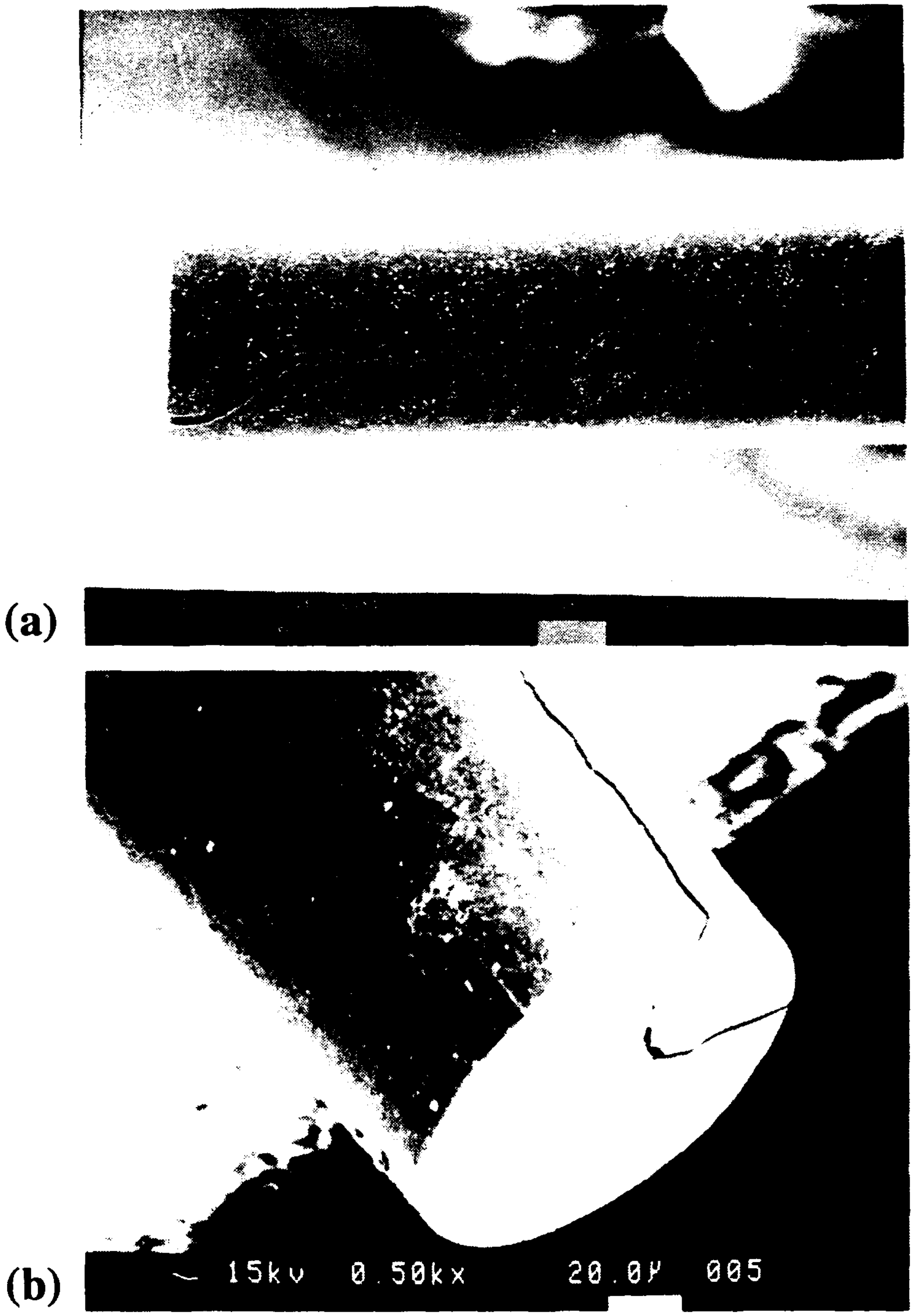

Figure 27. SEM micrographs showing the extent of fiber fracture and crack orientation with respect to the fiber axis in uncoated sapphire-reinforced Ti-48Al-1V (taken from [93]). (a) Characteristic zigzag crack path and (b) cracks on fiber end.

in Figure 28 which dramatically reveals a "saw-toothed" fracture surface. The average angle between the saw-toothed planes and the fiber axis (i.e., the c-axis of sapphire) is ≈59° (Figure 28b). This is in close agreement with 56° angles measured between rhombohedral planes and the c-axis in sapphire [38]. Similar saw-toothed fracture surfaces were reported by Wiederhorn [34] in room temperature fracture studies of sapphire using the double-cantilever-cleavage technique. He found that the jagged portions of the crack were bounded by rhombohedral planes [34]. Tressler and Crane [35] also reported fracture along rhombohedral planes in c-axis oriented sapphire fibers extracted from a Ti-6Al-4V matrix following composite fabrication by vacuum hot pressing. Close examination of the fracture surface in Figure 28b reveals the presence of several voids (arrowed) that may act as stress concentrations during fracture. As previously noted in section 2.2, shrinkage voids formed during growth of sapphire fibers lie along the rhombohedral planes [38].

On the other hand, Ta-coated fibers hot pressed in the same matrix (i.e., Ti-48-1) and under the same consolidation conditions as the uncoated fibers contained no cracks (for example, see Figure 21). Likewise, uncoated sapphire fibers in the multi-filament reinforced Ti-48-2-2 sample were not cracked during specimen preparation. An explanation for these observations in terms of relative fiber/matrix bond strength will be given in the next section.

4.2.2. Computational Analysis of Thermally-Induced Residual Stress States

A possible contributor to the fiber damage is the presence of residual tensile stresses within a fiber near a free surface. Separate computational analyses were performed to predict the thermally-induced residual stress states within a fiber given two different orientations with respect to a free surface. The case of a fiber intersecting a free surface

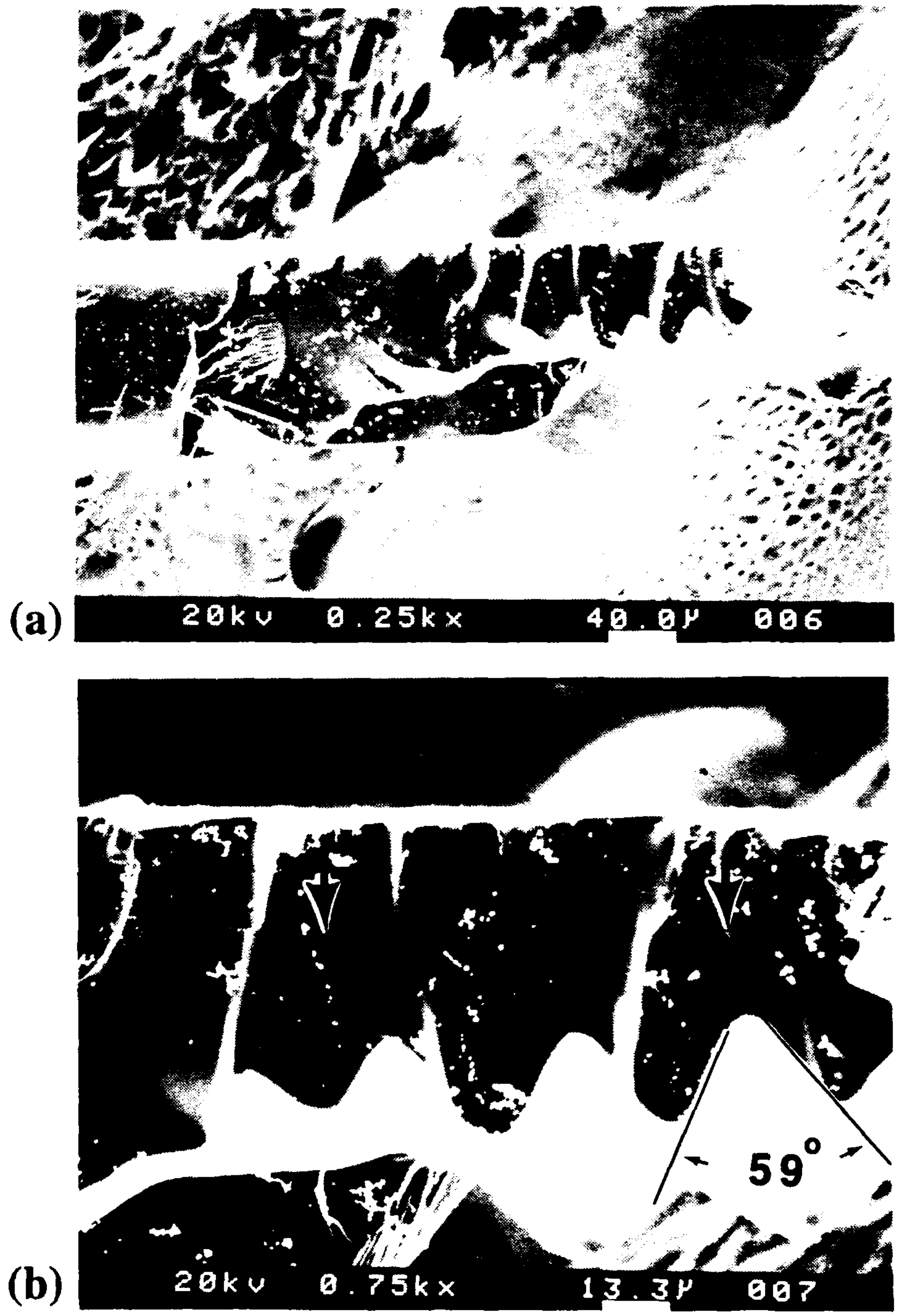
(a)
20kv 0.25kx 40.0µ 006
(b)
59°
20kv 0.75kx 13.3µ 007

Figure 28. Saw-toothed fracture surface showing (a) the crystallographic nature of the fracture path and (b) the presence of voids that may act as stress concentrations.

and with its axis normal to the surface is examined first. Later in this section, the case of a fiber very close to, or intersecting, a free surface and with its axis parallel to the surface will be examined.

4.2.2.1. Finite Element Analysis and Experimental Validation of its Predicted Stress State

In order to characterize the stress state in a fiber along its axis, axisymmetric finite element modeling (FEM) performed by Kallas [84] was used to emulate the actual thermal loading due to CTE mismatch during cool-down from the composite fabrication temperature[i] [93]. The element used for this analysis is a two-dimensional isoparametric element (ANSYS code) which has the capability of axisymmetric analysis [84]. The elastic-plastic model assumes that: (1) the fiber intersects a free surface at right angles, (2) the fiber is perfectly bonded to the matrix at a well-defined interface, and (3) the TiAl matrix is a bi-linear, kinematic hardening material. The model accounts for the temperature dependence of the constitutive material properties (i.e., elastic modulus, yield strength, and thermal expansion).

The temperature for the onset of significant residual stress build-up (i.e., the stress-free temperature) was assumed to be 800 °C based on the trends in data from elevated temperature compression tests of a Ti-48Al-1V alloy performed by Harbison [116]. At temperatures above 800 °C, he found that the yield strength and strain-hardening exponent decreased, and the strain-rate sensitivity increased [116]. These trends are indicative of the onset of time-dependent (i.e., creep) deformation.

---

[i] All computations using this finite element model [84] presented in this section and in sections 4.3.1 and 4.3.3 were performed by Kallas at Penn State University.

Since the CTE of the matrix is greater than that of the fiber, the fiber is subjected to a compressive triaxial stress state when end effects are ignored (i.e., as in an analytical concentric cylinder model). However, as illustrated in Figure 29a, thermally-induced displacements of the matrix and fiber surfaces during cross-sectioning create a "dome-shaped" fiber end. Within it, thermoelastic residual stresses occur, resulting in a tensile triaxial stress state within the fiber.

The profiles of radial and hoop stresses (i.e., stresses parallel to the free surface plane) within 127 μm diameter fibers at depths up to 20 μm from the free surface are illustrated in Figures 29b and c for a sapphire-reinforced TiAl composite with a 0.1 fiber volume fraction. Figures 29b and c show that: (1) at or near the free surface, a state of nearly equal biaxial tension exists and (2) the magnitude of the tensile stresses decrease rapidly with increasing depth, z, below the free surface. Experimental support of the presence of biaxial tension in the fiber's free surface is shown in Figure 30 of an uncoated fiber in Ti-48-1 cross-sectioned using a wire saw. This "mud cake" fracture pattern (Figure 30b) is characteristic of cracking in an equal biaxial tensile stress state.

The FEM computations suggest that, given a fiber of low toughness and the presence of a crack (e.g., a surface crack or flaw created during cross-sectioning or machining), the thermally-induced tensile stresses within the fiber may propagate the crack to a length dictated by the stress state and fracture toughness. Furthermore, subsequent removal of the matrix will cause the crack to propagate along the fiber, splitting it as the free surface and stress state are spatially displaced. A split fiber, such as shown in Figure 27a, results.

Finally, it is important to note that the magnitude of the residual stresses depends on not only the thermal expansion mismatch between constituents and the elastic/plastic properties of the interfacial region (namely, yield stress and ductility), but also the

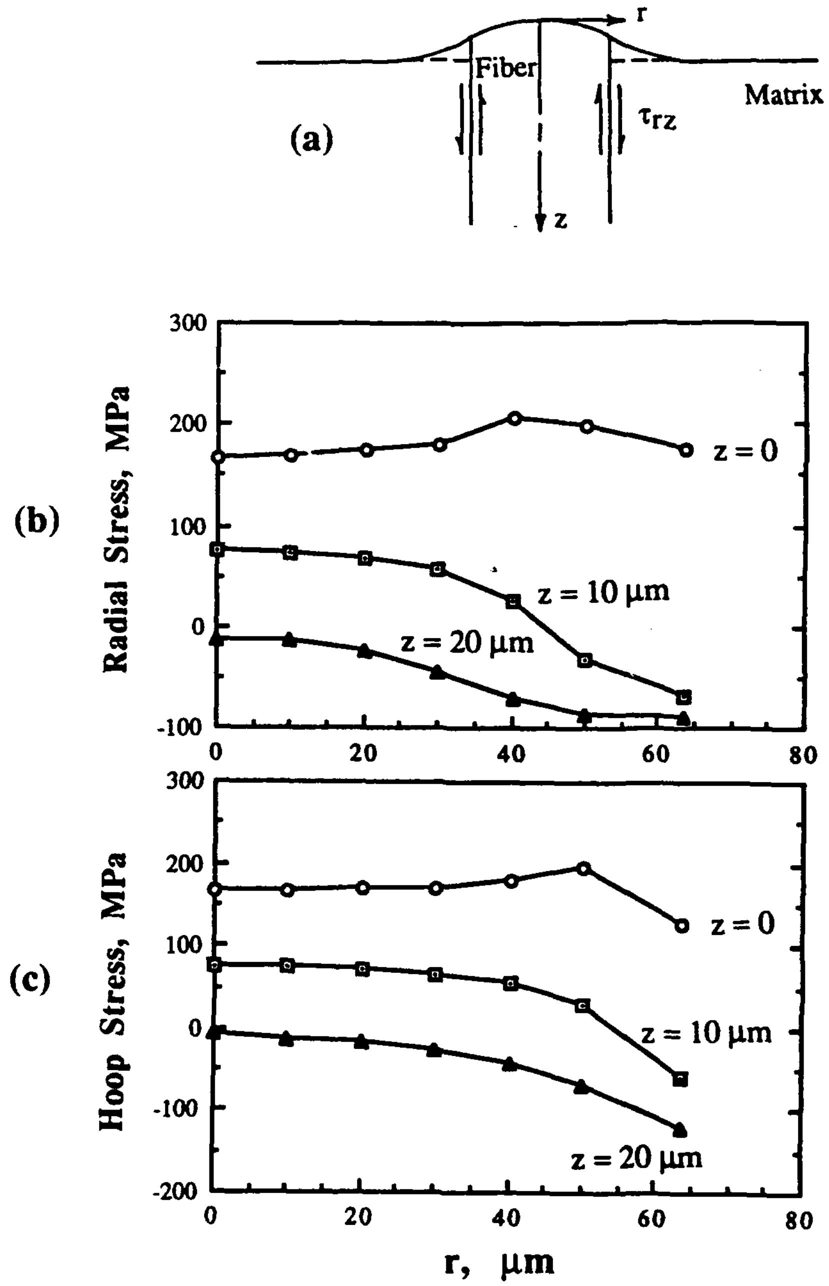

Figure 29. Free and sub-surface thermoelastic residual stress profiles in the fiber for a sapphire-reinforced TiAl composite with a 0.1 fiber volume fraction (predicted by FEM [84] and taken from [93]). (a) Fiber orientation showing the important role of the interfacial shear strength and resulting displacements of the matrix and fiber surfaces, (b) radial stress (σ_{rr}), and (c) hoop stress($\sigma_{\theta\theta}$).

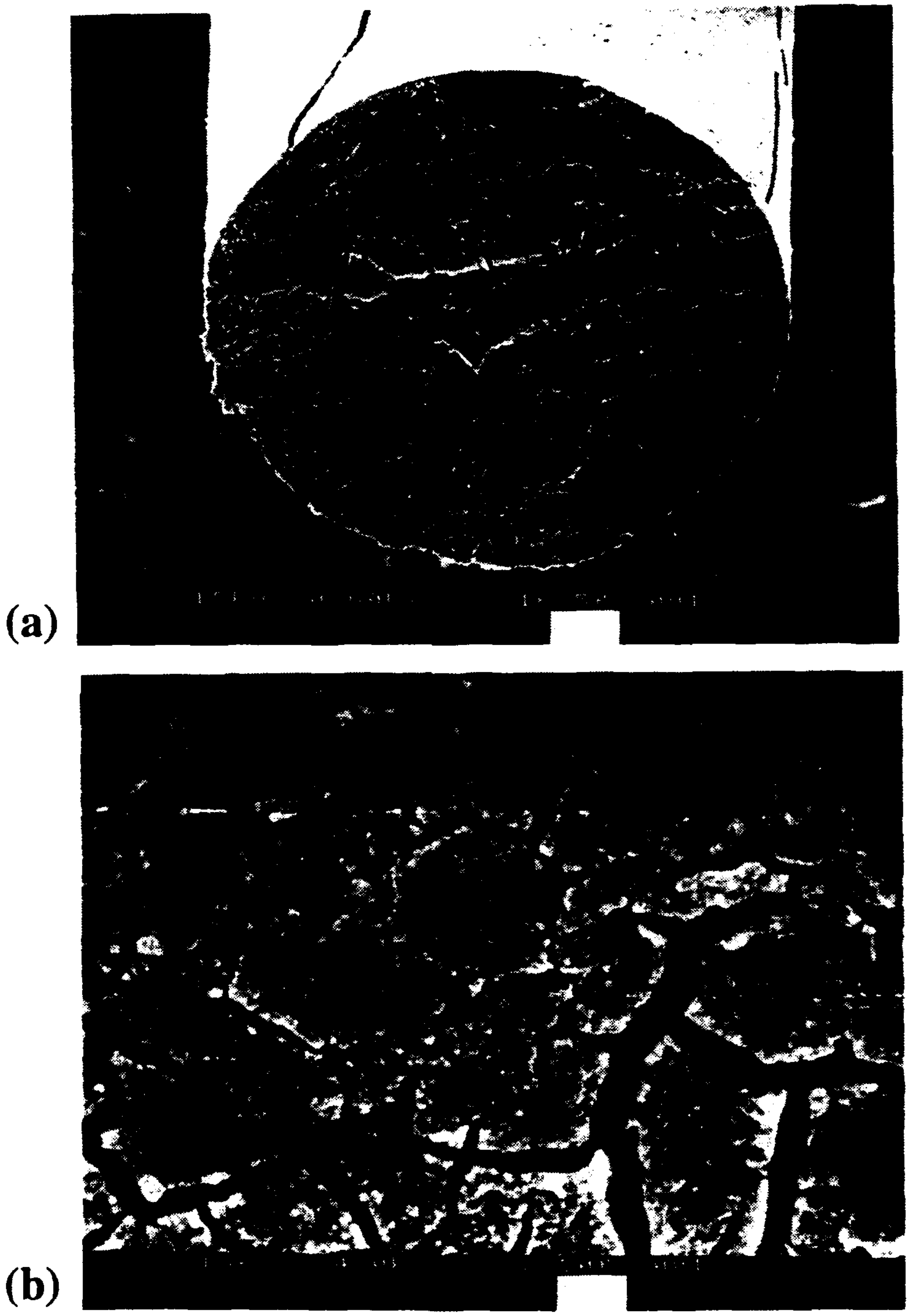

Figure 30. SEM micrographs showing the characteristic "mud cake" fracture pattern on the cross-sectioned fiber surface in sapphire-reinforced Ti-48Al-1V (taken from [93]). (a) Cross-sectioned fiber and (b) high magnification image of upper-right quadrant of fiber end.

interfacial shear strength. As suggested by Figure 29a, large residual tensile stresses will develop within the fiber only if the fiber/matrix interface has a high shear strength. These results suggest that the magnitude of the thermally-induced tensile stresses can be decreased by: (1) using soft and/or ductile fiber coatings (e.g., tantalum) and (2) decreasing the shear strength of the interface.

While the experimental observations of fiber damage are qualitatively in agreement with FEM predictions, indentation crack growth measurements provide experimental verification of the magnitudes of thermally-induced tensile stresses within the fiber near its end. The following relationship predicts the residual hoop stress profile as a function of depth (z) below the free surface as calculated by FEM (see Figure 29):

$$\sigma_{\theta\theta}(z) = 166.6(1 - 6.114\times10^{4}z + 4.520\times10^{8}z^{2} + 3.675\times10^{11}z^{3} - 9.760\times10^{15}z^{4})\mathrm{MPa}. \quad (14)$$

By substituting equation (14) into equation (11) given in section 3.4, the dependence of K_r (i.e., the stress intensity factor for a half-penny shaped crack subjected to a thermally-induced residual stress field) on crack length is plotted in Figure 31. As shown, the maximum value of K_r occurs for a crack length of 41 μm, which is well beyond the point of maximum stress at the fiber surface (i.e., at z = 0). This is a consequence of determining the stress intensity factor by a weighted summation of stresses acting over the entire crack surface [117].

Using equations (9) and (10) given in section 3.4, the plots of K_i (i.e., the stress intensity factor for the same half-penny shaped crack subjected to the indentation contact residual stress field) and the total stress intensity, K, are also shown in Figure 31 as a function of crack length for a 4.9 N indentation load in sapphire/TiAl. These results are representative of similar data for the other three indentation loads. The fracture toughness

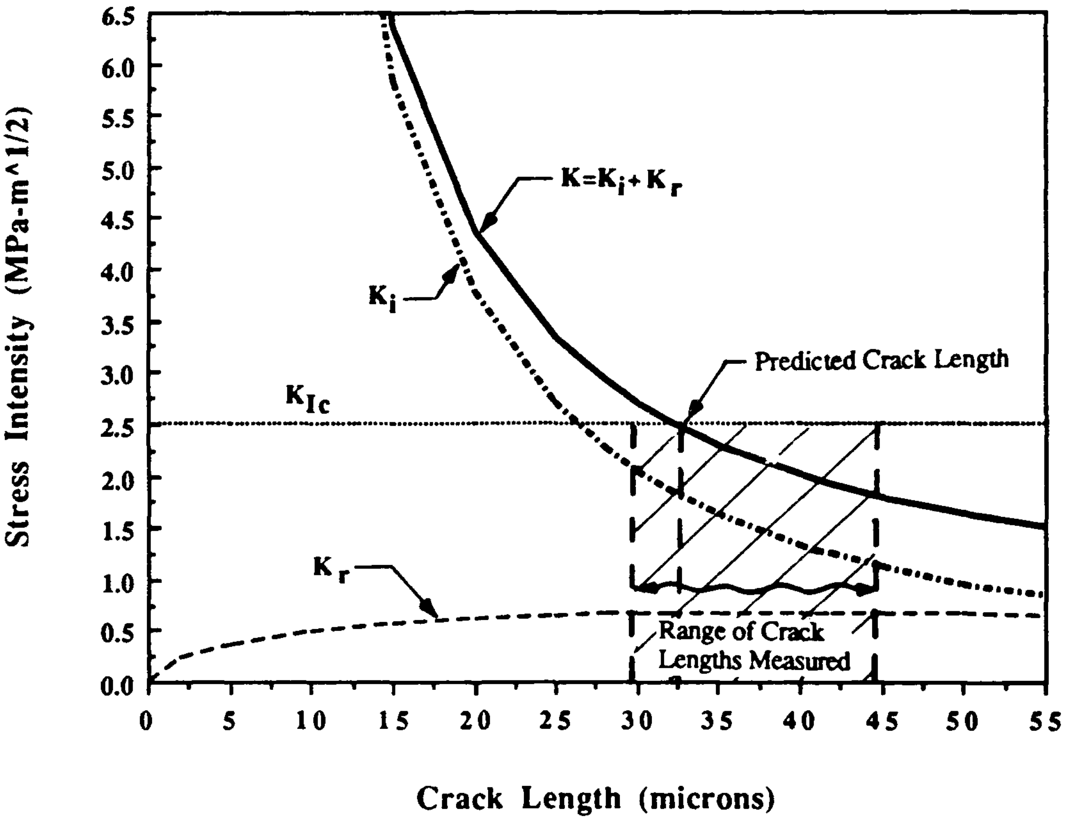

Figure 31. Predicted stress intensity as a function of crack size in sapphire-reinforced TiAl for a 4.9 N indentation load.

of sapphire (i.e., K_{Ic}) in an inert environment of dry nitrogen gas was measured by Wiederhorn [34] as 2.5 MPa-m$^{1/2}$ which is represented by a horizontal line on the figure.

Figure 31 indicates that the crack should propagate to a length of 33 µm (i.e., the value of c when $K = K_{Ic}$) and arrest, given the FEM-predicted, residual stress field and that induced by the indentation. This value lies between those measured for sapphire/Ti-48-2-2 (29.5 ± 6.5 µm, where ± one standard deviation is reported for 18 measurements) and Ta-coated sapphire/Ti-48-1 (44.7 ± 7.4 µm, where ± one standard deviation is reported for 4 measurements).

This range of crack arrest lengths can be understood given the lower yield strength of the Ti-48-2-2 matrix and the lower interfacial shear strength in the sapphire/Ti-48-2-2 system (i.e., see the fiber pushout test results presented in section 4.3.2) which suggest smaller thermally-induced residual stresses are present. Thus, the smaller crack length at arrest.

Reference to Figure 31 also shows that the maximum value of K_r, 0.68 MPa-m$^{1/2}$, is relatively small in comparison to the fracture toughness of sapphire, thus indicating that the thermally-induced residual stress intensity within a fiber near its end may not be sufficient to propagate surface cracks or flaws created during cross-sectioning. However, the fracture toughness value shown in Figure 31 was measured in an inert environment. It is well known that the presence of reactive species, especially water, significantly influence crack growth behavior in brittle materials [118]. This phenomenon can be explained by the weakening influence of the environment on the short-range interatomic bonds at the crack tip. This results in a lower, threshold stress intensity factor, K_{th}, for crack propagation in the reactive environment [33]. For a wide variety of brittle materials tested in air (i.e., at 25 °C and 60 ± 20% relative humidity), the ratio K_{th}^{air}/K_{Ic} is $\approx 0.7 \pm 0.1$ and is independent of material [33]. Thus, K_{th}^{air} for sapphire is ≈1.75 MPa-m$^{1/2}$. Furthermore, the K_{th} for sapphire in distilled water was measured by Cook [33] as 1.1 ± 0.05 MPa-m$^{1/2}$.

Figure 32 shows the importance of the lower, environmentally sensitive threshold stress intensity factors since all materials were exposed to water during sample preparation and all indentation experiments were performed in air. For clarity, only the plots of K_r and K are shown as a function of crack length for a 4.9 N indentation load. Figure 32 shows that: (1) the difference between K_r and the K_{th} values is small and (2) the predicted crack length in air or water (i.e., the value of c when $K = K_{th}$) is much larger than those measured for sapphire/Ti-48-2-2 and Ta-coated sapphire/Ti-48-1. This suggests that smaller thermally-induced residual stresses exist within the ends of fibers in the sapphire/Ti-48-2-2 and Ta-coated sapphire/Ti-48-1 systems than predicted in a perfectly bonded sapphire-reinforced TiAl composite modeled by FEM. This is in agreement with the experimental observation that only uncoated fibers embedded in Ti-48-1 contain cracks at their ends following cross-sectioning. It also suggests again that ductile fiber coatings (as in the Ta-coated sapphire/Ti-48-1 system) or a decreased interfacial shear strength (as in the sapphire/Ti-48-2-2 system) can decrease the thermally-induced tensile stresses and reduce or eliminate fiber damage.

4.2.2.2. Exact Elastic Analysis of a Fiber Parallel to a Free Surface

To illustrate further the significance of the redistribution of thermoelastic residual stresses in the vicinity of a free surface, the case of a fiber close to or just intersecting a free surface and with its axis parallel to the surface was analyzed using an exact elastic model developed by Lee, Jasiuk, and Tsuchida [119]. This situation can occur when cutting,

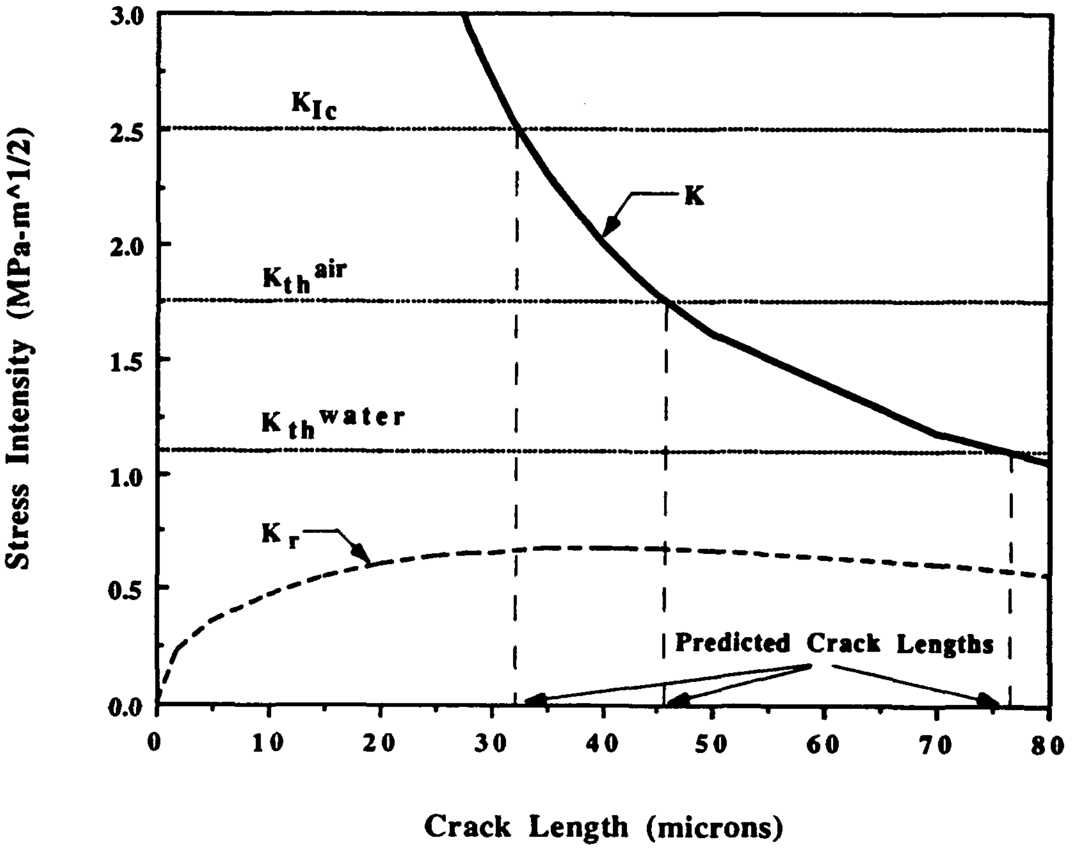

Figure 32. The plots of the predicted stress intensities K_r and K as a function of crack size in sapphire-reinforced TiAl (4.9 N indentation load) showing the importance of the threshold stress intensity factors for sapphire in reactive environments.

machining, or chemical etching operations remove matrix material near fibers oriented parallel to a free surface.

The analysis, which is given in an infinite series form, assumes that (1) perfect bonding exists between fiber and matrix, (2) the matrix is elastically isotropic, and (3) the fiber is transversely isotropic (i.e., isotropic in the r-θ plane shown in Figure 33) [119]. An application of the analysis[j] is based on the assumption that the thermally-induced residual stress states in the sapphire-reinforced TiAl system develop during a 775 °C cool-down from the composite's stress-free temperature. The geometry associated with this problem is illustrated in Figure 33. Here, a fiber of radius R, whose cross-section is shown in Figure 33, is located at a unit distance from the free surface [119]. Note that with this geometry, the axis of the fiber is oriented normal to the plane of the figure. The position of the fiber with respect to the free surface is varied by changing the value of R, the fiber's radius, while the distance from the fiber's center to the free surface remains fixed at unity. For example, the fiber just intersects the free surface when R = 1 [119].

The radial (σ_{rr}) and hoop ($\sigma_{\theta\theta}$) stress profiles shown in Figure 34 were calculated for a single fiber, sapphire-reinforced TiAl composite at five different locations. As shown in Figure 33, these locations are: (1) in the matrix at the free surface (point M), (2) in the matrix at x = -R (point N), (3) in the fiber at x = -R (point N'), (4) in the fiber at x = +R (point P'), and (5) in the matrix at x = +R (point P). The stress profiles shown in Figure 34 show that the proximity of a fiber to a free surface significantly influences the thermally-induced stress distributions in both the fiber and matrix, especially when the fiber is less than one fiber diameter away from the free surface (as measured from the fiber's center). This effect is most pronounced for the hoop stress component in the region of the matrix

---

[j] All calculations using this analysis [119] were performed by Jasiuk at Michigan State University.

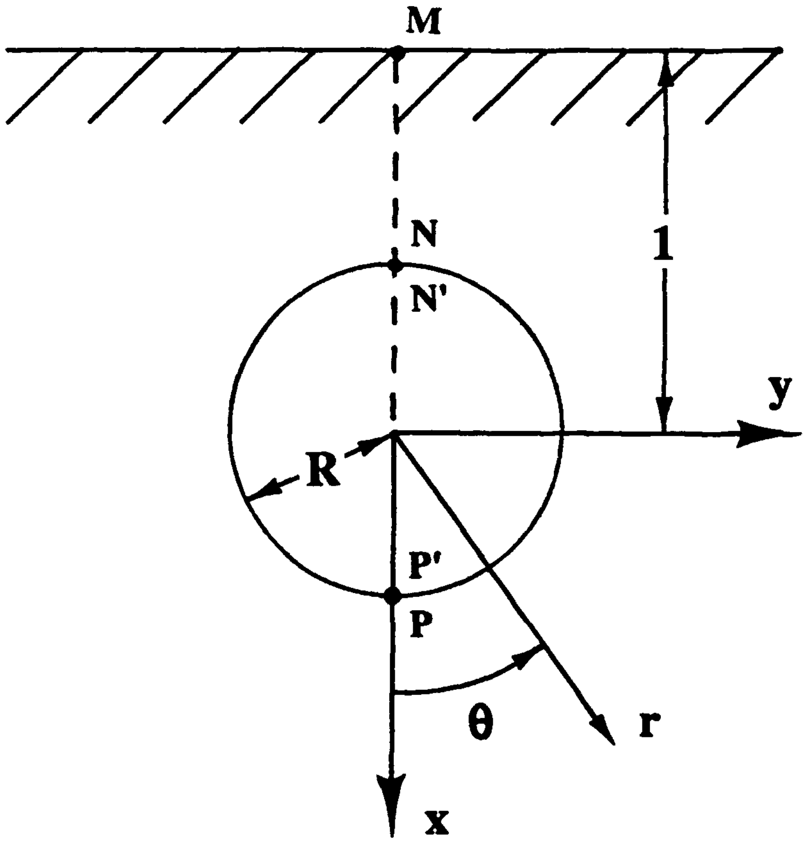

Figure 33. Fiber of radius R (whose cross-section is shown) embedded within the matrix and located near a free surface (adapted from Lee et al. [119]). Note that the axis of the fiber is oriented normal to the plane of the figure.

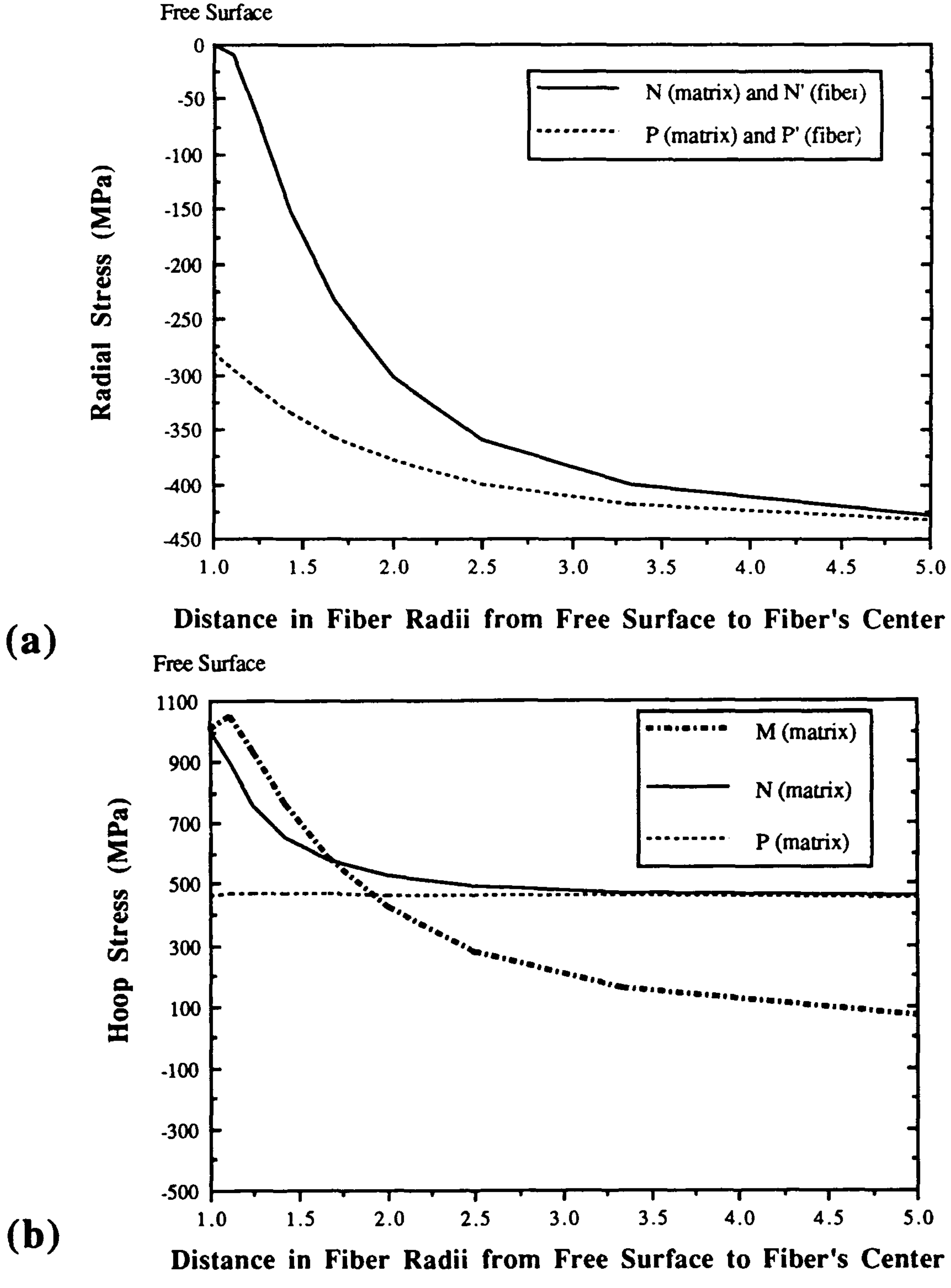

Figure 34. Thermally-induced residual stress profiles within a sapphire-reinforced TiAl composite as a function of the relative distance between a fiber and a free surface (predicted by exact elastic model). (a) Fiber and matrix radial stress (σ_{rr}), (b) matrix hoop stress ($\sigma_{\theta\theta}$), and (c) fiber hoop stress ($\sigma_{\theta\theta}$) profiles.

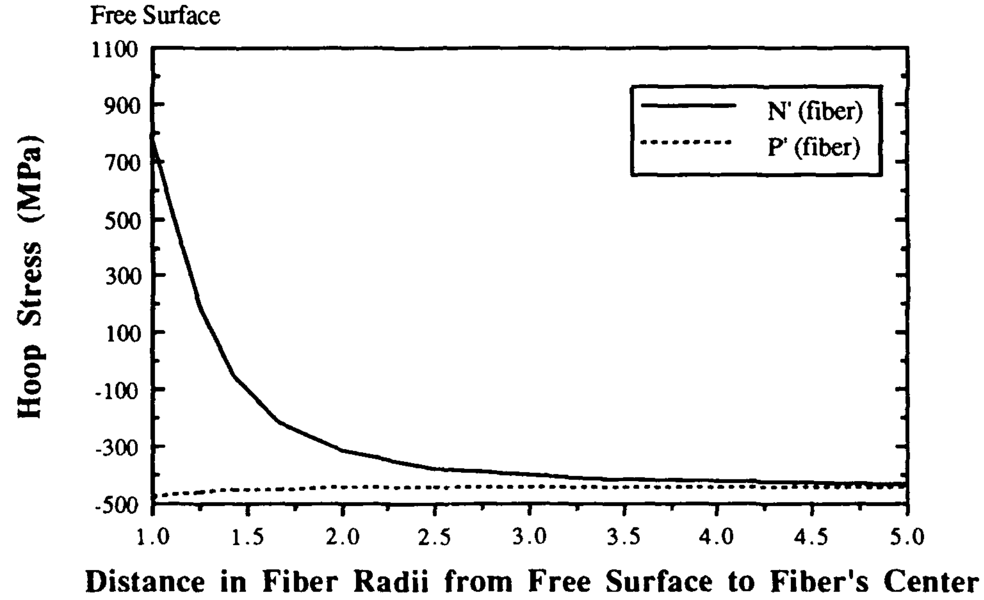

(c)

Figure 34. (cont.)

between the fiber and free surface and in the portion of the fiber that is closest to the free surface (i.e., points M, N, and N' shown in Figure 33). Thus, for a 160 μm diameter sapphire fiber, large tensile hoop stresses exist in and around the fiber when point N' on the fiber is less than 80 μm from the free surface.

Similar results were found by Brockenbrough [120] in an elastic finite element analysis of the thermally-induced residual stress distributions in a particulate-reinforced Al-Si-Mg alloy due to the CTE mismatch between the aluminum alloy matrix and spherical silicon particles. Assuming a perfectly bonded interface, Brockenbrough's FEM computations predict that, when a silicon particle is located very near a free surface, significant residual tensile stresses exist within the (1) region of the matrix between the particle and free surface, which can lead to matrix yielding, and (2) the portion of the particle closest to the free surface, which can result in particle fracture [120].

Figure 34a shows that, as the fiber approaches the free surface, radial clamping stresses decrease. As a result, this increases the likelihood that, in the absence of chemical bonding, "near surface" fibers will pullout during composite failure. Residual hoop stresses within the matrix adjacent to a fiber are tensile when free surface effects are ignored (i.e., the fiber is far removed from a free surface) since the CTE of the matrix is greater than that of the fiber. However, when a fiber is near (i.e., < one fiber diameter) a free surface, the matrix hoop stresses within the region between the fiber and the free surface are amplified (i.e., see the $\sigma_{\theta\theta}$ distributions for points M and N shown in Figure 34b) while those within the region adjacent to the fiber but farthest from the free surface are unaffected (i.e., see the $\sigma_{\theta\theta}$ distributions for point P in Figure 34b). One important implication of the matrix thermoelastic stress profiles shown in Figures 34a and b is that yielding, as well as possible crack formation in the low ductility TiAl matrix, will preferentially occur within the region between the fiber and the free surface. Even a conservative calculation of the matrix equivalent stress[k] (based on von Mises' yield criterion) shows that it far exceeds the matrix yield stress of 400 to 630 MPa. As a result, the fracture resistance of the composite can be adversely affected during monotonic or cyclic loading if the outer ply of fibers is within a fiber diameter of the surface.

Figure 34c indicates that the hoop stresses within the fiber (at point N') become tensile when the fiber's center is ≤1.4 fiber radii from the free surface. This corresponds to a distance of ≈32 μm from point N' to the free surface (i.e., see Figure 33) for a typical sapphire fiber embedded within a TiAl matrix. Although Figure 34c indicates that hoop stresses as high as 790 MPa can exist within the fiber when it just intersects the free surface (i.e., when R = 1), this value is unrealistic since matrix plasticity (not considered in this present analysis [119]) will limit the stress levels in both the fiber and matrix via stress relaxation in the matrix. Even so, experimental support for the existence of thermally-induced tensile hoop stresses within the fiber of sufficient magnitude to cause fracture within a fiber that intersects a free surface is shown in Figure 35. This figure shows a portion of an uncoated sapphire fiber that is partially embedded within the Ti-48-1 matrix and oriented nearly parallel to the free surface. The matrix was chemically removed to expose the fiber by etching with a concentrated Kroll's reagent. Evidence of a crack parallel to the fiber's axis, in the location of the fiber arrowed A in Figure 35a, is shown in Figure 35b. Careful examination of the exposed fiber revealed that this crack ran along its entire length. Examination of the fiber where it just intersects the free surface (arrowed B in Figure 35a) reveals the presence of two parallel cracks as shown in Figure 35c. It is important to note that these cracks do not follow a zigzag crack path as found when the fiber end was exposed normal to the free surface (i.e., see Figure 27a), but are straight.

---

[k] Calculation of the equivalent stress within the matrix requires a knowledge of all three principal stress components. Although, the longitudinal stress was not calculated in this analysis, it is known that it is tensile.

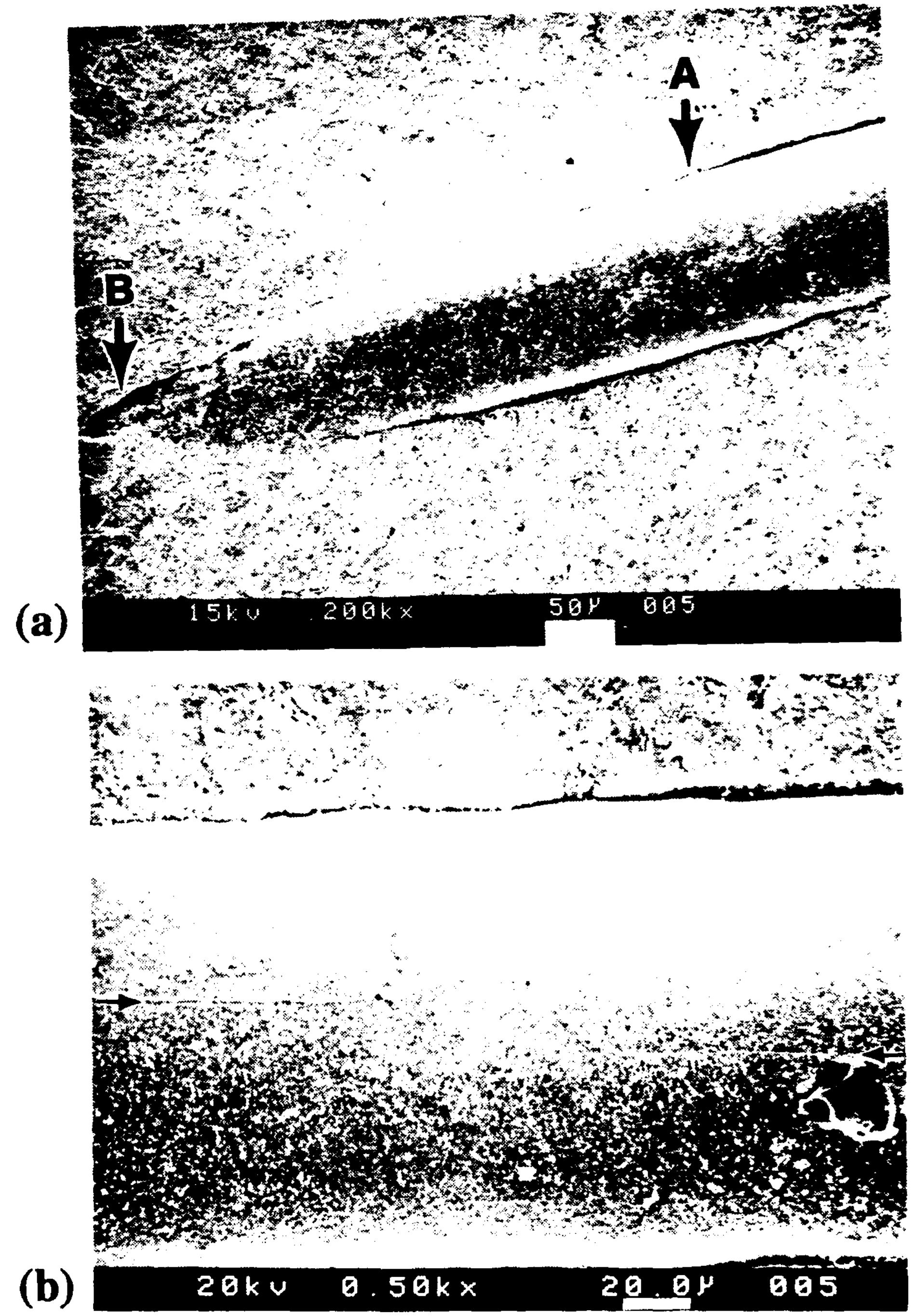
A
B
(a)
15kv 200kx 50μ 005
(b)
20kv 0.50kx 20.0μ 005

Figure 35. Micrographs showing the extent of fiber fracture and crack orientation with respect to the axis of a sapphire fiber that is partially embedded within the Ti-48Al-1V matrix and oriented nearly parallel to a free surface. (a) SEM image of the fiber and high magnification views of locations arrowed (b) A and (c) B in (a). (cont. on next page)

(c)

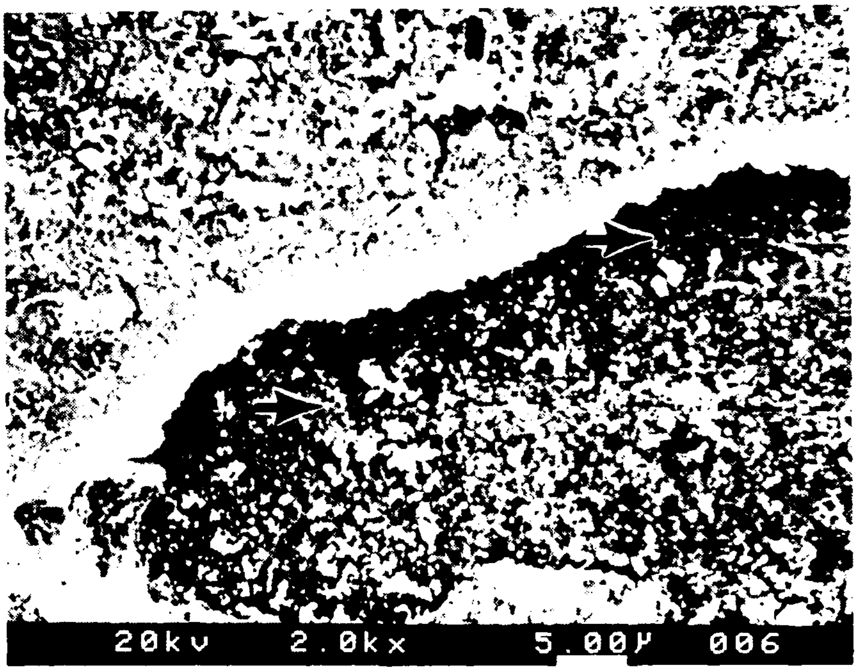
20kv 2.0kx 5.00µ 006

Figure 35. (cont.)

This suggests that: (1) the thermoelastic stress state responsible for fiber fracture and (2) the manner in which the cracks initiate and propagate are fundamentally different from those that occur when a fiber intersects a free surface with its axis normal to the surface (i.e., see section 4.2.2.1).

Figure 36 illustrates the stress state responsible for fiber fracture when a fiber just intersects a free surface (i.e., when R = 1 in Figure 33). In Figure 36b, the predicted hoop ($\sigma_{\theta\theta}$) and radial (σ_{rr}) stress profiles within a 160 μm diameter sapphire fiber are shown as a function of depth below the free surface (i.e., distance along the x-axis from point N' to P'). This figure shows that: (1) at or near the free surface, high tensile hoop stress exists within the fiber and (2) the magnitude of the tensile stress decreases rapidly with increasing depth below the free surface. These computations suggest that, given a fiber of low fracture toughness and the existence of a surface flaw (e.g., a surface crack or flaw created during cross-sectioning, machining, or chemical interaction with the matrix during composite fabrication), the thermally-induced tensile hoop stress within the fiber may propagate the crack to a length dictated by the stress state and fracture toughness.

Finally, it is important to note that the magnitude of the residual hoop stresses depends not only on the CTE mismatch between constituents and the elastic/plastic properties of the interfacial region, but also the interfacial shear strength. As suggested by Figure 36, large residual tensile hoop stresses will develop within the fiber only if the fiber/matrix interface has a high shear strength. This was verified in a separate analysis by Lee et al. [119] where the fiber/matrix interface was allowed to freely slide. Figure 37 shows the interfacial shear stress ($\tau_{r\theta}$) as a function of angular distance, θ, around the fiber/matrix interface (i.e., see Figure 33) for a sapphire-reinforced TiAl composite when a fiber just intersects a free surface. Assuming a perfect fiber/matrix bond, this figure suggests that the shear stress is not uniform around the interface but peaks near $\theta \approx 150°$.

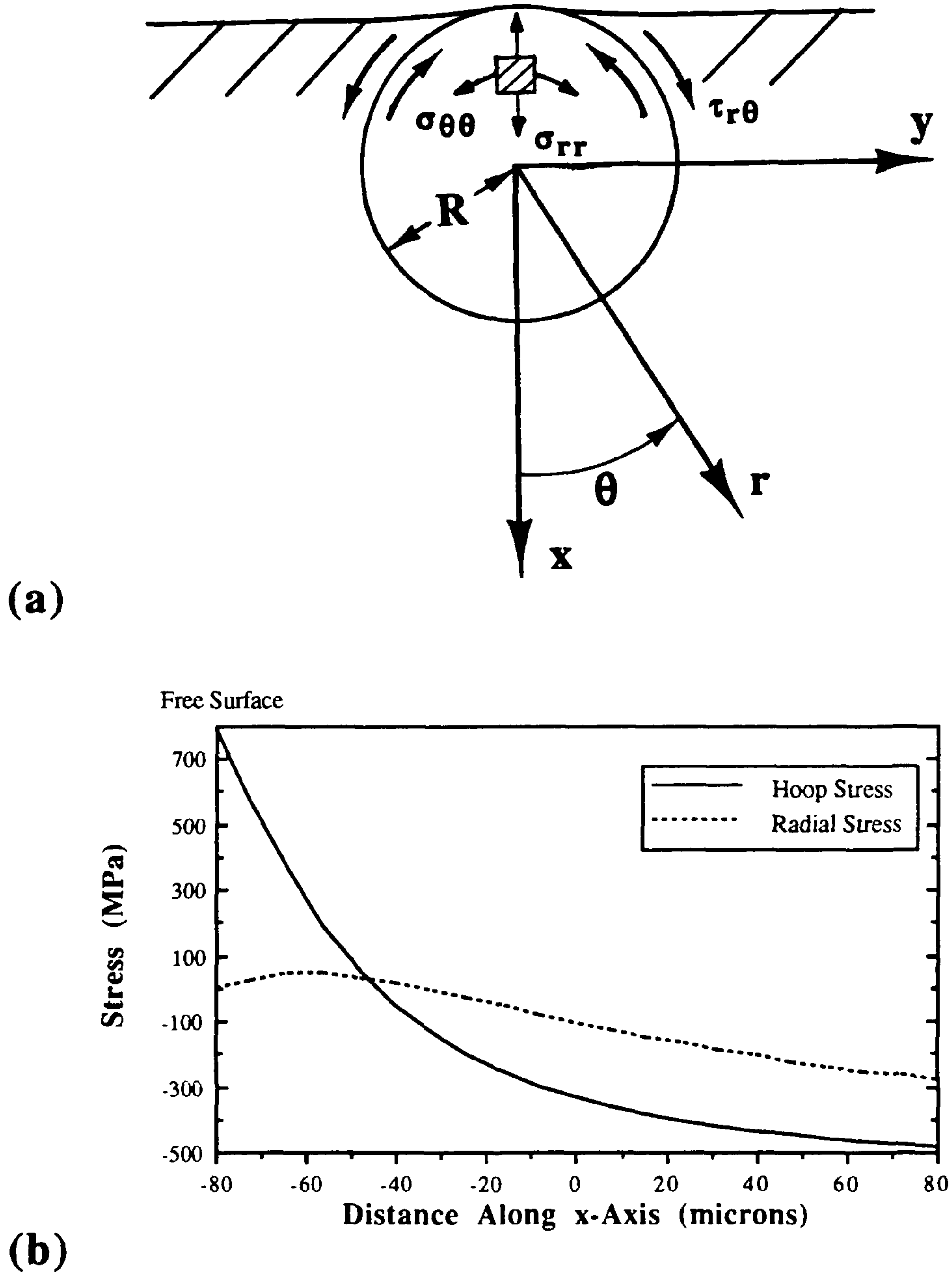

Figure 36. Thermoelastic residual stress profiles within a sapphire fiber when it just intersects a free surface. (a) Fiber orientation showing the stress state and important role of interfacial shear strength and (b) resulting hoop ($\sigma_{\theta\theta}$) and radial (σ_{rr}) stress profiles within a 160 μm diameter fiber.

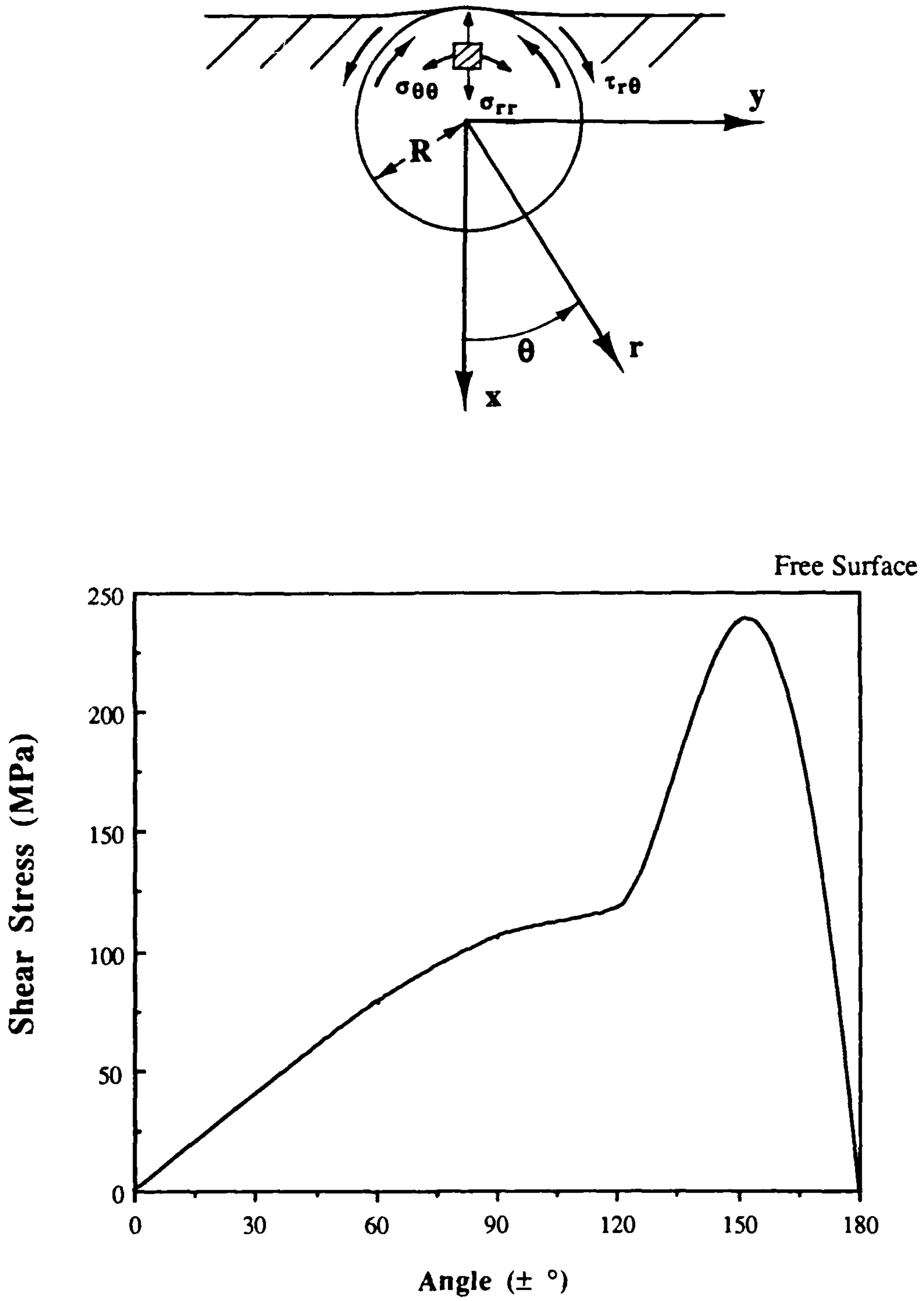

Figure 37. Thermally-induced interfacial shear stress ($\tau_{r\theta}$) as a function of angular distance, θ, around the sapphire/TiAl interface when a fiber just intersects a free surface.

If the fiber and matrix remain bonded, the shear stress will develop high tensile hoop stresses within the region of the fiber intersecting the free surface.

In summary, this portion of the research program demonstrates that the combination of well-bonded brittle fibers, significant tensile residual stress, and surface flaws or cracks created within the fibers during machining or chemical interaction with the matrix (i.e., during composite fabrication) can result in fiber fracture when a fiber intersects a free surface. It is suggested that surface cracks within fibers can adversely affect the crack growth behavior of sapphire-reinforced TiAl composites during subsequent monotonic or cyclic loading in the transverse direction. Given two possible orientations of a fiber with respect to a free surface, and assuming a perfectly bonded fiber/matrix interface, finite element and exact elastic computations predict that significant thermally-induced tensile stresses exist in sapphire fibers embedded within TiAl-based matrices when they intersect a free surface. In both cases, the results suggest that the magnitude of the thermally-induced tensile stresses can be decreased by: (1) using soft and/or ductile fiber coatings and (2) decreasing the shear strength of the interface.

4.3. Fiber/Matrix Interfacial Strength Behavior

In the previous section, it was suggested that the magnitude of thermoelastic residual tensile stresses that develop within fibers intersecting a free surface is a sensitive function of the interfacial bond strength in sapphire-reinforced TiAl composites. It is also recognized that the fiber/matrix interfacial shear strength controls the strength and crack growth behavior of fiber-reinforced composites [68]. The purpose of this portion of the research program is to characterize the interfacial shear behavior in sapphire-reinforced TiAl composites during thin-slice fiber pushout tests. In order to fully understand the interfacial failure process, finite element computations are used to predict the stress distributions along the interface during testing.

4.3.1. Finite Element Computations of the Interfacial Stress Distributions

The interfacial failure sequence that occurs during pushout testing of IMCs is a sensitive function of the overall stress distribution along the fiber/matrix interface. Since the typical thin-slice pushout test configuration (i.e., specimen supported over a hole or slot) results in specimen bending, the overall stress distribution is dependent on the interfacial shear strength, the magnitude of thermally-induced stresses, the indenter pressure (which controls the mechanical stresses), and the specimen thickness [68].

The stress distributions within the matrix adjacent to the fiber were computed by Kallas from the axisymmetric, elastic-plastic FEM model [84] previously described in section 4.2.2.1. The geometry of the model, loading arrangement, and boundary conditions were selected to emulate the actual fiber pushout specimen and test setup schematically shown in Figure 38. The analysis was performed over a range of indenter loads while assuming perfect bonding at the interface. The analysis includes two main steps: (1) determination of the thermally-induced residual stresses that develop during cool-down from the composite fabrication temperature and (2) determination of the mechanically-induced stresses that result from the indenter load on the fiber end [64].

The thermally-induced residual stress distributions within the matrix adjacent to the fiber are shown in Figure 39 as a function of position (z) along the fiber normalized with respect to specimen thickness (t). As shown in Figure 38, $z = 0$ denotes the specimen's backface. In all cases, the stress components are conveniently expressed in terms of cylindrical polar coordinates due to the cylindrical symmetry of the fiber/matrix system

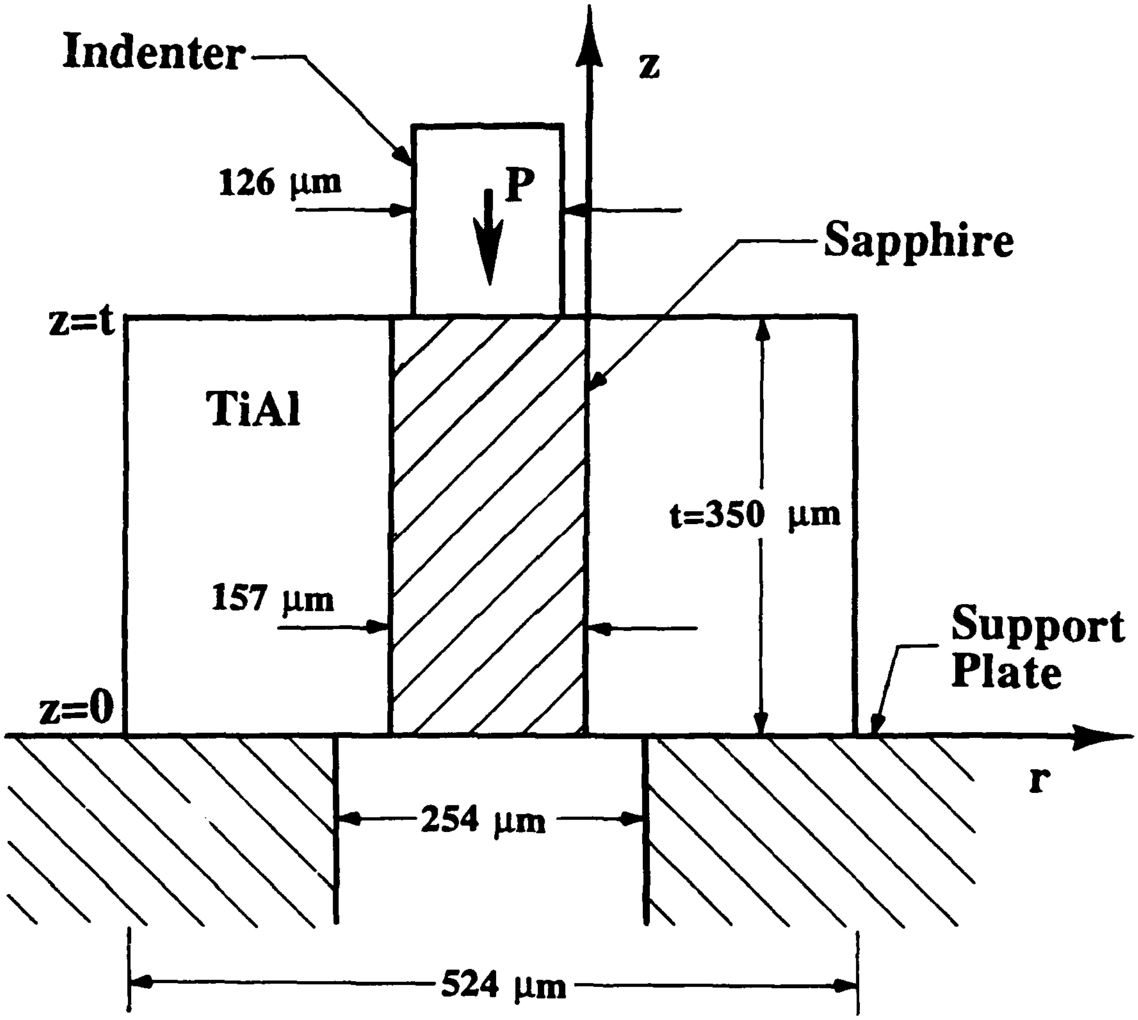
Indenter
z
126 μm
P
Sapphire
z=t
TiAl
t=350 μm
157 μm
Support
Plate
z=0
r
254 μm
524 μm

Figure 38. Schematic of the fiber pushout test configuration used for axisymmetric finite element modeling.

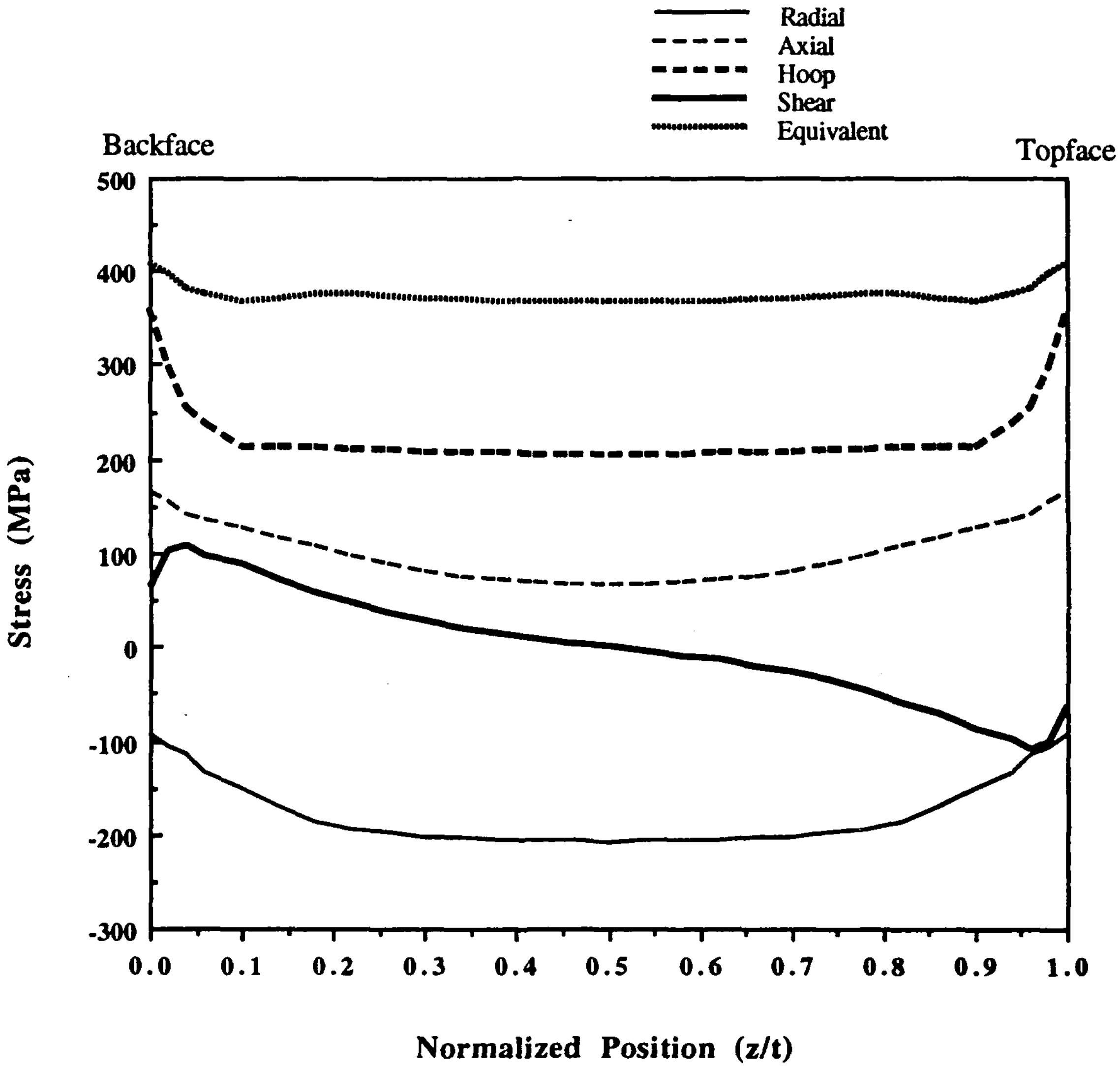

Figure 39. Thermally-induced residual stress distribution within the matrix adjacent to the fiber for a sapphire-reinforced TiAl composite with a 0.1 fiber volume fraction (predicted by FEM [84]).

(i.e., see Figure 1). In Figure 39, the interfacial stress components were computed for a sapphire-reinforced TiAl composite with a 0.1 fiber volume fraction and assuming the stress-free temperature as 800 °C (i.e., thermal residual stress build-up is computed over a 780 °C temperature change). (See section 4.2.2.1 for the rationale used to select this temperature.) It is shown that, thermal loading alone is not sufficient to cause plastic deformation in the matrix, since the equivalent stress (based on von Mises' yield criterion) is less than the matrix yield strength of ≈513 MPa. However, it is also important to note that significant radial clamping is predicted due to the sapphire/TiAl CTE mismatch.

The predicted magnitudes of the mechanically-induced stresses (i.e., ignoring the thermally-induced residual stresses for the moment) within the matrix adjacent to the fiber are shown in Figure 40. As shown in Figure 38, the analysis was performed for a 350 μm thick specimen containing a 157 μm diameter fiber and supported over a 254 μm diameter hole (i.e., support hole-to-fiber diameter ratio of ≈1.6). In addition, the analysis was performed over a range of indenter loads that correspond to the range of loads applied during actual pushout tests of the sapphire/Ti-48-2-2 and Ta-coated sapphire/Ti-48-1 systems.

As illustrated in Figure 40a, the mechanically-induced shear stress (τ_{rz}) is not uniform along the fiber length, especially at loads ≤30 N, but peaks at a location approximately one fiber radius below the topface (where the "topface" is the side of the specimen where the indenter is loaded onto the fiber). At higher loads, however, the shear stress becomes more uniform along the entire interface as a result of matrix plasticity (i.e., see Figure 40d). Figures 40b and c show that significant radial and hoop stresses are generated as a result of specimen bending. Most notable is the development of large tensile radial stresses on the specimen's backface opposite the indenter that may initiate mode I cracks at the fiber/matrix interface. The implications of this to the observed interfacial

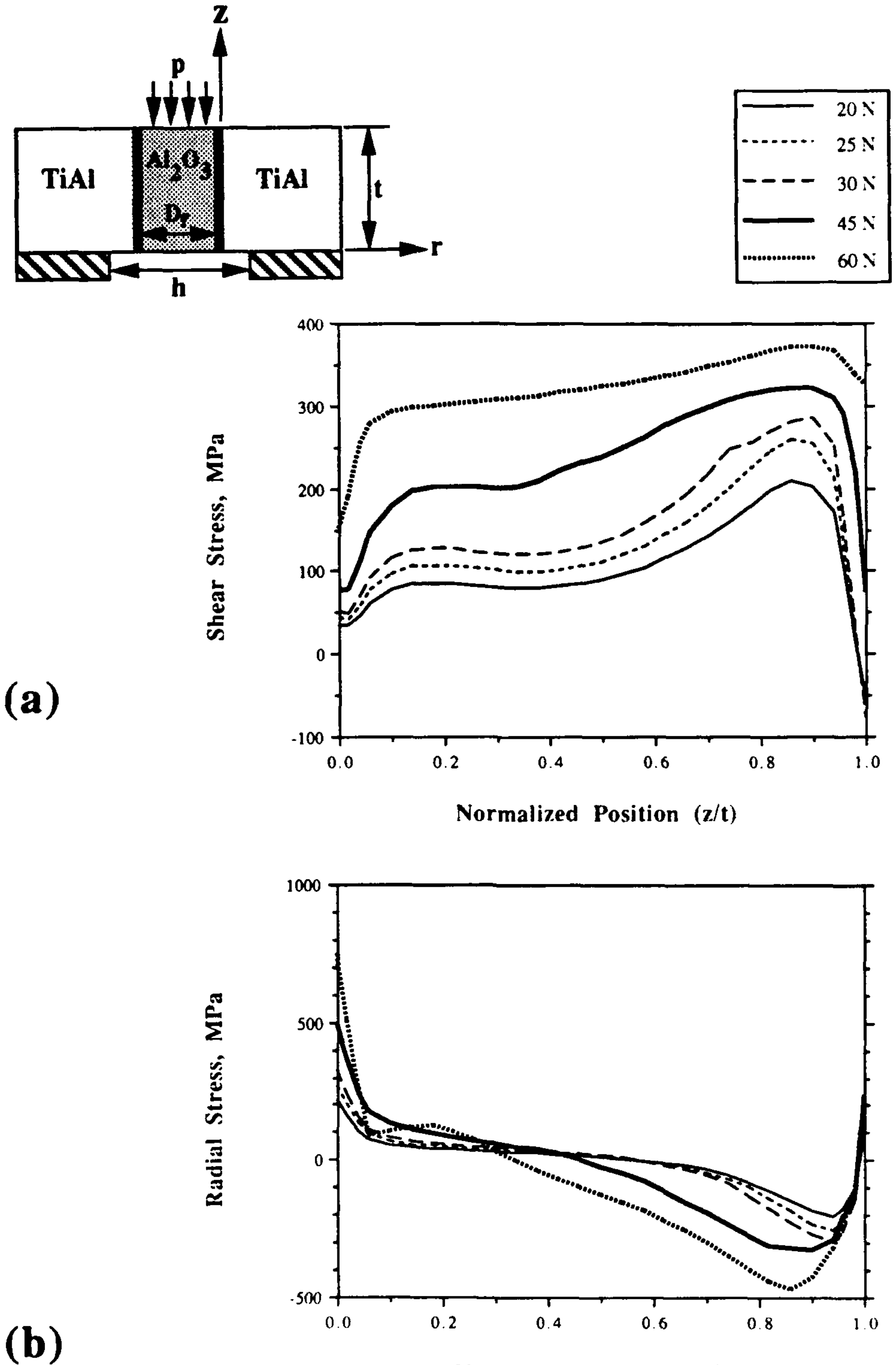

Figure 40. Mechanically-induced stress distributions within the matrix adjacent to the fiber for several indenter loads on a sapphire-reinforced TiAl pushout specimen (predicted by FEM). (a) Shear stress (τ_{rz}), (b) radial stress (σ_{rr}), (c) hoop stress ($\sigma_{\theta\theta}$), and (d) equivalent stress ($\bar{\sigma}$). (cont. on next page)

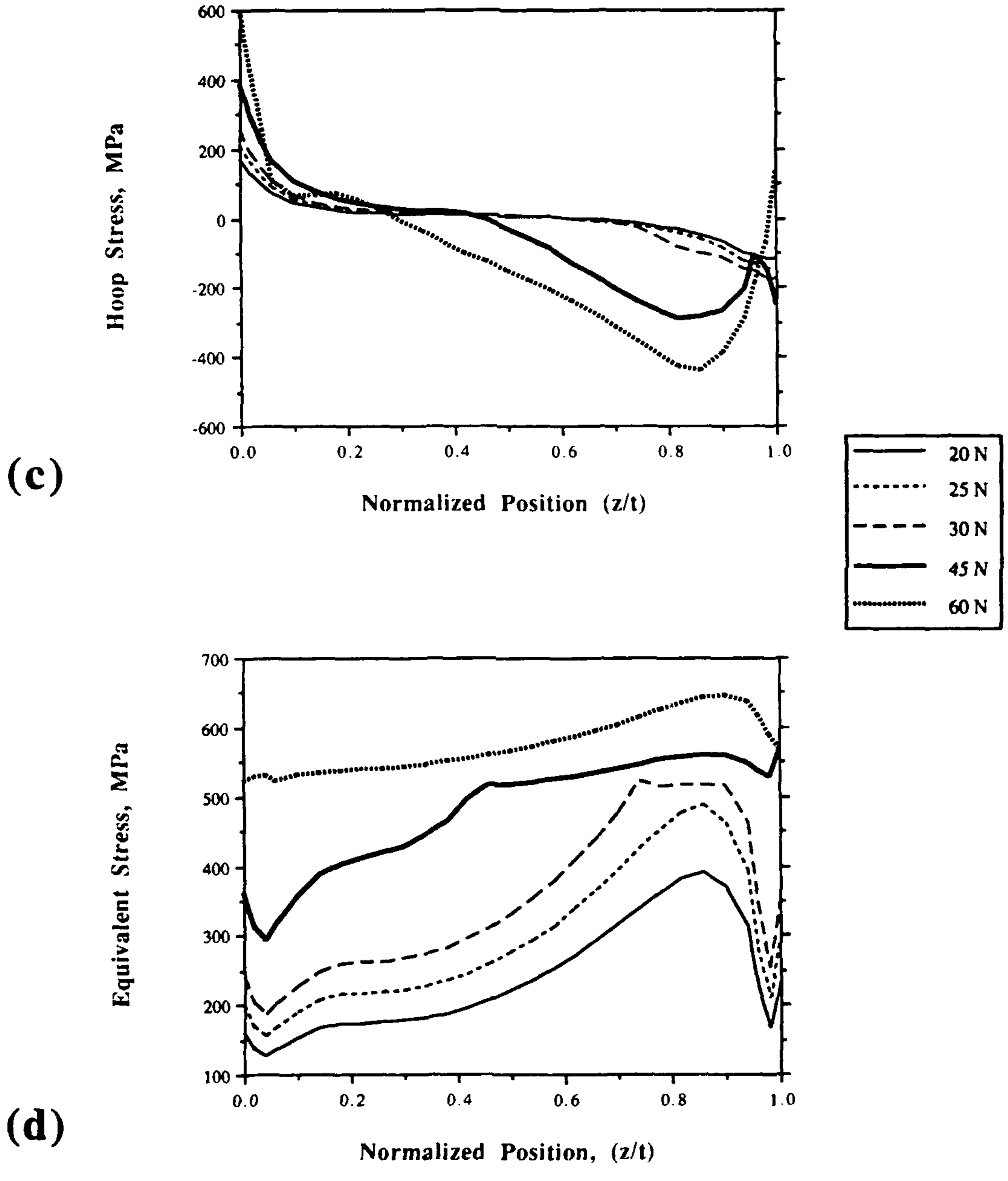

Figure 40. (cont.)

failure sequence will be discussed in the next section. Finally, Figure 40d shows that the predicted values of the equivalent stress ($\overline{\sigma}$) peak near the specimen's topface and increases with increasing indenter load. This should result in matrix plastic deformation (i.e., $\overline{\sigma} = \sigma_y$ of TiAl) near the topface at a load of ≈30 N. Such local deformation should subsequently spread along the entire interface at higher loads.

The interfacial failure sequence that occurs during fiber pushout testing, however, is a consequence of the combination of the thermal and mechanical stress states shown in Figures 39 and 40. Since the finite element computations must take matrix plasticity into consideration, these stress states can not be simply added to obtain the overall stress state. The combined thermal and mechanical interfacial stress distributions within the matrix adjacent to the fiber are plotted in Figures 41a and b for a thermal cool-down of 780 °C and indenter loads of 20 and 30 N respectively. Due to wide-spread matrix plasticity along the interface, the finite element code (i.e., a limited capability ANSYS code) could not accurately calculate combined thermal and mechanical stress distributions for indenter loads greater than 30 N (i.e., due to the prohibitively large number of required iterations).

A comparison between Figures 41 and 40 illustrates that the presence of thermally-induced stresses due to the thermal expansion mismatch between constituents has a significant effect on the overall interfacial stress distributions. The most notable effect is a consequence of the opposite sign of the thermally- and mechanically-induced shear stress components near the specimen's top and backface (i.e., compare τ_{rz} shown in Figures 39 and 40a). As shown in Figure 41, the net effect is to decrease the τ_{rz} value near the indenter and increase it at the backface.

The overall interfacial stress distributions shown in Figure 41 suggest that interfacial failure may occur by the initiation of a mode I and/or mode II debond crack at the specimen's backface. This is especially true at an indenter load of 20 N where both radial

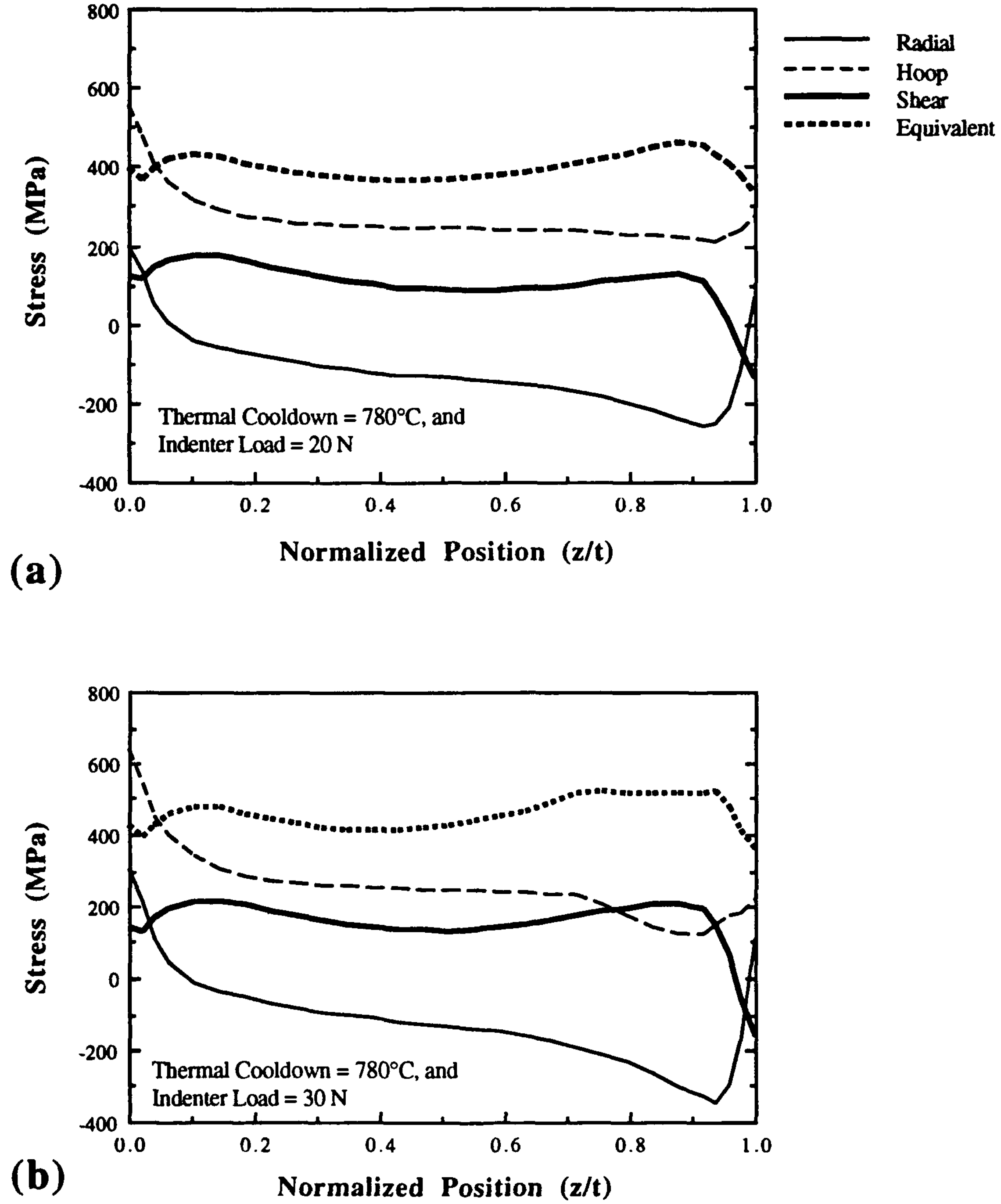

Figure 41. Combined thermal and mechanical interfacial stress distributions within the TiAl matrix for a thermal cool-down of 780 °C and indenter loads of (a) 20 N and (b) 30 N on a sapphire-reinforced TiAl pushout specimen.

and shear stress components peak near the backface with approximately the same magnitude (i.e., see Figure 41a). As expected, the radial stress is compressive along most of the fiber length, except near the specimen's backface where bending-induced tensile stresses dominate. However, the net shear stress component near the backface is actually larger than (i.e., at a 20 N indenter load) or the same (i.e., at a 30 N load) as that near the topface. Therefore, it is possible that interfacial failure may occur by the initiation of a mode II debond crack at the backface rather than the topface as is normally assumed in "thick-slice" specimens. Finally, it is important to note (1) the large tensile hoop stresses in the matrix along the fiber, especially at the specimen's backface, and (2) the nearly constant value of equivalent stress that occurs along the entire interface.

4.3.2. Interfacial Failure Sequence

Computational analysis of and experimental results from the thin-slice fiber pushout test reported by Koss et al. [68] for both MMCs and IMCs suggest that specimen bending can complicate the interpretation of results and create interfacial failure sequences that are test dependent. Most notable among these factors is the development of tensile bending stresses on the specimen's backface (i.e., opposite the indenter) that may initiate mode I cracks at the fiber/matrix interface [68]. To examine interfacial failure in the present sapphire-reinforced TiAl system, tests were performed using two configurations: (1) specimens supported over a hole with a diameter ≈1.6 times that of the fiber (i.e., see Figure 38) and (2) a back-plated configuration with a support hole the same size and shape as the fiber's cross-section. The latter configuration eliminates the specimen bending responsible for the large radial and hoop stresses shown in Figure 40. The results for tests performed using a support hole with a diameter ≈1.6 times that of the fiber will be presented in this section. Later, in section 4.3.4, comparison of these results with those without specimen bending will be presented.

Fiber pushout testing of Ta-coated sapphire/Ti-48-1 specimens supported over a hole with a diameter ≈1.6 times that of the fiber resulted in an average interfacial shear strength (i.e., maximum load recorded during fiber pushout divided by the interfacial area) of 336.3 ± 11.2 MPa[1]. However, in the sapphire/Ti-48-2-2 system, a much lower average interfacial shear strength, 170.5 ± 22.3 MPa[1], was measured, nearly half of the value measured for the Ta-coated sapphire/Ti-48-1 interface. Since the fibers in specimens of the uncoated sapphire/Ti-48-1 system were cracked, partly due to the high interface strength (i.e., see the discussion in section 4.2.2), fiber pushout testing of this system was impossible. To gain a more clear understanding of why the average interfacial shear strengths differ by nearly a factor of two, the interfacial failure sequence was carefully characterized in each system. This was accomplished by SEM examination and SLM surface profile measurements of top and backface fiber displacement at incremental loads up to large-scale fiber displacement/load-drop.

4.3.2.1. Interfacial Failure Sequence in the Tantalum-Coated Sapphire/Ti-48Al-1V System

Figure 42 shows a typical load versus cross-head displacement plot recorded during testing of a 0.35 mm thick Ta-coated sapphire/Ti-48-1 specimen. Based on the scanning electron microscope (SEM) examination and scanning laser microscope (SLM) fiber displacement measurements, the failure sequence has been divided into five regions as shown. The specimen is loaded elastically in region 1. At a load of ≈35 N, a circumferential interface crack initiates on the specimen's backface (i.e., opposite the

---

[1] In all cases, ± one standard deviation is reported for 3 to 5 tests.

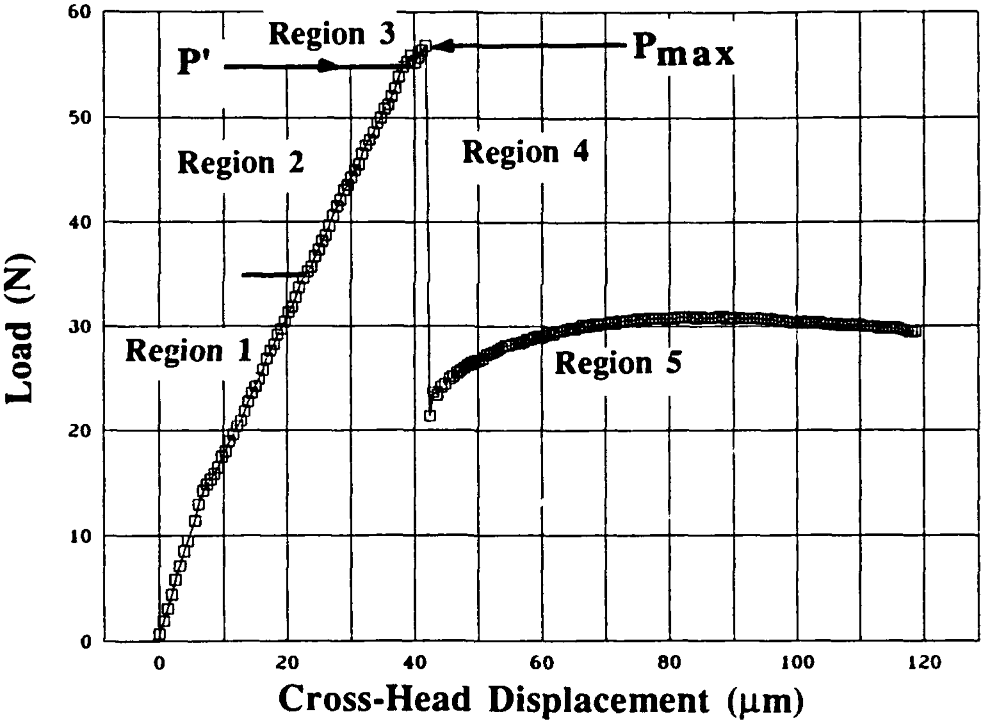

Figure 42. Typical load-displacement behavior of the Ta-coated sapphire/Ti-48Al-1V system during fiber pushout testing.

indenter) along approximately 25% of the fiber's perimeter. This occurrence is manifested by a small (≈0.25 μm) displacement of the fiber above the matrix on the backface along that portion of the fiber's perimeter where the crack exists. However, there was no detectable change in specimen compliance at this load. SLM surface profile measurements made at all other locations around the perimeter of the fiber, both on the specimen's top and backface, showed no other evidence of fiber displacement. For example, Figure 43 shows that at the same location on the fiber's perimeter, displacement of the fiber occurs on the backface (Figure 43a), but not on the topface (Figure 43b). Two factors combine to explain this net fiber displacement: (1) the fiber and matrix are elastically compressed and stretched respectively in the axial direction due to their CTE mismatch and a strong interfacial bond, and therefore, (2) the introduction of an interface crack at ≈35 N causes the fiber and matrix to partially relax to their unconstrained lengths over the debonded region. Thus, the magnitude of net fiber displacement above the matrix on the backface is a semi-quantitative measure of the debond crack length up along the interface. Details on the calculation of backface debond crack length based on this measurement will be given in section 4.3.3.

Two important conclusions can be made about the manner in which interfacial failure occurs during thin-slice fiber pushout testing of the Ta-coated sapphire/Ti-48-1 system: (1) interfacial failure initiates at the backface of the specimen opposite the indenter, not near the topface as assumed for "thick-slice" specimens and by current models of the fiber pushout test, and (2) the debond crack does not initially encompass the entire perimeter of the fiber. As a result of the thin-slice geometry of the specimen and magnitude of the thermally-induced residual stresses, the overall interfacial stress state dictates that interfacial failure should initiate on the backface. Reference to the overall interfacial stress distributions shown in Figure 42b (i.e., thermal cool-down of 780 °C and indenter load of 30 N) suggests that a mode I crack initiates on the backface at a load of ≈35 N since it

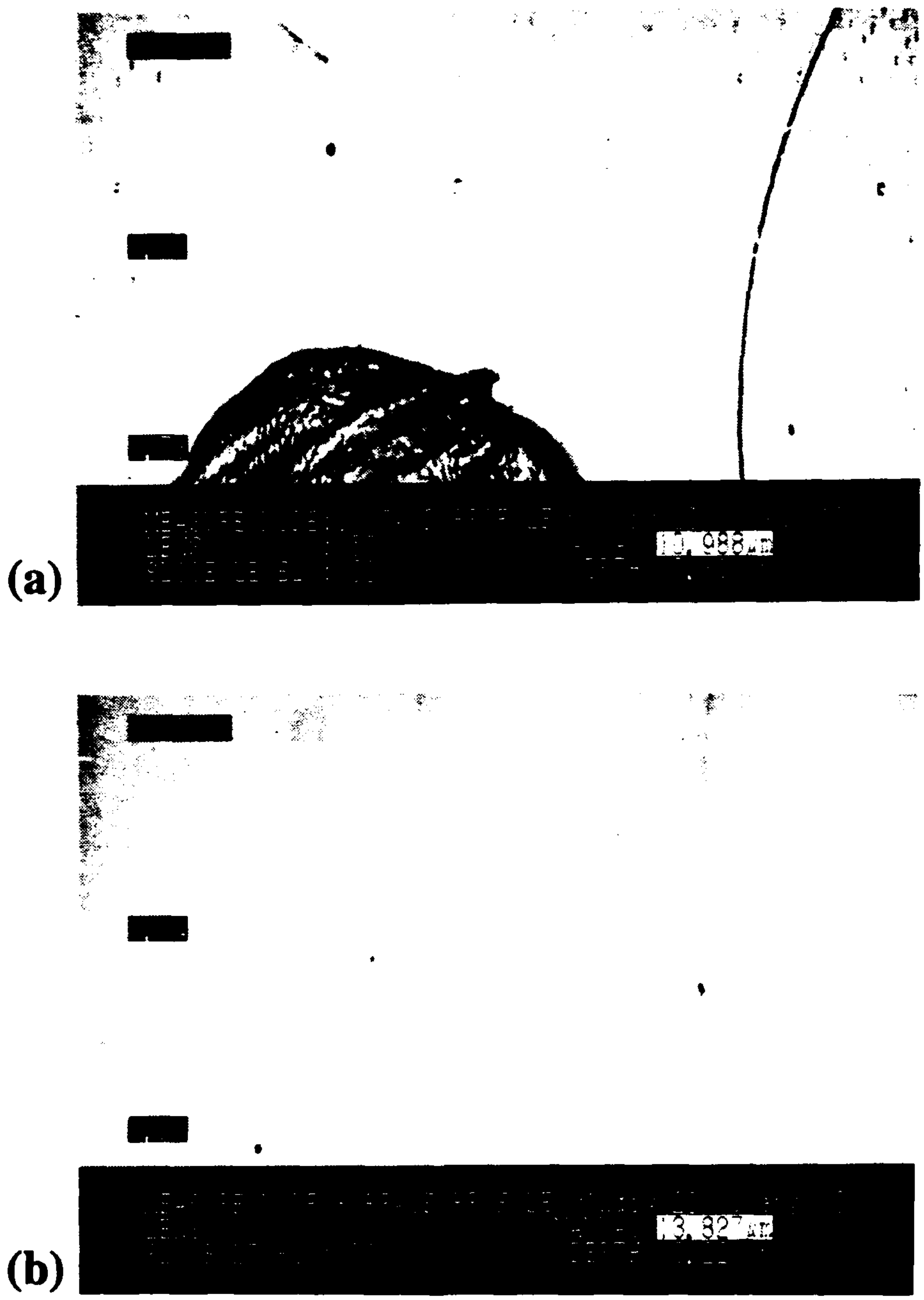

Figure 43. Micrographs of scanning laser microscope surface profile measurements made at the (a) backface and (b) topface, but at the same position on the fiber perimeter, of a Ta-coated sapphire/Ti-48Al-1V specimen during region 2 load-displacement behavior.

appears that bending-induced, radial tensile stresses dominate over shear stresses as the indenter load increases. However, since significant shear stresses also exist near the specimen's backface, initiation of a mode II crack on the backface can not be completely ruled out. This issue will be discussed in detail later.

In region 2, the circumferential interface crack on the backface grows around the fiber's perimeter and up along the interface in a mixed-mode I and II manner due to the large radial and shear stress components near the backface (i.e., see Figure 41). However, in the Ta-coated sapphire/Ti-48-1 system with the "high" interfacial shear strength, the crack does not propagate around the entire fiber perimeter. Instead it deviates into the matrix as shown in Figure 44a, presumably due to large tensile hoop stresses in the matrix (i.e., as shown in Figure 41a) and the apparently high normal bond strength/fracture resistance of the interface. This is in agreement with the high interfacial debond toughness, i.e., $\Gamma_i \approx 16.2$ J/m^2, reported by Evans et al. [72] for the TiAl/sapphire interface. (For comparison, the value of Γ_i reported for within a carbon coating on SiC is $\approx$0.1 J/m^2 [72].) The morphology of the resulting radial crack following large-scale fiber displacement is shown in Figure 44b.

Evidence from SLM surface profile measurements made during the latter stages of region 2 load-displacement behavior also indicates that a small circumferential mode II interface crack initiates on the topface along approximately 25% of the fiber's perimeter. This may be explained by the increase in shear stress within the bonded ligament that exists between the backface debond crack tip and specimen's topface as the crack propagates up from the backface. The redistribution of stresses along the interface, as a result of the crack tip stress field as well as the decreased ligament length, promotes such interfacial shear.

Region 3 begins at P', or approximately 57 N (see Figure 42), where the load-displacement plot deviates from linearity, indicating increased specimen compliance due

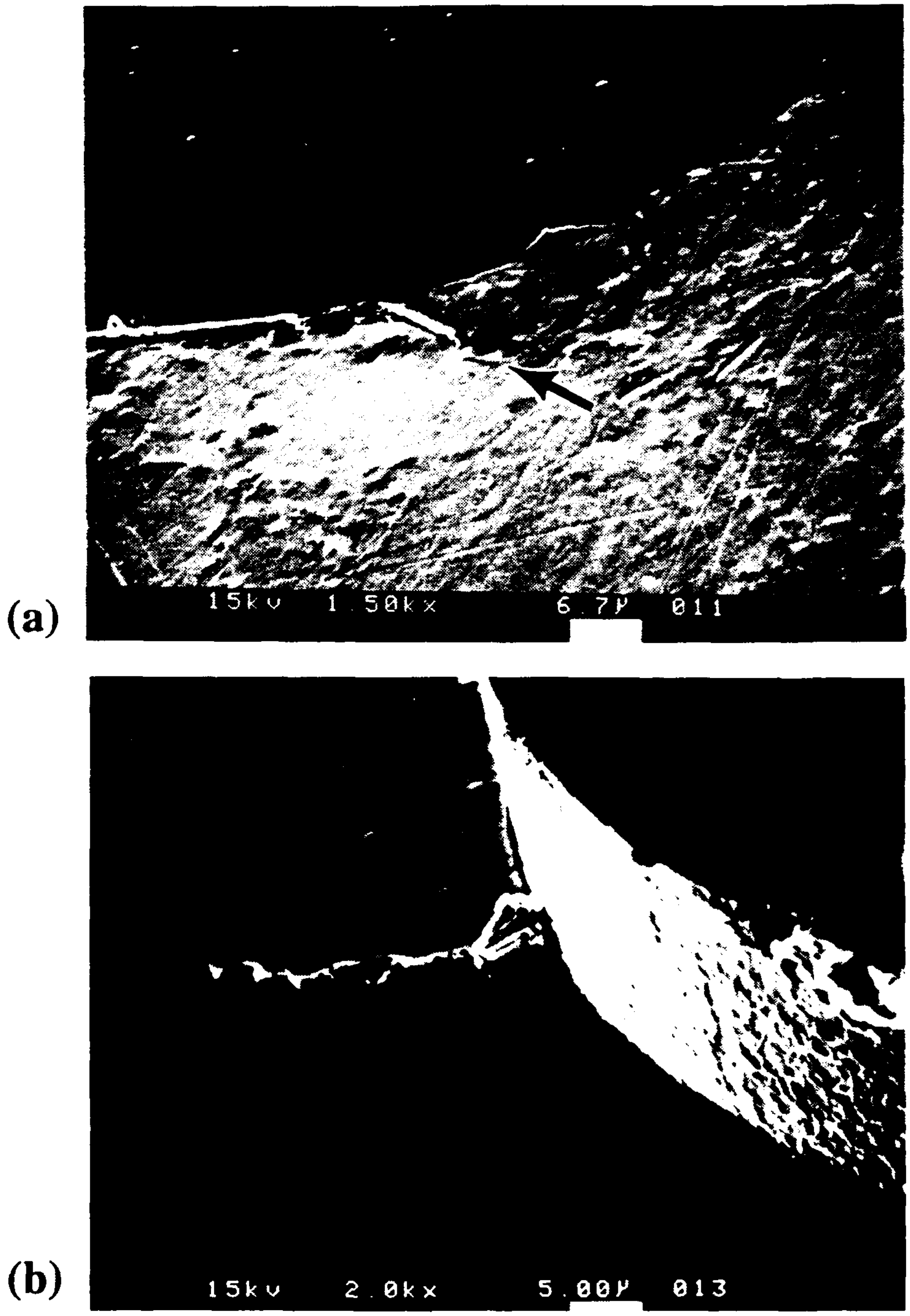
(a)
15kv 1.50kx 6.7µ 011
(b)
15kv 2.0kx 5.00µ 013

Figure 44. Evidence that the interfacial crack on the backface of a Ta-coated sapphire/Ti-48Al-1V specimen deviates into the matrix instead of propagating around the fiber's perimeter. SEM micrographs showing crack morphology (a) during region 2 load-displacement behavior and (b) following large-scale fiber displacement.

primarily to topface displacement of the fiber with respect to the matrix. At P', the average applied interfacial shear stress was found to be 311.9 ± 22.1 MPa from 5 tests of the Ta-coated sapphire/Ti-48-1 system. In this region, the circumferential interface cracks on both the specimen's top and backface grow around the fiber and along the interface. As P_{max} is approached, the top and backface cracks grow together but don't extend entirely around the fiber's perimeter. To characterize this "partial debond" scenario, SLM surface profile measurements of fiber displacement were made during region 3 load-displacement behavior of 3 separate tests. These measurements (to be presented in section 4.3.3) indicate that in all 3 tests the fiber appears to be debonded along its entire length, but only around 50 to 60% of its perimeter. The remaining interface ligament, however, remains bonded from the back to topface. This unusual scenario gives further evidence that the Ta-coated sapphire/Ti-48-1 interface has an apparently high bond strength/fracture resistance.

The above sequence, that was observed in all tests, is illustrated in the SEM examination and SLM surface profile measurements of a Ta-coated sapphire/Ti-48-1 specimen whose test was interrupted just before large-scale fiber displacement/load-drop occurred (i.e., the test was interrupted at an average applied interfacial shear stress of 338 MPa). At the 12 to 3 o'clock position on the perimeter of this fiber[m], SEM examination of the topface shows that a mode II interface crack doesn't extend entirely around the fiber's perimeter, but terminates at the location arrowed in Figure 45a. Several SLM surface profile measurements were made along the fiber perimeter shown in Figure 45a. At the 1 o'clock position on the fiber's perimeter, where the mode II debond crack exists, Figure 45b shows that the fiber's topface is displaced 0.40 μm below the matrix. However, at the 3 o'clock position, where the fiber and matrix remain bonded, topface fiber displacement

---

[m] Positions around the perimeter of each fiber tested are conveniently designated by imagining the cross-section of the fiber as the face of a clock.

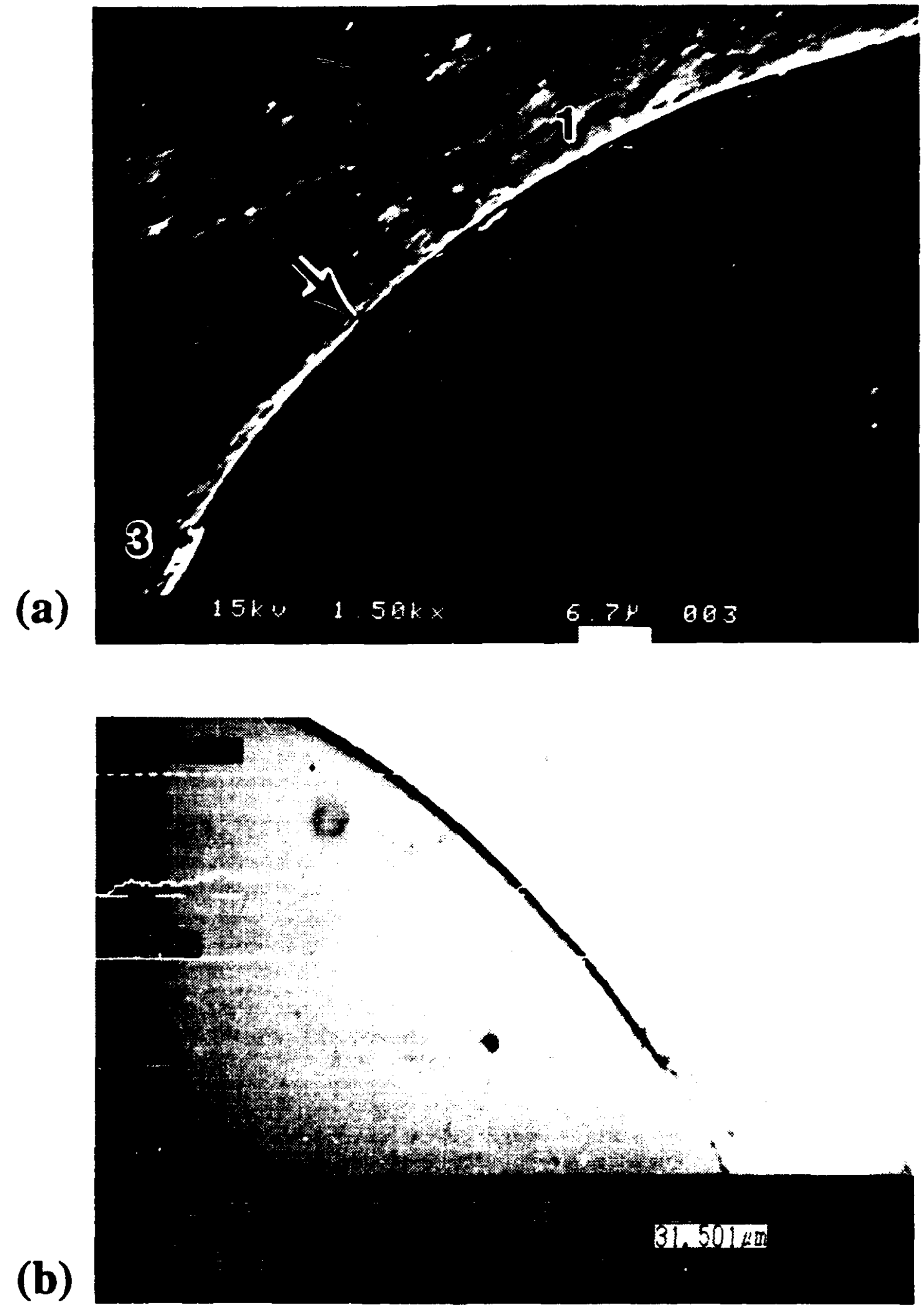

Figure 45. Characterization of interfacial failure during region 3 load-displacement behavior of a Ta-coated sapphire/Ti-48Al-1V specimen. (a) SEM micrograph of the specimen's topface, and corresponding micrographs of SLM surface profile measurements at (b) 1 o'clock on topface, (c) 3 o'clock on topface, (d) 3 o'clock on backface, (e) 9 o'clock on topface, and (f) 9 o'clock on backface. (cont. on next 2 pages)

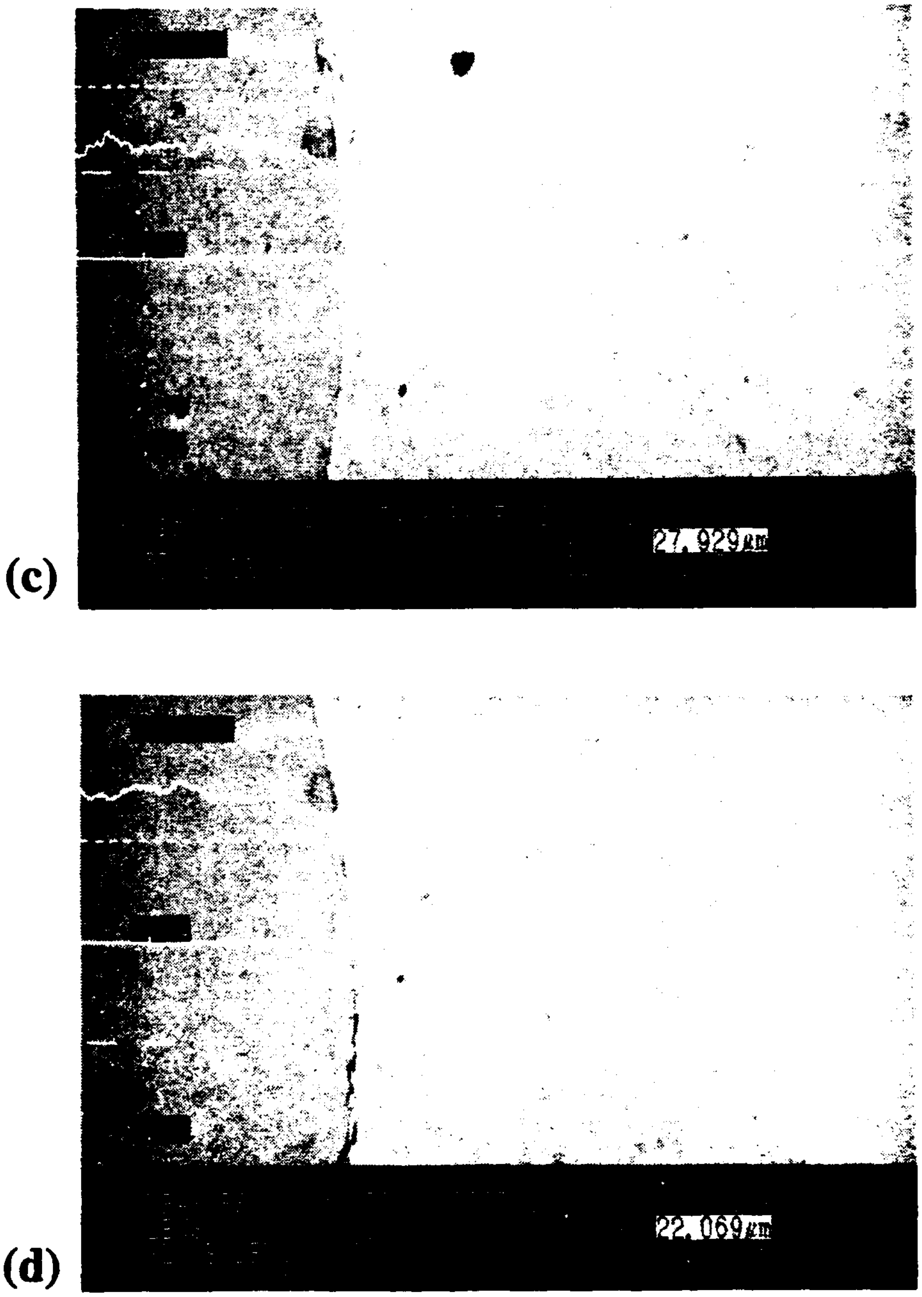
27.929µm
(c)
22.069µm
(d)

Figure 45. (cont.)

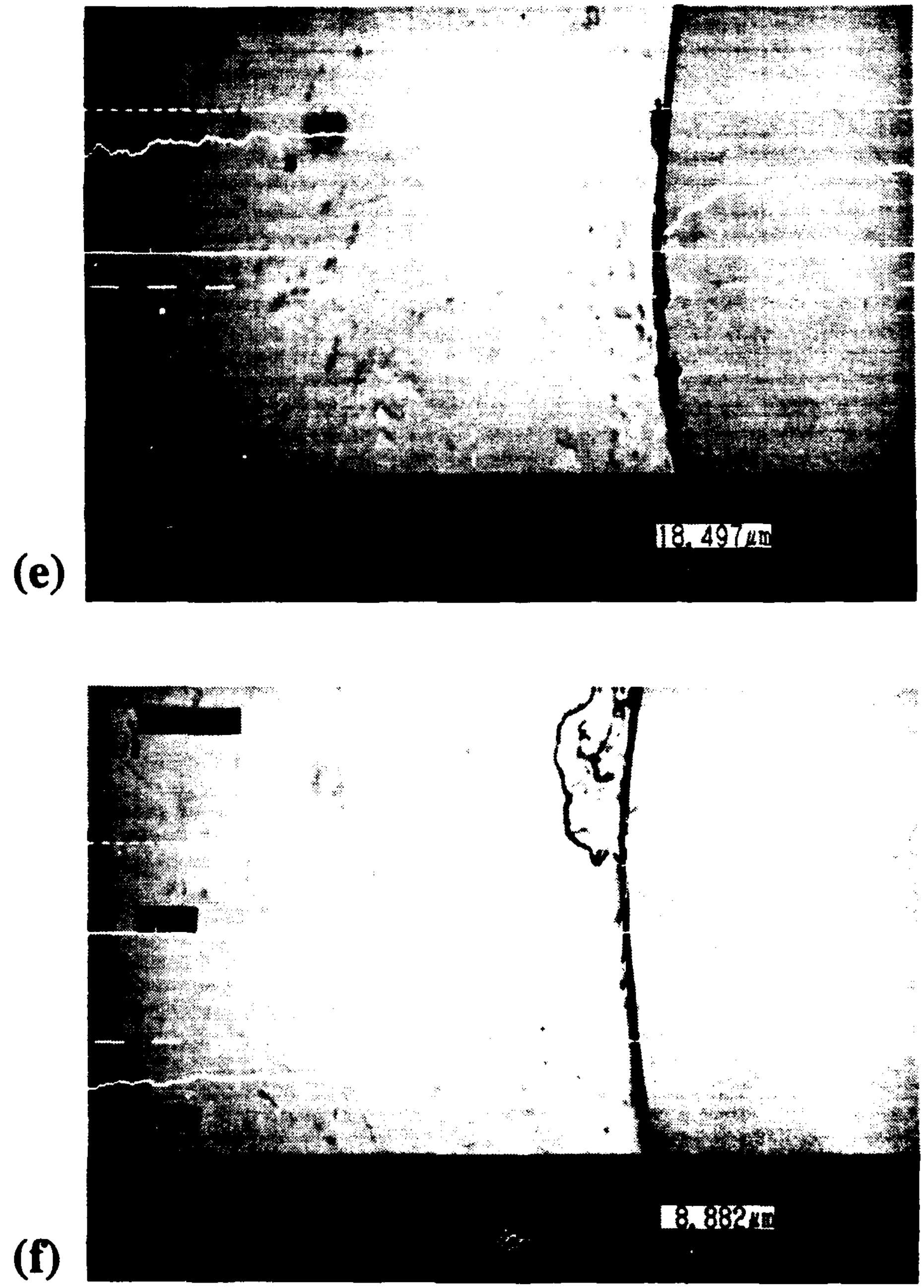
18.497μm
(e)
8.882μm
(f)

Figure 45. (cont.)

does not occur as shown in Figure 45c. In addition, a SLM surface profile measurement on the specimen's backface and at the same 3 o'clock fiber perimeter location also shows no fiber displacement (i.e., see Figure 45d), thus confirming that the fiber/matrix interface still remains bonded from back to topface, even near P_{max}. However, as shown in Figures 45e and f, surface profile measurements of top and backface fiber displacement at the 9 o'clock position on the perimeter of this same fiber suggest that the fiber is debonded along its entire length. A 0.88 μm displacement of the fiber topface below the matrix (i.e., shown in Figure 45e) and 1.31 μm displacement above the matrix on the backface (i.e., shown in Figure 45f) yields a 0.43 μm net fiber displacement. As will be shown in section 4.3.3, this net displacement is close to what is expected if the interface were to be debonded along its entire length, allowing both fiber and matrix to relax to their unconstrained lengths.

Finally, examination of the SLM micrographs of the Ta-coated sapphire/Ti-48-1 system shown in Figures 45c and d reveals that, during region 3 load-displacement behavior, permanent plastic deformation of the matrix occurs at both the specimen's top and backface in the region adjacent to that portion of the fiber's perimeter which remains bonded to the matrix up to P_{max}. This most likely results from the increased applied load and a reduced load-bearing ligament which acts to concentrate the shear stress (τ_{rz}) as well as the equivalent stress ($\overline{\sigma}$) components in a 23 to 47 μm wide strip of material adjacent to the bonded fiber/matrix interface [121] during region 3 load-displacement behavior. From several other SLM surface profile measurements of matrix deformation adjacent to the bonded interface ligament, an average shear strain (γ) in this strip of matrix at P_{max} was calculated using:

$$\gamma = \frac{\text{Depth}}{\text{Width}}, \tag{15}$$

where "depth" is the surface profile depth measurement and "width" is the width of the deformed strip of material (i.e., from the "width" measurements shown in Figures 45c and d). Measurements from 5 specimens' top and backfaces yield a plastic shear strain of approximately 0.03 within the strip of matrix adjacent to the bonded interface ligament.

The deformation of the matrix during region 3 load-displacement behavior occurs under increasing loads and increased debonding/crack growth along the interface. At maximum load, large-scale fiber displacement occurs. Examination of the specimen's topface following large-scale fiber displacement shows that, during interface shear in the remaining bonded ligament, the topface interfacial crack deviates into the fiber and leaves a bonded fiber fragment adhering to the matrix as shown in Figure 46. This observation was made in 4 out of 5 specimens and gives further evidence of the high bond strength/interfacial fracture resistance within the Ta-coated sapphire/Ti-48-1 system. As shown in Figure 42, large-scale fiber displacement is accompanied by a large load-drop as well as a large acoustic signal (region 4) followed by elastic re-loading and frictional fiber sliding (region 5). Immediately following load-drop the average fiber sliding stress in the Ta-coated sapphire/Ti-48-1 system was found to be 172.8 ± 58.2 MPa from 3 tests. The large load-drop indicates that a significant amount of elastic strain energy was required to propagate an interface crack and completely debond the interface. It also highlights the large difference in magnitude between the fiber/matrix debond stress ($\tau_{debond} = 336.3$ MPa) and fiber sliding stress ($\tau_{slide} = 172.8$ MPa) of the interface.

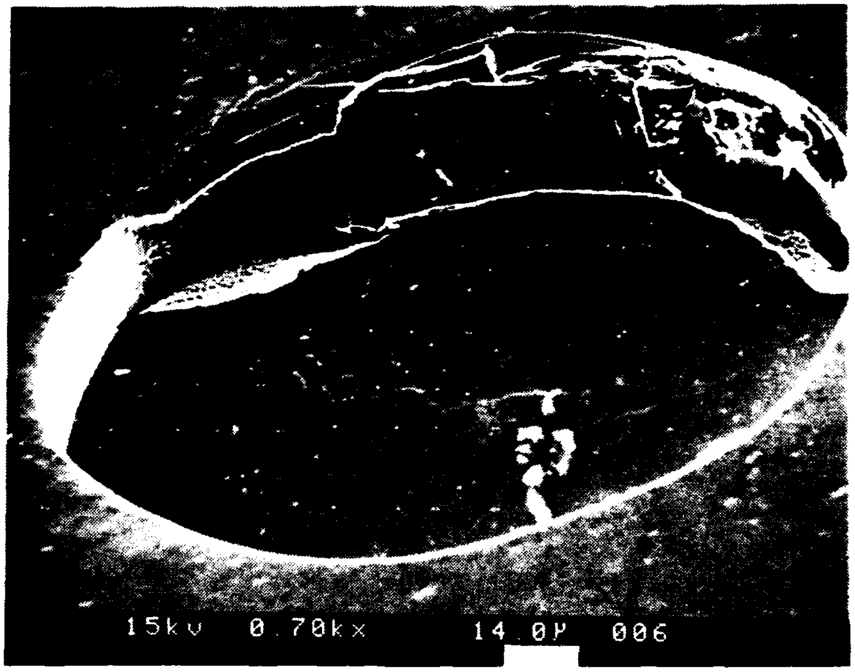

Figure 46. Evidence that the topface interfacial crack deviates into the fiber and leaves a bonded fiber fragment adhering to the matrix during interface shear in the remaining bonded ligament.

4.3.2.2. Interfacial Failure Sequence in the Sapphire/Ti-48Al-2Cr-2Nb System

Typical load versus cross-head displacement response of a 0.31 mm thick sapphire/Ti-48-2-2 specimen is shown in Figure 47. Again, the failure sequences can be divided into the same five similar regions as before, but with the following distinct differences. At a 15 N load, a circumferential interface crack initiates on the specimen's backface. This backface crack, however, quickly propagates around the fiber's entire perimeter (as indicated by SLM surface profile measurements of backface fiber displacement). This occurrence, coupled with the lower load required for backface crack initiation, indicates that a lower interfacial bond strength/fracture resistance exists in the sapphire Ti-48-2-2 system. Again, there was no evidence of an interfacial crack on the specimen's topface during region 2 load-displacement behavior. Reference to the overall interfacial stress distributions shown in Figure 41a (i.e., thermal cool-down of 780 °C and indenter load of 20 N) suggests that interfacial failure may occur by the initiation of either a mode I or mode II debond crack at the specimen's backface since both radial and shear stress components peak near the backface with approximately the same magnitude.

At P', or approximately 18 N (see Figure 47), the load-displacement plot deviates from linearity and is frequently accompanied by a slight (i.e., ≈1 N) load-drop. The average applied interfacial shear stress at P' was found to be 123.2 ± 10.5 MPa from 4 tests of the sapphire/Ti-48-2-2 system. At this load, a mode II circumferential interface crack initiates at the topface and quickly grows around the fiber's entire perimeter, leaving no bonded fiber/matrix ligament as in the Ta-coated sapphire/Ti-48-1 system. During the early stages of region 3 load-displacement behavior, the interface crack(s) subsequently propagate(s) along the entire interface, resulting in a totally debonded fiber. Again, this is verified by comparing the net fiber and matrix displacement found via SLM surface profile

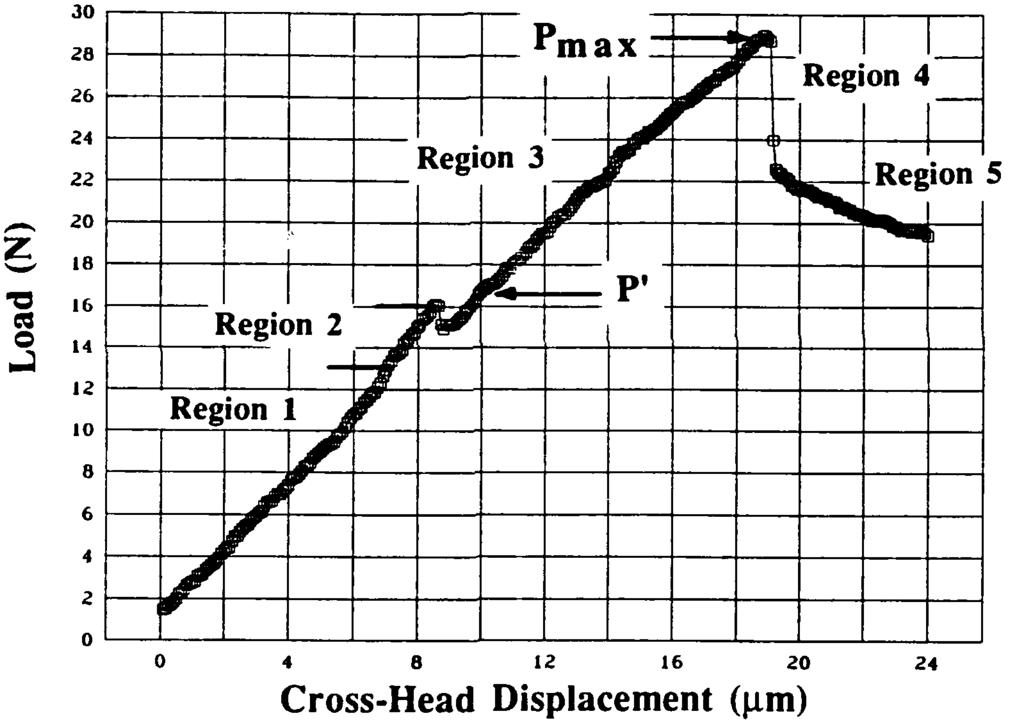

Figure 47. Typical load-displacement behavior of the sapphire/Ti-48Al-2Cr-2Nb system during fiber pushout testing.

measurements of the specimen's top and backface with what is expected if the interface were debonded along its entire length, allowing both fiber and matrix to relax to their unconstrained lengths (i.e., see section 4.3.3). Therefore, unlike the Ta-coated sapphire/Ti-48-1 system, region 3 load-displacement behavior in sapphire/Ti-48-2-2 occurs by stable fiber displacement (i.e., < 1.5 to 2.0 μm) of the debonded fiber with increasing load up to P_{max}.

Given the very rough fiber surface that results from severe fiber/matrix reaction during composite fabrication of this system (i.e., see Figure 25), it is postulated that fiber surface asperities lock the fiber in place, thus requiring plastic deformation of the matrix in the interfacial region before large-scale (i.e., > 1.5 to 2.0 μm) fiber displacement can take place. Reference to the overall interfacial stress distributions shown in Figure 41 suggests that, at the beginning of region 3 load-displacement behavior (i.e., when the applied indenter load = 20 N), the equivalent stress ($\overline{\sigma}$) is less than the matrix yield strength (i.e., $\sigma_y \approx 513$ MPa) along the entire interface. However, as the indenter load is increased to P_{max}, the equivalent stress increases along the entire interface to a point where matrix plasticity occurs and large-scale fiber displacement results. However, due to a weak interface bond and a lower load required for large-scale fiber displacement, matrix deformation does not occur in a strip of material (i.e., 20 to 40 μm wide) adjacent to the fiber as in the Ta-coated sapphire/Ti-48-1 system, but is localized to a layer of material (i.e., ≤ 1 μm wide) through which the rough fiber surface must be "plowed." As shown in Figure 48, examination of the matrix wall following fiber pushout shows that large-scale fiber displacement requires localized matrix plasticity in the form of grooves to accommodate asperities on the fiber surface.

Finally, as shown in Figure 47, large-scale fiber displacement is accompanied by little or no load-drop followed by frictional sliding of the fiber. Immediately following

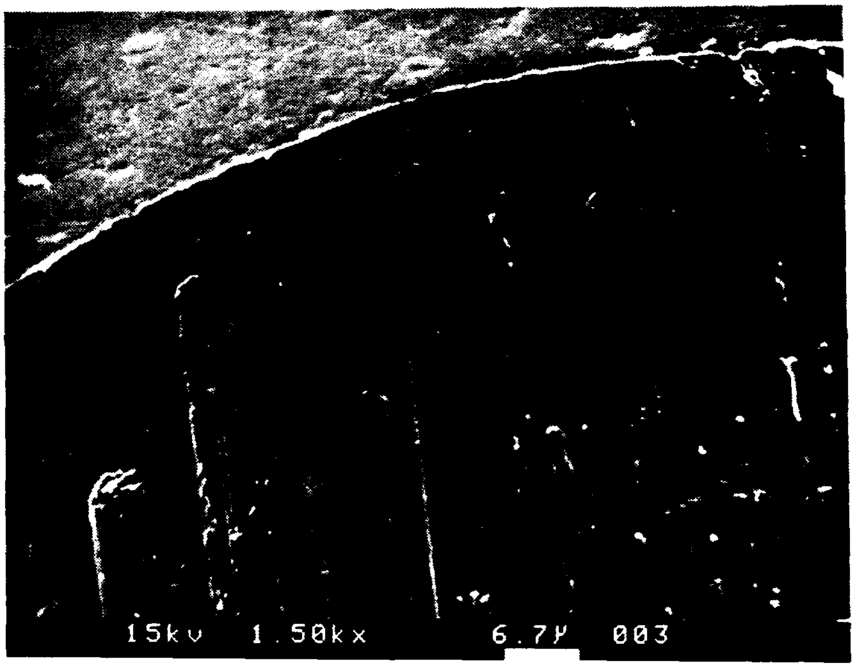

Figure 48. SEM micrograph of the topface of a sapphire/Ti-48Al-2Cr-2Nb specimen following fiber pushout shows that large-scale fiber displacement requires localized matrix plasticity to accommodate asperities on the fiber surface.

load-drop, the average fiber sliding stress was found to be 145.8 ± 9.5 MPa from 3 tests. The small load-drop indicates that only a small amount of elastic strain energy was stored in the fiber prior to failure. This gives further evidence that the fiber was debonded along its entire length prior to P_{max} and only held in place by mechanical interlocking with the matrix. The relatively small difference in magnitude between the fiber/matrix debond stress (τ_{debond} = 170.5 MPa) and the fiber sliding stress (τ_{slide} = 145.8 MPa) indicates that the transition from fiber debond to fiber sliding during interfacial shear is a nearly continuous process.

4.3.2.3. Comparison of Interfacial Failure Behaviors

The thin-slice fiber pushout test results for the Ta-coated sapphire/Ti-48-1 and sapphire/Ti-48-2-2 systems are summarized in Table 4. The markedly different interfacial failure behavior characterized during testing of these two composite systems can be explained in terms of differences in: (1) fiber/matrix chemical interaction during composite fabrication and (2) matrix plasticity in the interfacial region. In the Ta-coated sapphire/Ti-48-1 system, fiber/matrix chemical interaction results in a strong interfacial bond and

Table 4. Summary of the thin-slice fiber pushout test results for the Ta-coated sapphire/Ti-48Al-1V and sapphire/Ti-48Al-2Cr-2Nb systems. Test configuration was such that the support hole-to-fiber diameter ratio was ≈1.6. In all cases, ± one standard deviation is reported for 3 to 7 tests.

System	τ_{AVG} @ P'	τ_{AVG} @ P_{max}	τ_{slide}
Ta-coated sapphire/Ti-48Al-1V	311.9±22.1 MPa	336.3±11.2 MPa	172.8±58.2 MPa
Sapphire/Ti-48Al-2Cr-2Nb	123.2±10.5 MPa	170.5±22.3 MPa	145.8±9.5 MPa

relatively smooth fiber surface (i.e., see Figure 21). While in the sapphire/Ti-48-2-2 system, fiber/matrix chemical interaction results in a relatively weak interfacial bond and very rough fiber surface (i.e., see Figure 25).

Further evidence of little or no fiber/matrix chemical bonding in the sapphire/Ti-48-2-2 system is shown in Figure 49. Here it is shown that a piece of fiber fell out of the matrix (arrowed) when the sample was cut along the fiber axis. One possibility for the weak interfacial bond in the sapphire/Ti-48-2-2 system is that the organic binder mixed with the matrix during composite fabrication prevents fiber/matrix chemical bonding and, as a result, gives rise to the much lower measured interfacial shear strength in this system. Similar behavior was found in the sapphire-reinforced NiAl system by Bowman et al. [111, 112]. Using the fiber pushout test, they found that the sapphire/NiAl interface was "weak" (i.e., average interfacial shear strengths ranging from 20 to 80 MPa) when the matrix contained an organic binder during composite fabrication. However, when the composite was fabricated without an organic binder in the matrix, they found that the average interfacial shear strengths were significantly greater (i.e., > 250 MPa) [111]. The weak interface may be a result of carbon particles that Draper et al. [113] found to coat the sapphire fibers' surface following hot pressing in an organic binder-containing NiAl matrix. Although chemical microanalysis was not performed to verify the presence of carbon particles on the fiber's surface in the sapphire/Ti-48-2-2 system, it is feasible that, if carbon particles are present, they could prevent fiber/matrix chemical bonding yet result in a discrete interfacial reaction product (e.g., carbide precipitates) that leads to a rough fiber surface.

The yield strength and ductility of the material adjacent to the fiber as well as the amount of matrix plasticity required for large-scale fiber displacement appears to differ significantly in these two composite systems. Examination of the matrix wall following

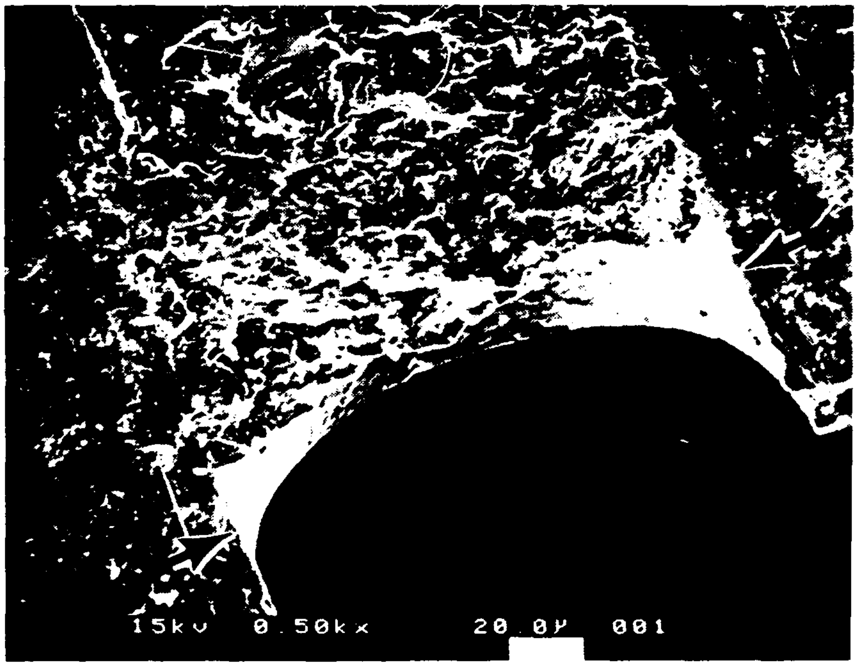
15kv 0.50kx 20.0µ 001

Figure 49. SEM micrograph of a sapphire/Ti-48Al-2Cr-2Nb specimen that was cut along a fiber axis. Note the hole that resulted when a piece of the fiber fell out of the matrix.

pushout of the Ta-coated sapphire/Ti-48-1 system (i.e., see Figure 50) shows that fiber displacement requires less matrix plasticity in the form of grooves to accommodate asperities on the fiber surface. This is probably due to: (1) a smoother fiber surface and (2) a 17 to 27% higher matrix hardness. Perhaps more significant is the presence of numerous interfacial cracks in the matrix shown in Figure 50 that suggest low ductility in this region. The high yield strength and low ductility of the Ti-48-1-matrix in the region adjacent to the fiber is probably a result of: (1) the high level of oxygen, nitrogen, and carbon contamination in the matrix (i.e., see Table 2) and (2) the presence of Ta-stabilized β-phase. Since the yield strength of β-Ti alloys can be approximately twice that of TiAl-based alloys, the yield strength of the strip of material (i.e., 1 to 3 μm wide) immediately adjacent to the fiber may be significantly higher than that of the rest of the matrix.

Further evidence that a considerable amount of localized matrix plasticity occurs during large-scale fiber displacement in the sapphire/Ti-48-2-2 system is shown by comparing Figures 51a and b. These SEM micrographs were taken of the matrix wall in samples where the fiber was pushed ≈100 μm out of the matrix and subsequently pushed ≈60 μm back in the reverse direction (i.e., the fiber was not pushed-back as far as its original position). Not only do these micrographs show that considerably more plastic grooving occurs in the sapphire/Ti-48-2-2 system (i.e., shown in Figure 51a) than in the Ta-coated sapphire/Ti-48-1 system (i.e., shown in Figure 51b), but they also give an indication of matrix ductility in the interfacial region. Close examination of Figures 51a and b reveals that, as the fiber was pushed back in the reverse direction, matrix material was plowed out in front of it, analogous to material plowed out in front of a cutting tool in a machining operation. The continuous ribbons of material plowed out of the Ti-48-2-2 matrix is characteristic of a ductile material (i.e., see Figure 51a). The discontinuous chips of Ti-48-1 material shown in Figure 51b, however, are characteristic of brittle materials

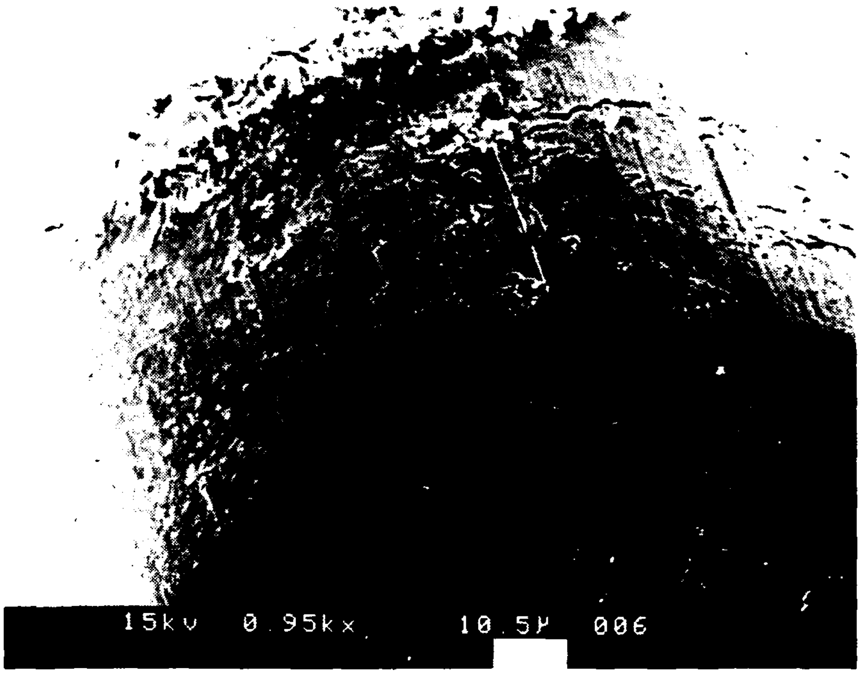

Figure 50. Evidence of less plastic grooving and the occurrence of numerous interfacial cracks in the matrix following fiber pushout testing of a Ta-coated sapphire/Ti-48Al-1V specimen.

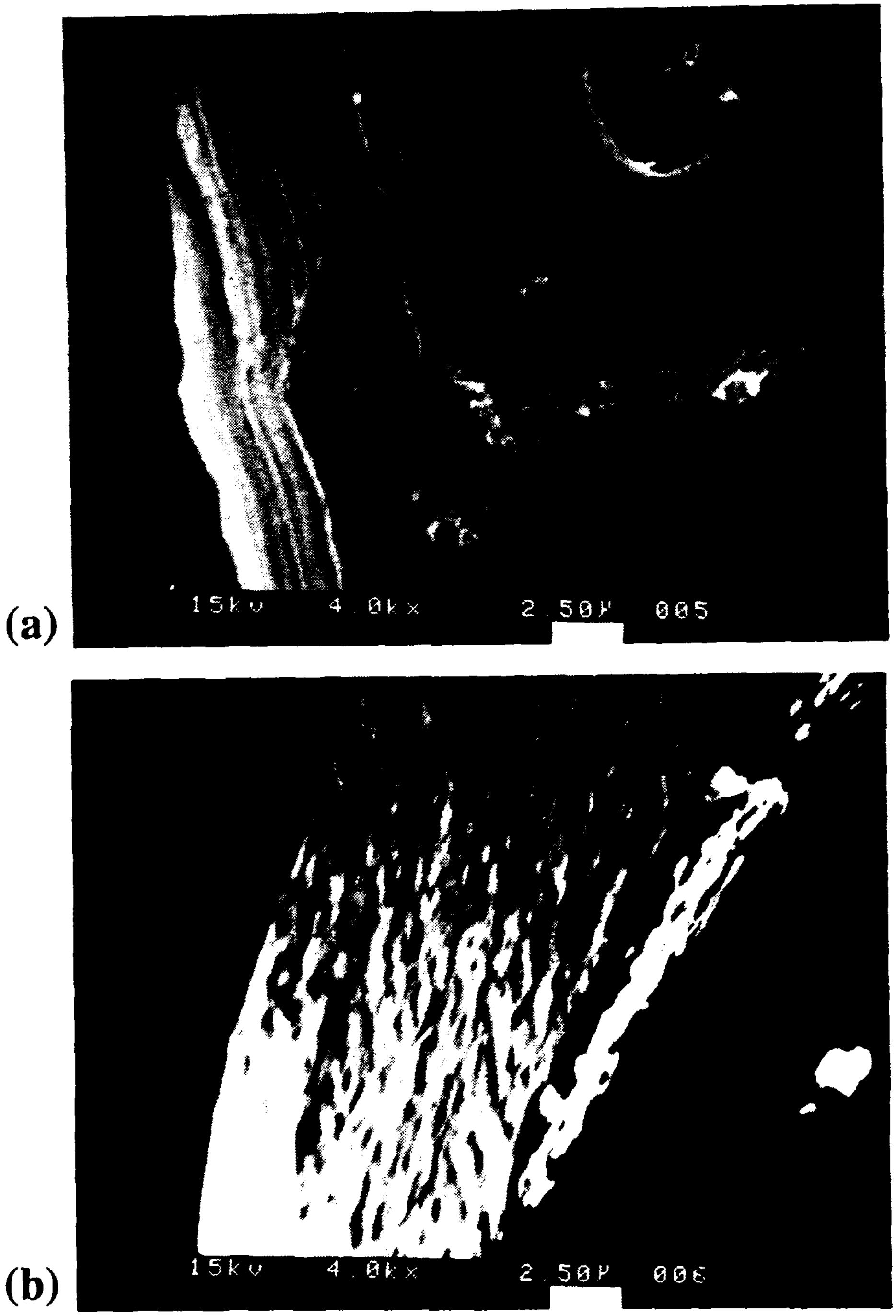
(a)
15kv 4.0kx 2.50µ 005
(b)
15kv 4.0kx 2.50µ 006

Figure 51. Comparison of the amount of matrix plasticity that occurs during fiber pushout and push-back testing of: (a) sapphire/Ti-48Al-2Cr-2Nb and (b) Ta-coated sapphire/Ti-48Al-1V.

which cannot withstand the high shear strains imposed in a machining process without fracture [122].

Examination of the fiber surface following pushout testing of a sapphire/Ti-48-2-2 specimen shown in Figure 52a gives further evidence of the important role of matrix plastic deformation during interfacial shear failure. Comparison of this micrograph with the appearance of the fiber surface following hot pressing in the matrix and subsequent chemical removal (i.e., see Figure 25) suggests that fiber surface asperities remove matrix material from the interface during fiber pushout. However, microanalysis of the fiber surface was not performed to confirm this observation. In contrast, the appearance, as well as energy-dispersive x-ray microanalysis, of the sapphire/Ti-48-1 specimen (shown in Figure 52b) reveals that very little matrix material remains on the fiber during interfacial shear.

In Figures 52a and b, it is also significant to compare the magnitude of mode I crack opening displacement that occurs on the backface of these two specimens. Since significantly higher indenter loads (i.e., ≈2 times greater) are required to cause interfacial failure in the Ta-coated sapphire/Ti-48-1 system, much larger tensile bending stresses develop on the specimen's backface resulting in a mode I circumferential crack opening displacement as shown in Figure 52b. On the other hand, interfacial failure in the sapphire/Ti-48-2-2 system may occur by the initiation of either a mode I or mode II debond crack on the specimen's backface since the magnitude of both radial and shear components are approximately equal at the lower indenter loads required for crack initiation (i.e., see Figure 41a). Indeed, very little or no circumferential crack-opening displacement is visible at the fiber/matrix interface shown in Figure 52a.

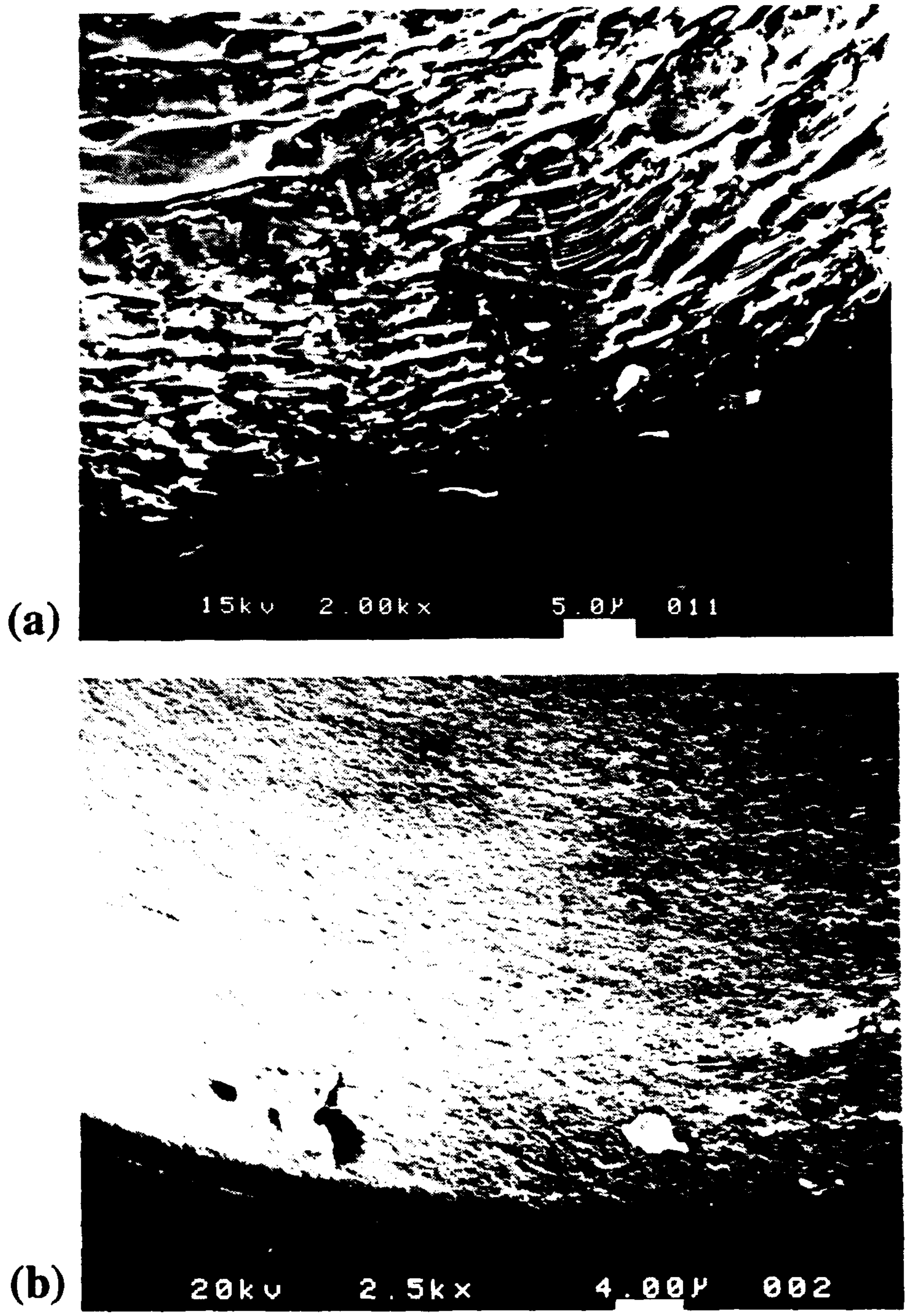
(a)
15kv 2.00kx 5.0µ 011
(b)
20kv 2.5kx 4.00µ 002

Figure 52. The backface of fiber pushout specimens showing the fiber surface following testing. (a) Sapphire/Ti-48Al-2Cr-2Nb and (b) Ta-coated sapphire/Ti-48Al-1V systems.

4.3.3. Analysis of Top and Backface Fiber Displacement Measurements

As discussed in the previous section, SLM surface profile measurements of fiber displacement at incremental loads up to complete fiber debond prove to be very important in characterizing the interfacial failure sequence during thin-slice fiber pushout testing. As shown in the previous sections, these measurements establish both the load and the location at which interface cracks initiate. As will be shown in this section, these measurements also (1) support the scale of the FEM-predicted thermally-induced residual stress states in the fiber and matrix and (2) allow quantitative estimates of the debond crack length.

Following each interrupted pushout test (i.e., a test that was stopped before load-drop/large-scale fiber displacement occurred), very accurate measurements of fiber displacement with respect to the matrix on the specimen's top (δ_T) and backface (δ_B) were obtained using the 1LM11 Scanning Laser Microscope (see section 3.6). These displacements are shown schematically in Figure 53, and their measurements are given as a function of average applied interfacial shear stress in Tables 5 and 6 for the Ta-coated sapphire/Ti-48-1 and sapphire/Ti-48-2-2 systems respectively. In Tables 5 and 6 results are shown from fiber pushout tests that used a 254 μm diameter support hole and a hole the same size and shape as the fiber's cross-section (i.e., via electroplating nickel onto the specimen's backface). In this section, attention is given to the results from tests that used the 254 μm diameter support hole. In the following section, results from tests using the second type of specimen support configuration will be examined.

First, it is important to note that the net fiber displacement measured with respect to the matrix (δ) is due to contributions from both the fiber and the matrix relaxing to their unconstrained lengths over the debonded region of length ℓ (i.e., u_{zz}^{f} and u_{zz}^{m} shown in Figure 53). Next, in order to give quantitative meaning to the displacement measurements,

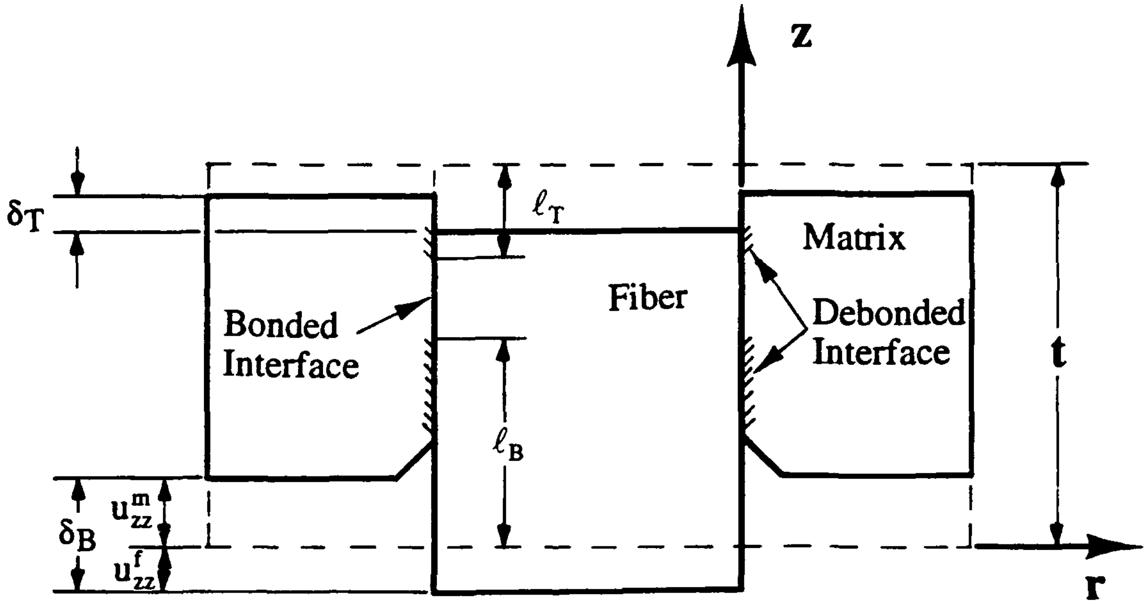
z
δT
ℓT
Matrix
Fiber
Bonded Interface
Debonded Interface
t
ℓB
δB
u^m_zz
u^f_zz
r

Figure 53. Schematic illustration of a thin-slice fiber pushout specimen following a test that was stopped prior to load-drop/large-scale fiber displacement. The displacements (δ_B and δ_T) of the partially debonded fiber are exaggerated relative to the specimen's thickness in order to add emphasis.

Table 5. Fiber displacement measurements (made with respect to the matrix) as a function of average applied interfacial shear stress (τ_{AVG}) during pushout testing of the Ta-coated sapphire/Ti-48Al-1V system. Measurements were made at 3, 6, 9, and 12 o'clock positions around the perimeter of the fiber. (cont. on next page)

Tests conducted with a 254 μm diameter support hole

Sample #	Applied τ_{AVG} (MPa)	Topface Displacement δ_T (μm)	Backface Displacement δ_B (μm)
13	230.3	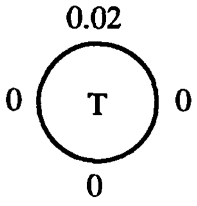	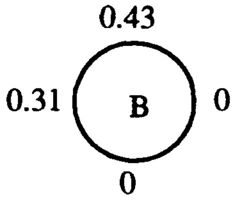
13	318.8	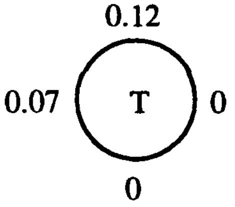	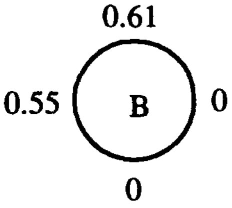
13	338.3	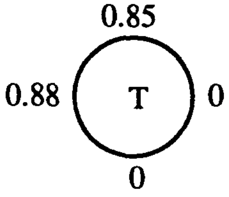	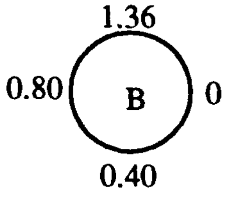 1.36 0.80 B 0 0.40
17	224.2	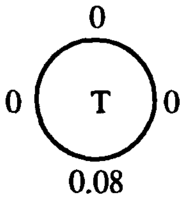	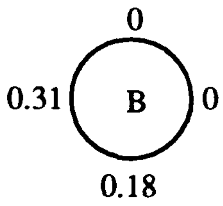
17	258.9	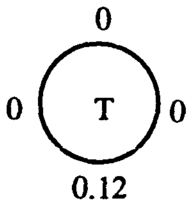	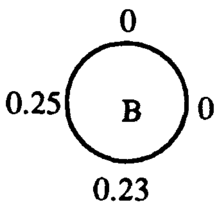

Table 5. (cont.)

Tests conducted with a 254 μm diameter support hole

Sample #	Applied τ_{AVG} (MPa)	Topface Displacement δ_T (μm)	Backface Displacement δ_B (μm)
12	305.0	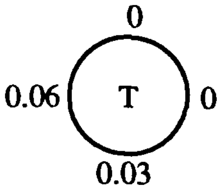	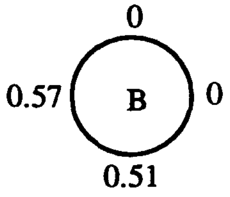
16	307.2	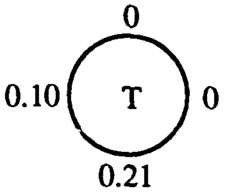	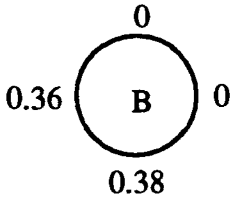

Tests conducted with a nickel back-plate

Sample #	Applied τ_{AVG} (MPa)	Topface Displacement δ_T (μm)	Backface Displacement δ_B (μm)
30	279.0	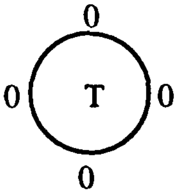	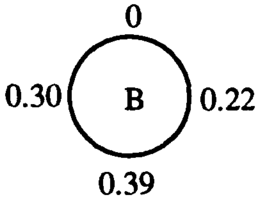 0 0.30 B 0.22 0.39

Table 6. Fiber displacement measurements (made with respect to the matrix) as a function of average applied interfacial shear stress (τ_{AVG}) during pushout testing of the sapphire/Ti-48Al-2Cr-2Nb system. Measurements were made at 3, 6, 9, and 12 o'clock positions around the perimeter of the fiber. (cont. on next page)

Tests conducted with a 254 μm diameter support hole

Applied τ_{AVG} (MPa)	Topface Displacement δ_T (μm)	Backface Displacement δ_B (μm)
80.0	0 0 T 0 0	0 0 B 0 0
97.3	0 0 T 0 0	0.18 0.23 B 0 0.18
133.3	1.06 1.04 T 1.05 1.07	1.39 1.23 B 1.49 1.42
155.5	0.69 0.74 T 0.83 0.66	1.19 1.04 B 1.19 1.11

Table 6. (cont.)

Tests conducted with a nickel back-plate		
Applied τ_{AVG} (MPa)	Topface Displacement δ_T (μm)	Backface Displacement δ_B (μm)
78.8	0 0 T 0 0	0 0 B 0 0
101.5	0 0 T 0 0.05	0.42 0.24 B 0.25 0
123.4	0 0.02 T 0 0	0.31 0.37 B 0.44 0.32
141.6	0.54 0.51 T 0.57 0.55	1.07 0.85 B 0.99 0.85
152.9	0.62 0.48 T 0.61 0.65	1.30 1.08 B 1.22 0.79

an expression that relates the net fiber displacement (δ) to the debond crack length (ℓ) is required. As a starting point, the generalized form of Hooke's law can be used to express the axial strain in the fiber (ε^f_{zz}) as:

$$\varepsilon^f_{zz} = \frac{1}{E^f}\left[\sigma^f_{zz} - \nu^f\left(\sigma^f_{rr} + \sigma^f_{\theta\theta}\right)\right], \tag{16}$$

where E^f (= 351 GPa) and v^f (= 0.3) are the fiber's elastic modulus and Poisson's ratio respectively [32]; and σ^f_{zz}, σ^f_{rr} and $\sigma^f_{\theta\theta}$ are the thermally-induced residual stress components within the fiber. By substituting the definition of normal strain:

$$\varepsilon^f_{zz} = \frac{\partial\, u^f_{zz}}{\partial z}, \tag{17}$$

into equation (16) and rearranging, a simple expression relating axial fiber displacement (u^f_{zz}) to the debond crack length (ℓ) is obtained:

$$u^f_{zz} = \int_0^\ell du^f_{zz} = \frac{1}{E^f}\left[\sigma^f_{zz} - \nu^f\left(\sigma^f_{rr} + \sigma^f_{\theta\theta}\right)\right]\int_0^\ell dz, \tag{18}$$

$$u^f_{zz} = \frac{\ell}{E^f}\left[\sigma^f_{zz} - \nu^f\left(\sigma^f_{rr} + \sigma^f_{\theta\theta}\right)\right]. \tag{19}$$

It is important to note that equation (19) gives axial fiber displacement for the case where all three residual stress components within the fiber are relaxed over its debonded length. However, it is expected that the matrix surrounding the debonded length of fiber will constrain the transverse stress components, σ_{rr}^{f} and $\sigma_{\theta\theta}^{f}$, from fully relaxing. In fact, the only portion of the debonded length of fiber where all three stress components may fully relax is that length at the specimen's backface which extends out of the matrix and is not in physical contact with the matrix due to the presence of a mode I crack. Given the small measured displacements (i.e., $\delta < 1.5\ \mu m$) in Tables 5 and 6, it is reasonable to assume that this portion of the debonded length is negligible in comparison to the entire debonded length of fiber. Therefore, assuming that only the axial residual stress component (σ_{zz}^{f}) may relax over the debonded length of fiber, equation (19) reduces to:

$$u_{zz}^{f} = \frac{\ell}{E^{f}}\sigma_{zz}^{f}. \tag{20}$$

In addition, for a debond crack of length ℓ, a similar expression for axial matrix displacement (u_{zz}^{m}) is given by:

$$u_{zz}^{m} = \frac{\ell}{E^{m}}\sigma_{zz}^{m}, \tag{21}$$

where E^{m} (= 174 GPa [26]) and ν^{m} (= 0.3 [28]) are the matrix's elastic modulus and Poisson's ratio respectively.

The interfacial failure sequences described in section 4.3.2 reveals that interfacial failure initiates at the specimen's backface in both the Ta-coated sapphire/Ti-48-1 and sapphire/Ti-48-2-2 systems. Furthermore, during region 2 load-displacement behavior, the backface crack subsequently propagates up along the fiber/matrix interface before shear displacement occurs at the topface. Therefore, it is of special interest to estimate the length of the backface debond crack during region 2 load-displacement behavior. An expression that relates the net measured backface displacement (δ_B) to the corresponding debond crack length (ℓ_B) is given by the sum of equations (20) and (21):

$$\delta_B = \ell_B\left(\frac{\sigma_{zz}^f}{E^f}+\frac{\sigma_{zz}^m}{E^m}\right). \tag{22}$$

For several reasons, however, equation (22) is an inaccurate description of the relationship between the measured value of δ_B (from Tables 5 and 6) and the predicted backface debond crack length (ℓ_B). First, the thermally-induced residual stress component (σ_{ZZ}) is not constant, but is a function of distance (z) along the fiber/matrix interface (e.g., see Figure 39). Perhaps more importantly, however, is that equation (22) fails to consider "frictional" resistance to fiber displacement along the debonded interface. Given the degree of radial clamping and fiber surface roughness in these composite systems, Coulomb friction and fiber/matrix mechanical interlocking must be considered. As a result, the axial residual stress components (σ_{ZZ}) within the fiber and matrix cannot fully relax along the debonded interface. Finally, consideration must also be given to the fiber displacement that occurs on the backface while the indenter load is applied during testing. As the mechanical load is applied to the fiber's topface, fiber/matrix interface debonding and subsequent fiber displacement occurs at the specimen's backface as a consequence of the combined mechanical and thermal stress state. During unloading, some fiber displacement occurs in the reverse direction. If a frictionless interface is assumed, the net backface displacement measured after the load is removed should be a result of only thermal stress relaxation (in both the fiber and matrix) over the debonded interface. On the other hand, "frictional" resistance to fiber sliding during unloading will result in a measured net displacement that includes a contribution from the mechanical stress after the load is removed.

Since the magnitude of the "frictional" resistance to fiber sliding is unknown and since it governs the amount of net backface displacement, rigorous predictions of the backface debond crack length (ℓ_B) are impossible. However, quantitative estimates can be made using equation (22) assuming (1) no "frictional" resistance to fiber sliding, (2) the values of the thermally-induced residual stress components (σ_{zz}) within the fiber and the matrix are independent of position along the interface, and (3) both fiber and matrix are elastically isotropic.

If ℓ_B is set equal to the specimen thickness (t) and the average FEM predicted, axial residual stress components (σ_{zz}) within the fiber and matrix[n] are substituted into equation (22), an estimate of the net axial fiber/matrix displacement can be made for the situation where the fiber is debonded along its entire length. In Figures 54 and 55, this estimate is compared with the value of δ_B - δ_T from SLM displacement measurements made during interrupted pushout tests (i.e., see Tables 5 and 6). (Note that the measurements plotted in Figures 54 and 55 are plotted from tests that were performed using a support hole and a nickel back-plated configuration, respectively.) The difference between the back and topface displacement measurements, i.e., the value of δ_B - δ_T, is the measured net displacement that both the fiber and the matrix undergo as they relax to their unconstrained lengths along the debonded interface (i.e., see Figure 53). Comparison of the estimated with the measured net displacement values also supports the scale of the FEM predicted stress state. For example, as shown in Figure 54, the δ_B - δ_T value for a fiber

---

[n] The average thermally-induced, axial residual stress components (σ_{zz}) within the fiber and the matrix adjacent to the fiber for a sapphire-reinforced TiAl composite with a 0.1 fiber volume fraction were predicted to be 235.7 MPa (compression) and 105.8 MPa (tension), respectively, by Kallas [84].

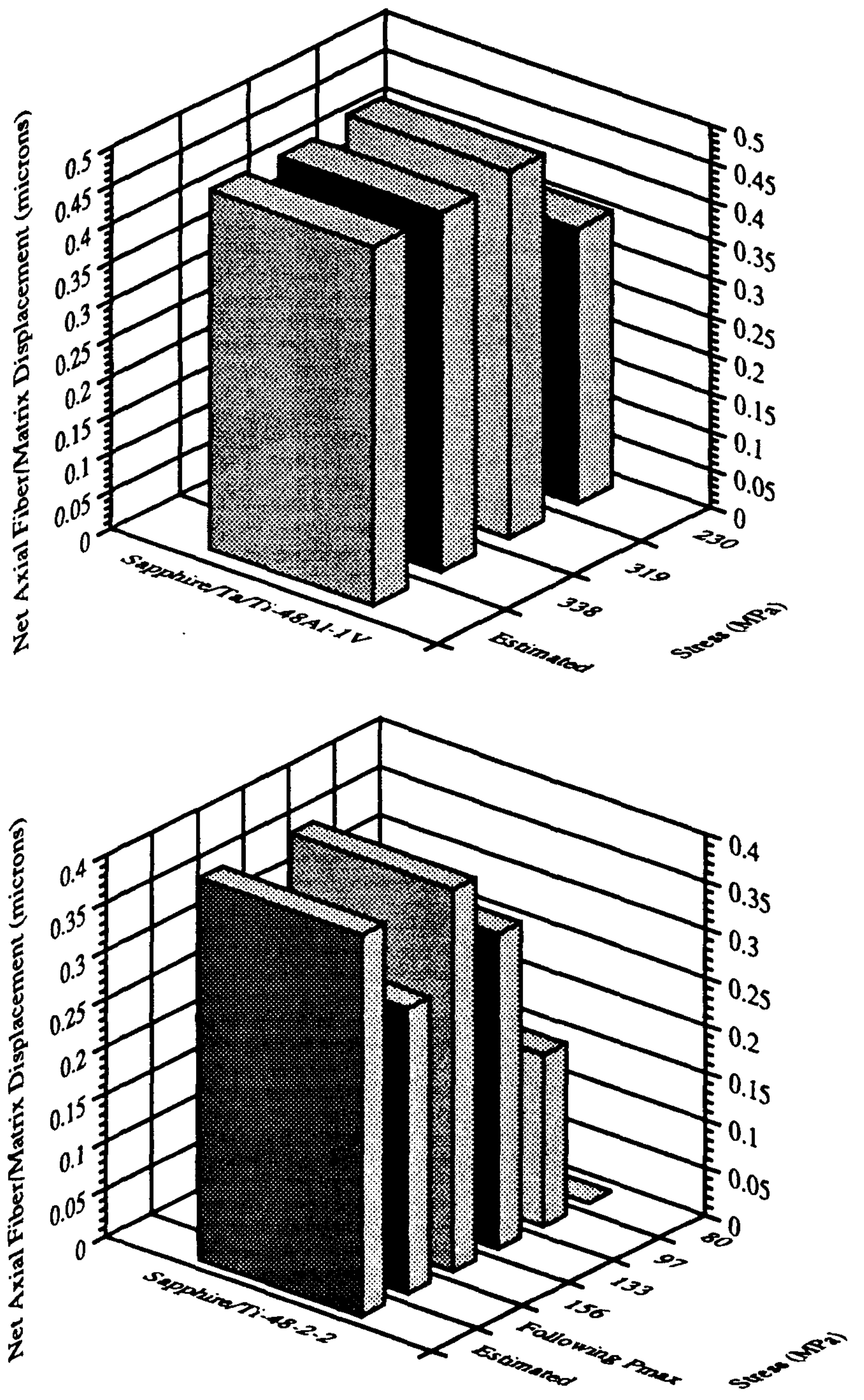

Figure 54. Net axial fiber/matrix displacement measurements (i.e., the differences between δ_B and δ_T given in Tables 5 and 6) as a function of average interfacial shear stress applied during interrupted pushout tests performed using a support hole configuration. For comparison, an estimate of net displacement is shown for the situation where the fiber is debonded along its entire length.

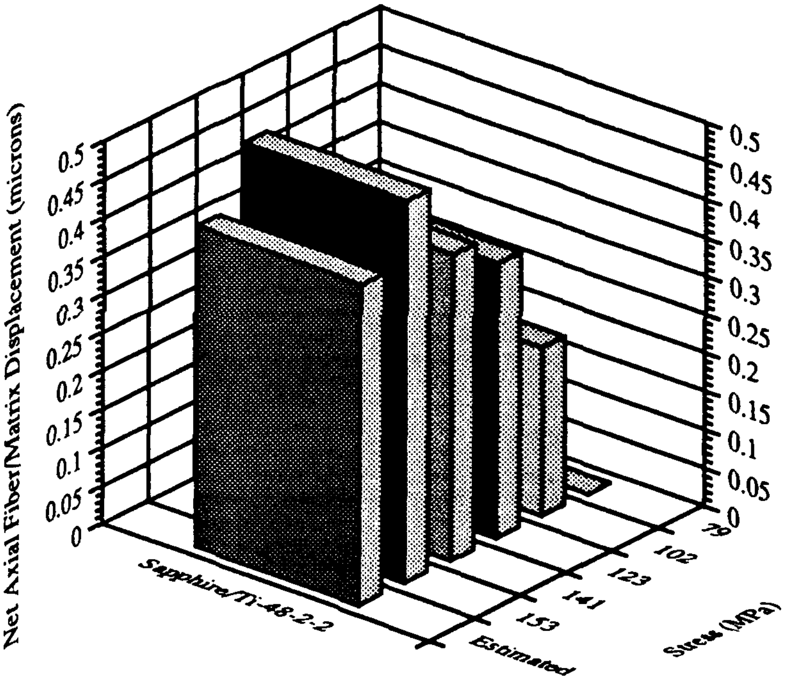

Figure 55. Net axial fiber/matrix displacement measurements (i.e., the differences between δ_B and δ_T given in Tables 5 and 6) as a function of average interfacial shear stress applied during interrupted pushout tests performed using a nickel back-plated configuration. For comparison, an estimate of net displacement is shown for the situation where the fiber is debonded along its entire length.

tested beyond P_{max} (i.e., a fiber that must be debonded along its entire length) in the sapphire/Ti-48-2-2 system closely agrees with the estimated value.

For the Ta-coated sapphire/Ti-48-1 system, only the net displacement measurements made at fiber perimeter positions where the interface was debonded are plotted in Figure 54. The remaining interface ligament appears to remain bonded from the back to the topface up to loads approaching P_{max} as indicated by the absence of displacement at these perimeter positions (i.e., see Table 5 and section 4.3.2.1). For the Ta-coated sapphire/Ti-48-1 system, Figure 54 reveals that the measured net fiber/matrix displacement remains constant and equals the estimated net displacement for a fiber debonded along its entire length ($\approx$0.47 µm) at loads greater than P' (i.e., at P', $\tau_{AVG} \approx$ 312 MPa for the Ta-coated sapphire/Ti-48-1 system). This suggests that, at loads greater than P', fibers are debonded along their entire length, but only around 50 to 60% of their perimeter in the Ta-coated sapphire/Ti-48-1 system. Similarly, for the sapphire/Ti-48-2-2 system, a comparison of the net estimated fiber/matrix displacement for a fiber debonded along its entire length ($\approx$0.40 µm) with the measured net displacement (see Figure 54) suggests that fibers are debonded along their entire length at loads greater than P' (i.e., $\tau_{AVG} \approx$ 123 MPa for the sapphire/Ti-48-2-2 system). Unlike the Ta-coated sapphire/Ti-48-1 system, however, the fiber is completely debonded around its entire perimeter in sapphire/Ti-48-2-2 at loads greater than P'.

For tests using the nickel back-plated support configuration, examination of Figure 55 suggests that fibers within the sapphire/Ti-48-2-2 system are also debonded along their entire length at loads greater than P' (where τ_{AVG} at P' is $\approx$125 MPa). This result will be discussed further in the next section. Since only one interrupted pushout test using the nickel back-plate support configuration was performed on the Ta-coated sapphire/Ti-48-1 system, the results are not shown in Figure 55.

Furthermore, making the assumptions previously mentioned (i.e., no "frictional" resistance to fiber sliding), quantitative estimates of backface debond crack length can be made by substituting the average FEM predicted, axial residual stress components (σ_{zz}) within the fiber and matrix (i.e., see footnote n), and solving for ℓ_B in equation (22). The purpose here is to estimate backface crack lengths before shear displacement occurs on the topface which signals the onset of complete interface debonding (but only around 50 to 60% of the fiber's perimeter in the Ta-coated sapphire/Ti-48-1 system). Therefore, these estimates are based on the backface displacement measurements given in Tables 5 and 6 for average applied interface shear stress levels corresponding to indenter loads less than P'.

Backface debond crack length estimates, normalized with respect to specimen thickness (i.e., ℓ_B/t), are given in Tables 7 and 8 as a function of average applied interfacial shear stress for the Ta-coated sapphire/Ti-48-1 and sapphire/Ti-48-2-2 systems respectively. For both composite systems, the estimates suggest that the backface debond crack may propagate over half of the total distance up along the fiber/matrix interface before a mode II crack initiates on the topface. However, due to the oversimplified assumption of no "frictional" resistance to fiber sliding used in evaluating equation (22), these estimates must be regarded with caution. Regardless, crack propagation up from the backface in turn increases the shear stress within the bonded ligament that remains between the debond crack tip and specimen's topface. This is a result of the crack tip stress field as well as the decreased ligament length. As a result, a mode II debond crack subsequently initiates at the specimen's topface near the indenter.

Table 7. Normalized backface debond crack length (l_B/t) estimates as a function of average applied interfacial shear stress (τ_{AVG}) during region 2 load-displacement behavior of the Ta-coated sapphire/Ti-48Al-1V system. (Estimates were made at 3, 6, 9, and 12 o'clock positions around the perimeter of the fiber.)

Tests conducted with a 254 μm diameter support hole

Sample #	Applied τ_{AVG} (MPa)	Normalized crack length (ℓ_B/t)
13	230.3	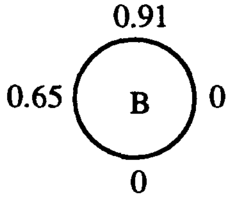
17	224.2	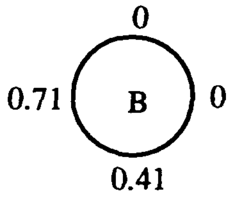
17	258.9	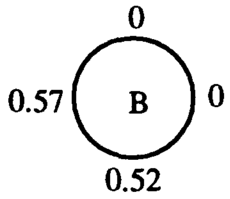
16	307.2	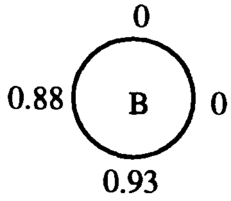

Tests conducted with a nickel back-plate

Sample #	Applied τ_{AVG} (MPa)	Normalized crack length (ℓ_B/t)
30	279.0	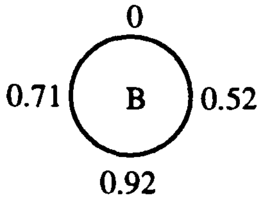

Table 8. Normalized backface debond crack length (l_B/t) estimates as a function of average applied interfacial shear stress (τ_{AVG}) during region 2 load-displacement behavior of the sapphire/Ti-48Al-2Cr-2Nb system. (Estimates were made at 3, 6, 9, and 12 o'clock positions around the perimeter of the fiber.)

Tests conducted with a 254 μm diameter support hole

Applied τ_{AVG} (MPa)	Normalized crack length (ℓ_B/t)
80.0	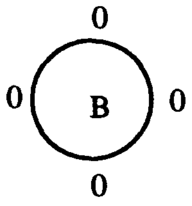
97.3	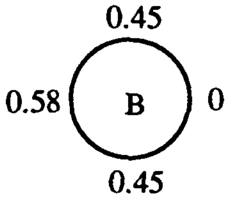

Tests conducted with a nickel back-plate

Applied τ_{AVG} (MPa)	Normalized crack length (ℓ_B/t)
78.8	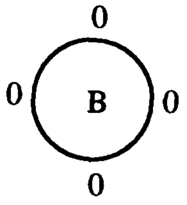
101.5	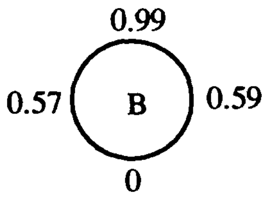
123.4	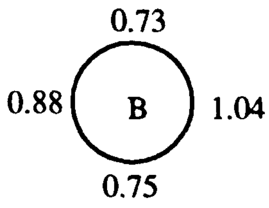

4.3.4. Influence of Specimen Bending on Interface Shear Behavior during Thin-Slice Pushout Testing

It has been suggested that interface shear behavior during thin-slice pushout testing is likely to be particularly sensitive to the distribution of both radial and shear stress components along the the fiber/matrix interface [105]. Consequently, radial stresses induced by specimen bending may influence: (1) the sequences leading to interfacial failure and (2) the measured interfacial shear strength value.

Results reported in section 4.3.2 were from pushout tests performed using a support hole-to-fiber diameter ratio of ≈1.6. Although this ratio is smaller than what is typically used by other researchers (i.e., typically ≥2), large radial tensile stresses can still develop on the specimen's backface due to specimen bending as indicated by FEM computations shown in Figure 40b. Thus, it is possible that the large radial tensile stresses may initiate mixed mode I/II interface cracks on the specimen's backface [68]. As a result, the measured interfacial shear strength values may be influenced by the magnitude of the bending-induced stresses. Unfortunately, the magnitude of the bending stresses depends not only on specimen configuration (i.e., specimen thickness and support hole-to-fiber diameter ratio) but also on the applied load, which in turn is sensitive to the interfacial shear strength of the composite system [105].

Since it is possible that specimen bending during thin-slice pushout testing may create failure sequences that are unique to a specific test configuration and, as a result, complicate the observed results, a more accurate test is one that eliminates specimen bending [68]. In this research program, this was accomplished through a nickel (Ni) electroplating procedure [105] that produces a support hole exactly the same size and shape as the fiber's cross-section. Experimental evidence that suggests that the Ni "back-plating" procedure is successful in eliminating specimen bending is shown in Figure 56. In both Figures 56a and b, the backface of Ta-coated sapphire/Ti-48-1 specimens are shown following large-scale fiber displacement. Since high indenter loads are required to cause interfacial failure in this system, large tensile stresses develop on the specimen's backface when supported over the 254 μm diameter hole, thus the ≈1 μm-wide, mode I, crack opening displacement observed in Figure 56a results. However, when supported over a hole exactly the same size and shape as the fiber's cross-section (i.e., via Ni back-plating), no observable mode I crack opening displacement occurs (Figure 56b).

A comparison of the measured interfacial shear strengths (i.e., average values) at P' and P_{max} from thin-slice specimens supported over a 254 μm diameter hole and a hole exactly the same size and shape as the fiber's cross-section is shown in Table 9. The significant difference between these two test configurations is the elimination of bending-induced tensile stresses on the specimen's backface when supported by a Ni back-plate. Reference to the measured values of τ_{AVG} at P' and P_{max} for the Ta-coated sapphire/Ti-48-1 system indicates that eliminating bending-induced tensile stresses actually lowers these values, especially at P'. This is an unexpected result since bending-induced stresses

Table 9. Effect of test configuration: comparison of results with (i.e., use of a support hole-to-fiber diameter ratio of ≈1.6) and without (i.e., use of a Ni back-plate) specimen bending. In all cases, ± one standard deviation is reported for the number of tests shown in parentheses.

	Sapphire/Ti-48Al-2Cr-2Nb		Ta-coated sapphire/Ti-48Al-1V	
	Support hole	Ni plate	Support hole	Ni plate
τ_{AVG} at P' (MPa)	123 ± 10 (4)	125 ± 16 (6)	312 ± 22 (7)	240 ± 30 (4)
τ_{AVG} at P_{max} (MPa)	170 ± 22 (3)	166 ±17 (4)	336 ± 11 (5)	294 ± 14 (3)

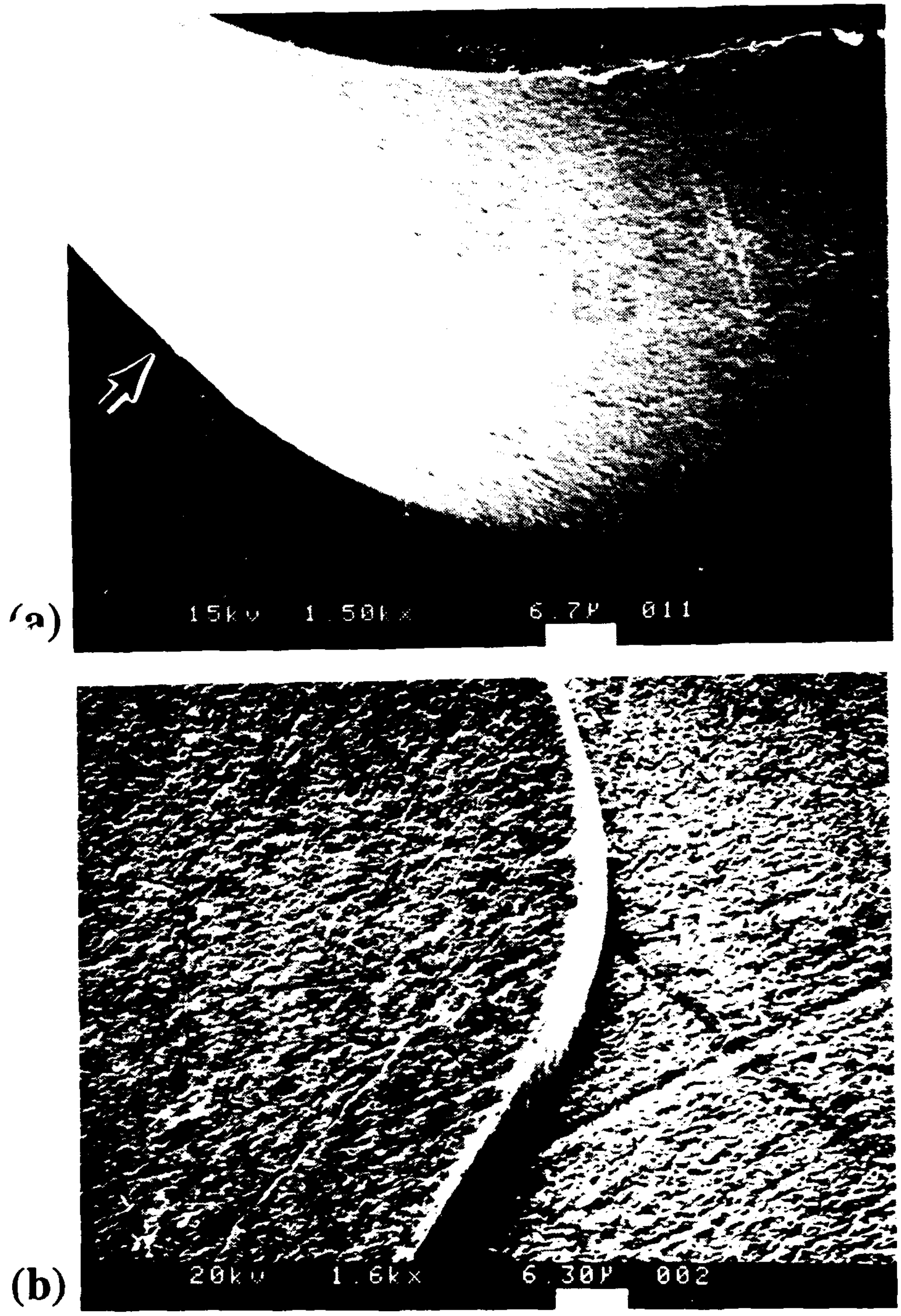
(a)
15kV 1.50kx 6.7μ 011
(b)
20kV 1.6kx 6.30μ 002

Figure 56. The fiber/matrix interface on the backface of Ta-coated sapphire/Ti-48Al-1V specimens following large-scale fiber displacement. Specimens were supported over (a) a 254 μm diameter hole and (b) a hole exactly the same size and shape as the fiber's cross-section.

at the backface are believed to initiate fiber/matrix failure by mixed-mode crack growth. Therefore, it has been proposed that eliminating specimen bending and backface mode I cracking should increase the loads necessary for interfacial shear [68].

In addition, limited experimental evidence from one interrupted pushout test indicates that the interfacial failure sequence in the Ta-coated sapphire/Ti-48-1 system *characterized during testing* over a 254 μm diameter support hole is unaffected when specimen bending is eliminated. The SLM surface profile measurements of fiber displacement on a Ni back-plated specimen (i.e., see Table 5) indicate that, just as in tests using a 254 μm diameter support hole: (1) interfacial failure initiates on the specimen's backface and (2) the backface debond crack appears to propagate over half of the total distance up along the fiber/matrix interface before a mode II crack initiates on the topface (i.e., also see Table 7). Furthermore, Figure 57a shows that, during the last stages of interfacial failure in a Ni back-plated specimen, the topface interfacial crack deviates into the fiber and leaves a bonded fiber fragment adhering to the matrix. This behavior was observed in 2 out of 3 Ni back-plated specimens of the Ta-coated sapphire/Ti-48-1 system. Figure 57b is a corresponding SLM surface profile measurement made at a fiber perimeter position similar to that shown in Figure 57a (but from another Ni back-plated specimen). Examination of this micrograph reveals that plastic deformation of the matrix occurs in the region adjacent to the bonded fiber fragment (arrowed). From several other SLM surface profile measurements of matrix deformation at the specimen's topface adjacent to the bonded interface ligament, the average plastic shear strain in an ≈26 μm wide strip of matrix at P_{max} was calculated to be ≈0.02 from using equation (15). (This is an average value from measurements made on a total of 3 specimens.) This plastic shear strain value is similar to the value of ≈0.03 previously calculated in Ta-coated sapphire/Ti-48-1 specimens supported over a 254 μm diameter hole (i.e., see section 4.3.2.1). Thus, these

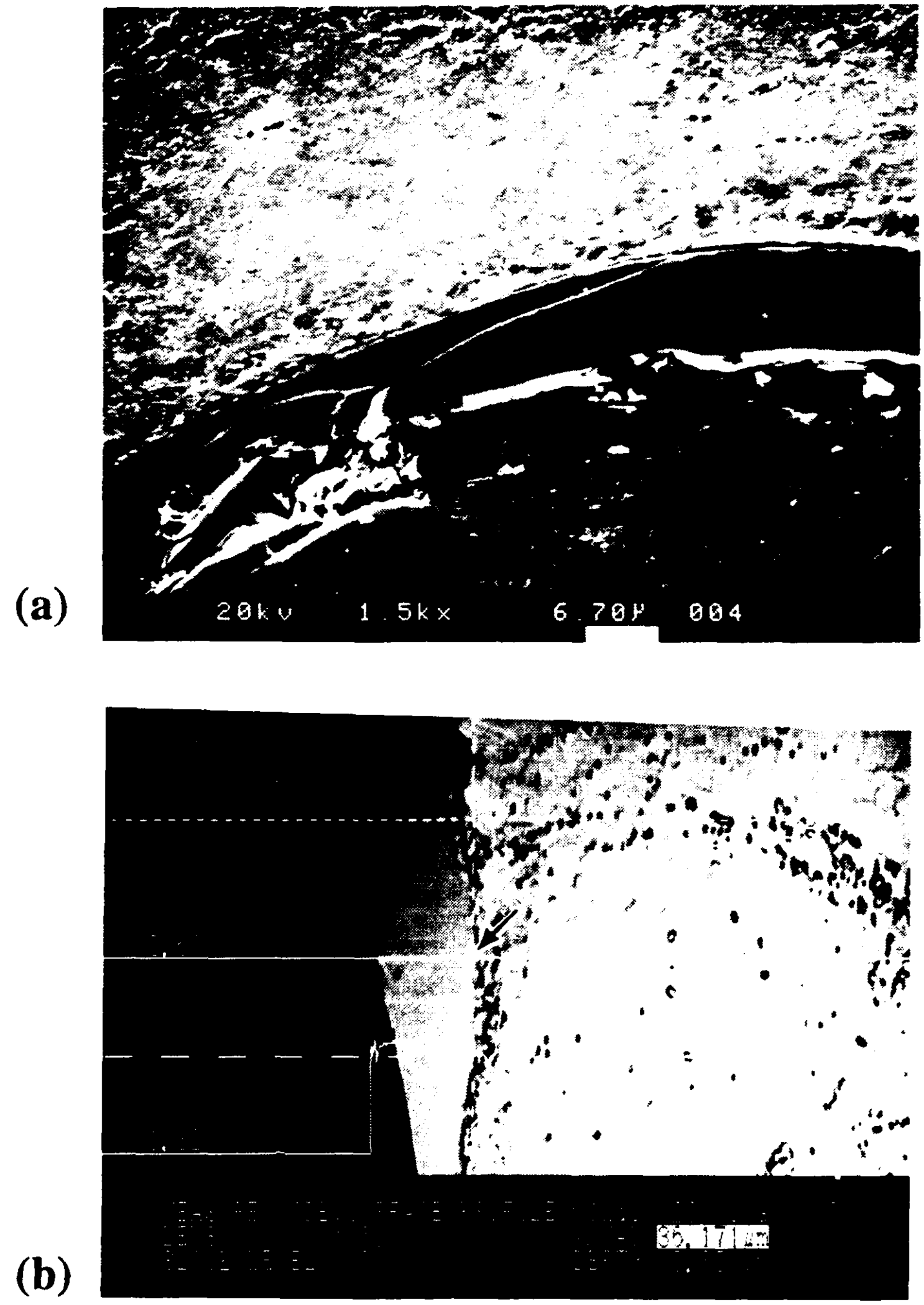

Figure 57. Evidence that the interfacial failure sequence in the Ta-coated sapphire/Ti-48Al-1V system is unaffected by test configuration. (a) A fiber fragment remains bonded to the matrix and (b) a corresponding surface profile measurement reveals that matrix deformation occurs in the region adjacent to the bonded fiber fragment.

observations substantiate that: (1) the general interfacial failure sequence in the Ta-coated sapphire/Ti-48-1 system is unaffected by the absence of specimen bending and (2) the fiber/matrix interface is not weakened by possible chemical attack during the photolithographic and electroplating procedures.

Reference to the values of τ_{AVG} at P' and P_{max} given in Table 9 for the sapphire/Ti-48-2-2 system indicates that test configuration (i.e., with or without specimen bending) has no effect on the measured values. In addition, evidence from SLM surface profile measurements of fiber displacement indicates that there is no change in the interfacial failure sequence (i.e., from that previously described in section 4.3.2.2) when specimen bending is eliminated. Comparison of fiber displacement measurements on samples tested with and without specimen bending (i.e., see Table 6) show that regardless of test configuration: (1) interfacial failure initiates on the specimen's backface at approximately the same average applied interfacial shear stress value, (2) the backface debond crack appears to propagate over half of the total distance up along the fiber/matrix interface before a mode II crack initiates on the topface (i.e., also see Table 8), and (3) the fiber is debonded along its entire length at indenter loads greater than P' (i.e., also see Figure 55).

Insight into why the measured values of τ_{AVG} at P' and P_{max} are lowered in the Ta-coated sapphire/Ti-48-1 system and unaffected in the sapphire/Ti-48-2-2 system when pushout tests are performed using Ni back-plated specimens can be gained by considering the influence of support hole-to-fiber diameter ratio on the mechanically-induced stress states within the matrix adjacent to the fiber. This has been studied by Kallas [84, 105] in the sapphire-reinforced NiAl system using the same finite element model as described in sections 4.2.2.1 and 4.3.1. The results of this study are shown in Figure 58 (taken from Koss et al. [105]). Comparison of Figure 58a (support hole-to-fiber diameter ratio of 2)

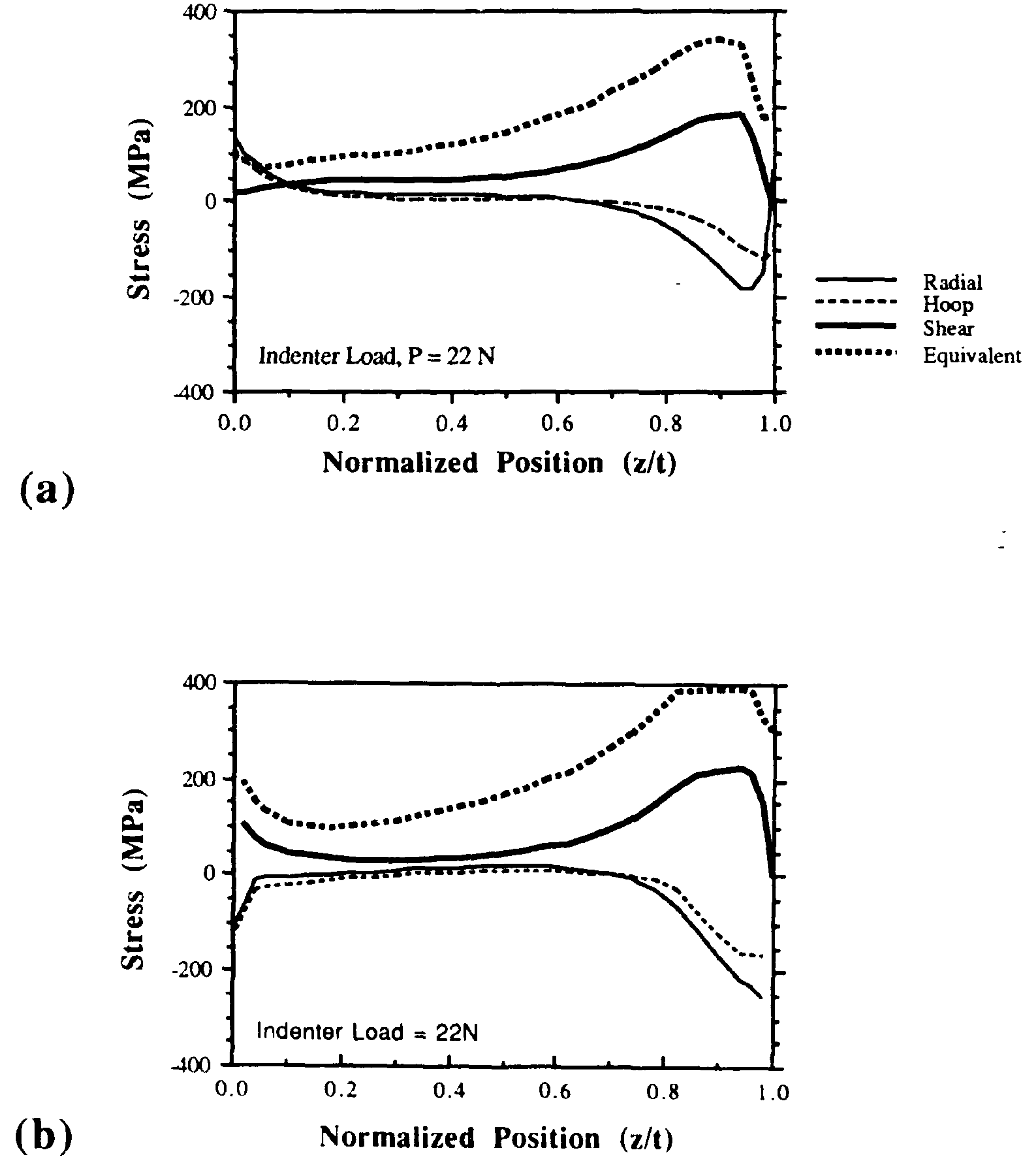

Figure 58. The influence of support hole-to-fiber diameter ratio on the mechanically-induced stress distributions within the matrix adjacent to the fiber for the sapphire/NiAl system (taken from Koss et al. [105]). Indenter load is 22 N and the support hole-to-fiber diameter ratios are (a) 2 and (b) 1.

with Figure 58b (support hole-to-fiber diameter ratio of 1) indicates that specimen support over a Ni back-plate results in stress distributions similar to support over a larger (i.e., 254 μm diameter) hole *except* for: (1) the absence of radial tensile stresses at the specimen's backface and (2) the increase in shear stress near the topface, but more notably at the backface of the specimen [105]. The sharp increase in shear stress at the backface is probably due to stress concentration at the Ni plate's edge. Although the elastic and plastic properties of the NiAl matrix differ from those of TiAl, the general trends in mechanical response shown in Figure 58 may also be assumed to occur in the sapphire/TiAl system.

In view of the fact that the elimination of radial bending stresses and an increase in shear stresses (most notably at the specimen's backface) *decreases* the measured τ_{AVG} values at P' and P_{max} in the Ta-coated sapphire/Ti-48-2-2 system, it appears that the criterion for interfacial shear failure is: (1) based on the maximum shear stress at the interface [123] and (2) not as sensitive to the development of radial tensile stresses induced by specimen bending as initially believed. Furthermore, examination of the mechanically-induced and the combined thermal and mechanical interfacial stress states plotted in Figures 40a and 41 respectively reveals that large radial tensile stresses induced by specimen bending develop only along the bottom 5% of the fiber/matrix interface. Thus, the influence of these bending-induced stresses on the overall interfacial shear behavior may not be very significant.

Since the magnitude of the mechanically-induced interfacial shear stress at the specimen's backface (i.e., shown in Figure 58b) scales with indenter load, its relative influence on interfacial shear behavior will depend on the applied load, which in turn is sensitive to the interfacial shear strength of the composite system. Thus, for IMCs with a weak or moderate fiber/matrix bond strength which require a relatively low indenter load to initiate a backface interfacial crack (e.g., the sapphire/Ti-48-2-2 system), the influence of the mechanically-induced interfacial stress component modified by the specimen support configuration (i.e., shear stress for Ni back-plated specimens and radial stress for specimens supported over a hole) is relatively small. As a result, the interfacial failure sequences and measured shear strength values for weakly to moderately bonded systems are relatively insensitive to the specimen support configuration. Even in composite systems with a relatively high interfacial bond strength, e.g., the Ta-coated sapphire/Ti-48-1 system, the influence of the type of specimen support employed during thin-slice pushout testing is not as important as initially believed.

4.3.5. Contribution of Matrix Plasticity to the "Frictional" Sliding Resistance of Debonded Fibers

In an attempt to quantify the shear behavior of a fiber/matrix interface in brittle matrix composites, both mechanics and experimental approaches have separated the interfacial shear process into two distinct events: (1) interface debonding characterized by an average interfacial shear strength (i.e., τ_{AVG} at P_{max}) and (2) subsequent large-scale fiber displacement described by a "frictional" sliding stress[o] (i.e., τ_{slide}) [72, 77, 78]. In the previous sections, attention was focused primarily on the interfacial failure sequences that lead to complete fiber debond (usually accompanied by a load-drop). This is usually interpreted in terms of fiber/matrix interface crack initiation and propagation, resulting in small-scale (< 1.5 to 2.0 μm) fiber displacement. In this section, results from large-scale fiber pushout and reverse push-back tests, coupled with SEM examination of the fiber/matrix interface, are used to address the "frictional" sliding resistance of debonded fibers and its role in interface wear/degradation when matrix plasticity occurs.

---

[o] The term "frictional sliding stress" is commonly used to describe the interfacial shear stress that resists large-scale fiber displacement following complete fiber debond. For most MMCs and IMCs, however, the sliding stress is not purely frictional, i.e., in order to accommodate asperities on the fiber surface, it must be of sufficient magnitude to plastically deform the matrix.

The large-scale "frictional" sliding behavior of debonded fibers during pushout and reverse push-back testing was similar in both the Ta-coated sapphire/Ti-48-1 and sapphire/Ti-48-2-2 systems. In both systems, the average fiber sliding stress (τ_{slide}) was found to be ≈160 MPa (from 6 tests) immediately following load-drop, but, after fiber displacements totaling ≈180 μm, τ_{slide} decreased to values ranging from 50 to 80 MPa (from 2 tests). Typical fiber sliding behavior during pushout and reverse push-back tests is shown in Figure 59. In order to account for the continuous change in interfacial area during large-scale fiber displacement, the interfacial shear stress (i.e., indenter load divided by the instantaneous interfacial area) is plotted as a function of cross-head displacement in this figure for a sapphire/Ti-48-2-2 specimen. An examination of the sliding stress response during forward pushout reveals that, following complete fiber debond (which signals the onset of large-scale fiber displacement), τ_{slide} decreases rapidly with increasing fiber displacement. Upon loading the fiber in the reverse direction, the stress increases until fiber displacement resumes. Again, τ_{slide} decreases with increasing fiber displacement, but at a slower rate.

By considering the generalized fiber sliding law proposed by Liang and Hutchinson [78] (see equation (8)), a decrease in τ_{slide} may be explained in terms of a decrease in the constant friction term (τ_0)[p] or the radial clamping stress (σ_{rr}) or both. In previous studies of SCS-6 (SiC) fiber-reinforced glass and metal matrix composites [85-87] (i.e., see section 2.7), the observed decrease in τ_{slide} during continued fiber displacement was accounted for by a decrease in τ_0 and σ_{rr} due to the fracture and wear of the outer carbon

---

[p] As previously noted in section 2.7, Mackin et al. [85] suggested that the constant friction term, τ_0, is the sliding stress that would be experienced by the fiber if $\sigma_{rr} = 0$, i.e., τ_0 is governed by the surface roughness of the fiber.

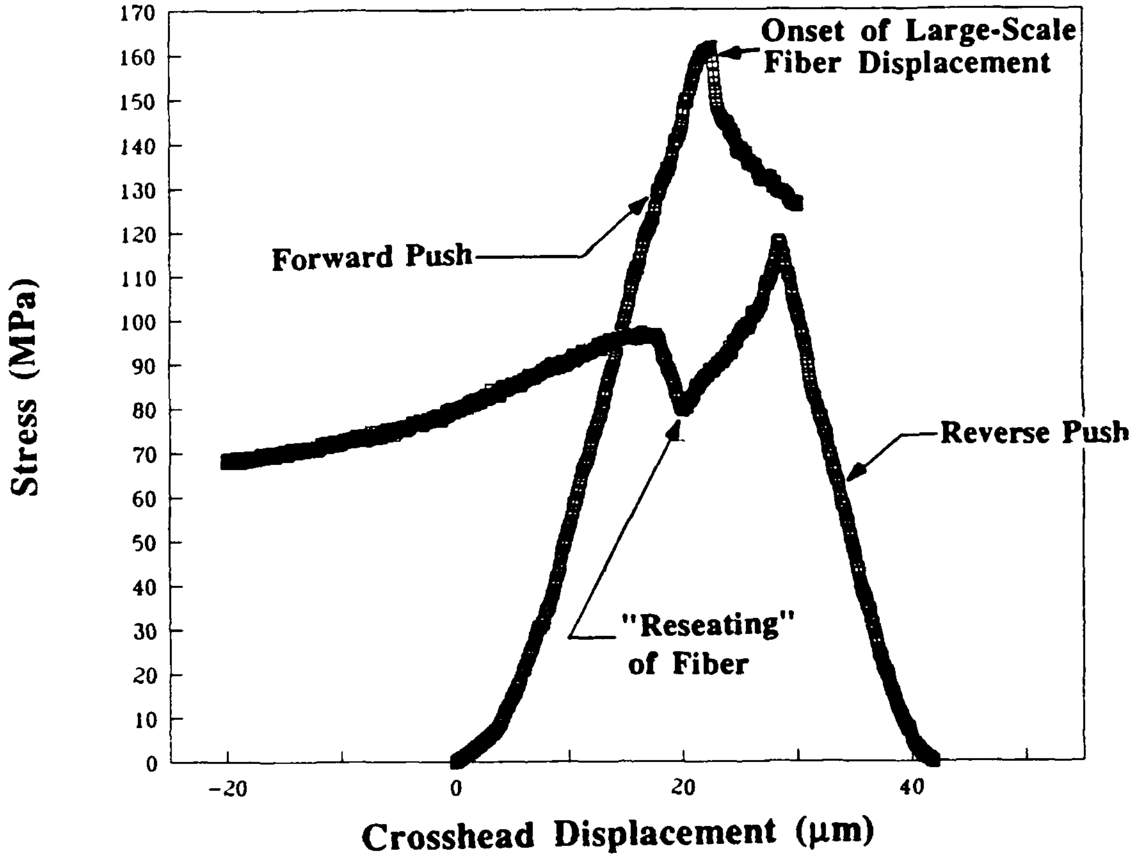

Figure 59. Typical fiber sliding behavior during pushout and reverse push-back tests of a sapphire/Ti-48Al-2Cr-2Nb specimen. In order to account for the continuous change in interfacial area during large-scale fiber displacement, interfacial shear stress is plotted as a function of cross-head displacement.

coatings on the SCS-6 fiber. (One exception was proposed by Mackin et al. [85, 86], who suggested that matrix plasticity may account for a reduction in radial clamping during pushout testing of a SiC/β-Ti system. However, they gave no explanation of how this may occur.)

In the sapphire/TiAl system, where fiber roughness/asperities will not "wear" as readily, it is suggested that matrix plasticity plays a dominant role in the observed decrease in τ_{slide}. For example, a decrease in the constant friction term (τ_0) may occur by wide-spread grooving of the matrix during continued fiber displacement as previously shown in Figures 48, 50, and 51, and not by fiber asperity wear. Thus, during continued fiber displacement, the fiber roughness perceived by the matrix decreases as the deformation-induced grooving increases. This effect should be most pronounced when the fiber is pushed-back in the reverse direction. In this case, the asperities are accommodated in the grooves formed during the forward push. As a result, the stress required to resume fiber displacement in the reverse direction is smaller than the sliding stress measured when the forward pushout test was stopped (i.e., see Figure 59).

Matrix plastic deformation during large-scale fiber displacement may also give rise to the relaxation of radial clamping on the fiber. However, in order to relieve fiber/matrix misfit strain, material must be removed from the interface [86]. By adapting the elasticity solution for internal pressure within a cylinder, Kantzos [90] used the following expression to calculate the thickness (t') of a concentric cylinder of material that must be removed from around the fiber in order to fully relax the residual radial clamping stress (σ_{rr}):

$$t' = \sigma_{rr}\left[\frac{R\left(1+\nu^{m}\right)}{E^{m}}\right]\left[\frac{V_f^{-1}+\left(\frac{1-\nu^{m}}{1+\nu^{m}}\right)}{V_f^{-1}-1}\right], \tag{23}$$

where R is the fiber's radius, V_f is the fiber volume fraction, ν^m is the Poisson's ratio of the matrix, and E^m is the matrix's elastic modulus. By substituting the appropriate values for the sapphire/TiAl system (i.e., see section 4.3.3) into equation (23) and solving for t', this solution predicts that only a 0.10 to 0.12 µm thick concentric cylinder of matrix material must be removed from the interface in order to fully relax radial clamping on the fiber.

Experimental evidence previously shown in Figure 52a suggests that fiber asperities in the sapphire/Ti-48-2-2 system remove matrix material from the interface during fiber pushout. It appears that this material remains adhered to the pushed-out fiber surface. This may account for the rapid decrease in τ_{slide} during forward fiber displacement shown in Figure 59 for this system, since only a relatively small amount of matrix material must be removed to relax the radial clamping stress. In contrast, an examination of the backface of Ta-coated sapphire/Ti-48-1 specimens reveals that very little matrix material appears to remain on the fiber during fiber pushout (i.e., see Figure 52b). This is consistent with the observation that τ_{slide} appears to decrease less rapidly during the initial forward push in the Ta-coated sapphire/Ti-48-1 system. (This observation was made when the sliding stress response of 2 out of a total of 3 large-scale fiber pushout tests of the Ta-coated sapphire/Ti-48-1 system was compared to that of 2 similar tests of the sapphire/Ti-48-2-2 system.)

Evidence that matrix material is removed from the interface during reverse push-back testing was previously shown in Figures 51a and b. These figures reveal that, as the fiber is pushed back in the reverse direction, matrix material is plowed out in front of it. Furthermore, close examination of Figure 51a shows that the continuous ribbons of material plowed out of the Ti-48-2-2 matrix are at least 0.1 μm thick. Thus, the measured decrease in τ_{slide} during reverse push-back testing can be directly related to the resulting relaxation of radial clamping on the fiber.

Another distinctive feature of the stress versus cross-head displacement response during the reverse push-back test shown in Figure 59 is the abrupt stress increase as the fiber is pushed back beyond its original position (i.e., the "origin"). In CMCs, however, "fiber reseating" is manifested by a distinct load (or stress) drop. Assuming that the fiber and matrix deform in a purely elastic manner, Jero et al. [65, 66] have given the following explanation for the fiber reseating phenomenon in CMCs: The translation of initially mating rough surfaces results in a radial displacement of the matrix equal to the amplitude of the fiber roughness [67]. This elastic displacement results in a compressive stress that adds to the existing radial clamping and subsequently increases τ_{slide}. When the fiber is pushed back to its original position, the fiber and matrix surface topographies mesh, and the additional sliding friction associated with their misfit disappears (resulting in a load drop in the load-displacement response) [65].

In IMCs (and MMCs), however, the matrix deforms elastically and plastically during fiber sliding. From the data presented in the papers by Warren et al. (SiC/β-Ti alloy) [86], Kantzos et al. (SiC/Ti-24Al-11Nb) [87], and Eldridge (SiC/Ti-24Al-11Nb) [88], fiber reseating is manifested by a distinct load increase, as it is in this study. The distinctively different behavior found between CMCs and IMCs (as well as MMCs) can be attributed to the manner in which the matrix deforms to accommodate asperities on the fiber surface during large-scale fiber displacement. In IMCs (and MMCs), fiber displacement requires matrix plasticity in the form of grooves to accommodate the fiber asperities, not elastic radial displacement as in the case of CMCs. When the fiber is pushed back to its original position, the asperities on the fiber surface, which had been accommodated in the grooves formed during the forward push, must now form new grooves in the matrix in order for continued fiber displacement to occur. Thus, as shown in Figure 59, fiber reseating is manifested by a temporary pause in fiber displacement as the interfacial shear stress increases to the magnitude required to form new grooves in the matrix. By comparing the slope of the stress versus displacement plot at fiber reseating with that before large-scale fiber displacement resumes (i.e., during the reverse push), it is evident that fiber displacement temporarily stops at the fiber's origin until sufficient stress is applied to re-initiate the grooving operation.

Finally, it was found that with increasing amounts of fiber displacement during forward pushout, the load increase at fiber reseating decreases. In fact, for fibers that undergo displacements >120 μm (during the forward push), evidence of fiber reseating disappears. The same explanation given for the decrease in the constant friction term (τ_0) during continued fiber displacement can be given for these observations: Grooving of the matrix becomes more wide-spread as fiber displacement increases. Thus, after large fiber displacements during the forward push, so much deformation-induced grooving of the matrix occurs that the fiber roughness perceived by the matrix becomes negligible. As a result, little or no additional stress is required for the fiber to be pushed back beyond its original position. Similar behavior during reverse push-back tests of a SiC-reinforced β-Ti composite has been reported by Mackin [89] for fibers displaced >60 μm during the forward push and Warren et al. [86] for specimens previously subjected to cyclic fatigue.

Chapter 5

SUMMARY

Interfacial shear behavior and its influence on fiber damage in sapphire fiber-reinforced TiAl composites was investigated using a combination of microscopic characterization, indentation crack growth results, thin-slice fiber pushout testing, fiber displacement measurements, and computational stress state analysis. Due to the nature of this investigation, results are separated into two, but inter-related, parts: (1) residual stresses and resulting damage within fibers intersecting a free surface and (2) fiber/matrix interfacial strength behavior.

The first part of this investigation was initiated by the observation that specimens of uncoated sapphire/Ti-48-1 contained fibers with cracks at their ends, regardless of the cross-sectioning or specimen preparation technique used. Crack depth measurements showed that incrementally removing the matrix by chemical etching caused the surface cracks to propagate, resulting in "split" fibers. On the other hand, fibers in the Ta-coated sapphire/Ti-48-1 and sapphire/Ti-48-2-2 systems did not contain cracks when they intersected a free surface.

Finite element and analytical analyses were performed to predict the thermally-induced residual stress states within a fiber intersecting a free surface for two different orientations: (1) the fiber axis normal to the surface and (2) the fiber axis parallel to the surface. Assuming a perfectly bonded fiber/matrix interface, both analyses predict that significant residual tensile stresses exist in sapphire fibers embedded within TiAl-based matrices when they intersect a free surface. Given a fiber of low fracture toughness, a high interfacial shear strength, and the presence of a surface flaw or crack, the computations suggest that the thermally-induced tensile stresses within the fiber may propagate the flaw or crack to a length dictated by the stress state and fracture toughness. Furthermore, subsequent removal of the matrix will cause the crack to propagate as the free surface and stress state are spatially displaced. Indentation crack growth behavior within the sapphire fibers (1) provided experimental verification of the FEM predicted stress state and (2) indicated that smaller thermally-induced residual stresses exist within fibers in the Ta-coated sapphire/Ti-48-1 and sapphire/Ti-48-2-2 systems than are predicted for a perfectly bonded sapphire-reinforced TiAl composite. Regardless of the orientation of a fiber with respect to a free surface, the results indicate that compliant fiber coatings (as in the Ta-coated sapphire/Ti-48-1 system) or a decreased interfacial shear strength (as in the sapphire/Ti-48-2-2 system) can decrease the thermally-induced tensile stresses and reduce or eliminate fiber damage.

The interfacial shear behavior was examined using thin-slice fiber pushout testing. The results (from specimens supported over a hole ≈1.6 times that of the fiber diameter) show that the Ta-coated sapphire/Ti-48-1 system had an average interfacial shear strength of 336.3 ± 11.2 MPa. However, in the sapphire/Ti-48-2-2 system, a much lower value, 170.5 ± 22.3 MPa, was measured. Since fibers in specimens of uncoated sapphire/Ti-48-1 were cracked, testing of this system was impossible.

Regardless of the significant difference in measured shear strengths, a comparison of the interfacial failure sequences in these two systems revealed several important similarities. First, interfacial failure was found to initiate at the specimen's backface, opposite the indenter. This is a significant observation since conventional analyses of the fiber pushout test assume that interface shear initiates near the topface (i.e., near the indenter). However, examination of the FEM predicted stress distribution along the fiber/matrix interface reveals that the net interfacial shear stress is actually larger at the specimen's backface than at the topface. Therefore, as a result of the thin-slice geometry of the specimen and magnitude of the thermally-induced residual stresses, the overall interfacial stress state dictates that interfacial failure should initiate on the backface. Furthermore, quantitative estimates suggest that the backface debond crack may propagate over half of the total distance up along the fiber/matrix interface before shear displacement initiates at the topface.

Differences in the sequences leading to interfacial failure do exist between the two systems. These differences can be directly attributed to the interface bond strength/fracture resistance of each system. In the Ta-coated sapphire/Ti-48-1 system, which appears to have a "high" bond strength, the interface debond crack does not encompass the entire perimeter of the fiber. Instead, it deviates into the matrix on the backface and into the fiber on the topface, leaving behind a fiber fragment adhering to the matrix following pushout. Even at loads approaching P_{max}, approximately 40% of the fiber's perimeter remains bonded along its entire length. Complete debond is accompanied by a large load-drop which indicates that a significant amount of elastic strain energy was required to propagate an interface crack and completely debond the interface.

In the sapphire/Ti-48-2-2 system, however, the debond crack initiates at the backface at a much lower load and quickly propagates around the fiber's entire perimeter. At loads greater than P' (where $P' \approx 0.7\ P_{max}$), the fiber becomes debonded along its entire length and topface fiber displacement initiates. Subsequent stable displacement (i.e., < 1.5 to 2.0 μm) of the debonded fiber occurs with increasing load up to P_{max}. Given the very rough fiber surface in this system, it is suggested that fiber surface asperities prevent large-scale fiber displacement until plastic deformation occurs in the layer of material through which the asperities are "plowed." The transition from fiber debond to fiber sliding is a nearly continuous process as evidenced by little or no load-drop at the onset of large-scale fiber displacement.

Results from previous studies suggest that specimen bending during thin-slice fiber pushout testing may create interfacial failure sequences that are test dependent and result in lower measured interfacial shear strength values [68]. Therefore, to determine the influence of specimen bending, comparative tests were performed using either (1) a support hole-to-fiber diameter ratio of ≈1.6 or (2) a support hole the same size and shape as the fiber's cross-section. A significant result is that the interfacial failure sequence in both composite systems appears to be unaffected by specimen bending. Furthermore, the measured values of the average interfacial shear strength at P' and P_{max} were actually lowered (especially at P') in the Ta-coated sapphire/Ti-48-1 system and unchanged in the sapphire/Ti-48-2-2 system when bending-induced stresses were eliminated. FEM computations indicate that using a support hole the same size and shape as the fiber's cross-section eliminates radial tensile stresses at the specimen's backface, but also increases the interfacial shear stress near the top and, more notably, at the backface. In view of the experimental results, this suggests that the criterion for interfacial shear during thin-slice fiber pushout testing is: (1) based on the critical value of the shear stress along the interface [123] and (2) not particularly sensitive to the development of bending-induced radial tensile stresses.

Finally, results from fiber pushout and reverse push-back tests were used to address the contribution of matrix plasticity to the "frictional" sliding resistance of debonded fibers and its role in interface wear/degradation. It was found that the large-scale sliding behavior of debonded fibers was similar in both composite systems and resulted in "frictional" sliding stress (i.e.,τ_{slide}) values of ≈160 MPa immediately following load-drop; these subsequently decreased to values ranging from 50 to 80 MPa following fiber displacements totalling ≈180 μm. Previous studies have attributed the decrease in τ_{slide} to the fracture and wear of fiber asperities [85-87]. However, given an IMC (or MMC) in which fiber asperities do not easily wear (e.g., the sapphire/TiAl system), it is shown that matrix plasticity plays a dominant role in the decrease of τ_{slide} with fiber displacement. Experimental evidence suggests that the observed decrease in τ_{slide} can be attributed to (1) a decrease in fiber roughness perceived by the matrix due to wide-spread matrix grooving and (2) a relaxation of radial clamping as a result of material removal from the interface.

REFERENCES

1. J. M. Larsen, W. C. Revelos, and M. L. Gambone, in "Intermetallic Matrix Composites II," edited by D. B. Miracle, D. L. Anton, and J. A. Graves, Mater. Res. Soc. Proc. 273, Pittsburgh, PA (1992) pp. 3-16.
2. H. G. Gray and C. A. Ginty, in "HITEMP Review 1991," NASA CP 10082, NASA Lewis Research Center, Cleveland, OH (1991) pp. 1-1 - 1-28.
3. J. S. Petty and T. G. Fecke, ibid., pp. 2-1 - 2-6.
4. T. M. F. Ronald, ibid., pp. 3-1 - 3-13.
5. G. J. DeBoer, "Titanium Aluminide Composites," Contract F33657-86-C-2136; P00014, G. E. Aircraft Engines, Cincinnati, OH (1991).
6. B. D. Agarwal and L. J. Broutman, "Analysis and Performance of Fiber Composites," John Wiley and Sons, Inc., New York, NY (1980) p. 33.
7. T. J. Mackin, J. Y. Yang, C. G. Levi, and A. G. Evans, accepted by Mater. Sci. Eng. (1992).
8. R. A. Amato, "Gamma Titanium Aluminide-Based Composites," G. E. Aircraft Engines Technical Memo., Cincinnati, OH (1991).
9. S. E. Bergquist and O. Y. Chen, "Sapphire Monofilament Reinforced Gamma Composites Study," Presentation at NASP Program Review, Pratt and Whitney Aircraft Div., East Hartford, CT (1989).
10. J-M. Yang, University of California, Los Angeles, CA, private communication (1992).
11. G. J. DeBoer, "Titanium Aluminide Composites," Contract F33657-86-C-2136; P00014, G. E. Aircraft Engines, Cincinnati, OH (1990).
12. J. A. Graves, Rockwell International Corp. Sci. Ctr., Thousand Oaks, CA, private communication (1991).
13. S. E. Bergquist, Pratt and Whitney Aircraft Div., East Hartford, CT, private communication (1991).
14. R. March, G. E. Aircraft Engines, Lynn, MA, private communication (1991).
15. J. W. Hutchinson, Harvard Univ., Cambridge, MA, via private communication with K. S. Chan, Southwest Research Inst., San Antonio, TX (1991).

16. J. M. Larsen, K. A. Williams, S. J. Balsone, and M. A. Stucke, in "High Temperature Aluminides and Intermetallics," edited by S. H. Whang, C. T. Liu, D. P. Pope, and J. O. Stiegler, TMS/ASM International, Metals Park, OH (1990) pp. 521-556.

17. S. Nourbakhsh and H. Margolin, in "Metal and Ceramic Matrix Composites: Processing Modeling and Mechanical Behavior," edited by R. B. Bhagat, A. H. Clauer, P. Kumar, and A. M. Ritter, The Minerals, Metals, and Materials Society, Warrendale, PA (1990) pp. 75-89.

18. S. Krishnamurthy, Y-W. Kim, G. Das, and F. H. Froes, ibid., pp. 145-155.

19. B. N. Cox, M. R. James, D. B. Marshall, W. L. Morris, and M. Shaw, in "Proceedings of the Department of Defense 8th Metal Matrix Composites (MMC) Technology Conference," MMCIAC - Kaman Tempo, Santa Barbara, CA (1989) pp. 18-1 - 18-8.

20. J. A. Graves and C. C. Bampton, "Direct Consolidation of Titanium Aluminide Matrix Composites Using Blended Powder: Quarterly Technical Report No. 3," Contract NAS1-18604, Rockwell International Corp. Sci. Ctr., Thousand Oaks, CA (1989).

21. C. G. Rhodes, C. C. Bampton, and J. A. Graves, in "Intermetallic Matrix Composites," edited by D. L. Anton, P. L. Martin, D. B. Miracle, and R. McMeeking, Mater. Res. Soc. Proc. 194, Pittsburgh, PA (1990) pp. 349-354.

22. L. J. Ghosn and B. A. Lerch, "Optimum Interface Properties for Metal Matrix Composites," NASA TM 102295, NASA Lewis Research Center, Cleveland, OH (1989).

23. S. M. Arnold, V. K. Arya, and M. E. Melis, "Elastic/Plastic Analyses of Advanced Composites Investigating the Use of a Compliant Layer Concept in Reducing Residual Stresses Resulting from Processing," NASA TM 103204, NASA Lewis Research Center, Cleveland, OH (1990).

24. S. M. Arnold and T. E. Wilt, "Influence of Engineered Interfaces on Residual Stresses and Mechanical Response in Metal Matrix Composites," NASA TM 105438, NASA Lewis Research Center, Cleveland, OH (1992).

25. Y-W. Kim and D. M. Dimiduk, J. of Metals, 43, 8 (1991) pp. 40-47.

26. Y-W. Kim, J. of Metals, 41, 7 (1989) pp. 24-30.

27. E. L. Hall and S. C. Huang, in "High-Temperature Ordered Intermetallic Alloys III," edited by C. T. Liu, A. I. Taub, N. S. Stoloff, and C. C. Koch, Mater. Res. Soc. Proc. 133, Pittsburgh, PA (1989) pp. 693-698.

28. R. P. Nimer, unpublished report, G. E. Corporate Research and Development, Schenectady, NY (1990).

29. H. E. LaBelle, Jr., J. Crystal Growth, 50, 9 (1980) pp. 8-17.

30. T. A. Hahn, "Standard Reference Material 732: Single Crystal Sapphire - Thermal Expansion," National Bureau of Standards, Washington, D. C. (1977).

31. D. Jewitt and M. Harrison, in "Proceedings of the Department of Defense 8th Metal Matrix Composites (MMC) Technology Conference," MMCIAC - Kaman Tempo, Santa Barbara, CA (1989) pp. 4-1 - 4-8.

32. L. Mitchell, "Saphikon Sapphire," Technical Data Sheet, Saphikon, Inc., Milford, NH.

33. R. F. Cook, J. Mater. Res., 1, 6 (1986) pp. 852-860.

34. S. M. Wiederhorn, J. Am. Ceram. Soc., 52, 9 (1969) pp. 485-491.

35. R. E. Tressler and R. L. Crane, in "Advanced Materials: Composites and Carbon," Am. Ceram. Soc., Columbus, OH (1972) pp. 59-68.

36. C. A. Calow and A. Moore, J. Mater. Sci., 7 (1972) pp. 543-558.

37. R. L. Mehan and T. A. Harris, "Stability of Oxides in Metal or Metal Alloy Matrices," AFML-TR-71-150, Air Force Materials Laboratory, Wright-Patterson AFB, OH (1971).

38. J. T. A. Pollock, J. Mater. Sci., 7 (1972) pp. 631-648.

39. J. I. Eldridge, NASA Lewis Research Center, Cleveland, OH, private communication (1992).

40. A. K. Misra, submitted to Composites Sci. and Tech. (1992).

41. P. R. Smith, C. G. Rhodes, and W. C. Revelos, in "Interfaces in Metal-Ceramic Composites," edited by R. Y. Lin, R. J. Arsenault, G. P. Martins, and S. G. Fishman, TMS-AIME, Warrendale, PA (1990) pp. 35-58.

42. A. K. Misra, in "Advanced Metal Matrix Composites for Elevated Temperatures," ASM International, Metals Park, OH (1991) pp. 49-56.

43. F. E. Wawner and D. B. Gundel, SAMPE Quarterly, 4 (1992) pp. 13-19.

44. B. N. Cox, M. R. James, D. B. Marshall, and R. C. Addison, Met. Trans., 21A, (1990) pp. 2701-2707.

45. S. D. Tsai, D. Mahulikar, H. L. Marcus, I. C. Noyan, and J. B. Cohen, Mat. Sci. Eng., 47 (1981) pp. 145-149.

46. K. L. Sewak, "Characterization of Interfacial Properties in Metal Matrix Composites," B. S. Thesis, The Pennsylvania State Univ., University Park, PA (1990).

47. A. G. Evans, in "Ceramic Microstructures '86: Role of Interfaces," edited by J. A. Pask and A. G. Evans, Mater. Sci. Res. 21, Plenum Press, New York, NY (1986) pp. 775-794.

48. R. P. Nimer and E. S. Russell, unpublished report, G. E. Aircraft Engines, Lynn, MA (1990).

49. A. K. Misra and S. M. Arnold,"Compliant Layer for the Ti_3Al+Nb/SCS-6 Composite System," NASA TM 105344, NASA Lewis Research Center, Cleveland, OH (1991).

50. G. A. Cooper and A. Kelly, in "Interfaces in Composites," ASTM STP 452, ASTM, Philadelphia, PA (1968) pp. 90-106.

51. R. J. Kerans, P. D. Jero, T. A. Parthasarathy, and A. Chatterjee, in "Intermetallic Matrix Composites," edited by D. L. Anton, P. L. Martin, D. B. Miracle, and R. McMeeking, Mater. Res. Soc. Proc. 194, Pittsburgh, PA (1990) pp. 263-270.

52. B. D. Agarwal and L. J. Broutman, "Analysis and Performance of Fiber Composites," John Wiley and Sons, Inc., New York, NY (1980) pp. 72-75.

53. M. Taya and R. J. Arsenault, "Metal Matrix Composites," Pergamon Press, New York, NY (1989) pp. 69-70.

54. M. Taya and R. J. Arsenault, ibid., pp. 80-91.

55. B. D. Agarwal and L. J. Broutman, "Analysis and Performance of Fiber Composites," John Wiley and Sons, Inc., New York, NY (1980) pp. 260-261.

56. P. W. R. Beaumont, J. Adhes., 6 (1974) pp. 107-137.

57. D. A. Koss, The Pennsylvania State Univ., University Park, PA, lecture notes (1990).

58. R. E. Tressler, in "Composite Materials: Volume 1, Interfaces in Metal Matrix Composites," edited by A. G. Metcalfe, Academic Press, New York, NY (1974) pp. 285-328.

59. A. K. Misra, Met. Trans., 22A (1991) pp. 715-721.

60. J. A. Dekock, Y. A. Chang, M-X. Zhang, and O. Y. Chen, in "Interfaces in Composites," edited by C. G. Pantano and E. J. H. Chen, Mater. Res. Soc. Proc. 170, Pittsburgh, PA (1990) pp. 173-178.

61. D. S. Shih and R. A. Amato, Scripta Metall. Mater., 24, 11 (1990) pp. 2053-2058.

62. G. Das and S. Krishnamurthy, in "Intermetallic Matrix Composites II," edited by D. B. Miracle, D. L. Anton, and J. A. Graves, Mater. Res. Soc. Proc. 273, Pittsburgh, PA (1992) pp. 93-101.

63. G. Eriksson, Chemica Scripta, 8 (1975) pp. 100-103.

64. C. A. Moose, "Interfacial Shear Studies of Sapphire Fiber-Reinforced Nickel Aluminide Matrix Composites," M. S. Thesis, The Pennsylvania State Univ., University Park, PA (1991).

65. P. D. Jero and R. J Kerans, Scripta Metall. Mater., 24, 12 (1990) pp. 2315-2318.

66. P. D. Jero, R. J. Kerans, and T. A. Parthasarathy, J. Am. Ceram. Soc., 74, 11 (1991) pp. 2793-2801.

67. R. J. Kerans and T. A. Parthasarathy, J. Am. Ceram. Soc., 74, 7 (1991) pp. 1585-1596.

68. D. A. Koss, M. N. Kallas, and J. R. Hellmann, in "Intermetallic Matrix Composites II," edited by D. B. Miracle, D. L. Anton, and J. A. Graves, Mater. Res. Soc. Proc. 273, Pittsburgh, PA (1992) pp. 303-313.

69. L. S. Sigl and A. G. Evans, Mech. Mater., 8 (1989) pp. 1-12.

70. A. G. Evans, A. Bartlett, J. B. Davis, B. D. Flinn, M. Turner, and I. E. Reimanis, Scripta Metall. Mater., 25 (1991) pp. 1003-1010.

71. M-Y. He and J. W. Hutchinson, Inst. J. Solids and Structures, 25, 9 (1989) pp. 1053-1067.

72. A. G. Evans, F. W. Zok, and J. Davis, Composites Sci. and Tech., 42 (1991) pp. 3-24.

73. S. M. Cardonne, P. Kumar, C. A. Michaluk, and H. D. Schwartz, Adv. Mater. and Proc., 142, 3 (1992) pp. 16-20.

74. W. D. Klopp, D. J. Maykuth, and H. R. Ogden, in "High Temperature Materials II," edited by G. M. Ault, W. F. Barclay, and H. P. Munger, Interscience Publishers, Cleveland, OH (1961) pp. 171-185.

75. A. Joshi, H. S. Hu, and J. Wadsworth, in "Interfaces in Composites," edited by C. G. Pantano and E. J. H. Chen, Mater. Res. Soc. Proc. 170, Pittsburgh, PA (1990) pp. 149-154.

76. S. Das and J. H. Perepezko , Scripta Metall. Mater., 25, 5 (1991) pp. 1193-1198.

77. J. W. Hutchinson and H. M. Jensen, Mech. Mater., 9 (1990) pp. 139-163.

78. C. Liang and J. W. Hutchinson, Harvard University, Cambridge, MA (1992) to be published.

79. M. K. Ferber, C. Hsueh, R. A. Lowden, and A. A. Wereszazak, "Interface Studies in Continuous Fiber Ceramic Composites," CFCC Working Group Meeting, Oak Ridge National Laboratory, Oak Ridge, TN (1992).

80. D. B. Marshall, J. Am. Ceram. Soc., 67, 12 (1984) pp. C-259 - C-260.

81. D. B. Marshall and W. C. Oliver, J. Am. Ceram. Soc., 70, 8 (1987) pp. 542-548.

82. D. B. Marshall, Acta Metall. Mater., 40 (1991) p. 427.

83. T. A. Parthasarathy, P. D. Jero, and R. J. Kerans, Scripta Metall. Mater., 25 (1991) p. 2457.

84. M. N. Kallas, D. A. Koss, H. T. Hahn, and J. R. Hellmann, J. Mater. Sci., 27 (1992) pp. 3821-3826.

85. T. J. Mackin, P. D. Warren, and A. G. Evans, Acta Metall. Mater., 40, 6 (1992) pp. 1251-1257.

86. P. D. Warren, T. J. Mackin, and A. G. Evans, Acta Metall. Mater., 40, 6 (1992) pp. 1243-1249.

87. P. T. Kantzos, J. I. Eldridge, D. A. Koss, and L. J. Ghosn, in "Intermetallic Matrix Composites II," edited by D. B. Miracle, D. L. Anton, and J. A. Graves, Mater. Res. Soc. Proc. 273, Pittsburgh, PA (1992) pp. 135-142.

88. J. I. Eldridge, ibid., pp. 325-330.

89. T. J. Mackin, University of California, Santa Barbara, CA, private communication (1992).

90. P. T. Kantzos, "Fatigue Crack Growth and Crack Bridging in Ti-Based Metal Matrix Composites," M. S. Thesis, The Pennsylvania State Univ., University Park, PA (1991).

91. M. Calabrese, Rockwell International Corp. Sci. Ctr., Thousand Oaks, CA, private communication (1991).

92. D. B. Marshall, ibid.

93. J. M. Galbraith, M. N. Kallas, D. A. Koss, and J. R. Hellmann, in "Intermetallic Matrix Composites II," edited by D. B. Miracle, D. L. Anton, and J. A. Graves, Mater. Res. Soc. Proc. 273, Pittsburgh, PA (1992) pp. 119-126.

94. B. R. Lawn and E. R. Fuller, Jr., J. Mater. Sci., 19 (1984) pp. 4061-4067.

95. D. B. Marshall and B. R. Lawn, J. Am. Ceram. Soc., 60, 1-2 (1977) pp. 86-87.

96. R. Tandon and D. J. Green, J. Am. Ceram. Soc., 73, 4 (1990) pp. 970-977.

97. M. F. Gruninger, B. R. Lawn, E. N. Farabaugh, and J. B. Wachtman, Jr., J. Am. Ceram. Soc., 70, 5 (1987) pp. 344-348.

98. J. R. Hellmann, D. A. Koss, C. A. Moose, R. R. Petrich, and M. N. Kallas, in "HITEMP Review 1990," NASA CP 10051, NASA Lewis Research Center, Cleveland, OH (1990) pp. 41-1 - 41-11.

99. B. R. Lawn and T. R. Wilshaw, J. Mater. Sci., 10 (1975) p. 1049.

100. B. R. Lawn and M. V. Swain, J. Mater. Sci., 10 (1975) p. 113.

101. D. B. Marshall and B. R. Lawn, J. Mater. Sci., 14 (1979) pp. 2001-2012.

102. B. R. Lawn, D. B. Marshall, and A. G. Evans, J. Am. Ceram. Soc., 63 (1980) pp. 574-581.

103. H. Tada, P. C. Paris, and G. R. Irwin, "The Stress Analysis of Cracks Handbook," Dell Research Corp., Hellertown, PA (1973) p. 24.2.

104. J. I. Eldridge and F. S. Honecy, in "HITEMP Review 1989," NASA CP 10039, NASA Lewis Research Center, Cleveland, OH (1989) pp. 74-1 - 74-10.

105. D. A. Koss, E. P. Rhyne, M. N. Kallas, and J. R. Hellmann, in "HITEMP Review 1992," NASA CP 10104, NASA Lewis Research Center, Cleveland, OH (1992) pp. 25-1 - 25-12.

106. "KTI Negative Photoresists," Technical Data Sheet, KTI Chemicals Inc., Sunnyvale, CA.

107. "Video Rate Confocal Imaging," 1LM11 Confocal Scanning Laser Microscope Technical Data Sheet, Lasertec Corp., San Jose, CA.

108. C. A. Moose, The Pennsylvania State Univ., University Park, PA, private communication (1992).

109. S. K. Chapman, "Working with a Scanning Electron Microscope," Lodgemark Press LTD, Kent, England (1986) pp. 47-48.

110. T. R. Grossman, unpublished report, G. E. Aircraft Engines, Cincinnati, OH (1991).

111. R. R. Bowman, R. D. Noebe, J. Doychak, K. S. Crandall, and I. E. Locci, in "HITEMP Review 1991," NASA CP 10082, NASA Lewis Research Center, Cleveland, OH (1991) pp. 43-1 - 43-14.

112. R. R. Bowman, in "Intermetallic Matrix Composites II," edited by D. B. Miracle, D. L. Anton, and J. A. Graves, Mater. Res. Soc. Proc. 273, Pittsburgh, PA (1992) pp. 145-155.

113. S. L. Draper, I. E. Locci, and J. I. Eldridge, in "HITEMP Review 1992," NASA CP 10104, NASA Lewis Research Center, Cleveland, OH (1992) pp. 17-1 - 17-13.

114. E. R. Trumbauer, J. R. Hellmann, D. L. Shelleman, and D.A. Koss, submitted to J. Am. Ceram. Soc. (1992).

115. S. Krishnamurthy, in "Titanium Aluminide Composites-Workshop Proceedings," WL-TR-91-4020, Wright Laboratory, Wright-Patterson AFB, OH (1991) pp. 135-148.

116. L. S. Harbison, "Deformation and Fracture of Titanium Aluminide Alloys at High Strain-Rates," M. S. Thesis, The Pennsylvania State Univ., University Park, PA, (1991).

117. R. Tandon and D. J. Green, J. Am. Ceram. Soc., 74, 8 (1991) pp. 1981-1986.

118. S. M. Wiederhorn, in "Fracture Mechanics of Ceramics, Volume 2," edited by R. C. Bradt, D. P. H. Hasselman, and F. F. Lange, Plenum Press, New York, NY (1983) pp. 613-646.

119. M. Lee, I. Jasiuk, and E. Tsuchida, J. Appl. Mech., 114, 2 (1992) pp. S57-S64.

120. J. R. Brockenbrough, "An Al-Si-Mg Composite Model System: Influence of Particles on Thermally Induced Near-Surface Residual Stresses," Report No. 57-92-11, Alcoa Technical Center, Alcoa Center, PA (1992).

121. J. R. Hellmann, D. A. Koss, and C. G. Pantano, in "Advanced High Temperature Composite Materials for Engine Applications," Grant No. NAGW-1381 Annual Report, Center for Advanced Materials, The Pennsylvania State Univ., University Park, PA (1991) pp. 111-224.

122. G. E. Dieter, "Mechanical Metallurgy," 2nd edition, edited by B. J. Clark and M. Gardner, McGraw-Hill, New York, NY (1976) pp. 709-710.

123. J. R. Hellmann, D. A. Koss, C. G. Pantano, and M. N. Kallas, in "Advanced High Temperature Composite Materials for Engine Applications," Grant No. NAGW-1381 Annual Report, Center for Advanced Materials, The Pennsylvania State Univ., University Park, PA (1992) pp. 67-138.

Vita

JAY M. GALBRAITH, CAPT, USAF

Education

Doctor of Philosophy in Metals Science and Engineering, The Pennsylvania State University, research presented in this thesis.

Master of Science in Metallurgy, The Pennsylvania State University, May 1986, research on the Microstructural Characterization of Al-Cu-Li-Zr Alloys.

Bachelor of Science in Metallurgy Conferred With Distinction, The Pennsylvania State University, May 1981.

Experience

Assistant Professor, Department of Engineering Mechanics, United States Air Force Academy, Colorado Springs, CO, June 1986-July 1989.

Flight Crew Systems Branch Chief, 6595th Space Shuttle Test Group, Vandenberg AFB, CA, September 1981-November 1984.

Professional

Author or co-author of seven publications dealing with aluminum-copper-lithium-zirconium alloys and sapphire-reinforced gamma titanium aluminide composites.

Member of Tau Beta Pi, Alpha Sigma Mu, Phi Lambda Upsilon, and Golden Key National Honor Societies.

Member of the American Society for Metals, the Metallurgical Society of AIME, and the Materials Research Society.

Personal

Born on December 12, 1959, in Harrisburg, PA.

Interests include Bible study, family, and outdoor activities.